UNIVERSITÉ CATHOLIQUE DE LOUVAIN

FACULTÉ DES SCIENCES APPLIQUÉES
DÉPARTEMENT DE MÉCANIQUE

ACCURACY AND CONSISTENCY IN FINITE ELEMENT OCEAN MODELING

DOCTORAL DISSERTATION PRESENTED BY

LAURENT WHITE

IN FULFILLMENT OF THE REQUIREMENTS
FOR THE DEGREE OF
DOCTOR IN APPLIED SCIENCES

Prof. Eric Deleersnijder (Supervisor)	Université catholique de Louvain
Prof. Eric Delhez	Université de Liège
Prof. Thierry Fichefet	Université catholique de Louvain
Prof. Vincent Legat (Supervisor)	Université catholique de Louvain
Prof. David Marshall	University of Reading
Prof. Jean-François Remacle	Université catholique de Louvain
Prof. Jean-Claude Samin (Chair)	Université catholique de Louvain

LOUVAIN-LA-NEUVE
MARCH 2007

Acknowledgments

Over the last three years, during the preparation of this PhD dissertation, I have been very fortunate to benefit from the invaluable assistance of a number of people.

I am most grateful to Professor Eric Deleersnijder for his unconditional support and trust. Our collaboration dates back to the time when I was working on my final engineering project. Since then, his help, advices and scientific rigor have always been of great value and proven extremely useful. In particular, his near literal interpretation of the famous saying "publish or perish" is worth gold. I owe Eric a lot and I would not be writing these lines if it were not for him.

With the ability to conciliate mathematical rigor with a hint of fun, a touch of humanity and just plain common sense, Professor Vincent Legat knows how to motivate and encourage his researchers to reach their objectives. This has often proven invaluable to me. In particular, I truly appreciate how Vincent accepts to sit three hours in a row with you before a white board to understand and seek solutions to a problem that let me spend sleepless nights.

By inviting me in Australia for a month to participate in the one-week Rattray research cruise, Doctor Eric Wolanski allowed me to fully appreciate the wide gap separating out reality from numerical marine models. This experience combined with my very pleasant stay at AIMS, the parties organized at Eric's place and simply my being in Tropical Australia made this trip one of the best ever.

I also wish to thank all members of my PhD committee for their comments and suggestions. In particular, I am grateful to them for tacitly raising to my attention how fixing a presentation is definitely easier than answering follow-on questions.

My gratitude also goes to my colleages and friends in ASTR and MEMA; especially Olivier, Olivier, Olivier, Maxime and Christophe with whom I not only shared many lunch times but also a few memorable parties and dinners beyond office hours.

The time spent with some of my longstanding friends, and more specifically Greg and Nico, was an alleviating refuge away from work even though work, together with beer and wine, was often on the table during our long conversations.

I am so deeply grateful to my family that it goes beyond my ability to express it. If it were only for their constant support, their priceless availability and their driving trust in my achieving my goals over the last three years, I would not have to stress the fact that their personal achievements are a perennial source of inspiration for me. This work is for them.

With your unselfish support, continual encouragements and loving understanding during these past years over which you had to put up with my distresses and periods of bad spirit, Laura, I would not be much without you. And I promise that I will not

bring my laptop along on our honeymoon.

Contents

Chapter 1

Introduction

> "Our planet is invested with two great oceans; one visible, the other invisible; one underfoot, the other overhead; one entirely envelopes it, the other covers about two thirds of its surface" *Matthew F. Maury (1855) The Physical Geography of the Seas and Its Meteorology.*

The oceans play a crucial role in our climate. Because of the high heat capacity of water (2.5 m of the upper ocean is equivalent to the entire troposphere) and the oceans' large extent (they cover over 70% of the Earth's surface), oceans act as a gigantic thermal flywheel, mitigating the fluctuations of our long-term weather. They are also huge reservoirs of CO_2 (containing about 60 times the amount of CO_2 in the atmosphere) and have a long memory. Oceans therefore play a pivotal role in determining the climatic conditions on our planet on a large variety of timescales. However, we still do not understand well the intricate details of their circulation and their interaction with the atmosphere. Furthermore, the oceanographers are data-poor in general. Even today, there are many regions in the southern hemisphere where not a single in situ observation of ocean properties has ever been made. The tedium and expense of making in situ measurements placed a severe limit on our ability to explore oceanic processes. Yet, even if in situ measurements were available throughout the oceans, models would still be necessary to understand their complex functioning, for the sole knowledge of in situ observations would not suffice to infer the details of the oceans circulation. For predicting the future state of the oceans, and hence of the climate, numerical models are indispensable.

1.1   Selected history of numerical ocean modeling

The first ocean general circulation model (OGCM) is credited to Dr. Kirk Bryan at the Geophysical Fluid Dynamics Laboratory (Princeton, USA) in the late 60's (*Bryan*, 1969). He is regarded by many as the founding father of numerical ocean modeling. The GFDL model was based upon a discretization of the equations of motions using low-order finite differences. Many improvements have occurred over the following years; among them the inclusion of free-surface dynamics (*Killworth et al.*, 1991), the

development of hybrid vertical coordinates (*Bleck*, 1978) and state-of-the-art parameterizations for unresolved processes such as vertical turbulence (*Mellor and Yamada*, 1982) and isopycnal mixing (*Redi*, 1982; *Gent and McWilliams*, 1990), to name just a few (thorough reviews are presented by *Griffies et al.* (2000) and *Griffies* (2004)). Some of the emerging models are highly modular, well documented and widely used such that POM (Princeton Ocean Model), MOM (Modular Ocean Model), MICOM (Miami Isopycnic Coordinate Ocean Model), HYCOM (HYbrid Coordinate Ocean Model), OPA (Océan PArallélisé), MITgcm (Massachusetts Institute of Technology Global Circulation Model). If current operational ocean models can be differentiated by their underlying parameterizations, often directed at better modeling selected processes, they share a common feature. The geophysical fluid dynamics equations are solved on structured grids using the finite difference method. Therefore, the discretization paradigm remains the same as that of Bryan's model. Some properties of structured grids, or lack thereof, tend to gradually render them out of date for ocean modeling while, at the same time, so-called second-generation ocean models, based on unstructured meshes, become increasingly popular.

The intrinsic flexibility of unstructured meshes is indeed compelling for numerical marine modeling. Unstructured meshes have the potential of circumventing the pole singularities encountered when using structured grids aligned with converging meridians. This can be done more elegantly than with structured meshes for which common tricks to avoid the singularities include using two (north) poles (OPA) or a spherical cube (MITgcm). Complex topographic features, such as coastlines, islands, narrow straits and sills, can faithfully be represented by locally increasing the mesh resolution and because there is no constraint on the mesh topology (e.g., *Legrand et al.*, 2006). The resolution can also be altered based upon other criteria such as the bathymetry (*Gorman et al.*, 2006; *Legrand et al.*, accepted) or the value of a state variable (*Legrand et al.*, 2000). In the latter case, the mesh can be dynamically adapted in the course of the simulation (*Piggott et al.*, 2005; *Power et al.*, 2006). Given the wide range in spatial scales of biophysical processes taking place in the ocean (Figure 1.1), a variable mesh resolution (in time and space) across the flow domain is of particular interest. Resolving the mesoscale variability in a large-scale ocean model without having to refine the mesh everywhere is now deemed feasible if mesh adaptivity is resorted to appropriately. Some illustrations of unstructured meshes are provided in Figures (1.2)-(1.4). Over the last decade, motivated by these concepts, there has been increasing effort into the development of marine models based on unstructured meshes. Three classes of numerical methods can readily handle unstructured meshes: the finite volume (FV), the spectral element (SE) and the finite element (FE) methods.

To a certain extent, each of these methods has been gaining popularity in the ocean modeling community. The FV method has been lately generalized to use unstructured orthogonal grids (*Casulli and Walters*, 2000; *Ham et al.*, 2005; *Fringer et al.*, 2006; *Stuhne and Peltier*, 2006), thereby enhancing its flexibility. It is also much appreciated for its properties of local conservation in terms of numerical fluxes across the boundary of each control volume, rendering the method well suited for transport problems (*Casulli and Zanolli*, 2005). The SE method forms the basis of SEOM (Spectral Element Ocean Model) described by *Iskandarani et al.* (1995) and *Iskandarani et al.*
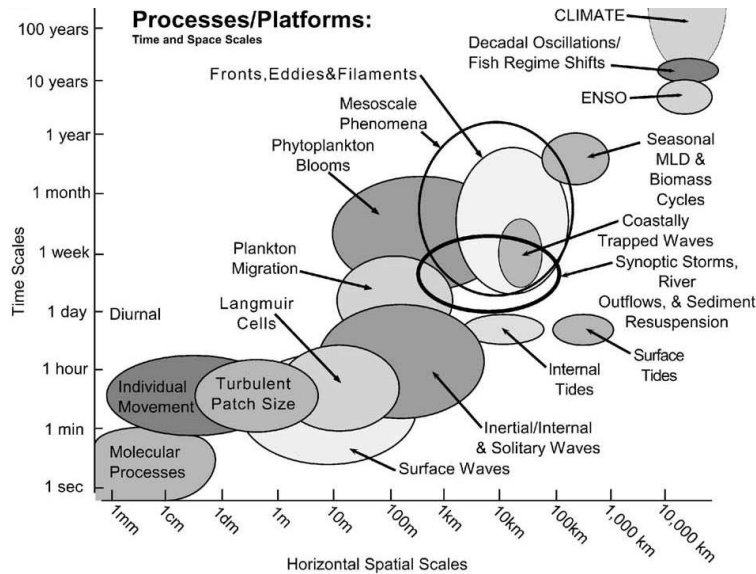
Figure 1.1: Time and horizontal space scales of some physical and biological processes in the ocean, from *Dickey* (2003).

(2003). A variant of SEOM based on a discontinuous representation of scalars and elevation is described by *Levin et al.* (2006). In principle, the SE method can handle unstructured meshes. However, using high-order spectral elements for the oceans with irregular boundaries typically lead to Gibbs oscillations in the numerical solution. The ocean modeling community is currently moving away from using the SE method on unstructured meshes. However, the method remains successful in atmospheric modeling, where using structured meshes is more appropriate. The use of the FE method for coastal, shelf and estuarine areas started somewhat earlier (*Lynch and Werner*, 1987; *Walters and Werner*, 1989; *Lynch and Werner*, 1991). During the nineties, aside from some results obtained with diagnostic finite element ocean models (*Myers and Weaver*, 1995; *Greenberg et al.*, 1998), we did not really see any revolutionary change. Over the last five years, with the initiation of new projects of finite element global ocean models, such as FEOM (Finite Element Ocean circulation Model) from the Alfred Wegener Institute for Polar and Marine Research, ICOM (Imperial College Ocean Model) from Imperial College and SLIM (Second-generation Louvain-la-Neuve Ice-ocean Model) from Université catholique de Louvain, we have been witnessing a new wave of thriving development (and funding) of prognostic finite element ocean models. As warranted by the literature, the FE method appears to be the most promising (e.g., *Pietrzak et al.*, 2005, 2006). There might be two main reasons for this. All the methods mentioned can handle unstructured meshes indeed but the finite element method offers additional flexibility in the choice of interpolation (it can be of low or high order and continuous or discontinuous) and is sustained by a rigorous mathematical framework, in which a priori and a posteriori error estimates can be established and upon which mesh adaptivity takes place.

3
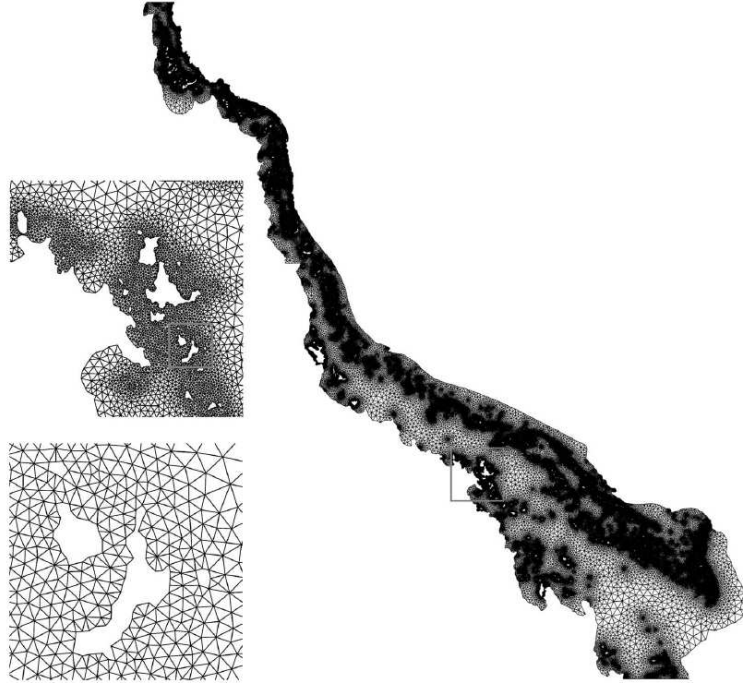
Figure 1.2: Mesh of the Great Barrier Reef (northeast Australia) with blowups of the Whitsunday area, from *Legrand et al.* (2006). The mesh size varies from 1 km to 20 km.

The idea of using the FE method for marine modeling together with unstructured meshes dates back to the work by *Fix* (1975), who was probably the first in the literature to recognize the potential of variable mesh resolution for ocean flows. The first developments of finite element marine models were based on the wave continuity equation (*Lynch and Gray*, 1979), whereby the primitive shallow-water equations are manipulated to form a wave equation for the free-surface elevation, with a subsequent harmonic decomposition in time. This formulation does not suffer from spurious oscillations occurring when using the primitive equations and the same interpolation for the velocity and the elevation. The generalization of the original method led to the generalized wave continuity equation (GWCE), documented by *Kinnmark* (1986) and *Kolar et al.* (1994). The GWCE has been extensively used over the past 20 years with successful applications in coastal regions for tidal predictions (*Lynch and Werner*, 1987, 1991; *Walters and Werner*, 1989; *Walters*, 1992; *Lynch and Naimie*, 1993; *Luettich and Westerink*, 1995; *Ballantyne et al.*, 1996; *Lynch et al.*, 1996; *Fortunato et al.*, 1997; *Cushman-Roisin and Naimie*, 2002). Despite these encouraging applications and the ongoing research to improve the method, it remains plagued by two caveats. (1) GWCE-based models are subject to advective instabilities (*Kolar et al.*, 1994). (2) The GWCE form sacrifices the primitive continuity equation, thus the primitive form is no longer satisfied in a discrete sense, which implies continuity (or mass) imbalances (*Blain and Massey*, 2005; *Dawson et al.*, 2006; *Massey and Blain*, 2006), rendering the method less suitable for coupling with transport equations, let alone for long time integrations (more than several years) in which conservation is crucial.
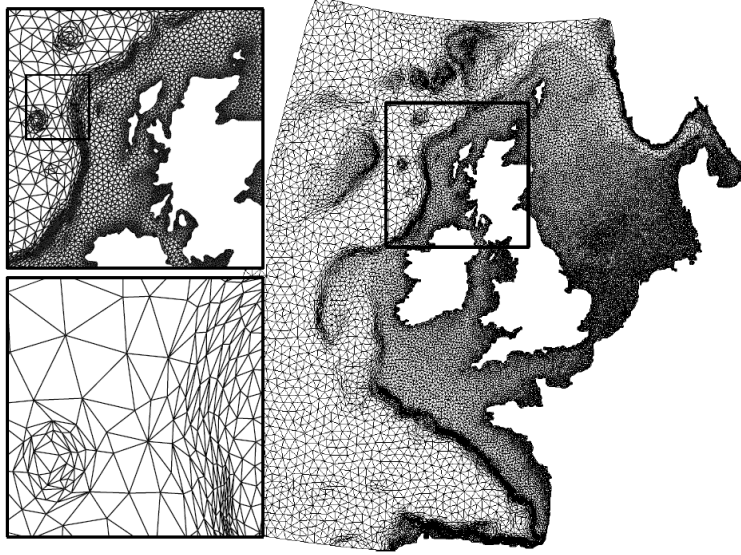
Figure 1.3: Mesh of the Northwestern European continental shelf with recursive blowups of the Hebridean shelf and Anton Dohrn seamount, from *Legrand et al.* (accepted).The mesh size varies from 0.5 km to 5 km.

In the meantime, more efforts have been directed towards finding a mixed finite element pair for the primitive shallow-water equations that does not support spurious oscillations (see e.g., *Hua and Thomasset*, 1984). Aware of the limitations of the GWCE and urged to develop primitive equations finite element ocean models, research towards this goal have intensified since the end of the nineties (*Le Roux et al.*, 1998; *Le Roux*, 2001; *Hanert et al.*, 2003; *Le Roux*, 2005; *Le Roux et al.*, 2005; *Walters*, 2006; *White et al.*, 2006b; *Le Roux et al.*, in press). Early issues of the method often cited as reasons not to use it – such as spurious oscillations, unphysical wave scattering due to the unstructured character of the mesh and lack of mass conservation – are starting to wither. Nowadays, applications of FE shallow-water models based on the primitive equations are becoming much less of an exception (*Nechaev et al.*, 2003; *Danilov et al.*, 2004; *Ford et al.*, 2004a,b; *Pain et al.*, 2004; *Danilov et al.*, 2005; *Hanert et al.*, 2005; *Labeur and Pietrzak*, 2005; *Walters*, 2006; *White et al.*, 2006a; *White and Deleersnijder*, in press; *White et al.*, submitted) and this trend is unlikely to lose its momentum.

Finite element methods based on the primitive equations encompass both the continuous Galerkin (CG) and discontinuous Galerkin (DG) methods. The latter applied to the shallow-water equations is newer than the former and has much to offer for solving hyperbolic systems of equation (*Flaherty et al.*, 2002) and advection-dominated flows (e.g., *Hanert et al.*, 2004; *Kubatko et al.*, 2006a) in general. Furthermore, the method is known to conserve flow properties elementwise in the intuitive meaning of the FV method (as opposed to the local conservation property of CG methods described by *Hughes et al.* (2000)). At least for now, DG methods remain less mature
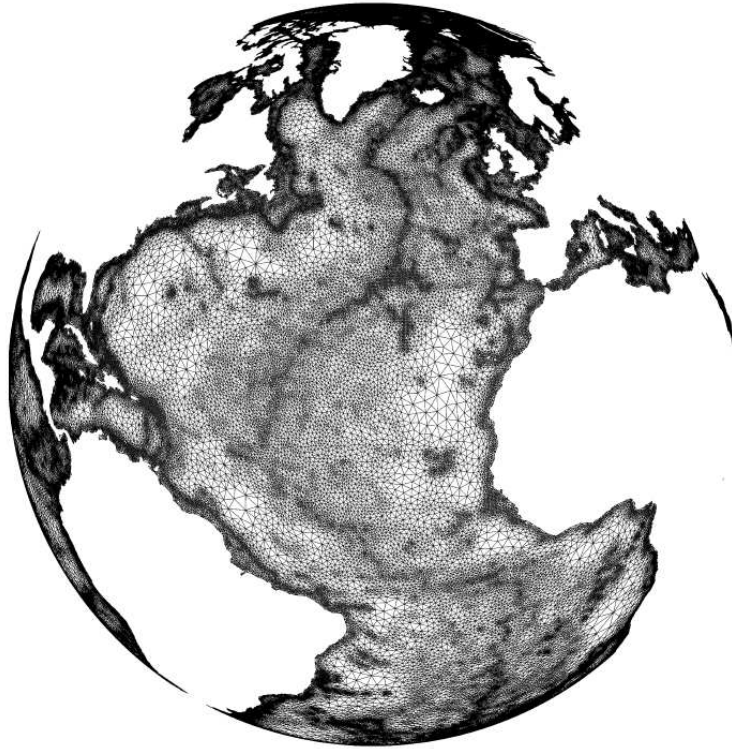
Figure 1.4: Mesh of the globe, from *Gorman et al.* (2006).

than CG methods for ocean modeling. They have nonetheless been gaining popularity for modeling shallow-water flows as well (*Schwanenberg et al.*, 2000; *Aizinger and Dawson*, 2002; *Schwanenberg and Harms*, 2004; *Nair et al.*, 2005; *Remacle et al.*, 2005; *Dawson et al.*, 2006; *Kubatko et al.*, 2006a; *Remacle et al.*, 2006; *White et al.*, 2006b; *Bernard et al.*, accepted) and are particularly well suited for transport problems (*Kubatko et al.*, 2006b).

1.2 Thesis objectives

This thesis was undertaken under the auspices of the SLIM[1] project that aims at building an unstructured mesh, finite element OGCM based on the primitive equations. It remains unclear at this stage whether the CG or the DG method is preferable for simulating shallow-water flows. Both methods have their advantages and drawbacks in terms of accuracy, robustness and efficiency. In this work, we do not intend to discriminate one method in favor of the other. As it turns out when flipping the pages of this thesis, each method happens to outperform the other depending on the application at hand.

---

[1]Second-generation Louvain-la-Neuve Ice-ocean Model (`http://www.climate.be/SLIM`).

The ultimate objective of this thesis is to provide the prototype of a three-dimensional, finite-element, marine circulation model, which solves the primitive equations and includes the following prominent features.

- The three-dimensional mesh is based on the downard extrusion of a two-dimensional, triangular, unstructured mesh. The extrusion generates columns that are subsequently split into prisms.

- The free-surface dynamics is included and the domain is allowed to move in the vertical to accomodate the free-surface motions and to respond to freshwater forcings.

- Mass and tracers are globally conserved up to machine precision. All equations are solved consistently so that a uniform tracer concentration remains equal to the initial value at all time, no matter which dynamics is considered but provided that there is no source term and no boundary flux.

- Stabilization is not required. The numerical solution does not support spurious oscillations.

- The dynamics and the equations are split between the external and internal modes. The external mode is solved semi-implicitly in time, which allows for using a unique time step for both modes.

- The computational cost of the solution scales linearly like the number of two-dimensional vertices. No system need be solved in three dimensions.

- Earlier studies within the research team have been fully taken into account. The two-dimensional structure of the current model relies on the work by *Hanert et al.* (2005).

In essence, the model that we present is fully operational to simulate three-dimensional flows in planar geometry without baroclinic forcing. Yet, it is conceived in such a way that any tracer can readily be added and will evolve in a conservative fashion.

1.3   Thesis synopsis

The free-surface dynamics is included in the model via the solution to the external mode (i.e., barotropic mode), for which an effective technique must be devised. In **Chapter 2**, we assess the accuracy and robustness of some finite element methods in solving the one-dimensional linearized shallow-water equations. The problem has a known analytical solution that includes a discontinuity in the elevation. The hyperbolic nature of the system of equations is emphasized by using the method of characteristics. While the continuous Galerkin method is shown to perform quite poorly, the discontinuous Galerkin method proves to be very accurate and robust, provided that the adequate numerical fluxes be enforced. In particular, it is shown that computing the right numerical fluxes comes down to weakly enforcing the continuity of the characteristic variables. This is the so-called Riemann solver used in higher dimensions for which a local change of variables allows to reduce the problem dimensions to one in the direction normal to the element boundary (edge or face).

An ocean model should be built with the physics in mind. We must not expect that any all-purpose computational fluid dynamics code will be able to decently model oceanic flows if it is not tailored to do so in the first place. Here, we opt for a step-by-step approach in which validation of each physical component is a key aspect. Since we not only aim at resolving the large-scale circulation but also most energetic mesoscale processes, it is of paramount importance to represent the mesoscale variability with as much accuracy as possible. Mesoscale variability partly originates from baroclinic instabilities and, to a lesser extent, from barotropic instabilities. In **Chapter 3**, we concentrate on the latter and evaluate three finite-element formulations in their ability to accurately represent geophysical fluid flow instabilities. Physical dissipation is absent from the equations, making it a challenging test case for numerical methods where any numerical dissipation is likely to produce erroneous results.

Large-scale free-surface ocean models designed to run over climatic timescales are required to globally conserve the volume and any tracer up to machine precision. In addition, the following property is critical. Setting a tracer to a uniform value throughout the closed domain and letting the free surface undulate, we must recover the same tracer concentration at any later time if there is no tracer source. This property of consistency, together with monotonicity, will ensure that no spurious tracer extrema occur. In **Chapter 4**, it is shown that achieving consistency requires a discrete compatibility between the tracer and continuity equations. In addition, to ensure global tracer conservation in a consistent way, a discrete compatibility between the tracer, continuity and free-surface equations must be fulfilled. It is suggested that this compatibility constraint, together with the use of a numerically stable scheme, severely restricts the choice of three-dimensional spatial discretizations.

In **Chapter 5**, the full three-dimensional model is presented. Since all but the momentum equations are treated in the previous chapter, only the momentum equations are considered in detail in this last chapter. The time-stepping algorithm is fully described. The model is validated against a realistic flow around a shallow-water island for which field measurements are available. A convergence analysis is carried out and we show that, as the mesh resolution is increased, the model is able to predict the correct velocity field in the island's wake. Very intense upwelling is also predicted off the northern island's tip during ebb and flood. We suggest that this upwelling might be the main cause for the presence of mud at the surface, rather than the much weaker upwelling predicted near the center of the eddies.

Marine flows are intrinsically complex and appropriate interpretation techniques ought to be used to fully exploit the results of a given model. A few two-dimensional cuts within the three-dimensional computational domain at some times gives a poor rendition of otherwise multidimensional processes involving several variables. Holistic tools, which take into account all processes and their history, are more appropriate. Among those tools are timescales such as the age and the residence time. In **Chapter 6**, the concept of age is used to devise two diagnoses of vertical transport in the vicinity of a shallow-water island, subject to tidal flow. The results confirm the presence of strong upwelling off the island's tip, suggested in the previous chapter.

Conclusions and perspectives are given in **Chapter 7**.

1.4 Supporting publications

This work is based upon the contents of the following refereed publications (published, in press or submitted). The publications for which I am not first author are not considered in this list.

1. White, L., Legat, V., Deleersnijder, E., Le Roux, D. (2006). A one-dimensional benchmark for the propagation of Poincaré waves. *Ocean Modelling*, 15, 101-123.

2. White, L., Beckers, J.-M., Deleersnijder, E., Legat, V. (2006). Comparison of free-surface and rigid-lid finite element models of barotropic instabilities. *Ocean Dynamics*, 56, 86-103.

3. White, L., Deleersnijder, E. Diagnoses of vertical transport in a three-dimensional finite-element model of the tidal circulation around an island. *Estuarine, Coastal and Shelf Science* (in press).

4. White, L., Deleersnijder, E., Legat, V. A three-dimensional unstructured mesh finite element marine model, with application to the flow around a shallow-water island. *Journal of Geophysical Research* (submitted[2]).

5. White, L., Legat, V., Deleersnijder, E. Tracer conservation in a three-dimensional, finite element, free-surface marine model on moving unstructured meshes. *Monthly Weather Review* (submitted[3]).

I have also contributed to the following publications.

1. Gourgue, O., Deleersnijder, E., White, L. Toward a generic method for studying water renewal, with application to the epilimnion of Lake Tanganyika. *Estuarine, Coastal and Shelf Science* (submitted[4]).

2. Blaise, S., White, L., Remacle, J.-F., Deleersnijder, E. Influence of the turbulence closure scheme on the finite-element simulation of the tidal flow around a shallow-water island. *Continental Shelf Research* (submitted[5]).

---

[2]Submission date: 18 October 2006
[3]Submission date: 9 January 2007
[4]Submission date: 10 August 2006
[5]Submission date: 8 December 2006

Chapter 2

Finite element methods for the external mode

Summary

Some finite element methods are employed to solve the linear shallow-water equations describing the propagation of Poincaré waves within a one-dimensional finite domain. An analytical solution to the problem, set off by a discontinuous steplike elevation, is known and allows for assessing the accuracy and robustness of each method. We evaluate the method of characteristics, the continuous Galerkin method and the discontinuous Galerkin method with two ways of computing the numerical fluxes.

Motion in the ocean spans a very wide range of timescales. While the large-scale circulation is characterized by velocities on the order of up to one meter per second and timescales that can be as large as hundreds of years, the fast-propagating inertia-gravity waves exhibit phase velocities on the order of hundreds of meters per second and much smaller timescales. Internal gravity waves propagate with velocities on the order of one meter per second or less. The vast disparity of ocean processes timescales poses a challenge in numerical ocean modeling. If an explicit time step is used, it is limited by the so-called Courant-Friedrichs-Lewy (CFL) condition, which states that the time step should not be larger than the travel time of the fastest physical process over the smallest space increment. In free-surface ocean models that allow for the existence of external inertia-gravity (Poincaré) waves, the upper bound on the time step is far smaller than more practical time steps that would permit time integration over thousands of years on today's computers. The first attempt at circumventing this problem by replacing the free surface by a rigid lid – thereby eliminating external inertia-gravity waves – has been widely dismissed. Among the rationales for such a design are that a rigid lid distorts the properties of large-scale barotropic Rossby waves, does not permit tidal modeling and complicates the inclusion of surface freshwater fluxes (*Killworth et al.*, 1991; *Dukowicz and Smith*, 1994; *Deleersnijder and Campin*, 1995; *Hallberg*, 1997; *Higdon and Szoeke*, 1997; *Griffies et al.*, 2000).

A common alternative no longer relies on the rigid-lid approximation. The ocean surface is free and remains a prognostic variable but the governing equations are split into subsystems that model the fast and slow motions separately. These subsystems are generally referred to as the barotropic and baroclinic systems, respectively, or the external and internal modes, respectively. Fast motions are approximately independent of the vertical coordinate z so that the external mode is two-dimensional and is well represented by the shallow-water equations that model the motion of fluid layers of constant density. Slow motions are fully three-dimensional, however, but the restriction on the time step is dictated by the internal dynamics, of which timescales are several orders of magnitude larger than that of the external mode. The latter can be solved explicitly with small time steps or implicitly with larger time steps. Choosing an implicit treatment eliminates the constraint imposed by the CFL condition but leads to large systems to be solved at each time step. This choice can be made for tidal and tsunami calculations provided that a reduced time step be used. If an explicit approach is considered for the barotropic mode, the number of small barotropic time steps for each large baroclinic time step is roughly the ratio of barotropic inertia-gravity wave speed to baroclinic internal gravity wave speed (*Killworth et al.*, 1991). Details on mode splitting implementations can be found in *Blumberg and Mellor* (1987), *Hallberg* (1997), *Higdon and Szoeke* (1997) and *Higdon* (2002).

Large-scale oceanic motions roughly obey the geostrophic equilibrium. When imbalances occur, the geostrophic balance is restored by means of Poincaré waves. In strongly stratified seas, internal inertia-gravity waves are generated when displacement of density surfaces occurs. Those waves respond to the same physical mechanism as external Poincaré waves (*Gill*, 1982). In models allowing for the existence of inertia-gravity waves, it is of paramount importance to represent those waves accurately. In that respect, the coupled issues of time and space discretization ought to be focused on. Time stepping is beyond the scope of this chapter (see e.g., *Beckers and Deleersnijder*, 1993) as we mainly concentrate on spatial discretization. A one-dimensional benchmark for the propagation of Poincaré waves is proposed. This problem bears many similarities with the classical geostrophic adjustment initially studied by Rossby and further investigated by *Gill* (1976) for the linear part and *Kuo and Polvani* (1996) for its nonlinear counterpart. In this chapter, the linearized shallow-water equations, in which homogeneity is assumed in the y-direction, are solved in a domain of finite length with an initial discontinuous elevation field. The design difference with adjustment problems lies in the finiteness of the domain in the x-direction. Whereas in adjustment problems, an infinite domain in the x-direction is considered, we study the case of Poincaré waves propagation in a finite domain. In so doing, no end state is ever reached and, in the absence of friction, wave propagation goes on forever within the domain. The persistence of the discontinuities is the prominent feature of the time-dependent solution presented by *Gill* (1976). It also appears in the solution to our benchmark, thereby posing a challenge for classical numerical methods to solve the problem. A numerical method will be appraised based upon its ability to capture the traveling discontinuity without generating spurious oscillations. The following methods are considered: the method of characteristics, the Galerkin finite element method (FEM) and the discontinuous Galerkin FEM with two different ways of computing the numerical fluxes.

2.1 A one-dimensional benchmark

The linearized governing equations for a single, inviscid, homogeneous shallow layer of fluid on an f-plane are the shallow-water equations, given by

$$
\begin{aligned}
\frac{\partial u}{\partial t} - fv &= -g\frac{\partial \eta}{\partial x}, \\
\frac{\partial v}{\partial t} + fu &= -g\frac{\partial \eta}{\partial y}, \\
\frac{\partial \eta}{\partial t} + h\frac{\partial u}{\partial x} + h\frac{\partial v}{\partial y} &= 0,
\end{aligned}
\tag{2.1}
$$

where u and v are the vertically-averaged horizontal velocity components in the x- and y-directions, respectively. The reference layer thickness is constant and denoted by h while η represents the free surface elevation. The Coriolis parameter f is taken to be constant under the f-plane approximation. Finally, g is the gravitational acceleration.

Linearization implies getting rid of advective terms and assuming that the free surface elevation be much smaller than the constant reference depth (i.e., $\eta \ll h$). The disposal of advective terms is legitimate as long as the Rossby number is much smaller than 1, in which case inertial terms are not dominant. We decide to focus on a set of linear equations, mainly for the sake of simplicity and because we will be able to interpret the results in the best way.

Within the frame of this work, we will further assume homogeneity in the y-direction so that all derivatives with respect to y vanish. The domain is thus infinite in the y-direction, which reduces the problem to a one-dimensional case. The domain remains finite in the x-direction. It should be noted that the problem we propose to solve does not consist of an adjustment problem as in *Gill* (1976) in which the domain is infinite – or large enough so that it can be deemed so numerically, as explained in *Kuo and Polvani* (1996). In that respect, we do not focus on the final state, which does not exist for finite domains. Instead, we study the wave propagation phenomenon. Reducing the system (2.1) to the unique x-direction yields

$$
\begin{aligned}
\frac{\partial u}{\partial t} - fv &= -g\frac{\partial \eta}{\partial x}, \\
\frac{\partial v}{\partial t} + fu &= 0, \\
\frac{\partial \eta}{\partial t} + h\frac{\partial u}{\partial x} &= 0,
\end{aligned}
\tag{2.2}
$$

where $x \in [-L/2, L/2]$ and $t \geq 0$. The boundary conditions are $u(x = \pm L/2, t) = 0$, which merely consists of boundary impermeability. We study the time evolution of an initially motionless fluid layer with a discontinuity in the elevation field. Thus, at $t = 0$

$$
\begin{aligned}
u(x,0) = v(x,0) &= 0, \\
\eta(x,0) = \eta_{\mathrm{o}}\mathrm{sign}(x) &= \begin{cases} -\eta_{\mathrm{o}} & \text{if } -L/2 \leq x < 0 \\ \eta_{\mathrm{o}} & \text{if } 0 < x \leq L/2. \end{cases}
\end{aligned}
$$

Nondimensionalization of (2.2) is obtained by introducing the following characteristic scales: f^{-1}, L, η_{o}, $Lh^{-1}f\eta_{\mathrm{o}}$, for the time, the space, the elevation and the velocities, respectively. Using the same symbols, the nondimensional equations become

$$\frac{\partial u}{\partial t} - v = -\alpha^2 \frac{\partial \eta}{\partial x}, \tag{2.3}$$

$$\frac{\partial v}{\partial t} + u = 0, \tag{2.4}$$

$$\frac{\partial \eta}{\partial t} + \frac{\partial u}{\partial x} = 0. \tag{2.5}$$

We have defined $\alpha = \frac{\sqrt{gh}}{fL}$, which is the ratio of the Rossby radius of deformation to the length scale, or a nondimensional Rossby radius of deformation. Note that (2.3)-(2.5) is now defined for $t \geq 0$ and $x \in [-1/2, 1/2]$. Boundary and initial conditions are adapted accordingly.

2.1.1 Analytical solution

As a first step, we present the analytical solution to (2.3)-(2.5). Differentiation of (2.3) and (2.5) with respect to t and x, respectively, gives rise to

$$\frac{\partial^2 u}{\partial t^2} - \frac{\partial v}{\partial t} = -\alpha^2 \frac{\partial^2 \eta}{\partial t \partial x},$$

$$\frac{\partial^2 \eta}{\partial x \partial t} + \frac{\partial^2 u}{\partial x^2} = 0.$$

Elimination of the mixed derivative and substitution of $-\frac{\partial v}{\partial t}$ by u from (2.4) leads to a single equation for the zonal velocity u:

$$\frac{\partial^2 u}{\partial t^2} + u = \alpha^2 \frac{\partial^2 u}{\partial x^2}. \tag{2.6}$$

Equation (2.6) can be analytically solved using the separation of variables method. This is shown in details in appendix A.1. Solution to (2.3)-(2.5) is

$$u(x,t) = \sum_{n=1}^{\infty} H_n (-1)^{n+1} \frac{\alpha^2 k_n}{\omega_n} \sin(\omega_n t) \cos(k_n x),$$

$$v(x,t) = \sum_{n=1}^{\infty} H_n (-1)^{n+1} \frac{\alpha^2 k_n}{\omega_n^2} [\cos(\omega_n t) - 1] \cos(k_n x), \tag{2.7}$$

$$\eta(x,t) = \sum_{n=1}^{\infty} H_n (-1)^n \sin(k_n x) \left\{ 1 - \frac{\alpha^2 k_n^2}{\omega_n^2} [1 - \cos(\omega_n t)] \right\},$$

where coefficients H_n amount to $H_n = \frac{4(-1)^n}{k_n}$. In Figure (2.1), we show the solution (2.7) for the elevation at different times and compare it with Gill's analytical solution to the adjustment problem (*Gill*, 1976). Solutions were computed with $\alpha = \sqrt{10}/10$. Left panels of Figure (2.1) show the solution within the left part of the *finite* domain ($x < 0$). Right panels show the solution within the right part of the *infinite* domain

$(x > 0)$. Thus, the panels separation is the axis $x = 0$. In both situations, the front moves at a speed equal to α, to the left and to the right, for the left and right panels, respectively. As long as the front does not hit the boundary of the finite domain, both solutions are the same (although antisymmetric). After reflection at the boundary, Poincaré waves evolve within the finite domain. For the adjustment problem, the front keeps moving to the right, trailing a wake of Poincaré waves behind it.

2.1.2 A hyperbolic problem

Because (2.3)-(2.5) is a system of first-order hyperbolic equations, there exist three real characteristics. We can write the system in compact form:

$$\mathbf{A}\frac{\partial \mathbf{u}}{\partial t} + \mathbf{B}\frac{\partial \mathbf{u}}{\partial x} = \mathbf{d},$$

where $\mathbf{A}$, $\mathbf{B}$, $\mathbf{u}$ and $\mathbf{d}$ are defined to obtain the following expression:

$$\begin{bmatrix} 1 & 0 & 0 \\ 0 & 1 & 0 \\ 0 & 0 & 1 \end{bmatrix} \frac{\partial}{\partial t} \begin{bmatrix} \eta \\ u \\ v \end{bmatrix} + \begin{bmatrix} 0 & 1 & 0 \\ \alpha^2 & 0 & 0 \\ 0 & 0 & 0 \end{bmatrix} \frac{\partial}{\partial x} \begin{bmatrix} \eta \\ u \\ v \end{bmatrix} = \begin{bmatrix} 0 \\ v \\ -u \end{bmatrix}.$$

In order to reduce (2.3)-(2.5) to a system of three ordinary differential equations (ODEs), we now compute the eigenvalues and eigenvectors of the generalized problem:

$$\begin{aligned} \mathbf{z}_i^T \left(\mathbf{B} - \lambda_i \mathbf{A} \right) &= 0 \\ \det\left(\mathbf{B} - \lambda_i \mathbf{A} \right) &= 0 \end{aligned}$$

for which we have

$$\begin{aligned} \lambda_1 &= 0 & \mathbf{z}_1 &= [0\ 0\ 1]^T, \\ \lambda_2 &= \alpha & \mathbf{z}_2 &= [\alpha\ 1\ 0]^T, \\ \lambda_3 &= -\alpha & \mathbf{z}_3 &= [\alpha\ -1\ 0]^T. \end{aligned}$$

For each eigenvector $\mathbf{z}_i$, an ODE is obtained by computing the following expression:

$$\mathbf{z}_i^T \frac{d}{dt} \mathbf{u} = \mathbf{z}_i^T \mathbf{d}.$$

The system of ODEs then is

$$\begin{cases} \dfrac{d}{dt}v = -u & \text{on } \dfrac{dx}{dt} = 0, \\[2mm] \dfrac{d}{dt}(\alpha\eta + u) = v & \text{on } \dfrac{dx}{dt} = \alpha, \\[2mm] \dfrac{d}{dt}(\alpha\eta - u) = -v & \text{on } \dfrac{dx}{dt} = -\alpha. \end{cases} \qquad (2.8)$$

The foregoing procedure has allowed for transforming the system of partial differential equations (2.3)-(2.5) into the system of ODEs (2.8) in the characteristic variables v, $\alpha\eta + u$ and $\alpha\eta - u$. Each ordinary differential equation is written on a characteristic curve $(x(t), t)$ defined by $\frac{dx}{dt} = \lambda_i$, where $\lambda_1 = 0$, $\lambda_2 = \alpha$ and $\lambda_3 = -\alpha$, for the first, second and third ODE. Because the position is dependent on time, only time integration needs be performed to compute the characteristic variables, as long as we remain located on the associated characteristic curve.

15
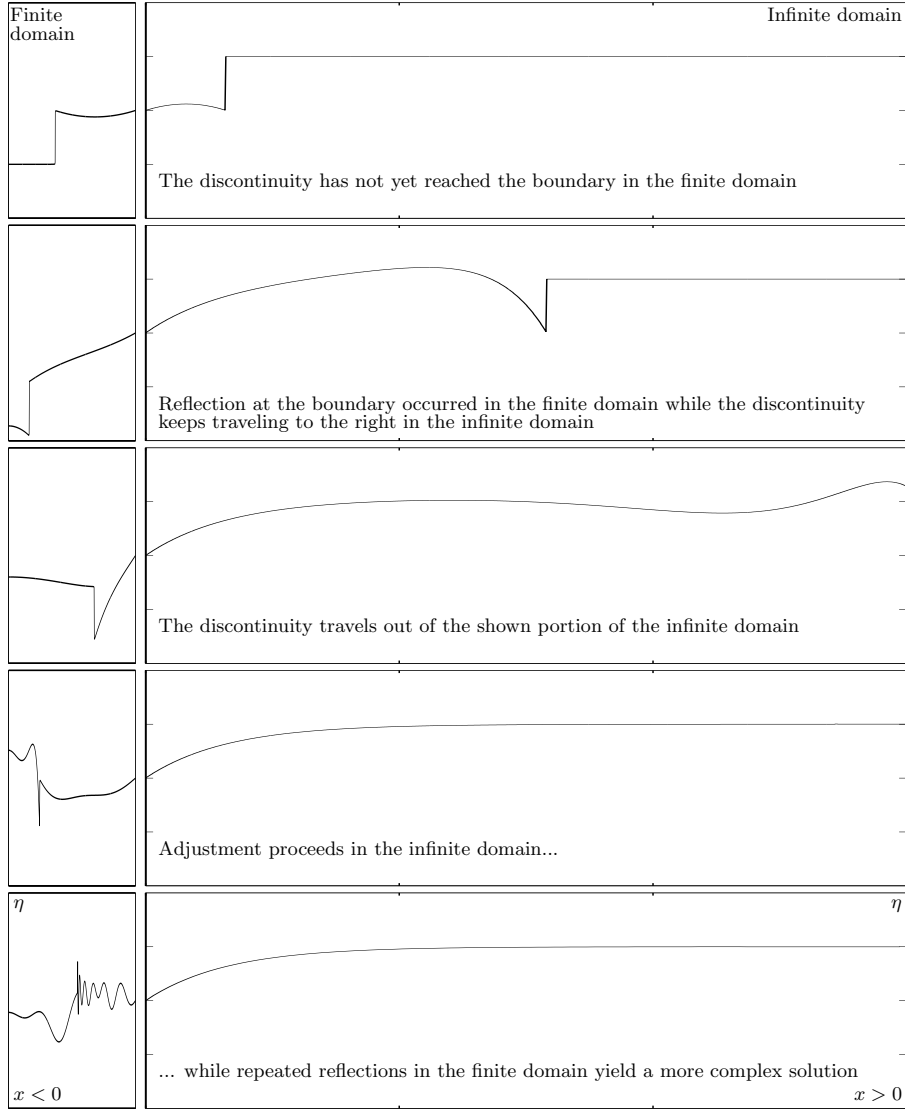
Figure 2.1: Exact solution for the elevation η. Left panels show solutions for the finite domain ($x < 0$) and right panels show solutions for the adjustment problem ($x > 0$), as provided by *Gill* (1976). The axis $x = 0$ separates left and right panels. Left panels are 0.5-unit long and right panels are 3-unit long. The ticks on the y-axis are one unit of elevation apart, the middle one being 0. From top to bottom, solutions are shown at $t = 1$, $t = 5$, $t = 10$ $t = 100$ and $t = 1000$. The parameter α is $\sqrt{10}/10$.

2.2   Analysis of some numerical methods

From our standpoint, the main interest of this problem lies in its ability to be a benchmark for numerical methods. Therefore, we may compare the accuracy and robustness between several numerical techniques to solve (2.3)-(2.5). The difficulty in solving these equations lies in the presence of the discontinuity. Any numerical scheme ought to be assessed based upon its ability to capture this discontinuity without generating spurious oscillations. In this section, we present the following methods: the method of characteristics, the galerkin finite element method (FEM), the discontinuous Galerkin FEM and the discontinuous Riemann-Galerkin FEM. All numerical experiments were conducted with $f = 10^{-4}$ s^{-1}, $g = 10$ m s^{-2}, $h = 100$ m, $L = 10^6$ m, $\eta_\mathrm{o} = 1$ m, leading to $\alpha = \sqrt{10}/10$.

2.2.1   Method of characteristics

Classical finite difference schemes may now be employed to solve (2.8), for which we are constrained to use a time step and a spatial increment satisfying $\frac{\Delta x}{\Delta t} = \alpha$, as suggested in Figure (2.2). For the sake of clarity, let us define the characteristic variables $w \doteq \alpha\eta + u$ and $q \doteq \alpha\eta - u$. A forward Euler stencil applied to (2.8) yields

$$\begin{cases} \dfrac{v_k^{n+1} - v_k^n}{\Delta t} = u_k^n, \\[2mm] \dfrac{w_k^{n+1} - w_{k-1}^n}{\Delta t} = v_{k-1}^n, \\[2mm] \dfrac{q_k^{n+1} - q_{k+1}^n}{\Delta t} = -v_{k+1}^n, \end{cases} \tag{2.9}$$

where all information at time step n has been taken along appropriate characteristics.
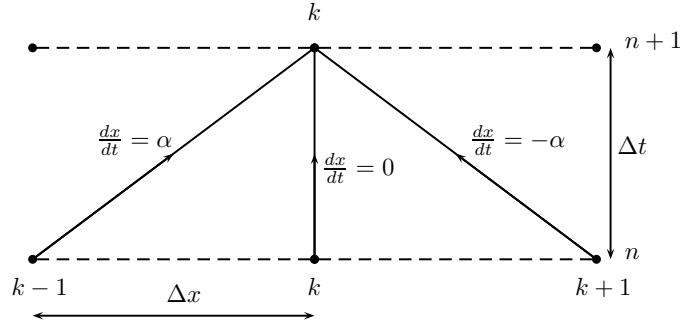
Figure 2.2: Time integration must be performed along characteristics. Indices k and n identify space and time discretization points, respectively.

The essence of the method of characteristics resides in its ability to carry the information along characteristics, which allows to focus solely on time integration. Therefore, we expect the method to be able to capture the traveling discontinuity at any time step provided that the time integration be sufficiently accurate. This issue is illustrated

in Figure (2.3), where the forward Euler and the second-order Runge-Kutta stencils have been used with $\Delta t = 0.01$. The solution for the elevation η is compared with the exact solution at dimensionless time $t = 200$. Notice how the approximate solution obtained with the first-order Euler scheme captures the discontinuity at the right location but is highly inaccurate overall. The second-order Runge-Kutta method performs much better, with an L^2-norm that is more than 20 times smaller. To assess the extra computational cost incurred by the use of the second-order Runge-Kutta method, a run with 400,000 time steps ($\Delta t = 0.001$) has been carried out with both methods. The forward Euler integration yields the solution after 54 s while the second-order Runge-Kutta integration does so after 83 s. Hence, there is roughly a fifty percent extra computational cost in using the latter method. It should be borne in mind that, however efficient the method of characteristics may be for this benchmark, a major drawback lies in the fact that such an approach cannot be straightforwardly extended to two-dimensional computations.
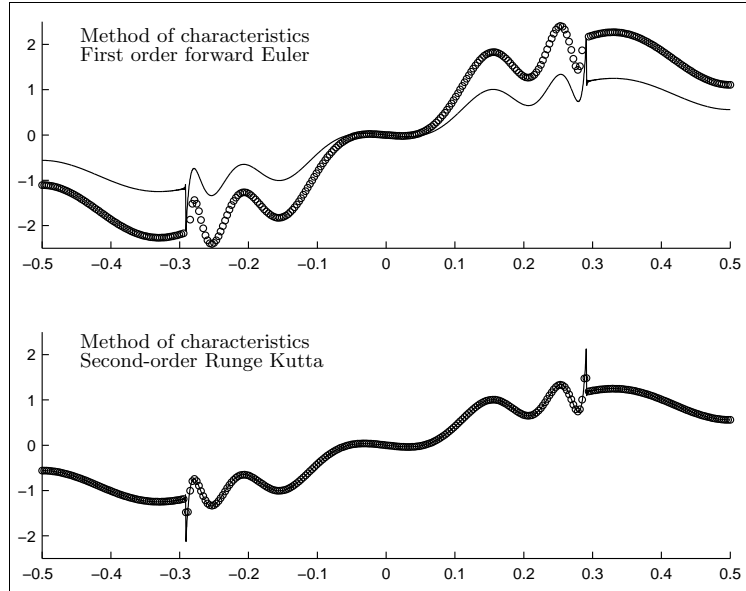
Figure 2.3: Approximate and exact solutions for η at dimensionless time $t = 200$ for the first-order forward Euler method (top) and the second-order Runge-Kutta method (bottom) with a time step of $\Delta t = 0.01$. The solid line represents the exact solution. The circles represent the approximate solution at grid points.

2.2.2 Continuous Galerkin

The continuous Galerkin method is the simplest of the considered methods to implement in two and three dimensions. A variational formulation can be derived by first time-discretizing (2.3)-(2.5). Each resulting equation is then mutliplied by a test function (symbolized by a hat) and integrated over the entire domain $\Omega = [-1/2, 1/2]$. If a so-called θ-scheme is employed for time discretization, the variational formulation

consists in finding $\mathbf{u}^{n+1} = (u^{n+1}, v^{n+1}, \eta^{n+1}) \in \boldsymbol{\mathcal{U}} = (\mathcal{U}, \mathcal{V}, \mathcal{E})$ such that

$$\int_\Omega \left(\frac{u^{n+1} - u^n}{\Delta t} \hat{u} - v^{n+\theta} \hat{u} + \alpha^2 \frac{\partial \eta^{n+\theta}}{\partial x} \hat{u} \right) \mathrm{d}x \quad = 0 \quad \forall \hat{u} \in \hat{\mathcal{U}},$$

$$\int_\Omega \left(\frac{v^{n+1} - v^n}{\Delta t} \hat{v} + u^{n+\theta} \hat{v} \right) \mathrm{d}x \qquad\qquad = 0 \quad \forall \hat{v} \in \hat{\mathcal{V}}, \qquad (2.10)$$

$$\int_\Omega \left(\frac{\eta^{n+1} - \eta^n}{\Delta t} \hat{\eta} + \frac{\partial u^{n+\theta}}{\partial x} \hat{\eta} \right) \mathrm{d}x \qquad\qquad = 0 \quad \forall \hat{\eta} \in \hat{\mathcal{E}},$$

where $a^{n+\theta} = \theta a^{n+1} + (1 - \theta)a^n$ and θ is an adjustable parameter that allows for choosing between time schemes. The so-called Crank-Nicolson scheme is obtained with $\theta = 0.5$. Note that u^n, v^n and η^n denote the functions evaluated at the previous time step and live in the same functional spaces as the unknowns. That is to say, a finite element problem is solved at each time step. We may also consider using the following alternative scheme that likens the classical forward-backward scheme, in which case a variational formulation consists in finding $\mathbf{u}^{n+1} \in \boldsymbol{\mathcal{U}}$ such that

$$\int_\Omega \left(\frac{u^{n+1} - u^n}{\Delta t} \hat{u} - \frac{1}{2}(v^{n+1} + v^n)\hat{u} + \alpha^2 \frac{\partial \eta^{n+1}}{\partial x} \hat{u} \right) \mathrm{d}x \quad = 0 \quad \forall \hat{u} \in \hat{\mathcal{U}},$$

$$\int_\Omega \left(\frac{v^{n+1} - v^n}{\Delta t} \hat{v} + \frac{1}{2}(u^{n+1} + u^n)\hat{v} \right) \mathrm{d}x \qquad\qquad = 0 \quad \forall \hat{v} \in \hat{\mathcal{V}}, \quad (2.11)$$

$$\int_\Omega \left(\frac{\eta^{n+1} - \eta^n}{\Delta t} \hat{\eta} + \frac{\partial u^n}{\partial x} \hat{\eta} \right) \mathrm{d}x \qquad\qquad = 0 \quad \forall \hat{\eta} \in \hat{\mathcal{E}},$$

where η^{n+1} is first computed from the continuity equation and used in the subsequent calculation of (u^{n+1}, v^{n+1}). The Coriolis term is treated semi-implicitly in both formulations so as to not artificially generate nor dissipate energy, which complies with the fact that no work is done by the Coriolis force. In formulations (2.10) and (2.11), $\mathbf{u}^{n+1}$ and $\hat{\mathbf{u}} = (\hat{u}, \hat{v}, \hat{\eta})$ belong to suitable infinite-dimensional function spaces. Each variable a^{n+1} is approximated as follows

$$a^{n+1} \simeq a_h^{n+1} = \sum_{j=1}^N A_j^{n+1} \phi_j(x),$$

where A_j^{n+1} are the nodal values and ϕ_j are the polynomial basis functions. The approximation $\mathbf{u}_h^{n+1} = (u_h^{n+1}, v_h^{n+1}, \eta_h^{n+1}) \in \boldsymbol{\mathcal{U}}_h^c = (\mathcal{U}_h^c, \mathcal{V}_h^c, \mathcal{E}_h^c)$, which are finite-dimensional subspaces of $(\mathcal{U}, \mathcal{V}, \mathcal{E})$. Note that the superscript c stands for *continuous*. Following the notation by *Hughes et al.* (2000), the test functions $\hat{\mathbf{u}}$ are similarly approximated by $\hat{\mathbf{u}}_h = (\hat{u}_h, \hat{v}_h, \hat{\eta}_h) \in \hat{\boldsymbol{\mathcal{U}}}_h^c = (\hat{\mathcal{U}}_h^c, \hat{\mathcal{V}}_h^c, \hat{\mathcal{E}}_h^c)$, which are finite-dimensional subspaces of $\hat{\boldsymbol{\mathcal{U}}} = (\hat{\mathcal{U}}, \hat{\mathcal{V}}, \hat{\mathcal{E}})$. Linear approximations are used for the test functions and for all variables for the sake of simplicity and for an easier interpretation. Hence, $\mathbf{u}_h^{n+1}$ and $\hat{\mathbf{u}}_h$ are continuous across Ω and piecewise linear over each element Ω_e. We bear in mind, however, that pressure modes may appear in two and three dimensions when the same interpolant order is used for the velocity and the elevation. Experiments with quadratic elements for the velocity and linear elements for the elevation, as well as linear elements for the velocity and constant elements for the elevation, have been conducted. The conclusions are the same as those presented hereafter.

In Figure (2.4), we show the elevation field obtained at time $t = 2$ using the forward-backward scheme. Spurious oscillations pollute the 100-element and the 400-element approximations. Experiments with finer meshes have been carried out and no improvment is brought about by the use of smaller element sizes. Nevertheless, if we set off the time integration with a smoother initial condition, the use of smaller elements eliminates spurious oscillations. In that respect, a hyperbolic tangent profile has been chosen for the initial elevation field, that is,

$$\eta(x, 0) = \tanh(Rx), \tag{2.12}$$

where R, the steepness parameter, controls how steep the transition is between -1 and 1. The larger R, the closer this initial condition will be to the sign function. The foregoing experiments have been repeated with the hyperbolic tangent initial condition (2.12), with a steepness parameter $R = 100$, and results are shown in Figure (2.5). Note that in the case of a hyperbolic tangent initial elevation field, coefficients H_n that appear in the exact solution (2.7) must be numerically evaluated.

Figure 2.4: The Galerkin finite-element approximations at dimensionless time $t = 2$ with 100 elements (top) and 400 elements (bottom) when the steplike initial elevation field is used. The time step is 0.001. The solid line is the exact solution.

The assessment of the finite-element scheme is not trivial because it includes both time and space discretizations. We do not wish to go into details regarding time discretization techniques here and for the convergence analysis only the forward-backward (FB) scheme has been explored. A comparison between approximate and exact solutions at dimensionless time $t = 1$ was performed on gradually-refined uniform meshes. It is reported in Section 2.2.5.
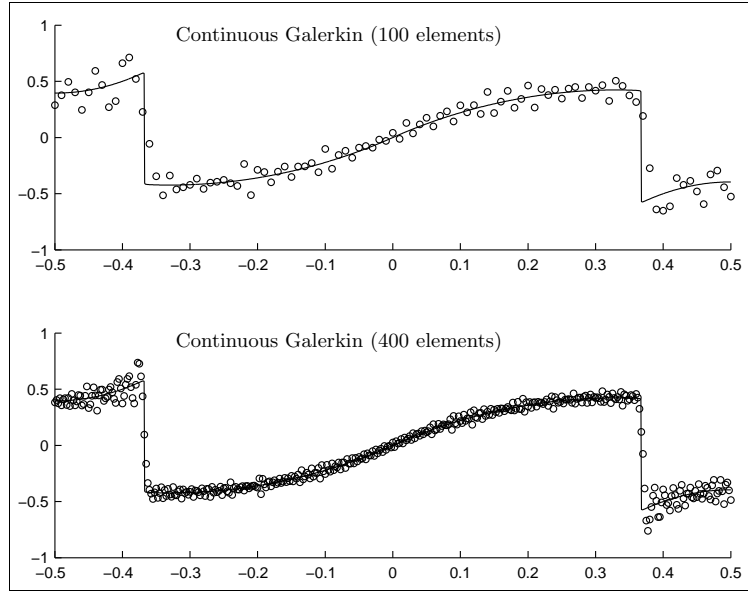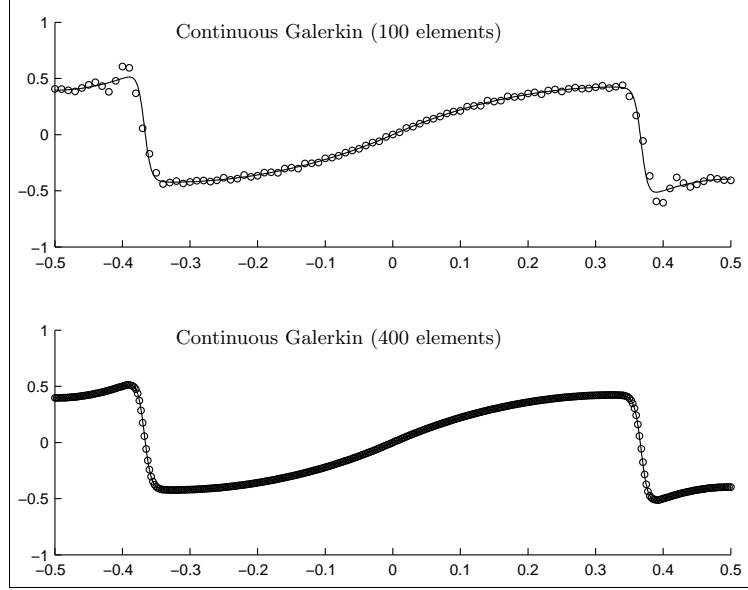
Figure 2.5: The Galerkin finite-element approximations at dimensionless time $t = 2$ with 100 elements (top) and 400 elements (bottom) when a hyperbolic tangent profile is used for the initial elevation field ($R = 100$). The time step is 0.001. The solid line is the exact solution.

2.2.3 Discontinuous Galerkin

The Discontinuous Galerkin method (DGM) provides an appealing approach to address problems having discontinuities. Another advantage of the DGM is that it is inherently locally conservative while continuous Galerkin methods are locally conservative provided that subsequent postprocessing be carried out (*Hughes et al.*, 2000). A broad review may be found in *Cockburn et al.* (2000). In the DGM, the solution is a piecewise-continuous function relative to a mesh (*Flaherty et al.*, 2002). As such, it is not required that the sought solution assume the same value at each physical mesh node because two computational nodes belong to the same physical node (in a one-dimensional mesh – see Figure 2.6). This property provides more flexibility in representing steep gradients and discontinuities. A steplike initial condition for the elevation field will be exactly represented, which is not the case with continuous methods.

In continuous finite element methods, two neighboring elements share a common computational node. This common node allows information to be conveyed from one element to its neighbor. In discontinuous methods, all the nodes lie in their respective element so that, a priori, there is no transfer of information between neighboring elements. One has to keep that in mind when deriving the weak formulation. In that respect, the weak formulation (2.11) will be altered in such a way that neighboring elements are able to exchange information between them. As for the continuous case, a variational formulation is obtained from the time-discretized equations. For

Figure 2.6: One-dimensional mesh for the discontinuous Galerkin method: there are two computational nodes (i.e., two nodal values, U_i^- and U_i^+) at each physical node, X_i.

the forward-backward scheme, the problem consists in finding $\mathbf{u}^{n+1}$ in $\mathcal{U}$ such that

$$
\sum_{e=1}^{N_e} \int_{\Omega_e} \left(\frac{u^{n+1} - u^n}{\Delta t}\hat{u} - \frac{1}{2}(v^{n+1} + v^n)\hat{u} + \alpha^2 \frac{\partial \eta^{n+1}}{\partial x}\hat{u} \right) \mathrm{d}x
$$

$$
+ \underbrace{\sum_{e=1}^{N_e} \left| a(\hat{u}) \left[\alpha^2 \eta^{n+1} \right] \right|_{\partial \Omega_e}}_{\mathcal{S}_1} \qquad\qquad = 0 \quad \forall \hat{u} \in \hat{\mathcal{U}},
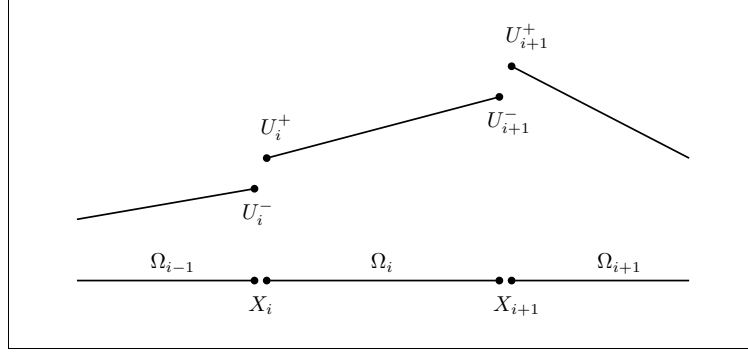$$

$$
\sum_{e=1}^{N_e} \int_{\Omega_e} \left(\frac{v^{n+1} - v^n}{\Delta t}\hat{v} + \frac{1}{2}(u^{n+1} + u^n)\hat{v} \right) \mathrm{d}x \qquad\qquad = 0 \quad \forall \hat{v} \in \hat{\mathcal{V}},
$$

$$
\sum_{e=1}^{N_e} \int_{\Omega_e} \left(\frac{\eta^{n+1} - \eta^n}{\Delta t}\hat{\eta} + \frac{\partial u^n}{\partial x}\hat{\eta} \right) \mathrm{d}x + \underbrace{\sum_{e=1}^{N_e} \left| a(\hat{\eta}) \left[u^n \right] \right|_{\partial \Omega_e}}_{\mathcal{S}_2} \quad = 0 \quad \forall \hat{\eta} \in \hat{\mathcal{E}}.
$$

$$(2.13)$$

where N_e is the number of elements. An approximation $\mathbf{u}_h^{n+1} = (u_h^{n+1}, v_h^{n+1}, \eta_h^{n+1})$ is sought within $\mathcal{U}_h^d = (\mathcal{U}_h^d, \mathcal{V}_h^d, \mathcal{E}_h^d)$, which are finite-dimensional subspaces of $\mathcal{U}$. The d superscript stands for *discontinuous*. Similarly, the test functions $\hat{\mathbf{u}}$ are approximated by $\hat{\mathbf{u}}_h = (\hat{u}_h, \hat{v}_h, \hat{\eta}_h) \in \hat{\mathcal{U}}_h^d = (\hat{\mathcal{U}}_h^d, \hat{\mathcal{V}}_h^d, \hat{\mathcal{E}}_h^d)$, which are finite-dimensional subspaces of $\hat{\mathcal{U}}$. As for the Galerkin method, a linear approximation is used for the test functions and all variables. However, because the discontinuous Galerkin method is employed here, the finite-dimensional subspaces $\mathcal{U}_h^d$ and $\hat{\mathcal{U}}_h^d$ allow discontinuities across elements:

$$
\mathcal{U}_h^d = \hat{\mathcal{U}}_h^d = \left\{ v \in L^2(\Omega) \quad | \quad v_{|\Omega_e} \in P^1(\Omega_e) \right\}^3 ,
$$

where $P^1(\Omega_e)$ is the set of linear polynomials on element Ω_e. Note that the following relationships hold for finite-dimensional subspaces of the Galerkin and discontinuous Galerkin methods: $\mathcal{U}_h^c \subset \mathcal{U}_h^d \subset \mathcal{U}$ and $\hat{\mathcal{U}}_h^c \subset \hat{\mathcal{U}}_h^d \subset \hat{\mathcal{U}}$. The role of $\mathcal{S}_1$ and $\mathcal{S}_2$ in the first and third equations is to weakly enforce continuity of η^{n+1} and u^{n+1},

respectively. The vertical bars indicate that expressions must be evaluated along the boundary of element Ω_e, that is at the extremities of element Ω_e for one-dimensional problems. The function $a(\hat{u})$ is defined as

$$a(\hat{u}) \doteq \left(\lambda - \frac{1}{2} \operatorname{sign}(\hat{n}) \right) \hat{u}$$

where $\hat{n}$ is the outward-pointing normal at each element boundary $\partial \Omega$. The interelement jump in the nodal values at a given physical node is defined as $[u^n(X_i)] = U_i^- - U_i^+$. The parameter $\lambda \in [-1/2, 1/2]$ is tunable in the sense that it allows for the interelement jump to be weighted. For example, the jump $[u^n]$ evaluated at the physical node X_i in Figure (2.6) is weighted by $(\lambda - 1/2)$ on computational node i^- and by $(\lambda + 1/2)$ on computational node i^+, given that the signs of the normal $\hat{n}$ at nodes i^- and i^+, are $+1$ and -1, respectively. A centered scheme is obtained by choosing $\lambda = 0$, in which case no preference is given to any of the nodes i^- or i^+. For transport problems, it is common to give more weight to node i^+ (or node i^-) if the advective flux is known to travel from left to right (respectively from right to left). As in *Hanert et al.* (2004), an alternative formulation can be derived by integrating the spatial derivatives by parts. In so doing, (2.13) expands to

$$\sum_{e=1}^{N_e} \int_{\Omega_e} \left(\frac{u^{n+1} - u^n}{\Delta t} \hat{u} - \frac{1}{2}(v^{n+1} + v^n)\hat{u} - \alpha^2 \eta^{n+1} \frac{\partial \hat{u}}{\partial x} \right) \mathrm{d}x$$

$$+ \alpha^2 \sum_{i=1}^{N_v} \left\{ \langle \eta^{n+1}(X_i) \rangle [\hat{u}(X_i)] + [\eta^{n+1}(X_i)] \langle \hat{u}(X_i) \rangle \right\}$$

$$+ \alpha^2 \sum_{i=1}^{N_v} [a(\hat{u}(X_i))] [\eta^{n+1}(X_i)] = 0,$$

$$\sum_{e=1}^{N_e} \int_{\Omega_e} \left(\frac{v^{n+1} - v^n}{\Delta t} \hat{v} + \frac{1}{2}(u^{n+1} + u^n)\hat{v} \right) \mathrm{d}x = 0, \qquad (2.14)$$

$$\sum_{e=1}^{N_e} \int_{\Omega_e} \left(\frac{\eta^{n+1} - \eta^n}{\Delta t} \hat{\eta} - u^n \frac{\partial \hat{\eta}}{\partial x} \right) \mathrm{d}x$$

$$+ \sum_{i=1}^{N_v} \left\{ \langle u^n(X_i) \rangle [\hat{\eta}(X_i)] + [u^n(X_i)] \langle \hat{\eta}(X_i) \rangle \right\}$$

$$+ \sum_{i=1}^{N_v} [a(\hat{\eta}(X_i))] [u^n(X_i)] = 0,$$

where N_v is the number of physical nodes and $\langle f(X_i) \rangle$ denotes the average of f at X_i, that is

$$\langle f(X_i) \rangle = \frac{1}{2}(f(X_i^-) + f(X_i^+)).$$

By combining all the terms involved in the summations, the foregoing formulation reduces to

$$\sum_{e=1}^{N_e} \int_{\Omega_e} \left(\frac{u^{n+1} - u^n}{\Delta t}\hat{u} - \frac{1}{2}(v^{n+1} + v^n)\hat{u} - \alpha^2 \eta^{n+1}\frac{\partial \hat{u}}{\partial x} \right) \mathrm{d}x$$

$$+ \alpha^2 \sum_{i=1}^{N_v} \left\langle \eta^{n+1}(X_i) \right\rangle_\lambda [\hat{u}(X_i)] \qquad\qquad = 0,$$

$$\sum_{e=1}^{N_e} \int_{\Omega_e} \left(\frac{v^{n+1} - v^n}{\Delta t}\hat{v} + \frac{1}{2}(u^{n+1} + u^n)\hat{v} \right) \mathrm{d}x \qquad\qquad = 0,$$

$$\sum_{e=1}^{N_e} \int_{\Omega_e} \left(\frac{\eta^{n+1} - \eta^n}{\Delta t}\hat{\eta} - u^n \frac{\partial \hat{\eta}}{\partial x} \right) \mathrm{d}x + \sum_{i=1}^{N_v} \left\langle u^n(X_i) \right\rangle_\lambda [\hat{\eta}(X_i)] \quad = 0,$$

(2.15)

where $\langle f(X_i)\rangle_\lambda$ is the weighted average of f at X_i, defined as

$$\langle f(X_i)\rangle_\lambda = (\frac{1}{2} + \lambda)f(X_i^-) + (\frac{1}{2} - \lambda)f(X_i^+).$$

In appendix A.2, we show how formulations (2.14) and (2.15) are derived.

The discontinuous finite element formulation (2.13) has been used to solve our benchmark problem with 100 and 400 elements. Results are shown in Figure (2.7) where approximate and exact solutions are compared at $t = 2$. A centered scheme is employed here ($\lambda = 0$). Severe oscillations pollute the solutions. The classical forward-backward time scheme is employed for better stability properties when boundary terms $\mathcal{S}_1$ and $\mathcal{S}_2$ are involved. In Figure (2.8), the top panel reproduces the 400-element solution with $\lambda = 0$ while the bottom panel shows the solution obtained with $\lambda = 0.001$. Hence, Figure (2.8) permits to compare a centered and a slightly off-centered scheme. The aim of these numerical experiments is twofold. Firstly, we wish to verify whether weakly enforcing continuity on u^h and η^h ensures stability of the formulation (2.13). Secondly, we would like to lower the level of arbitrariness associated with the weak enforcement of continuity by appraising the sensitivity of the parameter λ. Looking at Figure (2.8), we see that both choices for λ – the centered and the slightly off-centered schemes – do no prevent spurious oscillations. Moreover, the off-centered scheme makes it even worse, suggesting the importance of symmetry in the problem. Other experiments have been performed to test higher values (as well as negative values) of λ, only to further conclude that $\lambda = 0.0$ gives rise to the least severe oscillations. In Figure (2.9), we show how the solution behaves when the hyperbolic tangent (2.12) is used as initial condition (with $R = 100$). The same experiment as with the continuous Galerkin method has been conducted here. Figure (2.9) is to be compared with Figure (2.5) showing the solution obtained with the continuous Galerkin method. The latter clearly outperforms the DGM. The presence of spurious oscillations for all values of λ suggests that the wrong field is upwinded. The following question thus arises: What variables should we weakly enforce the continuity of ?
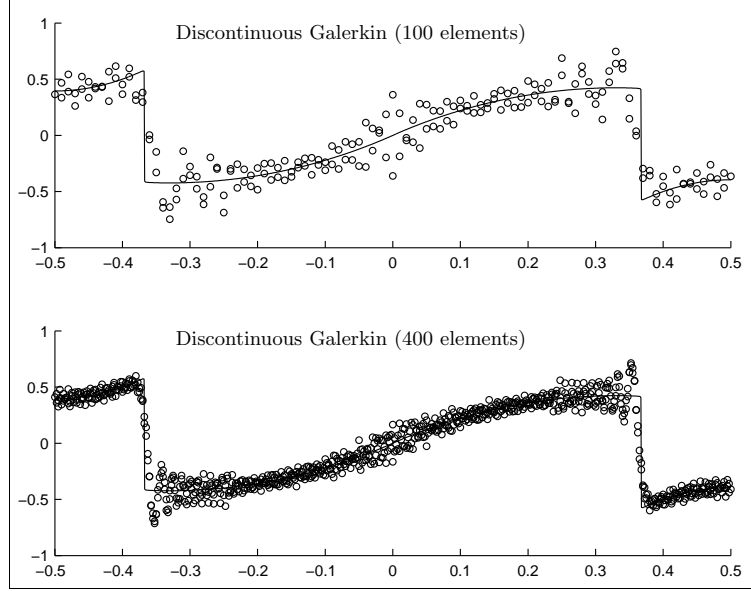
Figure 2.7: Discontinuous Galerkin finite-element approximation with 100 elements (top) and 400 elements (bottom) at dimensionless time $t = 2$ with a steplike initial condition. The time step is 0.001. Continuity is weakly enforced using $\lambda = 0.0$.
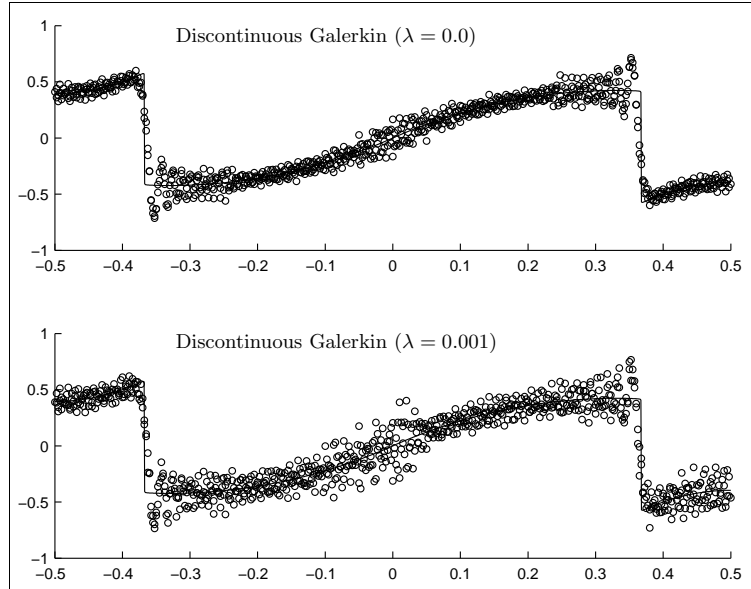
Figure 2.8: Discontinuous Galerkin finite-element approximation with 400 elements at dimensionless time $t = 2$ with a steplike initial condition. The time step is 0.001. Continuity is weakly enforced using $\lambda = 0.0$ (top) and $\lambda = 0.001$ (bottom).
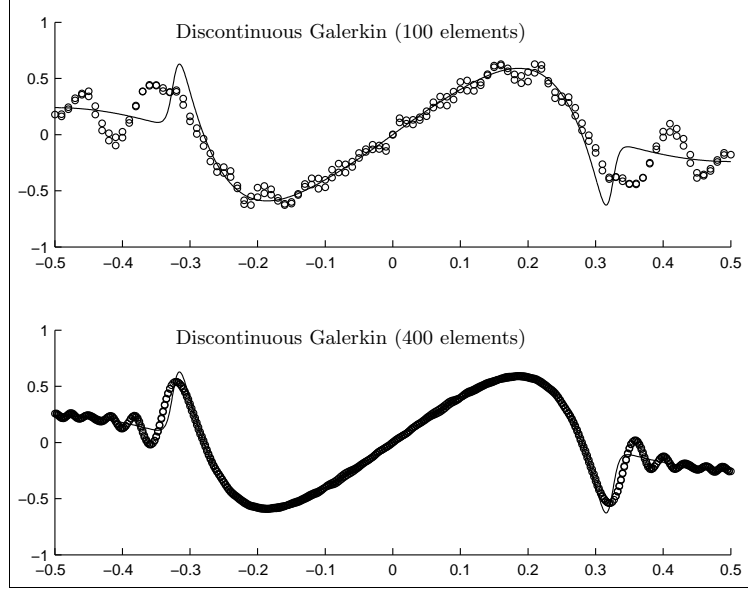
Figure 2.9: The discontinuous Galerkin finite-element approximations at dimensionless time $t = 20$ with 100 elements (top) and 400 elements (bottom) when a hyperbolic tangent profile is used for the initial elevation field ($R = 100$). The time step is 0.001 and continuity is weakly enforced with $\lambda = 0$. The solid line is the exact solution.

2.2.4 Discontinuous Riemann - Galerkin

To answer the previous question, a closer look at the way information is propagating is advisable. Since information is carried along characteristic curves by characteristic variables, a better approach would be to enforce continuity of those very variables that transport information. In addition, we know the direction of propagation of those variables so that weighting can adequately be adapted. This approach is commonly referred to as a Riemann solver (*Roe*, 1981; *Aizinger and Dawson*, 2002; *Schwanenberg and Harms*, 2004; *Remacle et al.*, 2005). A variational formulation similar to (2.13) may be derived. The difference will lie in the way continuity is enforced. The

problem consists in finding $\mathbf{u}^h$ in $\mathcal{U}$ such that

$$\sum_{e=1}^{N_e} \int_{\Omega_e} \left(\frac{u^{n+1} - u^n}{\Delta t} \hat{u} - \frac{1}{2} (v^{n+1} + v^n) \hat{u} + \alpha^2 \frac{\partial \eta^{n+1}}{\partial x} \hat{u} \right) \mathrm{d}x$$

$$+ \sum_{e=1}^{N_e} \left| a(\hat{u}) \left[\alpha u^n + \alpha^2 \eta^{n+1} \right] \right|_{\partial \Omega_e}$$

$$+ \sum_{e=1}^{N_e} \left| b(\hat{u}) \left[\alpha u^n - \alpha^2 \eta^{n+1} \right] \right|_{\partial \Omega_e} \qquad = 0 \quad \forall \hat{u} \in \hat{\mathcal{U}},$$

$$\sum_{e=1}^{N_e} \int_{\Omega_e} \left(\frac{v^{n+1} - v^n}{\Delta t} \hat{v} + \frac{1}{2} (u^{n+1} + u^n) \hat{v} \right) \mathrm{d}x \qquad = 0 \quad \forall \hat{v} \in \hat{\mathcal{V}},$$

$$\sum_{e=1}^{N_e} \int_{\Omega_e} \left(\frac{\eta^{n+1} - \eta^n}{\Delta t} \hat{\eta} + \frac{\partial u^n}{\partial x} \hat{\eta} \right) \mathrm{d}x$$

$$+ \sum_{e=1}^{N_e} \left| a(\hat{\eta}) \left[\alpha \eta^n + u^n \right] \right|_{\partial \Omega_e} + \sum_{e=1}^{N_e} \left| b(\hat{\eta}) \left[\alpha \eta^n - u^n \right] \right|_{\partial \Omega_e} \qquad = 0 \quad \forall \hat{\eta} \in \hat{\mathcal{E}}.$$

(2.16)

where functions $a(\hat{u})$ and $b(\hat{u})$ are defined as follows:

$$a(\hat{u}) \quad \doteq \quad \frac{1}{2} \left(\frac{1}{2} - \lambda \, \mathrm{sign}(\hat{n}) \right) \hat{u},$$

$$b(\hat{u}) \quad \doteq \quad \frac{1}{2} \left(\frac{1}{2} + \lambda \, \mathrm{sign}(\hat{n}) \right) \hat{u},$$

where we usually take $\lambda = 1/2$. Again, an alternative formulation can be obtained by integrating the spatial derivatives by parts and combining the sums, as we have

achieved for the previous DG formulation. It can be shown that (2.16) is equivalent to

$$\sum_{e=1}^{N_e} \int_{\Omega_e} \left(\frac{u^{n+1} - u^n}{\Delta t} \hat{u} - \frac{1}{2}(v^{n+1} + v^n)\hat{u} - \alpha^2 \eta^{n+1} \frac{\partial \hat{u}}{\partial x} \right) dx$$

$$+ \frac{1}{2}\alpha \sum_{i=1}^{N_v} [\hat{u}(X_i)] \left\{ \left(\alpha \eta^{n+1}(X_i^-) + u^n(X_i^-) \right) \right.$$

$$+ \left. \left(\alpha \eta^{n+1}(X_i^+) - u^n(X_i^+) \right) \right\}$$

$$+ (1 - 2\lambda) \sum_{i=1}^{N_v} \left[\alpha^2 \eta^{n+1}(X_i) \right] \langle \hat{u}(X_i) \rangle \qquad\qquad = 0,$$

$$\sum_{e=1}^{N_e} \int_{\Omega_e} \left(\frac{v^{n+1} - v^n}{\Delta t} \hat{v} + \frac{1}{2}(u^{n+1} + u^n)\hat{v} \right) dx \qquad\qquad = 0, \qquad (2.17)$$

$$\sum_{e=1}^{N_e} \int_{\Omega_e} \left(\frac{\eta^{n+1} - \eta^n}{\Delta t} \hat{\eta} - u^n \frac{\partial \hat{\eta}}{\partial x} \right) dx$$

$$+ \frac{1}{2} \sum_{i=1}^{N_v} [\hat{\eta}(X_i)] \left\{ \left(\alpha \eta^n(X_i^-) + u^n(X_i^-) \right) \right.$$

$$- \left. \left(\alpha \eta^n(X_i^+) - u^n(X_i^+) \right) \right\}$$

$$+ (1 - 2\lambda) \sum_{i=1}^{N_v} [u^n(X_i)] \langle \hat{\eta}(X_i) \rangle \qquad\qquad = 0.$$

Setting $\lambda = 1/2$ further reduces the foregoing formulation and we obtain

$$\sum_{e=1}^{N_e} \int_{\Omega_e} \left(\frac{u^{n+1} - u^n}{\Delta t} \hat{u} - \frac{1}{2}(v^{n+1} + v^n)\hat{u} - \alpha^2 \eta^{n+1} \frac{\partial \hat{u}}{\partial x} \right) dx$$

$$+ \frac{1}{2}\alpha \sum_{i=1}^{N_v} [\hat{u}(X_i)] \left\{ \left(\alpha \eta^{n+1}(X_i^-) + u^n(X_i^-) \right) \right.$$

$$+ \left. \left(\alpha \eta^{n+1}(X_i^+) - u^n(X_i^+) \right) \right\} \qquad\qquad = 0,$$

$$\sum_{e=1}^{N_e} \int_{\Omega_e} \left(\frac{v^{n+1} - v^n}{\Delta t} \hat{v} + \frac{1}{2}(u^{n+1} + u^n)\hat{v} \right) dx \qquad\qquad = 0, \qquad (2.18)$$

$$\sum_{e=1}^{N_e} \int_{\Omega_e} \left(\frac{\eta^{n+1} - \eta^n}{\Delta t} \hat{\eta} - u^n \frac{\partial \hat{\eta}}{\partial x} \right) dx$$

$$+ \frac{1}{2} \sum_{i=1}^{N_v} [\hat{\eta}(X_i)] \left\{ \left(\alpha \eta^n(X_i^-) + u^n(X_i^-) \right) \right.$$

$$- \left. \left(\alpha \eta^n(X_i^+) - u^n(X_i^+) \right) \right\} \qquad\qquad = 0.$$

Formulation (2.18) is elegant. In the first equation, the summation involves an average of characteristic variables at each physical node X_i. In particular, the average is computed by taking the characteristic variables $\alpha\eta + u$ and $\alpha\eta - u$ at nodes X_i^- and

X_i^+, which merely reflects the way information propagates. A similar comment can be made on the third equation where jumps of characteristic variables make up the summation.

Now, to understand the seemingly complicated formulation (2.16), let us evaluate the expressions that weakly enforce continuity of the characteristic variables. We focus on the first equation and assume $\hat{u} = \phi_i^-$, that is the shape function associated with computational node i^-. We further assume that the shape function is evaluated at node X_i^-.The outward-pointing normal is $+1$ so that the functions a and b take on the following expressions

$$a(\phi_i^-) = \frac{1}{2}(1/2 - \lambda),$$
$$b(\phi_i^-) = \frac{1}{2}(1/2 + \lambda),$$

and the expression associated with node i^- is

$$\frac{1}{2}(1/2 - \lambda)\left[\alpha u^n + \alpha^2 \eta^{n+1}\right] + \frac{1}{2}(1/2 + \lambda)\left[\alpha u^n - \alpha^2 \eta^{n+1}\right].$$

If we take $\lambda = 1/2$, the latter expression simply becomes $\frac{1}{2}[\alpha u^n - \alpha^2 \eta^{n+1}]$. Concretely, this is what has to be added to row i^- of the linear system. The same reasoning applied to node i^+ (i.e., shape function ϕ_i^+) gives rise to $\frac{1}{2}[\alpha u^n + \alpha^2 \eta^{n+1}]$. One can see that in both expressions, a linear combination of one of the characteristic variables is involved. The jump of $\alpha(u - \alpha\eta)$ is associated with node i^- while the jump of $\alpha(u + \alpha\eta)$ is associated with node i^+. This pattern consistently translates the way information is conveyed. So as to compare with the previous discontinuous method, the same experiment has been performed (a 400-element mesh and a solution analyzed at $t = 2$) with the Riemann-Galerkin formulation (2.16). Results are shown in Figure (2.10), where the superiority of the Riemann-Galerkin formulation is manifest when compared with Figure (2.7). Let us emphasize that the quality of the approximate solution suffers from numerical dissipation when long time integration is performed, a trend already observed by *Kuo and Polvani* (1996) with their shock-capturing numerical methods. This effect is illustrated in Figure (2.11) where the approximate solution is unable to capture higher-frequency features that make up the exact solution. Higher-order time discretization schemes should be able to tackle this problem, though, and it is indispensable to investigate the effect of such techniques on the accuracy.

2.2.5 Comparison between methods

Before comparing methods, it is of interest to assess the convergence rate of each of them by computing the L^2-norm of the error on gradually-refined meshes. The time step used in the following experiments is very small in order for the time discretization error to be negligible in contrast to the space discretization error. A time step of $\Delta t = 10^{-5}$ is used and the error at time $t = 1$ is computed. Meshes containing 25, 50, 100, 200 and 400 elements are used. The results of the convergence analysis are reported in Figure (2.12). The hyperbolic-tangent initial condition may be used to compare the three methods for different values of the steepness parameter. Results are shown on the top graph of Figure (2.13) where we can observe that for smooth initial

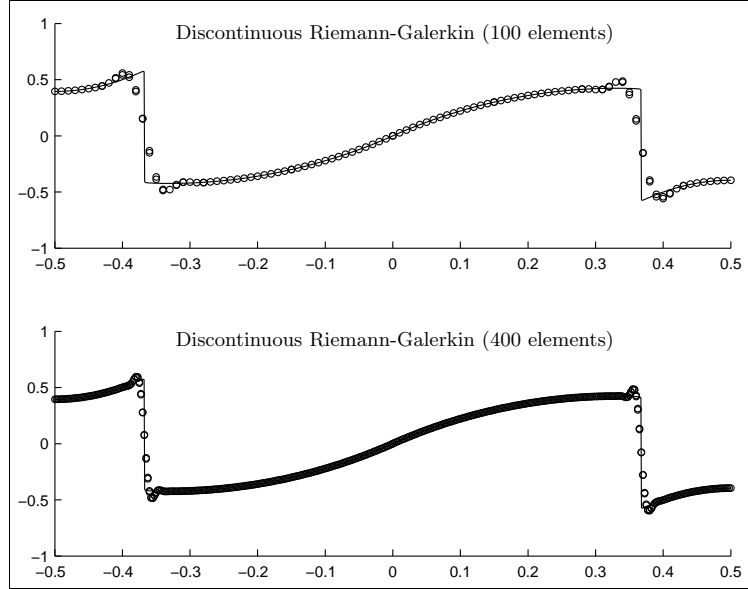**Figure 2.10:** Discontinuous Riemann-Galerkin finite-element approximation with 100 elements (top) and 400 elements (bottom) at dimensionless time $t = 2$ with a steplike initial condition. The time step is 0.001.
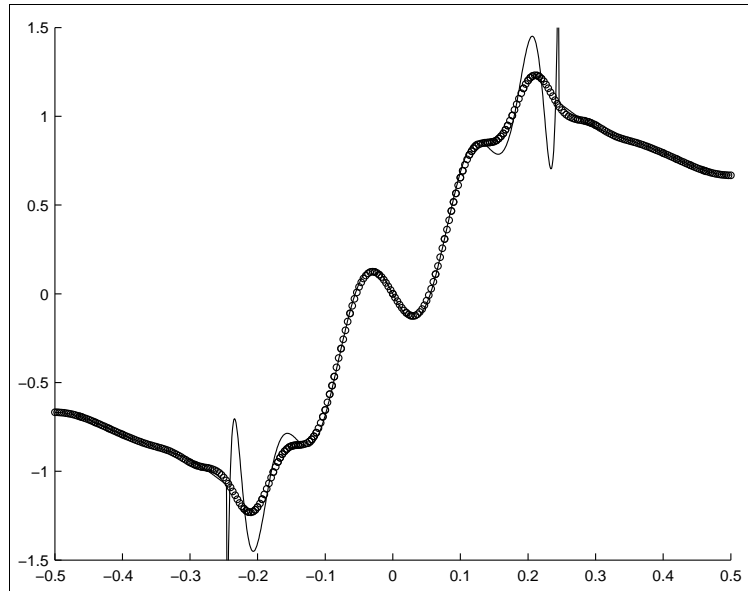

Figure 2.11: Discontinuous Riemann-Galerkin finite-element approximation with 300 elements at dimensionless time $t = 200$ with a steplike initial condition. The time step is 0.002.

30

conditions, the Galerkin method performs the best while for sharp initial conditions, the discontinuous Riemann-Galerkin method yields the best approximation. It should be pointed out, though, that the errors remain close to one another and that none of the methods could be immediately ruled out based upon this quantitative analysis. Moreover, the gap between the errors obtained for sharp initial conditions does not increase when using higher-resolution meshes. The bottom graph of Figure (2.13) shows the L^2-norm of the error computed on the restricted domain $\Omega_r = [-0.25, 0.25]$ that does not contain any of the discontinuities, as can be seen in Figure (2.4). In so doing, the error for the discontinuous Riemann-Galerkin method remains very close to 10^{-4} while it increases up to 10^{-2} for the two other methods. This behavior is caused by the spreading of spurious oscillations toward the inner part of the domain, where the solution should remain smooth. These oscillations do not exist for the discontinuous Riemann-Galerkin method, thereby leading to an error that is two orders of magnitude smaller for sharp initial conditions. A last comment may be made regarding the use of the L^2-norm. The latter may be misleading in the sense that, by examining the top graph of Figure (2.13), we are tempted to conclude that all methods are equivalent for sharp initial conditions. This is untrue and the problem is that the error is closely concentrated around the discontinuities for the discontinuous Riemann-Galerkin method (and reaches about 10^{-2}) while it remains as low as 10^{-4} away from the discontinuities. By contrast, as we can observe on the bottom graph of Figure (2.13), the error reaches 10^{-2} away from the discontinuities for the Galerkin and discontinuous Galerkin methods.

In Figure (2.14), the Galerkin and the discontinuous Riemann-Galerkin FEM are compared when solving the same problem with different mesh resolutions, starting at 0.1 and increasing it to 0.02 and 0.005. For the discontinuous Riemann-Galerkin method, using a coarse mesh does not produce spurious oscillations, even though high-frequency features are filtered out due to numerical dissipation. The same experiment has been carried out with the continuous Galerkin FEM, only to conclude that oscillations that characterize the method amplify when the resolution decreases. They do, however, remain finite. Note that no stabilization whatsoever has been used for the continuous Galerkin method so that care must be taken when comparing the latter with the Riemann-Galerkin method where characteristic variables are upwinded. As a final note, it must be stressed that such high resolutions as those previously employed are never used in large-scale ocean models. This is why the last experiment, carried out on low-resolution meshes, was presented. Namely to highlight the usability of the discontinuous Riemann-Galerkin method on low-resolution meshes. Nevertheless, it must be stressed that the use of discontinuous methods implies increasing the number of unknowns compared with continuous methods on meshes having the same resolution.

Finally, another way of comparing the three finite element methods is to determine the CFL condition for each of them. A von Neumann stability analysis allows to find – after quite tedious and lengthy computations – the maximum Courant number $C = \alpha \Delta t / \Delta x$ that guarantees numerical stability. For the continuous Galerkin method, we have $C \leq 2\sqrt{3}/3 \simeq 1.15$. For the discontinuous Galerkin method – that involves the determinant of a 6-by-6 matrix –, we have $C \leq 0.5$. Finally, the discontinuous

Riemann-Galerkin method yields the following condition: $C \leq 0.2564$. The latter was determined numerically while the first two were determined analytically.
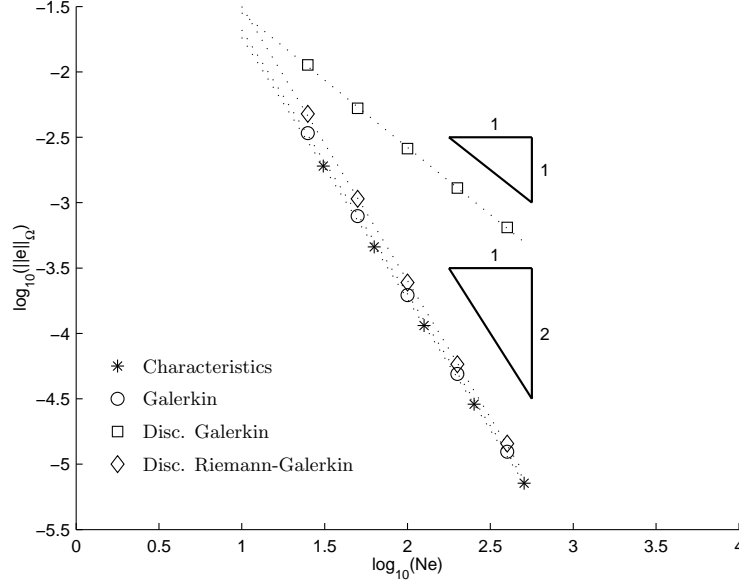
Figure 2.12: L^2-norm ($||e||_\Omega$) of the error in the elevation η on gradually-refined meshes for the three FEM with the hyperbolic-tangent initial condition ($R = 10$) at $t = 1$. Notice the second-order rate of convergence obtained with the Galerkin and discontinuous Riemann-Galerkin methods while the discontinuous Galerkin method yields a first-order rate. The dotted lines represent least-square approximations to experimental errors. The error is plotted versus the number of elements.

2.3 Conclusions

A benchmark for the propagation of Poincaré waves within a one-dimensional finite domain has been proposed and a comparison between four numerical methods to resolve it has been accomplished. The use of a steplike – and thus discontinuous – initial elevation field makes it challenging for numerical techniques to capture the traveling discontinuity without spawning spurious oscillations. Because the equations describing the physics of the problem are hyperbolic, the method of characteristics is a suitable way of solving for the wave propagation. If a sufficiently accurate time scheme is employed, this technique is able to solve the benchmark very satisfyingly.

More commonly used numerical methods were then presented. In the considerations that follow, we bear in mind that the issue of time discretization must be thoroughly investigated as well. As we already said it, this was not the subject of this chapter. The classical continuous Galerkin FEM has difficulties capturing steep gradients, let alone discontinuities. This was revealed by the experiment carried out with
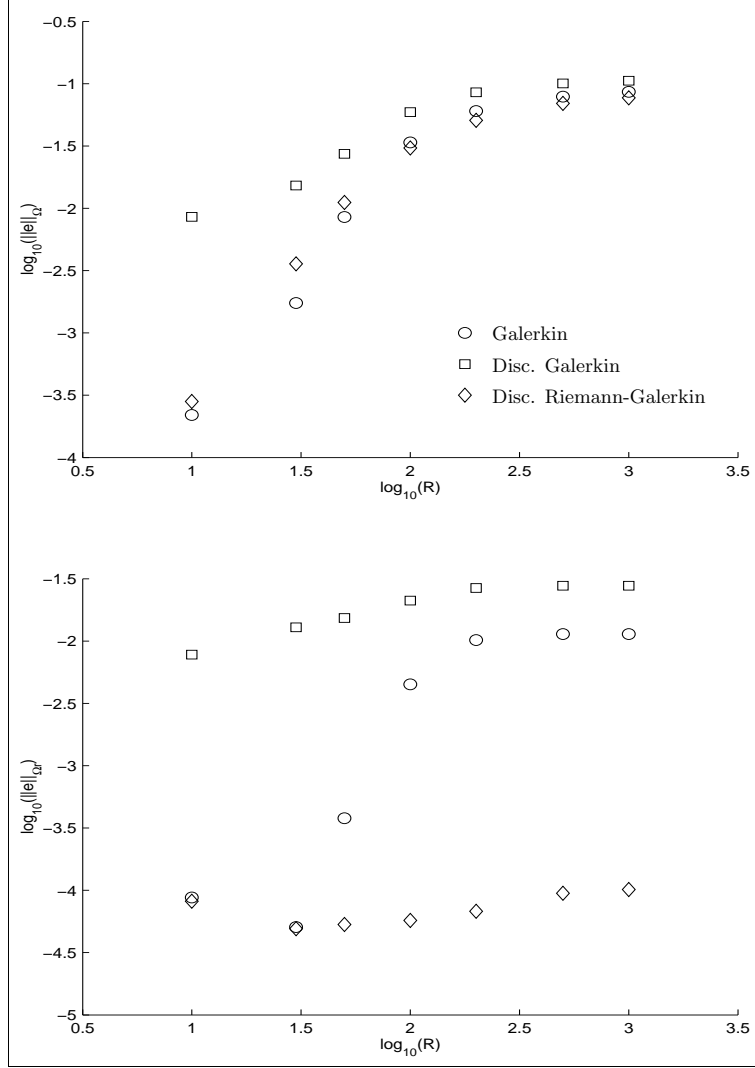
Figure 2.13: The top graph shows the L^2-norm of the error in the elevation η on a mesh containing 100 uniform elements for increasing steepness parameter R with the hyperbolic-tangent initial condition at $t = 2$. The bottom graph differs from the top graph in the calculation of the error: the error is computed on the restricted domain $\Omega_r = [-0.25, 0.25]$ that does not contain any of the discontinuities. The same symbols are used for both graphs. The bottom graph shows that for the Galerkin and discontinuous Galerkin methods, oscillations spread out to reach the inner region while the latter remains devoid of spurious oscillations for the discontinuous Riemann-Galerkin method.
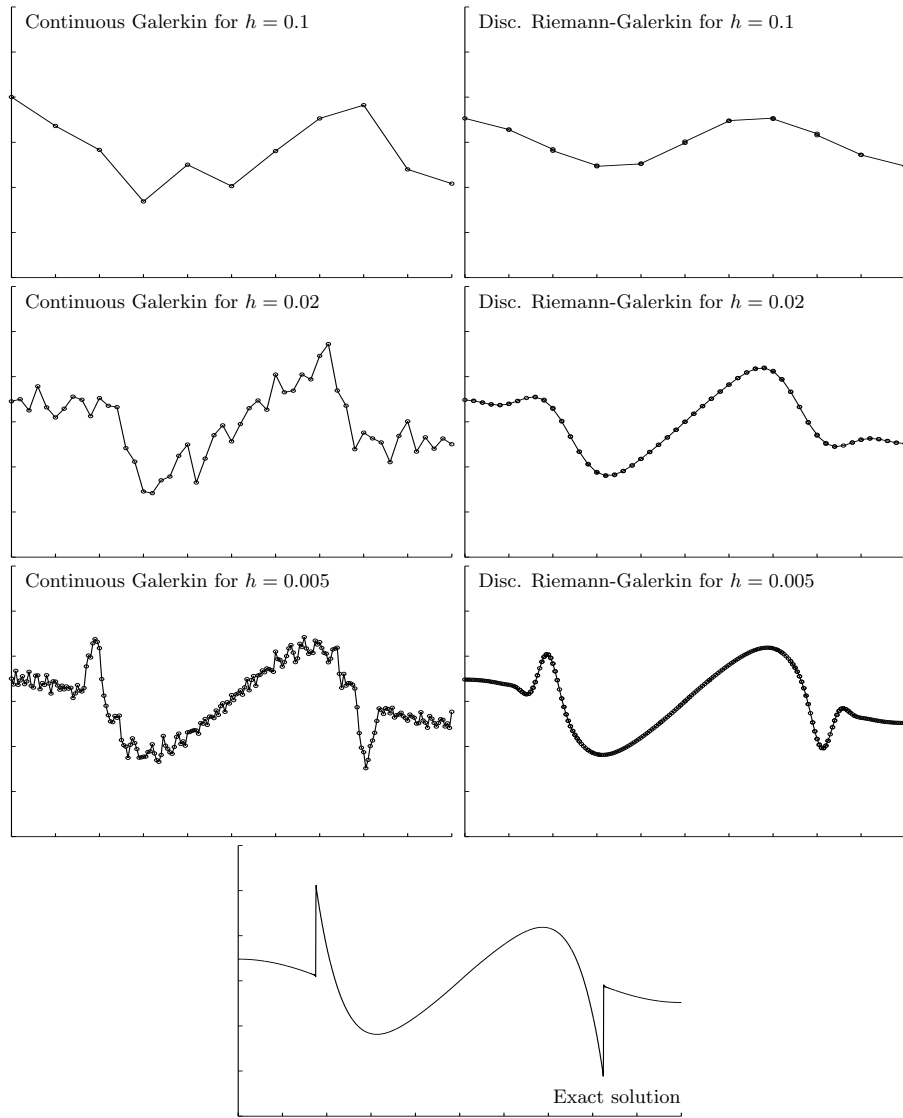
Figure 2.14: Comparison of the Galerkin and the discontinuous Riemann-Galerkin FEM at time $t = 20$ for a time step of 0.001. Left and right panels are the solutions for the Galerkin and the discontinuous Riemann-Galerkin method, respectively. The first, second and third rows show results for meshes containing 10 ($h = 0.1$), 50 ($h = 0.02$) and 200 ($h = 0.005$) elements. The bottom graph is the exact solution.

the hyperbolic tangent initial elevation field. Increasing the number of elements is not really a solution by itself, for an infinite number is necessary to resolve the discontinuity. In that respect, the discontinuous Galerkin (DG) method is appealing for its ability to exactly represent discontinuities. However, this may constitute an asset as much as a drawback in the sense that one has to carefully choose the variable of which continuity is weakly enforced. That statement is illustrated by comparing the classical DG method and the so-called discontinuous Riemann-Galerkin (DRG) method. In the former, we enforce continuity of the variables whose spatial derivatives appear in the formulation. Usual DG schemes where upwind weighting is naively applied to the primitive variables (velocity and elevation) appear to poorly perform for all values of λ. It is then mandatory to impose the continuity of suitable combinations of the primitive variables. It is well known that enforcing the weak continuity of the so-called Riemann variables would perform quite better. Such an approach is known as the DG method with a Riemann solver and its numerical performances have been well documented in the literature (*Roe*, 1981; *Schwanenberg et al.*, 2000; *Cockburn et al.*, 2001; *Aizinger and Dawson*, 2002; *Flaherty et al.*, 2002; *Schwanenberg and Harms*, 2004; *Kubatko et al.*, 2006a; *Remacle et al.*, 2006). In the one-dimensional framework, this established method is presented as the DG formulation expressed in terms of Riemann variables. The main contribution of this benchmark is to show that the one-dimensional counterpart of the DGM with a Riemann solver is the optimal technique. It is hardly feasible to extend the method of characteristics to 2D and 3D cases and the definition of Riemann variables in higher dimensions is not obvious. Hence, the classical approach consists in considering a simplified version of the one-dimensional Riemann problem along the normal direction of each segment, the functioning of which has been detailed in this chapter.

The continuous Galerkin and the discontinuous Galerkin methods can be both easily extended in higher dimensions without too much effort and the extensions of our results can be immediately derived. This benchmark appears to be very illustrative of the numerical behavior of wave propagation problems that model the barotropic systems of ocean models.

Chapter 3

Finite element methods for geophysical fluid flow instabilities

Summary

The mesoscale variability in the ocean originates from baroclinic and, to a lesser extent, barotropic instabilities. The equations describing those instabilities are inviscid, rendering their numerical modeling particularly challenging. In this chapter, some finite element formulations to model these instabilities are presented.

The numerical modeling of physical instabilities is prone to many difficulties and constitutes an interesting candidate for evaluating the performance of a method. Both space and time discretizations must be performed with great care to avoid any artificial amplification or damping of physical instabilities. In this kind of problems where physical dissipation is absent from the equations, this becomes challenging. Among physical instabilities observed in ocean flows, barotropic, baroclinic and a mixture of both are the most commonly encountered in the literature (*Pedlosky*, 1964; *Kuo*, 1973; *Hart*, 1974; *Killworth*, 1980).

The study of barotropic shear flow instabilities dates back to *Kuo* (1949). Kuo took one step further from the classical Rayleigh stability problem by incorporating the effect of latitude variation in the Coriolis parameter, the β-effect, whereby necessary conditions for instabilities are altered as compared with those derived for flows on an f-plane. These necessary conditions can be found in *Kuo* (1973) and *Cushman-Roisin* (1994) and are recalled in Appendix B. When a flow is unstable, the question that comes to mind is how fast perturbations grow. As growth rates are generally not derivable for arbitrary zonal currents – only bounds can be extracted (*Pedlosky*, 1979) –, many authors have investigated specific basic flows in the past with the aim of evaluating growth rates. The zonal currents generally considered serve as an idealization of observed oceanic and atmospheric patterns. In that respect, the hyperbolic-tangent profile has been used quite often. *Michalke* (1964) studied this profile on an f-plane

(no β-effect) system while *Dickinson and Clare* (1973) and *Kuo* (1973) computed perturbations growth rate and phase speed dependent on wavenumber and a dimensionless β parameter. Another typical basic state is a jet-type velocity profile, usually represented by a cosine squared or hyperbolic-secant squared (*Kuo*, 1973, 1978; *Killworth*, 1980). Further idealization of the hyperbolic-tangent profile as a piecewise linear profile is of interest for two reasons. First, as shown in *Cushman-Roisin* (1994), an analytical solution exists for the growth rate on an f-plane. Second, it is more amenable to numerical resolution, insofar as the profile is exactly represented – i.e., there is no truncation error – by low-order polynomial interpolation.

In this chapter, both the hyperbolic-tangent profile and its linear simplification are employed to investigate the behavior of a free-surface and of two rigid-lid finite-element formulations. The free-surface formulation solves the primitive shallow-water equations. The rigid-lid formulations are the standard vorticity-stream function and velocity-pressure formulations. Even though the ocean modeling community seems to depart from rigid-lid ocean models (see *Killworth et al.*, 1991; *Griffies et al.*, 2000, for discussions about rigid-lid and free-surface ocean models), this formulation is used here to compare our results with those theoretically predicted using the same set of equations. By doing so, all differences with theoretical results come from the numerical treatment of the equations and not the physics. The main goal of this chapter is to appraise the finite element method in the way it represents barotropic and baroclinic instabilities. To that end, it is first tested that all three finite element formulations are capable of maintaining the steady-state geostrophic equilibrium without artificial generation or dissipation of energy, nor distortion of the flow. We then compare all three methods within the scope of small pertubations so that linear stability analysis remains valid and, aside from intercomparison, a reference analytical solution exists. In particular, the influence of the free-surface is to be numerically assessed, since all theoretical results have been derived for the rigid-lid vorticity - stream function formulation. We finally extend the investigation to timescales that allow for nonlinear advective terms to play a more significant role, permitting the development of eddies. In that respect, the way advection is numerically treated is pivotal because the quest for numerical stability more often than not precludes the unfolding of physical instabilities.

3.1 Problem formulation

Since we will limit ourselves to motions whose scale is on the order of a few hundreds kilometers, the problem can be formulated in a cartesian coordinate system rather than in a spherical system. That is, the so-called annulus approximation will be made (*Pedlosky*, 1964): the two-dimensional domain of interest is deemed zonally infinite while the meridional extension remains finite. The β-effect is retained and flow occurs over a flat bottom. The unboundedness of the domain in the zonal direction is tackled by imposing periodicity in that direction. This design choice is mostly dictated by numerical feasability but hardly constrains our framework: the basic flows only vary non-periodically in the meridional direction and wavy disturbances are, by nature, periodic. To further set out the framework, we define the coordinates (x, y)

to be positive eastward and northward, respectively, while (u, v) are the corresponding velocity components. The system is assumed to be devoid of viscosity and all frictional effects at the bottom and the surface are neglected. Lateral boundaries are impermeable. The inviscid nonlinear shallow-water equations will be used to model the system:

$$\frac{\partial u}{\partial t} + \mathbf{u} \cdot \boldsymbol{\nabla} u - fv \quad = \quad -g\frac{\partial \eta}{\partial x}, \tag{3.1}$$

$$\frac{\partial v}{\partial t} + \mathbf{u} \cdot \boldsymbol{\nabla} v + fu \quad = \quad -g\frac{\partial \eta}{\partial y}, \tag{3.2}$$

$$\frac{\partial \eta}{\partial t} + \boldsymbol{\nabla} \cdot (H\mathbf{u}) \quad = \quad 0, \tag{3.3}$$

where η is the free-surface elevation with respect to an undisturbed reference level, f is the Coriolis parameter and is linearized about a reference latitude so that $f = f_0 + \beta_0 y$, g is the acceleration due to gravity and $H(x, y, t) = h + \eta(x, y, t)$ is the total fluid layer thickness with h being the constant undisturbed fluid thickness. In most barotropic shallow-water models, it is generally assumed that $\eta \ll h$ so that the divergence of the transport $H\mathbf{u}$ in (3.3) can be linearized to become $\boldsymbol{\nabla} \cdot (H\mathbf{u}) \simeq h\boldsymbol{\nabla} \cdot \mathbf{u}$, assuming also that the depth h is constant, as indicated above. Letting L be a characteristic length scale, the nondimensional form of (3.1)-(3.3) is

$$\frac{\partial u}{\partial t} + \mathbf{u} \cdot \boldsymbol{\nabla} u - (1 + \beta y)v \quad = \quad -\frac{\partial \eta}{\partial x}, \tag{3.4}$$

$$\frac{\partial v}{\partial t} + \mathbf{u} \cdot \boldsymbol{\nabla} v + (1 + \beta y)u \quad = \quad -\frac{\partial \eta}{\partial y}, \tag{3.5}$$

$$\frac{\partial \eta}{\partial t} + \alpha^2 \, \boldsymbol{\nabla} \cdot \mathbf{u} \quad = \quad 0, \tag{3.6}$$

where the velocity scale is $U = Lf_0$, the time scale is $T = L/U$ and the elevation scale $E = L^2 f_0^2 / g$ is defined so that the Coriolis force and the elevation gradient are both on the same order of magnitude. Finally, α is the ratio of the external deformation radius to the length scale

$$\alpha = \frac{\sqrt{hg}}{Lf_0}.$$

The dimensionless beta parameter is $\beta = \beta_0 L^2 / U$. Note that all variables are now dimensionless. Under typical oceanic shear flow conditions, we have $\sqrt{hg} \simeq 10^2$ m s^{-1}, $L \simeq 10^4 - 10^5$ m and $f_0 \simeq 10^{-5} - 10^{-4}$ s^{-1} so that α ranges from 10 to 1000 and β ranges from 10^{-3} to 10^{-1}. We see that under such conditions, a valid approximation to the continuity equation is that of a divergence-free velocity, also known as the rigid-lid approximation. Within that scope, (3.4)-(3.6) become

$$\frac{\partial u}{\partial t} + \mathbf{u} \cdot \boldsymbol{\nabla} u - (1 + \beta y)v \quad = \quad -\frac{\partial p}{\partial x}, \tag{3.7}$$

$$\frac{\partial v}{\partial t} + \mathbf{u} \cdot \boldsymbol{\nabla} v + (1 + \beta y)u \quad = \quad -\frac{\partial p}{\partial y}, \tag{3.8}$$

$$\boldsymbol{\nabla} \cdot \mathbf{u} \quad = \quad 0, \tag{3.9}$$

where p is the pressure to be applied on top of the fluid layer to keep the surface flat and it has been nondimensionalized with a pressure scale $P = \rho_0 L^2 f_0^2$, where ρ_0

is the fluid density. The continuity equation now acts as a constraint, effecting the velocity to be divergence-free. In that respect, the surface pressure is a diagnostic variable.

From (3.7)-(3.9), the vorticity-stream function formulation is derived by first defining the stream function $\psi(x, y)$ so that $u = -\frac{\partial \psi}{\partial y}$ and $v = \frac{\partial \psi}{\partial x}$ while the relative vorticity $\omega = \frac{\partial v}{\partial x} - \frac{\partial u}{\partial y} = \nabla^2 \psi$. In so doing, the continuity equation is identically satisfied and both velocity components are derivable from a unique scalar variable – the stream function –, which permits to reduce the number of direct unknowns from three to one. The vorticity equation is obtained by computing $\frac{\partial}{\partial x}(3.8)$ - $\frac{\partial}{\partial y}(3.7)$, which gives rise to

$$\frac{\partial \omega}{\partial t} + u \frac{\partial \omega}{\partial x} + v \frac{\partial \omega}{\partial y} = -\beta v.$$

Now, the two-equation system, whose vorticity equation is written in terms of the stream function, is

$$\frac{\partial \omega}{\partial t} - \frac{\partial \psi}{\partial y} \frac{\partial \omega}{\partial x} + \frac{\partial \psi}{\partial x} \frac{\partial \omega}{\partial y} = -\beta \frac{\partial \psi}{\partial x}, \tag{3.10}$$

$$\nabla^2 \psi = \omega. \tag{3.11}$$

Notice that this system could be collapsed onto a single equation for the stream function, without resorting to the substitution variable ω. However, advective terms would then take on third-order spatial derivatives, which would require undesirable, high-order interpolants. Furthermore, using the relative vorticity permits to treat the nonlinear terms more easily as if ω were simply be advected by the velocity field, derived from the stream function. We must bear in mind, though, that (3.10) is *not* a traditional advection equation, for the stream function depends on the vorticity. Hence, although it seems like we do away with the nonlinearity, it is concealed and entrenched within the problem. The stream function needs be specified at the southern and northern boundaries, where it has to be set to a constant that depends on the problem under consideration. It is also worth unveiling what looks like a paradox in (3.10). As far as the Coriolis term is concerned, only the β-effect remains. If only the f-plane approximation were made, the right-hand side of (3.10) would vanish and it would not be possible to say whether or not flow occurs within a rotating framework. In fact, any solution to (3.10) – with $\beta = 0$ – in a rotating framework or in an inertial framework would be the same because both would obey the same equation. The vorticity equation (3.10) is identical to the one derived within the scope of the geostrophic approximation in *Pedlosky* (1979), where the author concludes that the sole effect of the earth's sphericity on the geostrophic solution is due entirely to the variation of f with latitude but not on f itself.

Considering the rigid-lid approximation (3.7)-(3.9) again, another formulation can be had by taking the divergence of the momentum equations to derive a Poisson equation for the pressure. We first write the momentum equations (3.7)-(3.8) in vectorial form

$$\frac{\partial \mathbf{u}}{\partial t} + (\mathbf{u} \cdot \boldsymbol{\nabla}) \mathbf{u} + \mathbf{F}^c = -\boldsymbol{\nabla} p, \tag{3.12}$$

where $\mathbf{F}^c = (1 + \beta y)\hat{e}_z \wedge \mathbf{u}$ is the Coriolis force, with $\hat{e}_z$ being the upward-pointing unit vector. To derive the continuous pressure Poisson equation (PPE), we take the divergence of (3.12), giving rise to

$$-\nabla^2 p = \boldsymbol{\nabla} \cdot [(\mathbf{u} \cdot \boldsymbol{\nabla})\,\mathbf{u}] + \boldsymbol{\nabla} \cdot \mathbf{F}^c. \qquad (3.13)$$

In deriving (3.13), the divergence and time differentiation have been interchanged so that use could be made of the continuity equation. The issue of Neumann pressure boundary conditions has been settled by *Gresho and Sani* (1987): take the normal projection of (3.12) onto Γ, namely

$$\frac{\partial p}{\partial n} = -\hat{\mathbf{n}} \cdot \mathbf{g} \qquad \text{on } \Gamma, \qquad (3.14)$$

where the condition $\mathbf{u} \cdot \hat{\mathbf{n}} = 0$ on Γ was called on and where $\mathbf{g}$ regroups the advection and Coriolis terms of (3.12). Note that $\hat{\mathbf{n}}$ is the outward-pointing normal to the boundary. The pressure computed from (3.13) is known up to an arbitrary additive constant. To summarize, the velocity-pressure formulation is given by

$$\frac{\partial u}{\partial t} + \mathbf{u} \cdot \boldsymbol{\nabla} u - (1 + \beta y)v \;\; = \;\; -\frac{\partial p}{\partial x}, \qquad (3.15)$$

$$\frac{\partial v}{\partial t} + \mathbf{u} \cdot \boldsymbol{\nabla} v + (1 + \beta y)u \;\; = \;\; -\frac{\partial p}{\partial y}, \qquad (3.16)$$

$$-\nabla^2 p \;\; = \;\; \boldsymbol{\nabla} \cdot [(\mathbf{u} \cdot \boldsymbol{\nabla})\,\mathbf{u}] + \boldsymbol{\nabla} \cdot \mathbf{F}^c. \qquad (3.17)$$

Any given zonal flow $(\bar{u}(y), 0)$ – henceforth called basic state – is solution to the *steady-state* nonlinear system of equations (3.4)-(3.6), provided that the elevation be in geostrophic equilibrium. For the vorticity-stream function formulation (3.10)-(3.11), a zonal flow is obtained by requiring that the stream function only depend on y. For the velocity-pressure formulation (3.15)-(3.17), a zonal flow is solution to the steady-state equations if the pressure satisfies the geostrophic equilibrium, as was the role of the elevation in the free-surface formulation. Depending on its structure, a zonal flow may be unstable to small perturbations. Necessary conditions for instability are recalled in Appendix B.

The problem we wish to solve may be stated as follows: *given an unstable basic state and a disturbance of given wavenumber k, track the evolution of the disturbance and evaluate its growth rate kc_i.* Two benchmark shear flows, whose unstable modes have been studied in the past (*Dickinson and Clare*, 1973; *Kuo*, 1978; *Cushman-Roisin*, 1994), will be presented and will serve as comparative tools between the three finite element formulations that are outlined below.

3.2 Three finite element models

We now proceed with the presentation of three different manners of wielding the problem laid out in the foregoing section. The first finite element formulation deals with the free-surface elevation as a prognostic variable while the last two assume that a rigid lid is applied onto the top of the fluid layer. The three formulations follow the

same order as that used to introduce the equations in Section 2. That is, we present the free-surface, vorticity-stream function and velocity-pressure formulations, in that order. Even though for large-scale barotropic systems, the difference between free-surface and rigid-lid flows is marginal, as we will see, the differences bewteen the corresponding finite element formulations are quite striking and prone to comparative analysis. Ironically, the formulations that are analytically more obedient – the rigid-lid formulations – bring about numerical challenges. Our objective is definitely not to offer an overview of existing finite element formulations for the incompressible Navier-Stokes equations (see e.g., *Gresho and Sani*, 1998), but we thought it would be interesting to linger on two common formulations, not the least because the Coriolis term does not appear in the classical Navier-Stokes equations considered by Gresho and Sani and because the computation of the pressure sometimes remains subject to difficulties.
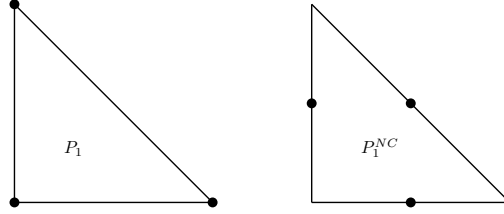
Figure 3.1: Nodes location for the P_1 and P_1^{NC} discretizations.

Because we essentially have to solve an initial-value problem, and because disturbances might not grow as fast as one expect them to, all formulations presented below must be able to preserve a geostrophic equilibrium (given as initial state) with neither dissipation nor distortion, at least until roundoff errors kick in and destabilize the flow, if the latter is physically unstable. Any violation of this statement would render the associated formulation questionable, for any numerically-generated deviation – that is, not generated by forced disturbances – from this initial state would most likely falsify the analysis. Prior to presenting the finite element formulations, it is worth saying a few words about the elements that are used to approximate the various variables – the velocity, the pressure, the elevation, the vorticity and the stream function, depending upon which formulation is under scrutiny. Linear conforming and non-conforming elements will be used throughout the remainder of this section. As illustrated in Figure (3.1), the linear conforming element (the so-called P_1 element) has its nodal values located at each vertex while the linear non-conforming element (the so-called P_1^{NC} element) has its nodal values located at the middle of each edge (see e.g., *Hua and Thomasset*, 1984; *Hanert et al.*, 2004). Their linear basis functions will be denoted by ϕ_i^p and ϕ_i^u, respectively, as a reminder that the pressure and elevation are conforming while the velocity is non-conforming. Conforming interpolation requires interpolated variables to be continuous across inter-element boundaries while non-conforming interpolation does not so; continuity is only ensured at the middle of each inter-element

boundary. Finally, we abide by the following conventions: for a given mesh, it is assumed that there are M vertices and N edges. A n-subscript indicates that the variable is time-discretized and evaluated at time t^n. The domain of interest is denoted by Ω and its lateral boundary is noted Γ.

3.2.1 The free-surface formulation

Space-discretization of (3.4)-(3.6) is conducted by using the P_1^{NC} element for each velocity component and the P_1 element for the elevation (see e.g., *Le Roux et al.*, 1998; *Hanert et al.*, 2003, 2005, for studies on finite elements for shallow-water flows). Opting for the Galerkin finite element method, where test functions in the variational formulation are taken to be basis functions, the system (3.4)-(3.6) mutates to the following system of $2N + M$ ordinary differential equations:

$$\mathbf{M^u}\frac{d\mathrm{R}}{dt} + \mathbf{A}\mathrm{R} + \mathbf{C}\mathrm{R} \quad = \quad -\mathbf{G}\mathrm{H}, \tag{3.18}$$

$$\mathbf{M^p}\frac{d\mathrm{H}}{dt} - \alpha^2 \mathbf{D}\mathrm{R} \quad = \quad 0. \tag{3.19}$$

In the above equations, $\mathbf{M^u}$ is the non-conforming mass matrix, $\mathbf{A}$ is the advection matrix, $\mathbf{C}$ is the Coriolis matrix, $\mathbf{G}$ is the gradient matrix and $\mathbf{M^p}$ is the conforming mass matrix. The divergence matrix $\mathbf{D}$ is obtained after integration by parts (the contour integral vanishes because $\mathbf{u_h} \cdot \hat{\mathbf{n}} = 0$ on Γ, where $\mathbf{u_h}$ is the discrete velocity field). Those matrices are written out below.

$$\mathbf{M^u} = \left[\begin{array}{cc} <\phi_i^u \phi_j^u> & 0 \\ 0 & <\phi_i^u \phi_j^u> \end{array} \right] \quad \in \mathbb{R}^{2N \times 2N},$$

$$\mathbf{A} = \left[\begin{array}{cc} <\phi_i^u \mathbf{u}_h \cdot \boldsymbol{\nabla} \phi_j^u> & 0 \\ 0 & <\phi_i^u \mathbf{u}_h \cdot \boldsymbol{\nabla} \phi_j^u> \end{array} \right] \quad \in \mathbb{R}^{2N \times 2N},$$

$$\mathbf{C} = \left[\begin{array}{cc} 0 & -<(1 + \beta y)\phi_i^u \phi_j^u> \\ <(1 + \beta y)\phi_i^u \phi_j^u> & 0 \end{array} \right] \quad \in \mathbb{R}^{2N \times 2N},$$

$$\mathbf{G} = \left[\begin{array}{c} <\phi_i^u \frac{\partial \phi_j^p}{\partial x}> \\ <\phi_i^u \frac{\partial \phi_j^p}{\partial y}> \end{array} \right] \quad \in \mathbb{R}^{2N \times M},$$

$$\mathbf{D} = \left[\begin{array}{cc} <\frac{\partial \phi_i^p}{\partial x} \phi_j^u> & <\frac{\partial \phi_i^p}{\partial y} \phi_j^u> \end{array} \right] \quad \in \mathbb{R}^{M \times 2N},$$

$$\mathbf{M^p} = \left[<\phi_i^p \phi_j^p> \right] \quad \in \mathbb{R}^{M \times M},$$

where $< >$ indicates integration over Ω. It is conspicuous that the gradient matrix is the transpose of the divergence matrix, because integration by parts was carried out in the continuity equation. The classical treatment of the Navier-Stokes equations, though, usually implies integrating the pressure gradient by parts but not the divergence of the velocity, which leads to the same result whatsoever. Our choice is justified by the fact that we use non-conforming velocity elements. The vector R contains the nodal values of both velocity components, that is

$$\mathrm{R} = \left[\begin{array}{c} \mathrm{U} \\ \mathrm{V} \end{array} \right],$$

where U and V denote the nodal values of each velocity component. The vector H contains the elevation nodal values. Note that the advection matrix $\mathbf{A}$ depends upon the velocity, All three variables of the free-surface formulation – both components of the velocity and the elevation – are solved for in a coupled fashion. This allows for varying the degree of implicitness of the elevation gradient and the divergence of the velocity in the continuity equation. Time-discretization of (3.18) and (3.19) leads to

$$\mathbf{M^u}\frac{R^{n+1} - R^n}{\Delta t} + \mathbf{A}R^n + \frac{1}{2}\mathbf{C}\left(R^{n+1} + R^n\right) = -\mathbf{G}\left(\frac{1}{2}H^{n+1} + \frac{1}{2}H^n\right),$$

$$\mathbf{M^p}\frac{H^{n+1} - H^n}{\Delta t} - \alpha^2\mathbf{D}\left(\frac{1}{2}R^{n+1} + \frac{1}{2}R^n\right) = 0.$$

Rearranging the above expressions so that all nodal values at time step t^{n+1} appear in the left-hand side while all nodal values at time step t^n appear in the right-hand side, we arrive at the following coupled linear system in the $2N + M$ nodal values:

$$\begin{cases} \left(\dfrac{\mathbf{M^u}}{\Delta t} + \dfrac{1}{2}\mathbf{C}\right)R^{n+1} + \dfrac{1}{2}\mathbf{G}H^{n+1} = \left(\dfrac{\mathbf{M^u}}{\Delta t} - \mathbf{A} - \dfrac{1}{2}\mathbf{C}\right)R^n - \dfrac{1}{2}\mathbf{G}H^n, \\[2ex] -\dfrac{1}{2}\alpha^2\mathbf{D}R^{n+1} + \dfrac{\mathbf{M^p}}{\Delta t}H^{n+1} = \dfrac{1}{2}\alpha^2\mathbf{D}R^n + \dfrac{\mathbf{M^p}}{\Delta t}H^n. \end{cases}$$

$$(3.20)$$

The Coriolis term is always treated semi-implicitly so as to not artificially generate nor dissipate energy, complying with the fact that the Coriolis force does not physically do work. The free-surface formulation allows for the propagation of fast surface waves (e.g., Poincaré waves) whose phase speed is on the order of $\sqrt{gh}$ and can therefore reach up to hundreds of m s^{-1}. If an explicit, foward-backward time scheme is used (see e.g., *Beckers and Deleersnijder*, 1993), the CFL condition imposes too stringent of a time step, as compared with climatic timescales. A semi-implicit treatment of the terms governing the propagation of those surface waves relaxes the constraint on the time step – the scheme becomes unconditionally stable – and serves the purpose of modeling large-scale features without resolving fast-propagating smaller-scale features. There is nevertheless a cost to unconditional stability: the system (3.20) is fully coupled and all variables must be solved for together. Note that advection is explicit. An alternative consists in treating the advected field implicitely while the advecting field remains explicit, which imposes the reconstruction of the full system left-hand side at each time step. Another alternative is to treat both the advecting and advected fields implicitely, a method that implies solving a nonlinear system at each time step. Both these alternatives are beyond the scope of the present chapter.

3.2.2 The vorticity - stream function formulation

Both the vorticity and the stream function are discretized using the P_1 element so that (3.10)-(3.11) is converted to the following system of $2M$ ordinary differential equations

$$\mathbf{M^p}\frac{d\mathrm{W}}{dt} + \mathbf{N}\mathrm{W} = \mathrm{B}_\omega, \tag{3.21}$$

$$\mathbf{L}\mathrm{S} = \mathrm{B}_\psi, \tag{3.22}$$

where W and S are vectors of vorticity and stream function nodal values, respectively. The matrices $\mathbf{N}$ and $\mathbf{L}$ and the vectors B_ω and B_ψ take on the following form:

$$\mathbf{N} = \left[< \phi_i^p \left(-\frac{\partial \psi_h}{\partial y} \frac{\partial \phi_j^p}{\partial x} + \frac{\partial \psi_h}{\partial x} \frac{\partial \phi_j^p}{\partial y} \right) > \right] \quad \in \mathbb{R}^{M \times M},$$

$$\mathbf{L} = \left[< \boldsymbol{\nabla} \phi_i^p \cdot \boldsymbol{\nabla} \phi_j^p > \right] \quad \in \mathbb{R}^{M \times M},$$

$$B_\omega = \left[-\beta < \phi_i^p \frac{\partial \psi_h}{\partial x} > \right] \quad \in \mathbb{R}^M,$$

$$B_\psi = \left[- < \phi_i^p \omega_h > \right] \quad \in \mathbb{R}^M,$$

where ω_h and ψ_h are the discrete vorticity and stream function fields. Note that the contour integral emanating from integration by parts of the Laplacian vanishes because only Dirichlet boundary conditions are enforced on ψ_h. Time-discretization of (3.21) yields

$$\mathbf{M^p} \frac{W^{n+1} - W^n}{\Delta t} + \frac{1}{2} \mathbf{N} W^{n+1} + \frac{1}{2} \mathbf{N} W^n = B_\omega^n. \tag{3.23}$$

Rearranging (3.23), the full system is

$$\begin{cases} \mathbf{L} S^n = B_\psi^n, \\ \left[\dfrac{\mathbf{M^p}}{\Delta t} + \dfrac{1}{2} \mathbf{N} \right] W^{n+1} = \left[\dfrac{\mathbf{M^p}}{\Delta t} - \dfrac{1}{2} \mathbf{N} \right] W^n + B_\omega^n, \end{cases} \tag{3.24}$$

and is set off by an initial condition on the vorticity. Notice that the advection matrix $\mathbf{N}$ is always evaluated at time step t^n because decision was made to first solve for the stream function and then, for the new vorticity in terms of the stream function. In other words, the system is sequential in time. This procedure allows for a convenient way of handling the nonlinear advection term.

3.2.3 The velocity-pressure formulation

Discretization in space of (3.15)-(3.17) must be done carefully. A naive approach is to start with the continuous pressure Poisson equation (3.17) and discretize it. In so doing, the discretized Laplacian takes on the same expression as that obtained in the previous vorticity-stream function formulation. That is, the matrix $\mathbf{L}$ is used to approximate $-\nabla^2$. This, however, yields an inconsistent – and unstable – discretization in the sense that the discrete pressure and velocity fields are incompatible with one another, for the velocity boundary conditions are not consistently incorporated within the discrete Laplacian operator. In fact, as shown in *Gresho et al.* (1984), the issue of deriving the discrete consistent pressure Poisson equation (PPE) must be addressed the other way around by working on the space-discretized form of the momentum and continuity equations to extract the discrete Laplacian operator. Both components of the velocity are discretized using the P_1^{NC} element while the pressure is interpolated with the P_1 element. Space-discretization of (3.12), together with the continuity equation (3.9), lead to

$$\mathbf{M^u} \frac{d\mathbf{R}}{dt} + \mathbf{A} \mathbf{R} + \mathbf{C} \mathbf{R} = -\mathbf{G} \mathbf{P}, \tag{3.25}$$

$$\mathbf{D} \mathbf{R} = 0, \tag{3.26}$$

which consists of a system of $2N$ ODEs in the nodal values R, subject to the constraint that the velocity field be discretely divergence-free. All matrices and vectors used in this formulation were defined earlier when dealing with the free-surface formulation. We shall now proceed with the derivation of the so-called *consistent* PPE or CPPE. From (3.26), we may write

$$\mathbf{D}\frac{d\mathrm{R}}{dt} = 0,$$

and deduce that the discrete acceleration is divergence-free. Because the mass matrix $\mathbf{M^u}$ is non-singular, we may isolate $d\mathrm{R}/dt$ in (3.25) and substitute it into the newly-derived statement of divergence-free acceleration, leading to the following equation:

$$\mathbf{D}\frac{d\mathrm{R}}{dt} = \mathbf{DM^{u}}^{-1}\left(-\mathbf{A}\mathrm{R} - \mathbf{C}\mathrm{R} - \mathbf{G}\mathrm{P}\right),$$

whose left-hand side may be time-discretized, which, using the fact that we set the velocity at time step t^{n+1} to be discretely divergence-free, produces the following equation

$$-\frac{1}{\Delta t}\mathbf{D}\mathrm{R}^n = \mathbf{DM^{u}}^{-1}\left(-\mathbf{A}\mathrm{R}^n - \mathbf{C}\mathrm{R}^n - \mathbf{G}\mathrm{P}^n\right),$$

whereupon P^n is to be solved for and is the discrete pressure corresponding to the discrete velocity field at time step t^n. Hence, the linear system is

$$\mathbf{DM^{u}}^{-1}\mathbf{G}\mathrm{P}^n = \mathbf{DM^{u}}^{-1}\left(\frac{1}{\Delta t}\mathbf{M^u}\mathrm{R}^n - \mathbf{A}\mathrm{R}^n - \mathbf{C}\mathrm{R}^n\right), \qquad (3.27)$$

where $-\nabla^2$ is now approximated by $\mathbf{DM^{u}}^{-1}\mathbf{G}$, which automatically incorporates the appropriate boundary conditions for the pressure (*Gresho et al.*, 1984). The previous expression loses its effectiveness if the matrix $\mathbf{M^u}$ is not diagonal beacause $\mathbf{M^{u}}^{-1}$ will, in general, be dense. It is common practice to lump the mass when this occurs. This is where one of the key properties of the P_1^{NC} element comes into play: its basis functions are orthogonal to one another, which renders the matrix $\mathbf{M^u}$ diagonal without having to resort to mass-lumping. Once the pressure is known at time step t^n, we may march in time and use (3.25) to compute the velocity at the next time step. Time-discretization of (3.25), together with (3.27), yields the full consistent velocity-pressure formulation:

$$\begin{cases} \mathbf{DM^{u}}^{-1}\mathbf{G}\mathrm{P}^n &= \mathbf{DM^{u}}^{-1}\left(\frac{1}{\Delta t}\mathbf{M^u}\mathrm{R}^n - \mathbf{A}\mathrm{R}^n - \mathbf{C}\mathrm{R}^n\right), \\ \left(\frac{\mathbf{M^u}}{\Delta t} + \frac{1}{2}\mathbf{C}\right)\mathrm{R}^{n+1} &= \left(\frac{\mathbf{M^u}}{\Delta t} - \mathbf{A} - \frac{1}{2}\mathbf{C}\right)\mathrm{R}^n - \mathbf{G}\mathrm{P}^n. \end{cases} \qquad (3.28)$$

The algorithm is started by specifying an initial velocity field, from which the initial pressure may be computed.

3.3 Two benchmark shear flows

The first basic state is a shear-zone type flow, consisting of two parallel and uniform currents on both sides of the shear layer, one oriented eastward and the other westward.

Both currents have the same magnitude and the dimensionless analytical expression to represent this first basic state is

$$\bar{u}(y) = -\tanh(y), \qquad (3.29)$$

The zonal flow (3.29) is represented on top panels of Figure (3.2). The second basic state is a piecewise linear function, whose expression is

$$\bar{u}(y) = \begin{cases} 1 & \text{if } y > 1 \\ y & \text{if } -1 < y < 1 \\ -1 & \text{if } y < -1 \end{cases} \qquad (3.30)$$

and is featured on bottom panels of Figure (3.2). Panels on the left of Figure (3.2) show the meridional extent of the domain used in numerical experiments. In that particular case, the extension is 10 times larger than the shear layer width so as to emulate the absence of boundaries. Care will have to be taken to ensure sufficient mesh resolution within the shear layer. The basic flow (3.30) is less realistic than the hyperbolic-tangent (3.29) – the first derivative is discontinuous – but this simplification presents two advantages. First, an analytical expression for the dispersion relation of perturbations exists when the problem is formulated on an f-plane in a zonal channel of infinite width. Therefore, the growth rate of any wavelike disturbance of a given wavenumber if known. Second, because the profile is linear, it can be interpolated with low-order elements without any truncation errors. This ensures that no spurious surface waves propagate due to the inexact representation of the initial state. For such a profile, the issue of determining whether or not those spurious surface waves have an influence on the growth rate is obviated.

3.4 Numerical experiments

As already mentioned, any of the presented finite element formulations is to be ruled out, were it not able to preserve the unperturbed steady-state basic flow (in geostrophic equilibrium). The three methods, together with the *inconsistent* velocity-pressure formulation, are hereafter tested for their capacity in maintaining the steady state without artificial generation or dissipation of energy, nor distortion of the flow. It should be borne in mind that, since the free-surface formulation allows for the propagation of surface waves, distortion may occur but it ought to be energy-preserving. In Figure (3.3), the relative deviation of the total energy is shown for a 140-day run starting with an unperturbed hyperbolic-tangent basic flow. The mesh contains 8192 triangles and the time step is 2500 s. Whereas the rigid-lid vorticity-stream function formulation is energy-preserving (up to roundoff errors), the free-surface and consistent velocity-pressure formulations yield coinciding curves and feature maximum deviations of about 0.01%. The inconsistent velocity-pressure formulation is shown for illustrative purposes an is found to lose about 30% of the initial total energy and is thus highly dissipative. It must be eliminated on that ground. The fact that the free-surface and consistent velocity-pressure formulations are not as accurate as the vorticity-stream function formulation is caused by a treatment of advective terms that is explicit in time. In what follows, wavenumbers κ, wavelengths λ and growth rates δ are always dimensionless, unless otherwise specified.
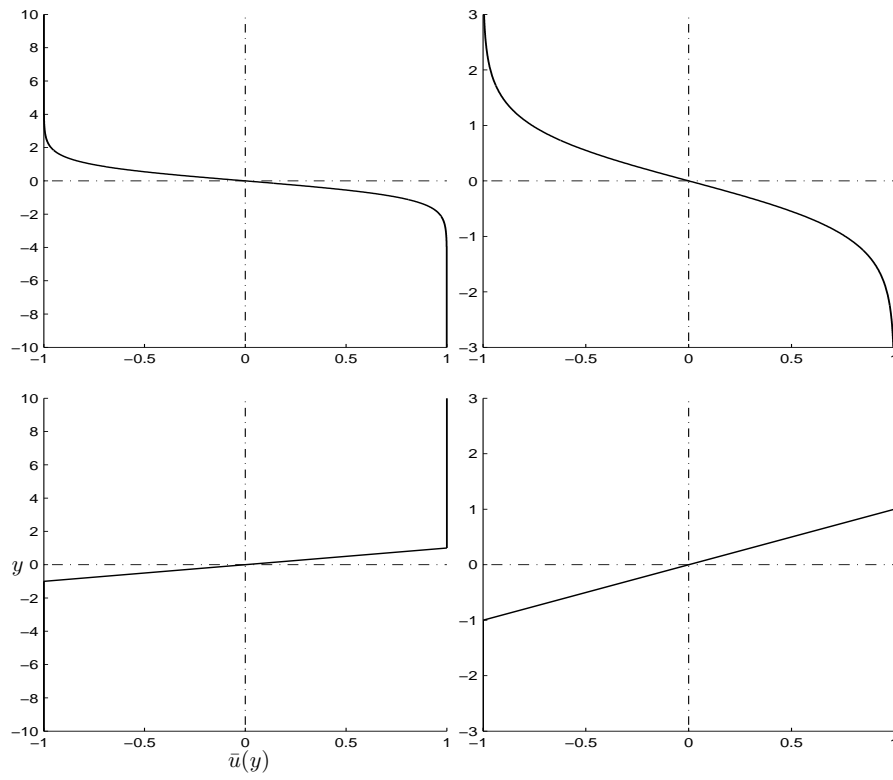
Figure 3.2: Top and bottom panels show the hyperbolic-tangent and piecewise linear basic shear flows, respectively. Panels on the right are blowups of those on the left, where focus is on the sheared zone.
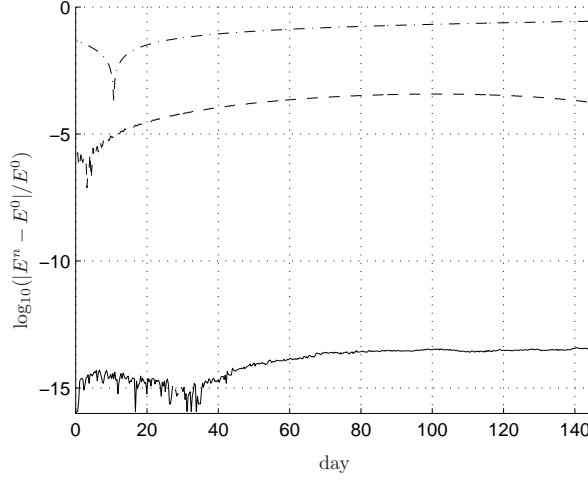
48

Figure 3.3: Relative energy deviation with respect to the total initial energy (E^0) for the four formulations, starting with an unperturbed hyperbolic-tangent profile (E^n is the total energy at step n). Whereas the vorticity-stream function formulation exactly conserves energy (solid line), the deviation for the free-surface and consistent velocity-pressure formulations reaches about 0.01% (dashed line). The inconsistent velocity-pressure formulation sees its deviation attain an unacceptable level of 30% (dash-dotted line), and keeps increasing.

3.4.1 The hyperbolic-tangent shear flow

The hyperbolic-tangent profile has been investigated by many authors in the past. For example, *Michalke* (1964) has determined the unstable eigenvalues on an f-plane ($\beta = 0$) while *Dickinson and Clare* (1973) considered the β-plane system. All these studies are based on the rigid-lid, inviscid, equations (3.7)-(3.9) in an infinitely-wide, zonally periodic channel. Without delving into details – see *Kuo* (1973, 1978) instead –, we now give some key features. The hyperbolic-tangent velocity profile (3.29) is unstable to long waves, with a cutoff dimensionless wavenumber of $\kappa = 1$ when $\beta = 0$. That is, the basic state will not grow unstable with a disturbance whose wavenumber exceeds $\kappa = 1$. On a β-plane, as β increases, the instability region narrows and for $\beta > \frac{4}{3\sqrt{3}} = 0.7698$, the flow is stable. The wavenumber of the most favored disturbance – i.e., the disturbance whose growth rate δ is the largest – is 0.4449 when $\beta = 0$ and shifts to higher values as β increases. On an f-plane, the dimensionless growth rate of the gravest mode is $\delta = 0.188$. On a β-plane, the growth rate of the most favored disturbance diminishes down to 0 as β increases.

When $\beta = 0$, instability may occur with disturbances characterized by wavenumbers ranging from 0 to 1. The basic state is disturbed with a wave of the form

$$\begin{cases} u' &= 0, \\ v' &= Ae^{-ry^2}\sin(\kappa x), \end{cases} \tag{3.31}$$

where A is the perturbation amplitude and κ is the wavenumber. The exponential function multiplying the sine wave confines the perturbation around $y = 0$. Wavenumbers

49
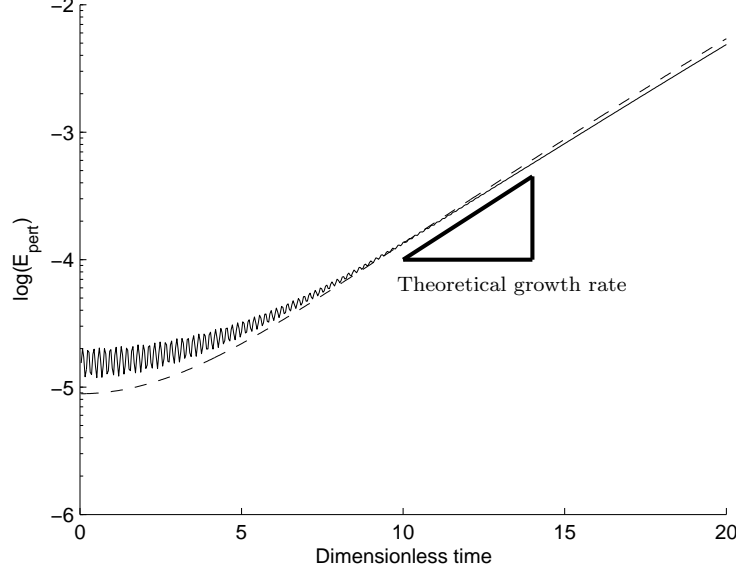
Figure 3.4: Evolution of perturbations kinetic energy for the vorticity-stream function (dashed line) and free-surface (solid line) formulations when the hyperbolic-tangent profile is perturbed with (3.31), where $\kappa = 0.4$. Note the presence of oscillations on the free-surface curve, caused by propagating truncation errors. The theoretical growth rate is that computed by *Kuo* (1978) for the vorticity-stream function formulation in an infinitely-wide channel.

ranging from 0.1 to 0.8, with an 0.1-increment, are chosen and, for each of them, the growth rate is determined by computing the perturbation kinetic energy. This procedure is repeated for each formulation, namely the vorticity-stream function, the velocity-pressure and the free-surface formulations. When the former is employed, the vorticity is to be perturbed. We do so by taking the *curl* of (3.31). The amplitude is taken to be one percent of the maximum value of the basic-state speed. Finally, the length of the numerical domain is $L_x = n\lambda$, where n is an integer and $\lambda = 2\pi/\kappa$ is the wavelength to ensure that the perturbations be consistent with the periodic boundary conditions. In Figure (3.4), the evolution of perturbations kinetic energy is shown for the vorticity-stream function and the free-surface formulations when the hyperbolic-tangent profile is perturbed with (3.31), where $\kappa = 0.4$. A logarithmic y-scale emphasizes the exponential growth rate. The oscillations visible on the free-surface curve are spawned by the propagation of truncation errors. These are dominant until perturbations overcome them, which occurs around time 9.

To directly compare all three formulations, an initial hyperbolic-tangent velocity profile is prescribed, for which the shear layer occupies one tenth of the total domain width. The structured mesh used in this experiment and most subsequent ones is shown in Figure (3.9). It will be shown below that the same experiments carried out on meridionally extended meshes hardly alter the computed growth rates. Hence, a shear layer filling one tenth of the domain suffices to emulate the absence of north-

50
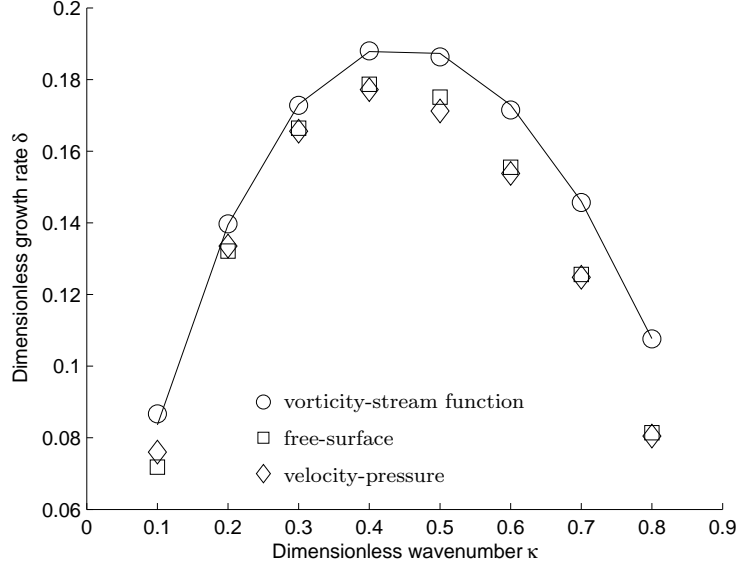
Figure 3.5: Growth rates for the three formulations on the same structured mesh resolving the shear layer with about 6 elements (see mesh M_1 in Figure 3.9). The shear-layer width is a tenth of the domain width and the basic state is the hyperbolic-tangent profile. The solid line is the theoretical growth rate for the vorticity-stream function formulation.

ern and southern boundaries. This modeling aspect need not draw our attention as of now. The shear layer is resolved with about 6 elements. Results are shown in Figure (3.5), where it clearly appears that both the velocity-pressure and free-surface formulations yield growth rates that are smaller than that obtained with the vorticity-stream function formulation. The latter gives rise to growth rates that are very close to theoretical ones. The mean relative deviation amounts to less than 1 percent of theoretical growth rates while the mean relative deviation for the free-surface formulation is about 10 percent. The influence of the free surface and truncation errors can be further appraised by conducting the same experiment with the free-surface formulation on gradually-refined meshes. In particular, meshes resolving the shear layer with 5, 6 and 10 elements are employed and growth rates are reported in Figure (3.6). Convergence towards theoretical growth rates is achieved as resolution increases and we obtain mean relative deviations of 18, 10 and 5 percent, respectively. With increased resolution, truncation errors decrease and do not have as much ability of altering the linear unfolding of instabilities. Nonetheless, it should be kept in mind that, however high the resolution might be, the free-surface formulation remains intrinsically different from rigid-lid formulations and should not be expected to behave identically. The time derivative of the elevation is present and only can we hope to converge to theoretical growth rates in the limit of an infinite α, multiplying the velocity divergence in the continuity equation (3.6).
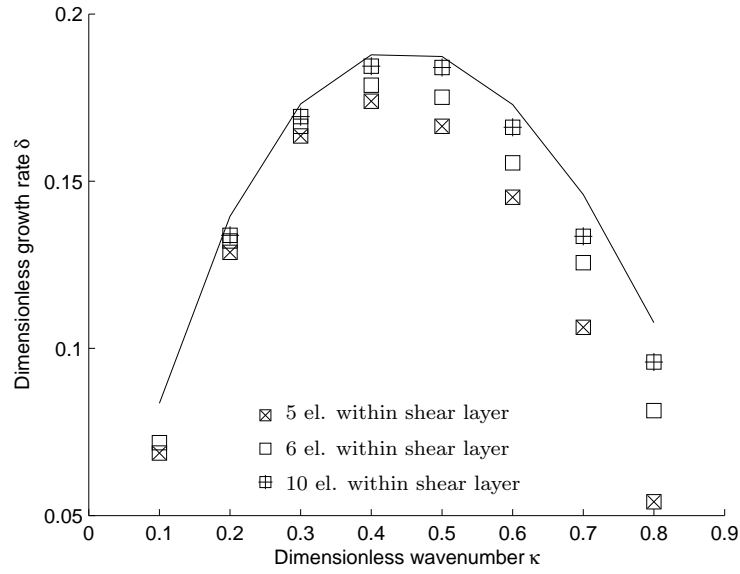
Figure 3.6: Growth rates for the free-surface formulation with gradually-refined *structured* meshes. In all experiments, the shear layer width is a tenth of that of the domain. As the mesh is refined, convergence towards theoretical growth rates is observed. Truncation errors associated with the initial basic state decrease with refinement. The value for $\kappa = 0.1$ with the highest resolution is missing because the model grew numerically unstable (because of advection) before physical instabilities had time to develop. The basic state is the hyperbolic-tangent profile.

As already mentioned, theoretical results are valid for infinitely-wide zonal channels but the numerical domain contains northern and southern boundaries. Those, however, should be located far enough from the shear layer so that their presence is hardly felt by the shear flow. An extended mesh is used to carry out the same experiments as those reported in Figure (3.5). That is, the shear-layer width remains the same but the meridional extent of the domain is three times that of the original domain. The domain extension uses a coarser resolution. In Figure (3.7), growth rates computed within the original and extended domains are reported for the vorticity-stream function and free-surface formulations. No significant difference can be brought to light between both domains. Thus, taking the shear-layer width to be one tenth of the computational domain width ensures that the boundaries have very little influence on the shear flow behavior. In our quest for the appraisal of the boundaries influence, a series of runs are now performed with shear flows contained within variable-width shear layers. Concretely, the shear-layer width increases while the computational domain remains unchanged. The vorticity-stream function formulation is employed for three different shear-layer widths: one tenth, one fifth and one third of the domain width. A shear-layer width of one third is depicted on the top right panel of Figure (3.2). As can be seen in Figure (3.8), the general trend is a gradual stabilization as the domain is more and more restricted by the presence of solid boudaries. This observation is in agreement with theoretical results presented by *Howard* (1964), where it is shown that the restriction of the domain raises the eigenvalues of the Sturm-Liouville problem associated with the Rayleigh equation (B.4). Unstable modes correspond to negative eigenvalues, which in turn correspond to positive wavenumbers. When the solid boundaries get closer to each other, the eigenvalues increase and the wavenumbers decrease, leading to slower growth until boundaries get close enough to completely stabilize the flow.

Unstructured meshes are inherent to the use of the finite element method. They are very attractive for their flexibility in representing complex boundaries and in refining regions of interest. We first consider the uniform, unstructured mesh M_2 in Figure (3.9) containing roughly the same number of elements as the structured mesh M_1. However, since the dynamics of instabilities takes place within the shear layer, this is where the mesh should be refined. Meshes M_3 and M_4 in Figure (3.10) both have their resolution increased within the shear layer but M_3 contains much fewer elements. Now, the experiment with the hyperbolic-tangent profile is repeated by using the unstructured meshes M_2, M_3 and M_4. The shear-layer width is a tenth of that of the domain. Results obtained with the vorticity-stream function formulation are depicted in Figure (3.11). The mean relative deviations for meshes M_2, M_3 and M_4 amount to 9, 7 and 5 percent, respectively. It should be stressed that we get more accurate results with the mesh M_3 than the mesh M_2, even though the latter contains 60 % more elements. However, the uniformity of mesh M_2 also implies that the same amount of computation is done within the dynamically-active shear layer and in the outer part of the domain, where the flow remains almost uniform. Refined meshes elegantly avoid this drawback. The same experiment was performed with the free-surface formulation but for all three unstructured meshes, growth rates for all wavenumbers were crudely overestimated and were close to that of the gravest mode (about 0.18). The reason might be the following. As the basic flow is perturbed, interferences between wave
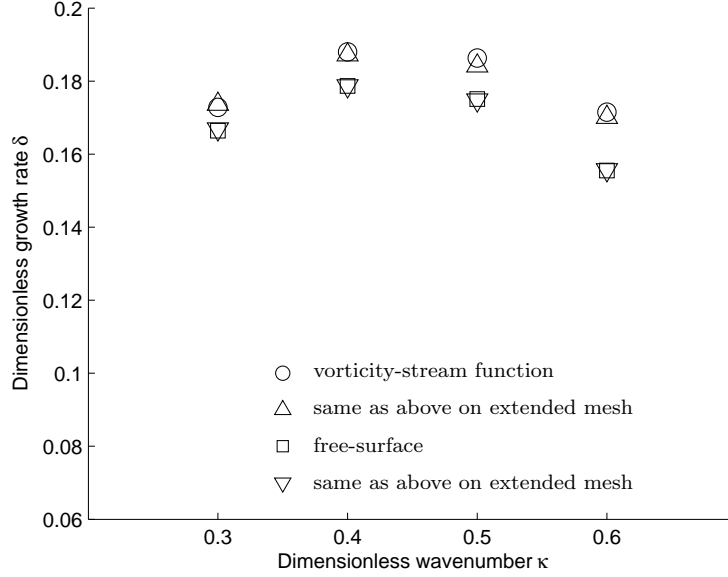
Figure 3.7: Experiments conducted on an extended mesh are compared with the same experiments conducted on the original mesh. No significant difference between the use of both domains can be reported. The shear-layer width is one tenth of the original domain width (hence 30 times thinner than the extended domain). The basic state is the hyperbolic-tangent profile.

troughs and peaks that occur by propagating truncation errors may do so in random directions, unlike structured meshes for which propagation mostly takes place along the y-axis. When this occurs, the perturbation wavenumber is not as definite and the system is free to grow unstable with a mode that is closer to the gravest one. Results regarding these experiments are not shown. This is a by-product of unstructured meshes but should in no way discredit them. So far, no special treatment of advection terms has been done (only surface integrals were performed). If we repeat the computations with an enhanced advection scheme based upon streamline upwind weighting – whose details of implementation can be found in *Hanert et al.* (2004), we obtain the results shown in Figure (3.12). Overall, growth rates are too low by about 20 %. In spite of this, not only do they respect the trend of the theoretical curve, but they are also more accurate with meshes M_3 and M_4, as expected. Therefore, the new advection scheme improves the results but is clearly too numerically dissipative compared with, e.g., Figure (3.6). The effect of including streamline upwinding filters out high-frequency oscillations, hence damping out the scattering of fast-propagating waves but also has the undesirable consequence of slowing down the growth of physical instabilities.

3.4.2 The piecewise linear shear flow

We push further the idealization of the zonal flow by using the piecewise linear shear flow. As in the case of the hyperbolic-tangent shear flow, the domain is a periodic, infinitely wide zonal channel. As shown in *Cushman-Roisin* (1994), the dispersion
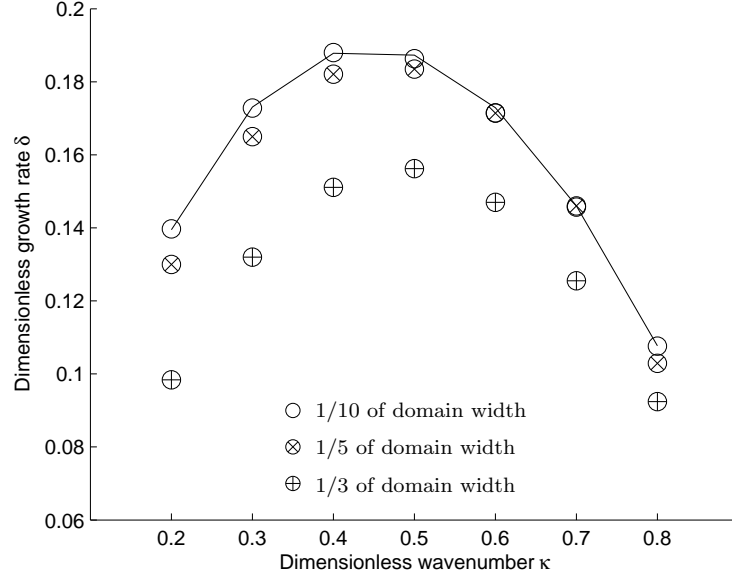
Figure 3.8: Growth rates computed with the vorticity-stream function formulation for varying shear-layer widths. Gradual stabilization is observed as the domain is more and more restricted by the presence of solid boudaries, which agrees with the theoretical results by *Howard* (1964). The basic state is the hyperbolic-tangent profile.
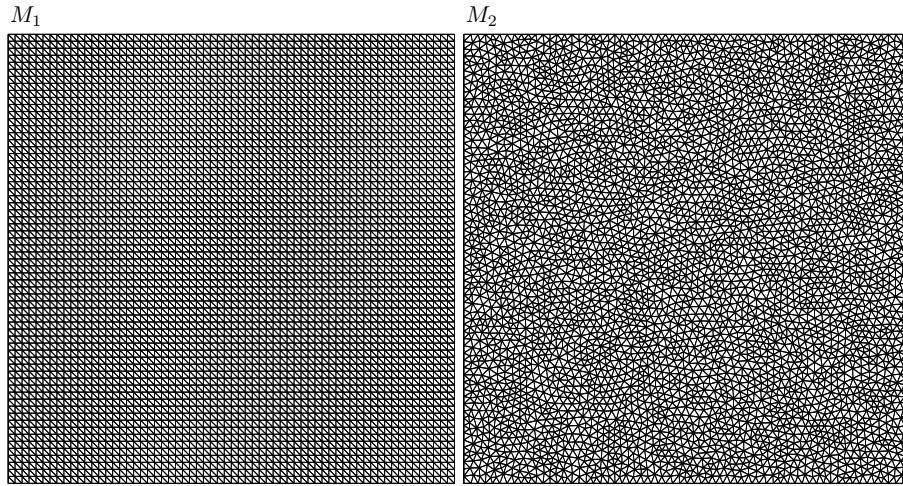
Figure 3.9: The structured mesh on the left (M_1) contains 8192 triangles and the unstructured mesh on the right (M_2) contains 8124 triangles. Both meshes have a resolution of about 0.020. Note that the aspect ratio of length to width is 1:1 in the illustration but other aspect ratios are used for computations to ensure periodicity of perturbations (e.g., π:1). In that case, anisotropic elements are used.
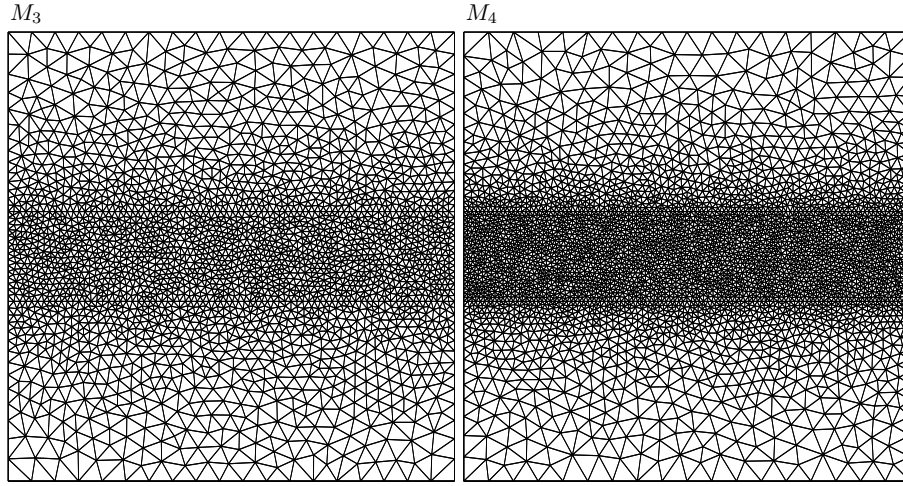
Figure 3.10: The unstructured, non-uniform mesh on the left (M_3) contains 4984 triangles and is locally refined within the shear layer. The mesh on the right (M_4) contains 8150 triangles and should be compared with the unstructured uniform mesh (M_2) in Figure (3.9) containing roughly the same number of elements. The resolution in the outer part of the domain is about 0.050 for both meshes but within the shear layer, the resolution is approximately 0.015 for M_3 and 0.010 for M_4.
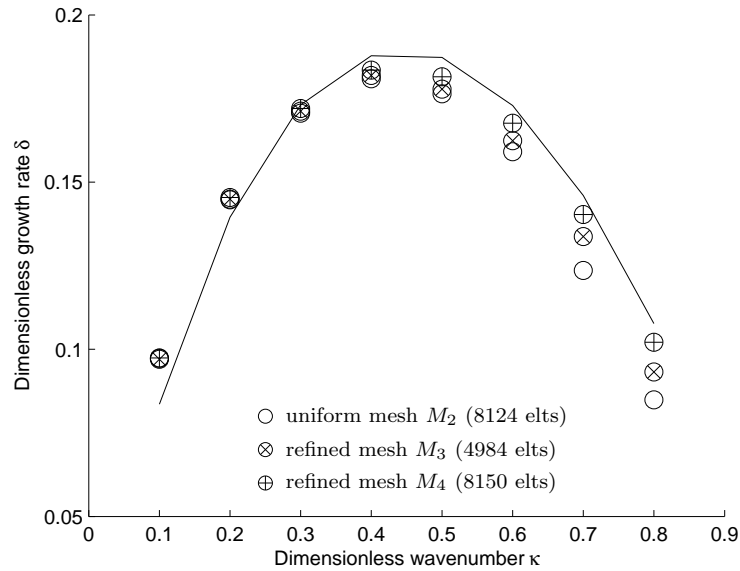
Figure 3.11: Growth rates for the vorticity-stream function formulations on the unstructured meshes M_2, M_3 and M_4 shown in Figures (3.9) and (3.10). The shear-layer width is a tenth of the total domain width and the basic state is the hyperbolic-tangent profile. The solid line is the theoretical growth rate for the vorticity-stream function formulation.

56
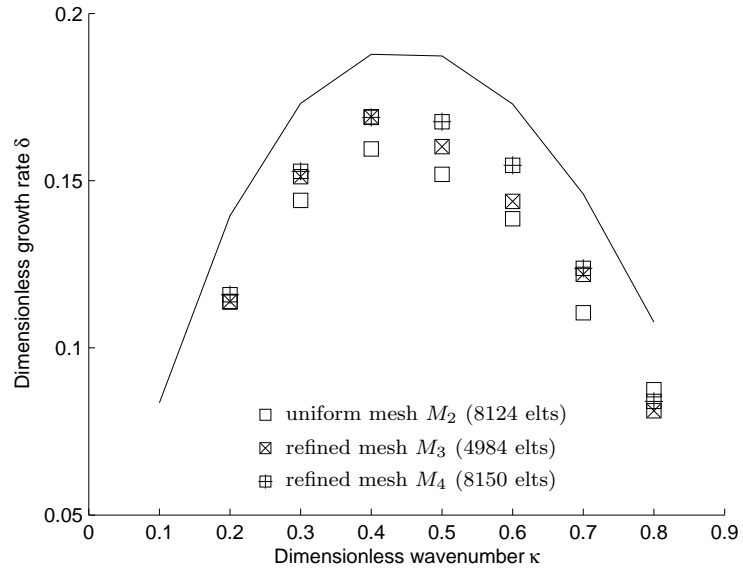
Figure 3.12: Growth rates for the free-surface formulation on the unstructured meshes M_2, M_3 and M_4 shown in Figures (3.9) and (3.10). The shear-layer width is a tenth of the total domain width and the basic state is the hyperbolic-tangent profile. The solid line is the theoretical growth rate for the vorticity-stream function formulation. The growth rates for $\kappa = 0.1$ fall below 0.05.
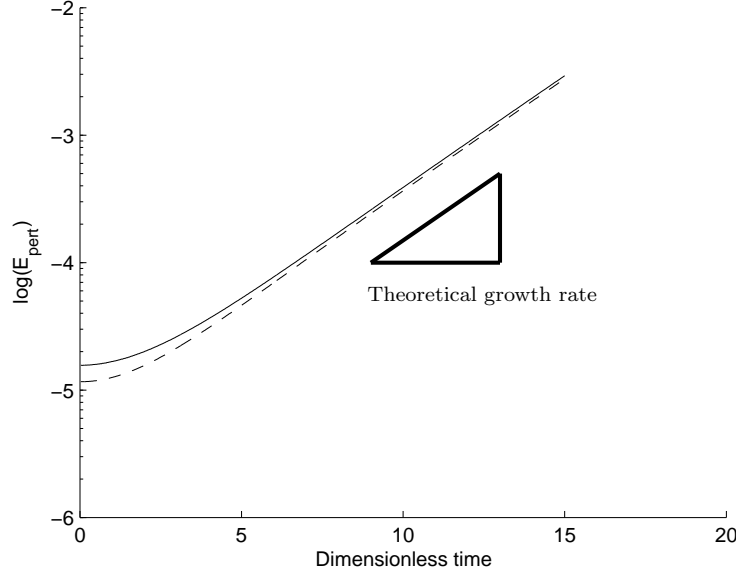
Figure 3.13: Evolution of perturbations kinetic energy for the vorticity-stream function (dashed line) and free-surface (solid line) formulations when the piecewise linear profile is perturbed with (3.31), where $\kappa = 0.4$. This should be compared with Figure (3.4) where oscillations made up the onset of the free-surface curve.

relation for perturbations, providing the wave velocity c in terms of the wavenumber κ, may be derived. The growth rate $\delta = \kappa c$ is then given by

$$\delta(\kappa) = \frac{1}{2} \left[e^{-4\kappa} - (1 - 2\kappa)^2 \right]^{1/2} .$$

Besides the possibility of deriving an analytical expression for the growth rate, the velocity is exactly interpolated with linear elements. A severe drawback of such a profile, though, is its lack of realism. However, the aim is here to be able to compare rigid-lid and free-surface formulations without having to deal with wavelike propagation of truncation errors. To illustrate this statement, the evolution of perturbations kinetic energy is shown in Figure (3.13), where the absence of oscillations at the onset of the free-surface curve is to be remarked. At this point, it must be stressed that, unlike the zonal velocity field and because the vorticity is discontinuous across the shear-layer frontiers, the vorticity cannot be interpolated exactly – unless the discontinuous finite element method is employed (see *Cockburn et al.* (2000) for a comprehensive review of discontinuous finite element methods). This situation is depicted in Figure (3.14) and explained in detail in the caption.

In Figure (3.15), growth rates computed for all three formulations are shown and compared with the analytical results. The mesh resolves the shear layer with 5 elements (the meridional resolution is 20 km). The mean relative deviations are 4, 2 and 3 percent for the vorticity-stream function, free-surface and velocity-pressure formulations, respectively. Hence, none of them may significantly be categorized as yielding
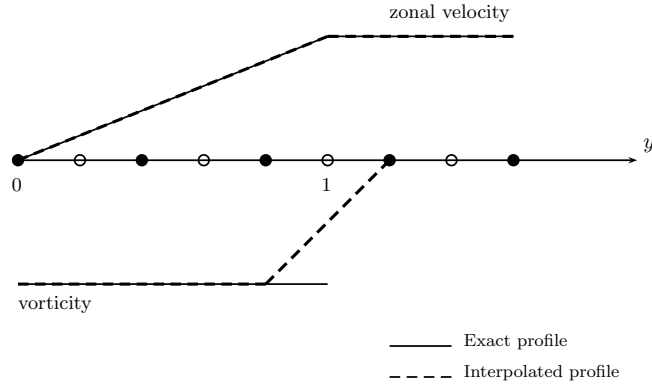
Figure 3.14: Since the zonal velocity is continuous, it is exactly interpolated with linear elements. On the other hand, the discontinuous vorticity cannot be interpolated and the discontinuity is, at best, linearly represented (see the dashed line). This leads to a poorer representation of the shear layer. The growth rate is directly proportional to the shear-layer width and it is unclear which length scale is to be used to compute the dimensionless growth rate when such an approximation prevails. Filled and empty circles represent vorticity and velocity nodes, respectively.

better results. The only trend, however, is a slight overestimate obtained when using the vorticity-stream function formulation. This might be due to the discontinuous nature of the initial vorticity field. A last experiment is carried out on a coarser mesh resolving the shear layer with 3 elements and having a meridional resolution of 50 km. Results are reported in Figure (3.16) and mean relative deviations are 8 and 6 percent for the free-surface and vorticity-stream function formulations, respectively. Because large-scale ocean models do not easily run on meshes with resolutions as high as 20 km (unless local refinement is implemented), the last experiment has been carried out to show that the use of a coarser mesh yields decent results.

3.4.3 Evolution on longer timescales

So far, all runs have been conducted over timescales that did not allow for nonlinear advective terms to become significant. Typical dimensionless run times were on the order of 20. That is, real run times of about 4 months. We now extend the dimensionless run time up to 100 (i.e., about 20 months). The phenomena that we witness in this case are not faithful representations of what could happen in the real ocean or atmosphere, because no physical process would have so much time to develop without interacting with external processes. Bearing that in mind, we now show the unfolding of eddies on meshes M_1 and M_4 (see Figures 3.9 and 3.10) for the vorticity-stream function and free-surface formulations. Recall that both meshes have approximately the same number of elements but M_4 is refined within the shear layer with a resolution that is about twice that of M_1.
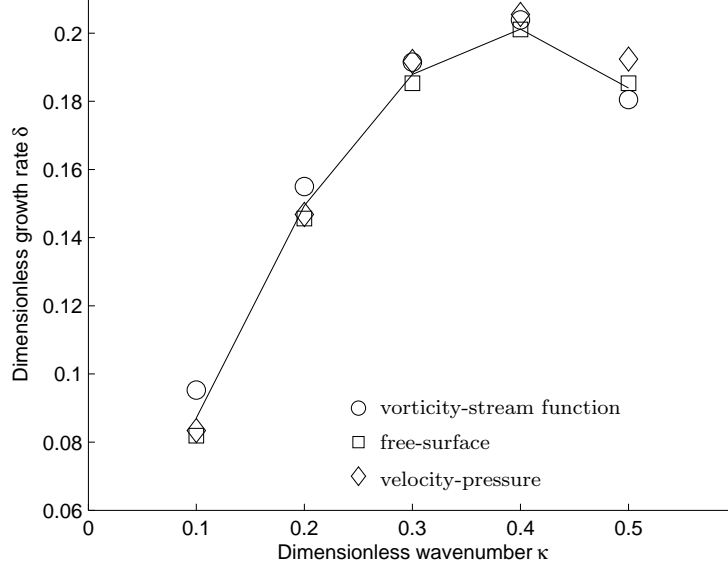
Figure 3.15: Growth rates for the three formulations on the same mesh resolving the shear layer with 5 elements (meridional resolution is 20 km). The shear-layer width is a tenth of the domain width and the basic state is the piecewise linear profile. The solid line is the theoretical growth rate for rigid-lid vorticity-stream function formulation.

In both series of experiments, advection in the free-surface formulation is treated with streamline upwind weighting (*Hanert et al.*, 2004) as it was already the case for previous experiments on unstructured meshes presented earlier on (see Figure 3.12). With this advection scheme, some numerical dissipation is added, without which the scheme would be unstable. In comparison, the vorticity-stream function formulation does not include any dissipation, be it physical or numerical. A striking difference between both formulations on mesh M_1, as can be seen in Figure (3.17), is that eddies do not tend to merge in the free-surface formulation. It can be hypothesized that numerical dissipation is too substantial for this mesh, which inhibits the coalescence of eddies. When the same experiment is carried out on mesh M_4 – with increased resolution within the shear layer –, two important features appear (Figure 3.18). First, the merging of eddies also occur with the free-surface formulation, although delayed compared with the vorticity-stream function formulation. Second, the dynamics of the merging for the latter formulation appears to be mesh-dependent, as it is not identical to that observed with mesh M_1 (compare left panels of Figures 3.17 and 3.18), although all other parameters are the same. Some explanations on the coalescence of eddies may be found in *Michalke* (1964). The first feature stresses the importance of using an adapted mesh to resolve the dynamics. For the free-surface formulation, numerical dissipation added to the flow diminishes as the element size decreases. Nevertheless, as can be seen by comparing panels in Figure (3.18), there is still some dissipation whose main effect is to delay the coalescence of eddies. Despite all this, it should be kept in mind that all ocean models include some phyical dissipation. In
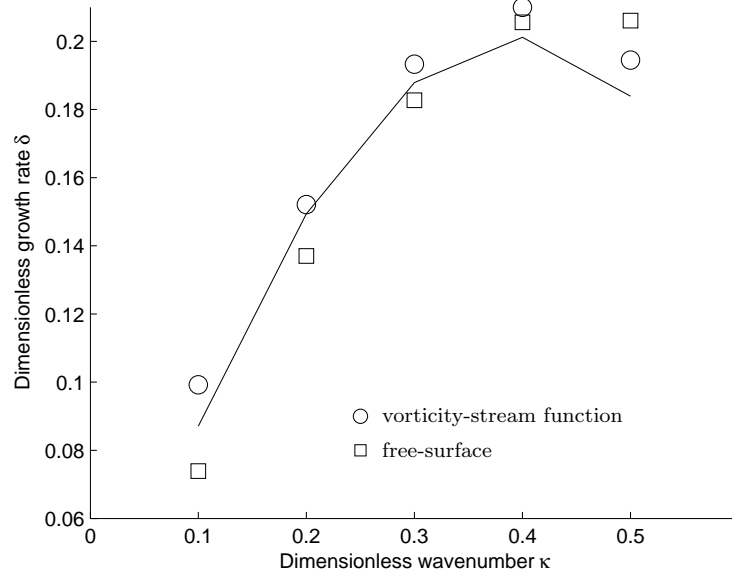
Figure 3.16: Growth rates for the vorticity-stream function and free-surface formulations on a coarse mesh resolving the shear layer with only 3 elements (meridional resolution is 50 km). The shear-layer width is 0.15 times the domain width (i.e., slightly wider than in previous experiments) and the basic state is the piecewise linear profile. The solid line is the theoretical growth rate for rigid-lid vorticity-stream function formulation.

that respect, the rigid-lid, vorticity-stream function formulation devoid of any kind of dissipation might not be closer to reality than the free-surface formulation with some dissipation proportional to the mesh size, as in our situation.

3.5   Conclusions

The objective was to compare free-surface and rigid-lid finite element models of barotropic instabilities. For large-scale ocean modeling, the time derivative of the sea surface elevation appearing in the continuity equation (3.6) is at least two orders of magnitude smaller than the velocity divergence, hence a priori justifying the rigid-lid assumption. Therefore, any differences in the growth rates were expected to be small. Two series of experiments were conducted to assess the role of the free surface and both were aimed at computing growth rates and comparing them to theoretical solutions valid for the vorticity-stream function formulation. In the first series, the hyperbolic-tangent profile was used and it was shown that the free-surface formulation yielded growth rates that converged to theoretical ones as the mesh was refined. For coarser meshes, initial truncation errors are fairly important and are allowed to propagate as surface waves. Growth rates thus computed were smaller than theoretical ones and more so for low-resolution meshes. It is believed that propagation of truncation errors as surface waves allows for energy to be redistributed and carried away from within the shear flow towards the boundaries. The velocity-pressure formulation yielded results that were roughly identical to that of the free-surface formulation. The surface pressure merely plays the role of elevation by providing enough pressure to keep the sea surface flat. This formulation thus allows for pressure waves to propagate.

Because theoretical results were derived for infinitely-wide channels, it was important to carry out a sensitivity analysis with respect to the location of boundaries. The original computational domain was ten times wider than the shear-layer width (an aspect ratio of $1/10$). Growth rates were then computed for increasing aspect ratios. The vorticity-stream function was utilized to perform this analysis. The general trend is a decreasing growth rate for an increasing aspect ratio. Gradual stabilization is thus observed as the domain is more and more restricted by the presence of solid boudaries, which agrees with the theoretical results by *Howard* (1964). Finally, an experiment using a mesh having an aspect ratio of $1/30$, with coarser southern and northern mesh extensions, was shown to yield the same results as that obtained with the original mesh.

In order to do away with this issue of truncation errors, a piecewise linear profile was then used. Although velocity was exactly interpolated with linear elements, the discontinous vorticity could not be so. This permitted to concentrate on the free surface, not as a carrier of truncation errors but as a variable per se. On a moderate-resolution mesh (meridional resolution of 20 km), all three formulation gave rise to growth rates close to theoretical ones and, most importantly, no one furnished results that could have allowed us to choose it as the right one.
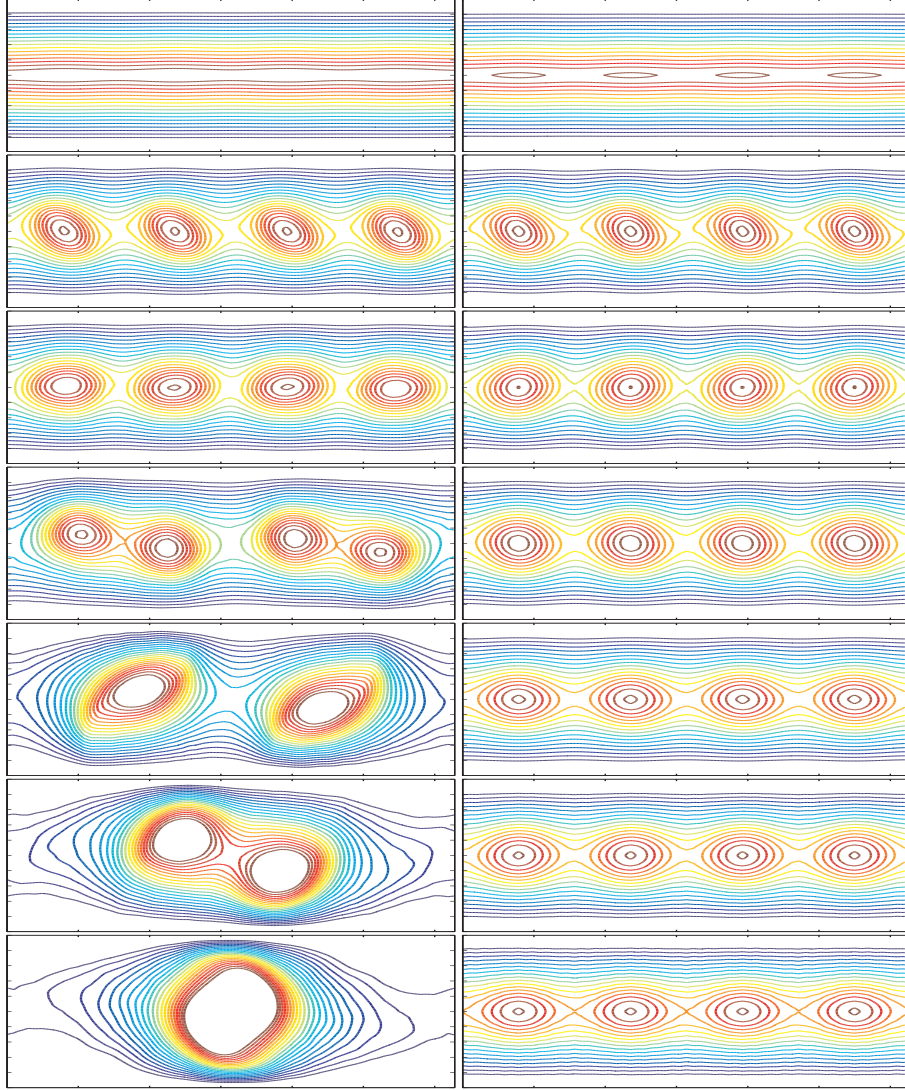
Figure 3.17: Comparison between the vorticity-stream function (left panels) and free-surface (right panels) formulations on longer timescales on the structured mesh M_1. The stream function is shown. Dimensionless snapshot times are 0, 20, 30, 50, 70, 90 and 100. Distances between two x-tics and two y-tics are 500 km and 100 km, respectively. The time step is 0.01. The basic state is the piecewise linear profile.
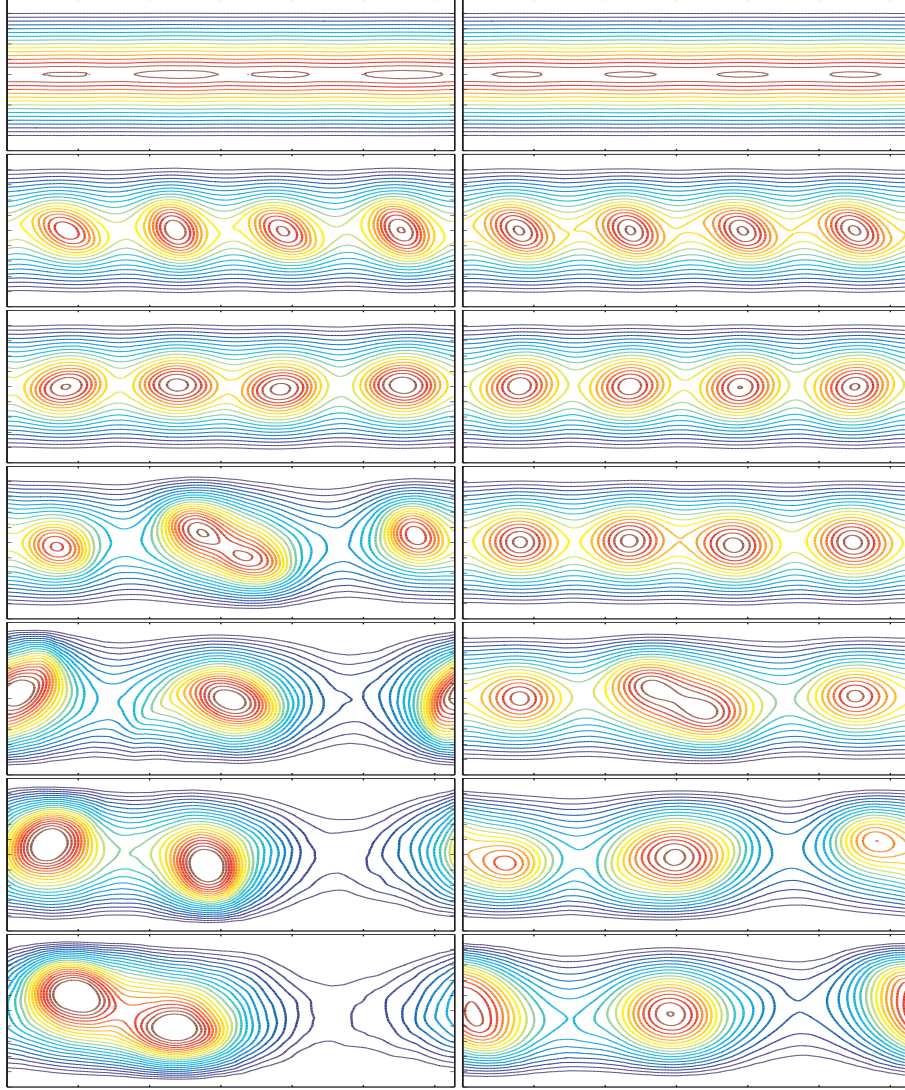
Figure 3.18: Comparison between the vorticity-stream function (left panels) and free-surface (right panels) formulations on longer timescales on the unstructured, non-uniform mesh M_4 The stream function is shown. Notice how the increase in mesh resolution within the shear layer limits the numerical dissipation incurred by the advection scheme and permits the merging of eddies for the free-surface formulation, although more slowly than for vorticity-stream function formulation. Dimensionless snapshot times are 0, 20, 30, 50, 70, 90 and 100. Distances between two x-tics and two y-tics are 500 km and 100 km, respectively. The time step is 0.01. The basic state is the piecewise linear profile.

All experiments were carried out with $\alpha = 27$. In order to have a grasp on the role of the free surface, one should work with α close to 1. However, only two parameters may vary: the layer depth h and the shear-layer length scale L. To achieve a value of 1, those two parameters have to assume values that would either break down the assumtions underlying the model upon which theoretical results are drawn, or render the domain unphysical. Decreasing h down to a few tens of meters while keeping the domain width at 1000 km is certainly numerically feasible but would produce unapplicable results. At the other end of the spectrum, increasing the shear-layer width by a factor of 10 implies having a domain width of ten thousand kilometers, whereupon the β-plane approximation does not hold any more.

Unstructured meshes were then employed and it was shown that by refining the mesh in dynamically-active regions, it was possible to decrease the computational cost while performing better in terms of accuracy. This is of paramount importance for ocean modeling where unstructured meshes and the finite element method make their way in the community. By locally increasing the resolution of the mesh, we easily concentrate the computational cost onto regions that require greater accuracy. To achieve numerical stability with the the free-surface formulation on *unstructured meshes*, advection terms were computed with streamline upwind weighting. The growth rates followed the theoretical trend and a higher accuracy was obtained with refined meshes but numerical dissipation had the effect of slightly slowing down the growth of instabilities.

The coalescence of eddies was then examined by extending the run time up to 100, that is, 10 times longer than in all previous runs. This experiment proved very illustrative of the necessity of using adapted meshes for ocean modeling. On the structured mesh, the merging of eddies characterized the solution for the vorticity-stream function formulation while this did not occur for the free-surface formulation, presumably due to numerical dissipation accompanying the streamline upwind weighting treatment of advection terms. However, when the unstructured mesh was used, the free-surface formulation was able to reproduce the coalescence of eddies by limiting the numerical dissipation thanks to an increase in resolution within the right region of the domain. The growth of eddies was slowed down in comparison with that for the vorticity-stream function formulation. Nonetheless, the latter, which does not include dissipation of any kind, does not necessarily comply with reality and actual ocean models. To summarize, we showed that the finite element method for free-surface models was effective at representing barotropic instabilities when it is combined with an appropriate advection scheme and, most importantly, adapted meshes.

Chapter 4

Three-dimensional tracer conservation

Summary

Sufficient conditions to consistently achieve global tracer conservation are derived. This entails a discrete compatibility beteween the elevation, continuity and tracer equations. This compatibility constraint, together with the use of a numerically stable scheme, severely restricts the choice of usable three-dimensional spatial discretizations. The issue of time discretization is touched upon. Some illustrative three-dimensional test cases are presented where the method is shown to satisfy all conservation properties. We also carry out a few experiments where consistency breaks down and investigate the consequences thereof.

Despite the many recent achievements of the FE method, many challenges still lie ahead of us. Admittedly, switching from structured meshes to unstructured meshes requires developers to build new models from scratch rather than converting existing ones piece by piece. Quite ironically, with this approach, we find ourselves in need of addressing issues that have been solved in finite difference (FD) models but that remain somewhat problematic or controversial with finite element models. Ensuring global tracer conservation while preserving consistency (i.e., compatibility) between equations in finite element shallow-water models is one of these issues and the core of this chapter. This very issue has already been thoroughly addressed in FD models (*Deleersnijder*, 1993; *Roullet and Madec*, 2000; *Griffies et al.*, 2001; *Campin et al.*, 2004; *Griffies*, 2004). A common deceitful criticism of the CG method is the lack of elementwise conservation. Several attempts at proving those criticisms wrong have been made by defining interelement fluxes appropriately using so-called nodal fluxes (*Hughes et al.*, 2000; *Berger and Howington*, 2002). Those efforts, however, have not really mitigated the widespread belief that the finite element method is not conservative and, thereby, not suitable for ocean modeling.

In this chapter, we demonstrate how to achieve global tracer conservation and consistency in a three-dimensional, free-surface FE shallow-water model on a moving

mesh. Global tracer conservation is attained if the volume integral of any tracer concentration within the domain is fixed in time, in the absence of boundary fluxes and source/sink terms. It is unquestionable to us that any ocean model aimed at running over climatic timescales must achieve global conservation. Consistency or compatibility is meant in the following sense: in a discrete model, set a tracer concentration to a uniform value throughout the domain and let the free surface undulate, yet do not add boundary fluxes; the tracer concentration must maintain the same uniform value at all time. If this property is not satisfied, artificial tracer extrema might appear with the indirect effect of generating unphysical currents (in case the tracer is the temperature or the salinity). For this reason, it is indispensable that any ocean model solve the elevation, continuity and tracer equations in a consistent way. That is, they must be discretely compatible. Note that in FD models, consistency is commonly referred to as local conservation (*Griffies et al.*, 2001; *Campin et al.*, 2004; *Griffies*, 2004). This is so because ensuring conservation at the cell level in terms of fluxes does imply consistency. This is not necessarily true in FE models where the scheme could be locally conservative in terms of nodal fluxes without solving the equations consistently. In addition to these properties, we opted for a free-surface formulation. Rigid-lid formulations are now deemed obsolete for several reasons (*Killworth et al.*, 1991; *Deleersnijder and Campin*, 1995; *Griffies et al.*, 2000), one of them being the inability to easily account for surface freshwater fluxes. Finally, the domain is time-dependent to accommodate the free-surface motions. All layers within the domain are free to move in the vertical so that the free-surface displacement is distributed over the vertical to avoid the occurrence of overly thin layers near the surface. As will be shown, the volume change due to freshwater input (output) automatically leads to dilution (concentration) of salt without having to resort to salt fluxes.

Using a formalism applicable to both the CG method and the DG method, we derive sufficient conditions regarding the spatial discretization to ensure global tracer conservation and consistency. We show that the same interpolation in the horizontal must be used for the elevation, the vertical velocity and the tracers. Moreover, the same interpolation in the vertical must be used for the vertical velocity and the tracers. It is also demonstrated that computing the vertical velocity via the continuity equation, integrating it upwards or downwards subject to one boundary condition, is well posed and does not lead to an accumulation of errors as was earlier suggested by some authors (*Lynch and Naimie*, 1993; *Muccino et al.*, 1997; *Danilov et al.*, 2004). This remains true as long as the upper boundary of the domain coincides with the free surface and a consistent horizontal velocity is used. Some illustrative test cases are presented where the method is shown to satisfy all conservation properties. We also carry out a few experiments where consistency breaks down and investigate the consequences therefrom.

4.1 Mathematical formulation

We shall now describe the minimum set of equations needed in our study. In this section, all classical conservation properties are inferred from the continuous equations. In section 4.2, we will derive a set of conditions for which these properties carry

68
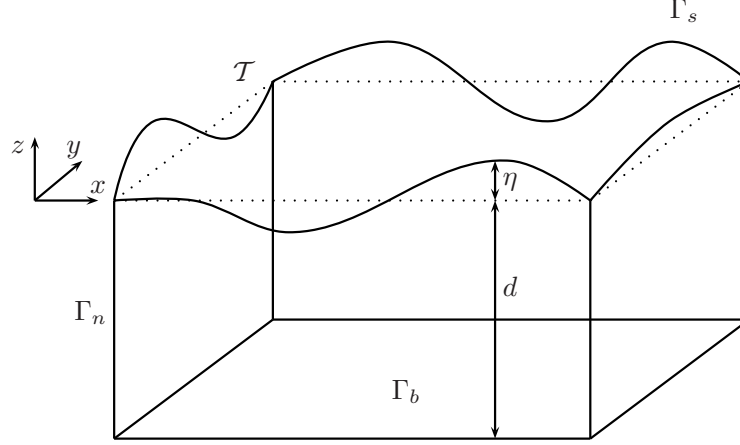
Figure 4.1: Notations used to describe the three-dimensional time-dependent domain Ω. The seabed and the free surface are denoted by Γ_b and Γ_s, respectively. The unperturbed plane defined by $z = 0$ is noted $\mathcal{T}$ and is represented by the dotted lines. The lateral boundary is noted Γ_n. At any location (x, y), the depth $d(x, y)$ and the elevation $\eta(x, y, t)$ are both defined with reference to $\mathcal{T}$. The displacement of the free surface is exaggerated.

over to the discrete equations. Let $\Omega(t)$ be the three-dimensional, time-dependent domain of interest. It is bounded below by the seabed, defined by Γ_b and above by the free surface, defined by Γ_s, as depicted in Figure (4.1). The seabed is considered time-independent. The free surface, on the other hand, is time-dependent. The lateral boundary, defined by Γ_n, is parallel to the z-direction. Note that because the free-surface elevation varies in time, so does the lateral boundary. However, it has a constant (x, y) position. For simplicity, we do not consider open boundaries in this work. The domain boundary can thus be written as $\partial\Omega = \Gamma_n \cup \Gamma_b \cup \Gamma_s$. The unperturbed surface defined by $z = 0$ is noted $\mathcal{T}$. We work within the scope of the Boussinesq and hydrostatic approximations.

4.1.1 Equations and boundary conditions

Let $\mathbf{u}(x, y, z, t) = (u, v)$ be the horizontal velocity, with components u and v in the x and y directions, respectively. The vertical velocity is the component in the z direction and is denoted by $w(x, y, z, t)$. The free-surface elevation $\eta(x, y, t)$ does not depend on z and is defined with respect to the reference level $\mathcal{T}$. The unperturbed depth $d(x, y)$, also defined with respect to $\mathcal{T}$, is assumed to be time-independent, does not depend on z and is everywhere nonnegative. The layer thickness, H, is the sum of the depth and the free-surface elevation: $H(x, y, t) = d(x, y) + \eta(x, y, t)$. With those notations, the lower and upper domain boundaries are charcterized by $\Gamma_b \equiv z = -d$ and $\Gamma_s \equiv z = \eta$.

For the purpose of deriving the statements of volume and tracer conservation, there is no need to write out the full horizontal momentum equations. We simply assume

69

that the horizontal velocity $\mathbf{u}$ is known in $\Omega(t)$ and that it satisfies the impermeability condition on the lateral boundary Γ_n, that is

$$\mathbf{u} \cdot \mathbf{n} = 0 \qquad \text{on } \Gamma_n, \tag{4.1}$$

where $\mathbf{n} = (n_x, n_y)$ is the unit outward-pointing normal to Γ_n. We will also note n_z the vertical component of the normal. In hydrostatic models, the vertical momentum equation reduces to hydrostatic equilibrium. Hence, there is no prognostic equation for the vertical velocity. However, the vertical velocity is computed diagnostically via the continuity equation

$$\boldsymbol{\nabla} \cdot \mathbf{u} + \frac{\partial w}{\partial z} = 0 \qquad \text{in } \Omega, \tag{4.2}$$

where $\boldsymbol{\nabla}$ is the horizontal gradient operator. Eq. (4.2) is a statement of volume conservation. Another statement of volume conservation can be obtained by depth-integrating Eq. (4.2). This yields the following prognostic equation for the free-surface elevation:

$$\frac{\partial \eta}{\partial t} + \boldsymbol{\nabla} \cdot \int_{-d}^{\eta} \mathbf{u} \, \mathrm{d}z = q_w \qquad \text{on } \mathcal{T}, \tag{4.3}$$

for which use has been made of the impermeability of the seabed and the free surface. Note that in (4.3), $\mathcal{T}$ is the projection of the three-dimensional domain Ω on the horizontal plane defined by $z = 0$. These impermeability conditions (the so-called kinematic boundary conditions) read

$$w = -\mathbf{u} \cdot \boldsymbol{\nabla} d \qquad \qquad \text{on } \Gamma_b, \tag{4.4}$$

$$w = \frac{\partial \eta}{\partial t} + \mathbf{u} \cdot \boldsymbol{\nabla} \eta - q_w \qquad \text{on } \Gamma_s, \tag{4.5}$$

where q_w is the net freshwater volume flux per unit area (with units of a velocity) due to precipitation ($q_w > 0$), evaporation ($q_w < 0$) and river runoffs ($q_w > 0$), if not formulated as lateral boundary conditions. Note that boundary conditions (4.4) and (4.5) are equivalent to

$$\mathbf{u} \cdot \mathbf{n} + w n_z = 0 \qquad \qquad \text{on } \Gamma_b, \tag{4.6}$$

$$\mathbf{u} \cdot \mathbf{n} + w n_z = \left(\frac{\partial \eta}{\partial t} - q_w \right) n_z \qquad \text{on } \Gamma_s, \tag{4.7}$$

In (4.6) and (4.7), the unit outward-pointing normals take on the following expressions

$$(n_x, n_y, n_z) = \frac{\left(-\frac{\partial d}{\partial x}, -\frac{\partial d}{\partial y}, -1 \right)}{\sqrt{\|\boldsymbol{\nabla} d\|^2 + 1}} \qquad \text{on } \Gamma_b, \tag{4.8}$$

$$(n_x, n_y, n_z) = \frac{\left(-\frac{\partial \eta}{\partial x}, \frac{\partial \eta}{\partial y}, 1 \right)}{\sqrt{\|\boldsymbol{\nabla} \eta\|^2 + 1}} \qquad \text{on } \Gamma_s. \tag{4.9}$$

and we also assume that the orientation of the freshwater flux is the same as that defined by the normal at the free surface. The notations $\mathbf{v}^T$ and $\|\mathbf{v}\|$ denote the transpose

and the Euclidian norm, respectively, of the vector $\mathbf{v}$. Finally, a given tracer with concentration C obeys an advection-diffusion equation (with no source/sink term and no boundary fluxes) of the form

$$\frac{\partial C}{\partial t} + \boldsymbol{\nabla} \cdot (\mathbf{u}C) + \frac{\partial (wC)}{\partial z} = \boldsymbol{\nabla} \cdot (\kappa \boldsymbol{\nabla} C) + \frac{\partial}{\partial z} \left(\kappa \frac{\partial C}{\partial z} \right) \qquad \text{in } \Omega, \qquad (4.10)$$

with a condition of no boundary flux:

$$\kappa \frac{\partial C}{\partial n} = 0 \qquad \text{on } \partial \Omega, \qquad (4.11)$$

where $\frac{\partial C}{\partial n}$ is the normal derivative.

4.1.2 Conservation properties

From the equations presented above, we may now derive the statements of volume and tracer conservation and check the consistency between the tracer and continuity equations. We also set the freshwater flux to zero, $q_w = 0$.

Volume conservation

By integrating Eq. (4.3) over the time-independent, two-dimensional domain $\mathcal{T}$ and using the divergence theorem to compute the second integral, we obtain

$$\int_{\mathcal{T}} \frac{\partial \eta}{\partial t} \, \mathrm{d}\mathcal{T} + \int_{\Gamma_n} \mathbf{u} \cdot \mathbf{n} \, \mathrm{d}\Gamma = 0,$$

which, by using the boundary condition (4.1), further reduces to

$$\frac{\mathrm{d}}{\mathrm{d}t} \int_{\mathcal{T}} \eta \, \mathrm{d}\mathcal{T} = 0. \qquad (4.12)$$

Eq. (4.12) is the statement of volume conservation.

Global tracer conservation

Integrating Eq. (4.10) over $\Omega(t)$, using the divergence theorem for the advection and diffusion terms and enforcing the boundary condition (4.11) leads to

$$\int_{\Omega(t)} \frac{\partial C}{\partial t} \, \mathrm{d}\Omega + \int_{\Gamma_n} \mathbf{u} \cdot \mathbf{n} \, C \, \mathrm{d}\Gamma + \int_{\Gamma_b} (\mathbf{u} \cdot \mathbf{n} + wn_z) \, C \, \mathrm{d}\Gamma$$
$$+ \int_{\Gamma_s} (\mathbf{u} \cdot \mathbf{n} + wn_z) \, C \, \mathrm{d}\Gamma = 0. \qquad (4.13)$$

The integrals over Γ_n and Γ_b vanish by enforcing boundary conditions (4.1) and (4.6). Using the Reynolds transport theorem, the first term of the expression above becomes

$$\int_{\Omega(t)} \frac{\partial C}{\partial t} \, \mathrm{d}\Omega = \frac{\mathrm{d}}{\mathrm{d}t} \int_{\Omega(t)} C \, \mathrm{d}\Omega - \int_{\Gamma_s} C \frac{\partial \eta}{\partial t} n_z \mathrm{d}\Gamma,$$

reducing Eq. (4.13) to

$$\frac{\mathrm{d}}{\mathrm{d}t} \int_{\Omega(t)} C \, \mathrm{d}\Omega + \int_{\Gamma_s} \left(\mathbf{u} \cdot \mathbf{n} + w n_z - \frac{\partial \eta}{\partial t} \right) C \, \mathrm{d}\Gamma = 0.$$

Now, using boundary condition (4.7) yields the statement of global tracer conservation:

$$\frac{\mathrm{d}}{\mathrm{d}t} \int_{\Omega(t)} C \, \mathrm{d}\Omega = 0. \tag{4.14}$$

Consistency

The property of consistency is equivalent to verifying that a constant tracer concentration is solution to (4.10)-(4.11). Setting $C = C_0 \neq 0$ in Eq. (4.10), C_0 being a constant, we simply obtain

$$C_0 \left(\boldsymbol{\nabla} \cdot \mathbf{u} + \frac{\partial w}{\partial z} \right) = 0 \qquad \text{in } \Omega.$$

Therefore, the continuity and tracer equations are consistent (or compatible) with each other when the following relation holds true

$$C_0 \left(\boldsymbol{\nabla} \cdot \mathbf{u} + \frac{\partial w}{\partial z} \right) = 0 \iff \boldsymbol{\nabla} \cdot \mathbf{u} + \frac{\partial w}{\partial z} = 0 \qquad \text{in } \Omega \text{ and for } C_0 \neq 0. \tag{4.15}$$

4.2   The discrete conservation laws

The purpose of this section is to derive the discrete counterparts of Eqs (4.12), (4.14) and (4.15). We start by describing the mesh topology and introducing a few useful notations. We then present the variational formulations of the elevation, continuity and tracer equations, followed by their discretization based upon the Galerkin procedure. The discrete conservation laws will then be inferred from the discrete equations. In order to keep notations more concise, all subsequent developments are carried out for the CG method. The equivalent for the DG method is presented in Appendix C.1.

4.2.1   Mesh topology

The numerical solution is sought in the three-dimensional domain Ω^h. The latter consists of an approximation of the physical domain, obtained by interpolating the boundaries of topographical features and the bathymetry. Within this framework, all boundaries are also interpolated so that we have $\partial \Omega \simeq \partial \Omega^h = \Gamma_b^h \cup \Gamma_s^h \cup \Gamma_n^h$. The three-dimensional finite element mesh (Figure 4.2) is obtained by first partitioning $\mathcal{T}^h$ into N_t open non-overlapping triangles $\mathcal{T}_e$. That is, we have

$$\overline{\mathcal{T}^h} = \bigcup_{e=1}^{N_t} \overline{\mathcal{T}_e} \qquad \text{and} \qquad \mathcal{T}_e \cap \mathcal{T}_f = \emptyset \quad (e \neq f),$$
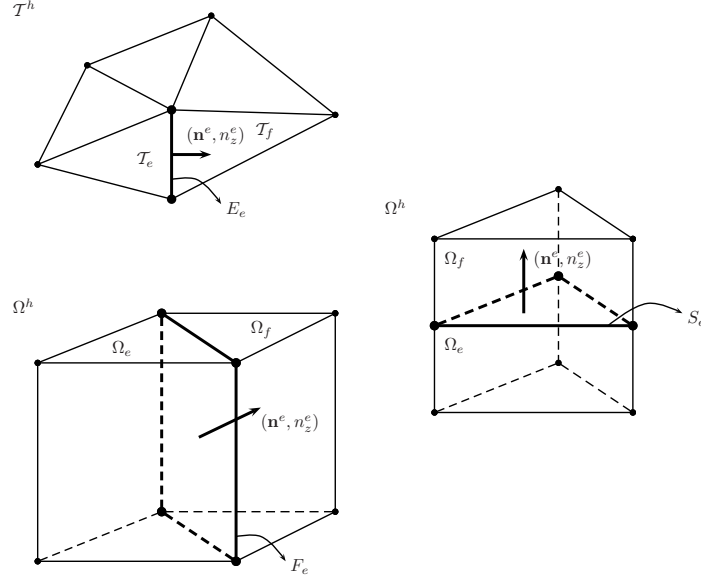
Figure 4.2: Main notations used to describe the mesh topology. In two dimensions, any interior edge E_e is shared by two triangles $\mathcal{T}_e$ and $\mathcal{T}_f$. In three dimensions, any interior vertical face F_e is common to adjacent prisms Ω_e and Ω_f (lying within a common layer). Two stacked prisms Ω_e and Ω_f share an interior triangular face S_e. A unit normal vector $(\mathbf{n}^e, n_z^e)$ is associated to each of these interior geometric items, with the superscript e indicating that it is oriented from e to f (with $e > f$).

where $\overline{\mathcal{T}_e}$ denotes the closure of $\mathcal{T}_e$. Extrusion of each triangle $\mathcal{T}_e$ into prismatic columns is then performed so as to exactly fit the sea bottom Γ_b^h and the free surface Γ_s^h. The domain Ω^h is then naturally partitioned into N_p open non-overlapping prisms Ω_e:

$$\overline{\Omega^h} = \bigcup_{e=1}^{N_p} \overline{\Omega_e} \qquad \text{and} \qquad \Omega_e \cap \Omega_f = \emptyset \quad (e \neq f).$$

4.2.2 Variational statements

The variational statements involve integrations over geometrical items in two and three dimensions. The following notations are used:

$$\int \square \, d\Omega: \quad \text{3D integration over prisms,}$$

$$\int \square \, d\Gamma: \quad \text{2D integration over rectangular faces (vertical faces),} \qquad (4.16)$$

$$\int \square \, d\tau: \quad \text{2D integration over triangles.}$$

Free-surface elevation equation

For the free-surface equation (4.3), the variational statement for any given time t consists in finding $\eta(x, y, t) \in \mathcal{H}$ such that

$$\int_{\mathcal{T}^h} \left\{ \frac{\partial \eta}{\partial t} + \boldsymbol{\nabla} \cdot \left(\int_{-d}^{\eta} \mathbf{u} \, \mathrm{d}z \right) \right\} \hat{\eta} \, \mathrm{d}\tau = 0 \quad \forall \hat{\eta} \in \mathcal{H}, \qquad (4.17)$$

where $\mathcal{H}$ is the Sobolev space $\mathcal{L}_2(\mathcal{T}^h)$ defined in Appendix C.2. Integrating the divergence term by parts leads to

$$\int_{\mathcal{T}^h} \left\{ \frac{\partial \eta}{\partial t} \hat{\eta} - \left(\int_{-d}^{\eta} \mathbf{u} \, \mathrm{d}z \right) \cdot \boldsymbol{\nabla} \hat{\eta} \right\} \mathrm{d}\tau + \int_{\Gamma_n^h} \mathbf{u} \cdot \mathbf{n} \, \hat{\eta} \, \mathrm{d}\Gamma = 0. \quad \forall \hat{\eta} \in \mathcal{H},$$

By using the fact that $\boldsymbol{\nabla} \hat{\eta}$ is independent of z and by enforcing the impermeability condition (4.1), the above expression reduces to

$$\int_{\mathcal{T}^h} \frac{\partial \eta}{\partial t} \hat{\eta} \, \mathrm{d}\tau - \int_{\Omega^h} \mathbf{u} \cdot \boldsymbol{\nabla} \hat{\eta} \, \mathrm{d}\Omega = 0 \quad \forall \hat{\eta} \in \mathcal{H}. \qquad (4.18)$$

Continuity equation

For the continuity equation, the variational statement for any given time t consists in finding $w(x, y, z, t)$ with $(u, v, w) \in \mathcal{H}_{div}(\Omega^h)$ (see Appendix C.2), such that

$$\int_{\Omega^h} \left(\boldsymbol{\nabla} \cdot \mathbf{u} + \frac{\partial w}{\partial z} \right) \hat{w} \, \mathrm{d}\Omega = 0 \quad \forall \hat{w} \in \mathcal{W}, \qquad (4.19)$$

where $\mathcal{W}$ is defined in Appendix C.2. By integrating the above expression by parts, we obtain

$$- \int_{\Omega^h} \left(\mathbf{u} \cdot \boldsymbol{\nabla} \hat{w} + w \frac{\partial \hat{w}}{\partial z} \right) \mathrm{d}\Omega + \underbrace{\int_{\Gamma_n^h} \hat{w} \, \mathbf{u} \cdot \mathbf{n} \, \mathrm{d}\Gamma}_{1} + \underbrace{\int_{\Gamma_b^h} \hat{w} \left(\mathbf{u} \cdot \mathbf{n} + w n_z \right) \mathrm{d}\tau}_{2}$$

$$+ \underbrace{\int_{\Gamma_s^h} \hat{w} \left(\mathbf{u} \cdot \mathbf{n} + w n_z \right) \mathrm{d}\tau}_{3} = 0 \quad \forall \hat{w} \in \mathcal{W}.$$

A closer look at the terms labeled 1 to 3 will shed light on their meaning. By enforcing the impermeability condition of the lateral boundary and the sea bed, namely conditions (4.1) and (4.6), integrals 1 and 2 vanish. Integral 3 does not vanish and must be computed in order to determine the vertical velocity on Γ_s^h. Note that the boundary condition (4.6) at the seabed is a natural boundary condition that is automatically incorporated into the variational statement. The continuity equation must then be integrated from the seabed upwards. This can be done by using upwind-biased test functions for the CG method or upwind-biased fluxes for the DG method (the latter approach is described in detail in Appendix C.1). In an intuitive interpretation, the continuity equation can be viewed as a steady-state advection equation (with

the advective velocity equal to one) with source term (the horizontal velocity divergence), which might help clarify the approach described herebefore. We end up with the following variational statement:

$$-\int_{\Omega^h} \left(\mathbf{u} \cdot \boldsymbol{\nabla} \hat{w} + w \frac{\partial \hat{w}}{\partial z} \right) \mathrm{d}\Omega + \int_{\Gamma_s^h} \hat{w} \left(\mathbf{u} \cdot \mathbf{n} + w n_z \right) \mathrm{d}\tau = 0 \quad \forall\, \hat{w} \in \mathcal{W}.$$
(4.20)

Tracer equation

We now turn our attention to the tracer equation (4.10). Since the domain of integration Ω^h is time-dependent and a time derivative appears in Eq. (4.10), a little more work is needed prior to deriving the variational statement. We will recast the original equation into the so-called arbitrary Lagrangian-Eulerian (ALE) form. With this formulation, the mesh is neither fixed in space, nor does it follow the fluid. It is therefore neither Eulerian nor Lagrangian. A good review of ALE methods is presented by *Donea et al.* (2004). Following *Farhat et al.* (2001), we define a reference fixed mesh Ω_0^h and a mapping function $\mathbf{x}$ between Ω_0^h and Ω^h:

$$\mathcal{A} : \Omega_0^h \rightarrow \Omega^h : \boldsymbol{\xi} \rightarrow \mathcal{A}\left(\boldsymbol{\xi}, t\right) = \mathbf{x}.$$

This mapping simply associates a three-dimensional coordinate $\boldsymbol{\xi}$ of the reference mesh Ω_0^h to a three-dimensional coordinate $\mathbf{x} = (x, y, z)$ in the physical moving mesh Ω^h. We further assume that this transformation is invertible:

$$J = \left(\frac{\partial \mathbf{x}}{\partial \boldsymbol{\xi}} \right) > 0,$$

where J is the Jacobian of the transformation. We also require that the mapping associate the boundary of the reference mesh to the boundary of the physical mesh, i.e., $\mathcal{A}(\partial\Omega_0^h) = \partial\Omega^h$ without any other constraint on interior coordinates aside from some smoothness requirement. The conservative ALE form of Eq. (4.10) then reads (*Formaggia and Nobile*, 2004):

$$\left.\frac{\partial(JC)}{\partial t}\right|_{\xi} + J\boldsymbol{\nabla} \cdot (\mathbf{u}C) + J\frac{\partial\left(\tilde{w}C\right)}{\partial z} =$$
$$J\boldsymbol{\nabla} \cdot (\kappa\boldsymbol{\nabla}C) + J\frac{\partial}{\partial z}\left(\kappa\frac{\partial C}{\partial z} \right) \quad \text{in } \Omega_0^h$$
(4.21)

where all terms are computed in the reference domain Ω_0^h. In particular, the time derivative is computed with respect to a fixed position in Ω_0^h. We have defined $\tilde{w} = w - w_m$ where the mesh velocity w_m is given by

$$w_m = \left.\frac{\partial z}{\partial t}\right|_{\xi}.$$
(4.22)

With the presence of the mesh velocity, vertical advection is relative to the moving mesh. The variational statement for the tracer equation is obtained by multiplying Eq. (4.21) by a test function $\hat{C}$, integrating the result over the reference mesh and using

75

the fact that $\mathrm{d}\Omega = J\mathrm{d}\Omega_0$. We seek $C \in \mathcal{G}$ such that

$$\frac{\mathrm{d}}{\mathrm{d}t} \int_{\Omega^h(t)} C\hat{C} \,\mathrm{d}\Omega + \int_{\Omega^h(t)} \left[\boldsymbol{\nabla} \cdot (\mathbf{u}C) + \frac{\partial (\tilde{w}C)}{\partial z} \right] \hat{C} \,\mathrm{d}\Omega =$$
$$\int_{\Omega^h(t)} \left[\boldsymbol{\nabla} \cdot (\kappa \boldsymbol{\nabla}C) + \frac{\partial}{\partial z} \left(\kappa \frac{\partial C}{\partial z} \right) \right] \hat{C} \,\mathrm{d}\Omega \quad \forall \hat{C} \in \mathcal{G}, \tag{4.23}$$

where $\mathcal{G}$ is the Sobolev space $\mathcal{H}_1(\Omega^h)$ defined in Appendix C.2. The first term in the above expression was obtained by using the following result:

$$\int_{\Omega_0^h} \frac{\partial (JC)}{\partial t} \Big|_{\xi} \hat{C} \,\mathrm{d}\Omega_0 = \frac{\mathrm{d}}{\mathrm{d}t} \int_{\Omega_0^h} JC\hat{C} \,\mathrm{d}\Omega_0 = \frac{\mathrm{d}}{\mathrm{d}t} \int_{\Omega^h(t)} C\hat{C} \,\mathrm{d}\Omega,$$

where we used the fact that the test function does not depend on time in the reference mesh. It does, however, depend on time in the physical domain Ω^h. The advection and diffusion terms can be integrated by parts, which yields

$$\int_{\Omega^h(t)} \left[\boldsymbol{\nabla} \cdot (\mathbf{u}C) + \frac{\partial (\tilde{w}C)}{\partial z} \right] \hat{C} = - \int_{\Omega^h(t)} C \left(\mathbf{u} \cdot \boldsymbol{\nabla}\hat{C} + \tilde{w} \frac{\partial \hat{C}}{\partial z} \right) \mathrm{d}\Omega$$
$$+ \int_{\Gamma_s^h} C\hat{C} \left(\mathbf{u} \cdot \mathbf{n} + \tilde{w}n_z \right) \mathrm{d}\tau \tag{4.24}$$

and

$$\int_{\Omega^h(t)} \left[\boldsymbol{\nabla} \cdot (\kappa \boldsymbol{\nabla}C) + \frac{\partial}{\partial z} \left(\kappa \frac{\partial C}{\partial z} \right) \right] \hat{C} \,\mathrm{d}\Omega =$$
$$- \int_{\Omega^h(t)} \kappa \left(\boldsymbol{\nabla}\hat{C} \cdot \boldsymbol{\nabla}C + \frac{\partial \hat{C}}{\partial z} \frac{\partial C}{\partial z} \right) \mathrm{d}\Omega, \tag{4.25}$$

where we used the no-flux conditions (4.1), (4.6) and (4.11). Note that the left-hand side of Eq. (4.24) is nothing but the variational statement of the continuity equation (see Eq. 4.20) in which the velocity is multiplied by the tracer concentration C, the test function $\hat{w}$ is replaced by $\hat{C}$ and the modified vertical velocity $\tilde{w}$ is used in place of the vertical velocity w. Now, using Eq. (4.24) and Eq. (4.25) in Eq. (4.23) gives rise to

$$\frac{\mathrm{d}}{\mathrm{d}t} \int_{\Omega^h(t)} C\hat{C} \,\mathrm{d}\Omega - \int_{\Omega^h(t)} C \left(\mathbf{u} \cdot \boldsymbol{\nabla}\hat{C} + \tilde{w} \frac{\partial \hat{C}}{\partial z} \right) \mathrm{d}\Omega$$
$$+ \int_{\Gamma_s^h} C\hat{C} \left(\mathbf{u} \cdot \mathbf{n} + \tilde{w}n_z \right) \mathrm{d}\tau \tag{4.26}$$
$$+ \int_{\Omega^h(t)} \kappa \left(\boldsymbol{\nabla}\hat{C} \cdot \boldsymbol{\nabla}C + \frac{\partial \hat{C}}{\partial z} \frac{\partial C}{\partial z} \right) \mathrm{d}\Omega = 0 \quad \forall \hat{C} \in \mathcal{G}.$$

4.2.3 Finite element discretization

We now seek approximations $\eta^h \simeq \eta$, $w^h \simeq w$ and $C^h \simeq C$ in finite-dimensional subsets of $\mathcal{H}$, $\mathcal{W}$ and $\mathcal{G}$, respectively. Each of those subsets, marked by a superscript

h, is spanned by a finite number of polynomial basis functions. The basis functions will be noted ψ. The finite element approximations are

$$\eta \quad \simeq \eta^h = \sum_{j=1}^{N_\eta} H_j(t)\psi_j^\eta \quad \in \mathcal{H}^h = \text{span}\left\{\psi_1^\eta,\ \psi_2^\eta,\ \ldots,\ \psi_{N_\eta}^\eta\right\} \subset \mathcal{H},$$

$$w \quad \simeq w^h = \sum_{j=1}^{N_w} W_j(t)\psi_j^w \quad \in \mathcal{W}^h = \text{span}\left\{\psi_1^w,\ \psi_2^w,\ \ldots,\ \psi_{N_w}^w\right\} \subset \mathcal{W}, \quad (4.27)$$

$$C \quad \simeq C^h = \sum_{j=1}^{N_C} C_j(t)\psi_j^C \quad \in \mathcal{G}^h = \text{span}\left\{\psi_1^C,\ \psi_2^C,\ \ldots,\ \psi_{N_C}^C\right\} \subset \mathcal{G}.$$

Note that, strictly speaking, the three-dimensional basis functions depend on time due to the mesh motions. This, however, only has an implication on the tracer equation where a time derivative occurs. We now opt for the Galerkin method, which is equivalent to the following procedure. Consider each variational statement, Eqs (4.18), (4.20) and (4.26), in which the sought variable (η, w and C) is substituted for its approximations (η^h, w^h and C^h, respectively) and hold it true when the test function is substituted for any of the basis functions spanning the corresponding subset to which the test function belongs. We also assume that we possess an approximation $\mathbf{u}^h$ of the horizontal velocity field, the obtention of which is beyond the scope of this chapter (see Chapter 5 instead).

The discrete formulation for the elevation, Eq. (4.18), now consists in finding $\eta^h \in \mathcal{H}^h$ such that

$$\int_{\mathcal{T}^h} \frac{\partial \eta^h}{\partial t} \psi_i^\eta \, \mathrm{d}\tau - \int_{\Omega^h} \mathbf{u}^h \cdot \boldsymbol{\nabla}\psi_i^\eta \, \mathrm{d}\Omega = 0 \quad \forall\, i = 1,\ 2,\ \ldots,\ N_\eta. \qquad (4.28)$$

For the continuity equation, the discrete formulation consists in finding $w^h \in \mathcal{W}^h$ such that

$$- \int_{\Omega^h} \left[\mathbf{u}^h \cdot \boldsymbol{\nabla}\psi_i^w + w^h \frac{\partial \psi_i^w}{\partial z}\right] \mathrm{d}\Omega$$
$$+ \int_{\Gamma_s^h} \psi_i^w \left(\mathbf{u}^h \cdot \mathbf{n} + w^h n_z\right) \mathrm{d}\tau = 0 \quad \forall\, i = 1,\ 2,\ \ldots,\ N_w. \qquad (4.29)$$

Finally, the discrete variational statement for the tracer equation consists in finding $C^h \in \mathcal{G}^h$ such that

$$\frac{\mathrm{d}}{\mathrm{d}t} \int_{\Omega^h(t)} C^h \psi_i^C \, \mathrm{d}\Omega - \int_{\Omega^h(t)} C^h \left(\mathbf{u}^h \cdot \boldsymbol{\nabla}\psi_i^C + \tilde{w}^h \frac{\partial \psi_i^C}{\partial z}\right) \mathrm{d}\Omega$$
$$+ \int_{\Gamma_s^h} C^h \psi_i^C \left(\mathbf{u}^h \cdot \mathbf{n} + \tilde{w}^h n_z\right) \mathrm{d}\tau$$
$$+ \int_{\Omega^h(t)} \kappa \left(\boldsymbol{\nabla}\psi_i^C \cdot \boldsymbol{\nabla}C^h + \frac{\partial \psi_i^C}{\partial z}\frac{\partial C^h}{\partial z}\right) \mathrm{d}\Omega = 0 \qquad (4.30)$$
$$\forall\, i = 1,\ 2,\ \ldots,\ N_C.$$

4.2.4 Discrete conservation laws

Starting from the discrete formulations (4.28), (4.29) and (4.30), we now investigate under which conditions global volume and tracer conservation as well as consistency (i.e., compatibility) are achieved in the discrete sense.

Volume conservation

Since Eq. (4.28) must be valid for any ψ_i^η, it must hold true for $\psi_i^\eta = 1$ as well (which belongs to $\mathcal{H}^h$). Setting $\psi_i^\eta = 1$ in Eq. (4.28) and using the fact that $\mathcal{T}^h$ is time-independent gives rise to

$$\frac{\mathrm{d}}{\mathrm{d}t} \int_{\mathcal{T}^h} \eta^h \, \mathrm{d}\tau = 0, \tag{4.31}$$

which is the discrete statement of volume conservation. The fulfillment of the latter is assured by the way we wrote the variational statement for the free-surface elevation. It is readily shown that the volume variation can only be caused by freshwater fluxes. By including the latter in the discrete variational statement for the free-surface elevation, Eq. (4.28), the expression above simply becomes

$$\frac{\mathrm{d}}{\mathrm{d}t} \int_{\mathcal{T}^h} \eta^h \, \mathrm{d}\tau = \int_{\mathcal{T}^h} q_w \, \mathrm{d}\tau.$$

Global tracer conservation

The property of global tracer conservation is investigated by setting $\psi_i^C = 1$ in the discrete variational statement for the tracer equation, Eq. (4.30). We then obtain

$$\frac{\mathrm{d}}{\mathrm{d}t} \int_{\Omega^h(t)} C^h \, \mathrm{d}\Omega + \int_{\Gamma_s^h} C^h \left[\mathbf{u}^h \cdot \mathbf{n} + (w^h - w_m^h) n_z \right] \mathrm{d}\tau = 0, \tag{4.32}$$

where we used $\tilde{w}^h = w^h - w_m^h$. In view of Eq. (4.32), providing that the integral over the free surface Γ_s^h is discarded, the tracer is globally conserved, namely

$$\frac{\mathrm{d}}{\mathrm{d}t} \int_{\Omega^h(t)} C^h \, \mathrm{d}\Omega = 0. \tag{4.33}$$

However, discarding this integral consistently, that is while preserving the discrete compatibility between the elevation, continuity and tracer equations, brings about additional constraints as we will now see.

Consistency

According to the definition presented earlier, consistency is equivalent to requiring that a constant concentration be solution to Eq. (4.30). Setting $C^h = C_0 \neq 0$ in Eq. (4.30), factoring out C_0 and separating out the terms depending on the mesh velocity (and integrating them by parts) from those that do not, we end up having to satisfy the

following equation

$$
\underbrace{\frac{\mathrm{d}}{\mathrm{d}t} \int_{\Omega^h(t)} \psi_i^C \, \mathrm{d}\Omega}_{A_1} - \underbrace{\int_{\Omega^h(t)} \psi_i^C \frac{\partial w_m^h}{\partial z} \, \mathrm{d}\Omega}_{A_2}
$$

$$
\underbrace{- \int_{\Omega^h(t)} \left(\mathbf{u}^h \cdot \boldsymbol{\nabla} \psi_i^C + w^h \frac{\partial \psi_i^C}{\partial z} \right) \mathrm{d}\Omega}_{B_1} \tag{4.34}
$$

$$
\underbrace{+ \int_{\Gamma_s^h} \psi_i^C \left(\mathbf{u}^h \cdot \mathbf{n} + w^h n_z \right) \mathrm{d}\tau = 0}_{B_2} \quad \forall \, i = 1, \, 2, \, \ldots, \, N_C.
$$

The A_2-labeled term is the result of integrating by parts all terms involving the mesh velocity. The set of B-labeled terms in the above expression and the discrete variational statement for the continuity equation, Eq. (4.29), are identical under the following two conditions:

1. the subsets $\mathcal{W}^h$ and $\mathcal{G}^h$ are the same (in which case we have $\psi_i^w = \psi_i^C \; \forall i = 1, \, 2, \, \ldots \; N^w = N^C$),

2. the B-labeled terms and Eq. (4.29) are computed on the same mesh $\Omega^h(t)$.

These two conditions may be summarized by simply demanding that Eq. (4.29) and the advection terms in Eq. (4.34) be discretely compatible, a condition that we will call discrete compatibility between the continuity and tracer equations. Concretely, this entails that the same elements must be used to compute w^h and C^h. Note that this condition is conceptually the same as that derived when using finite differences (*Griffies et al.*, 2001). Now, the fulfillment of this condition does not necessarily ensure that Eq. (4.34) is satisfied. The following relation between the A-labeled terms of Eq. (4.34) must also hold true :

$$
\frac{\mathrm{d}}{\mathrm{d}t} \int_{\Omega^h(t)} \psi_i^C \, \mathrm{d}\Omega = \int_{\Omega^h(t)} \psi_i^C \frac{\partial w_m^h}{\partial z} \, \mathrm{d}\Omega. \tag{4.35}
$$

When using a discontinuous representation, the above expression must be true for each element $\Omega_e(t)$ individually when $\psi_i^C = 1$, which a stricter condition. When discretized in time and expressed for an individual element Ω_e, Eq. (4.35) becomes

$$
\mathrm{VOL}\left(\Omega_e^{n+1} \right) - \mathrm{VOL}\left(\Omega_e^n \right) = \int_{t^n}^{t^{n+1}} \left(\int_{\Omega_e(t)} \frac{\partial w_m^h}{\partial z} \, \mathrm{d}\Omega \right) \mathrm{d}t, \tag{4.36}
$$

where the time step shall be defined as $\Delta t = t^{n+1} - t^n$. Eq. (4.36) is known as the Discrete Geometric Conservation Law (DGCL) (*Farhat et al.*, 2001; *Donea et al.*, 2004; *Formaggia and Nobile*, 2004) and states that the variation in volume of a given element over Δt must be equal to the volume swept by the element boundaries (with velocity w_m) during that time interval. Note that if the volume is computed exactly, then the time integration in the right-hand side of (4.36) must be exact. Depending

upon the hypotheses made regarding the time dependence of w_m, a proper quadrature rule must then be used. Hence, to ensure consistency, the following two conditions at least must be fulfilled:

1. the continuity and tracer equations must be discretely compatible (i.e., the way we compute the vertical velocity must be discretely compatible with the way we compute the advection terms in the tracer equation),

2. the mesh update procedure must comply with the DGCL (see Eq. 4.36).

It should be emphasized that these conditions involve the continuity and tracer equations as well as the mesh update procedure. So far, nothing has been said regarding the free-surface elevation equation.

Conserving the tracer globally while preserving the consistency between the continuity and tracer equations requires that the surface integral on Γ_s^h automatically vanish when $C^h = 1$ in Eq. (4.32). This will happen only if the computation of the vertical velocity guarantees it. We now verify that this is the case. Let us now return to the continuity equation and focus on the discrete variational statement, Eq. (4.29). Since the mesh is made up of prisms with vertical faces, we can readily add up the components of Eq. (4.29) written for ψ_i^w sharing the same two-dimensional support. We note I the set of indices i corresponding to the basis functions ψ_i^w aligned on the same vertical. By definition, all these basis functions satisfy the following two properties:

$$\sum_{i \in I} \psi_i^w(x, y, z) = \psi_I^{w,2D}(x, y),$$

$$\sum_{i \in I} \frac{\partial \psi_i^w}{\partial z}(x, y, z) = 0,$$

where $\psi_I^{w,2D}$ is simply the projection of ψ_i^w ($i \in I$) onto the plane (x, y). With an abuse of notation, this projection is identified by I. With the first summation, the vertical dependences of all basis functions cancel out. Now, adding up the components of (4.29) in the vertical gives rise to

$$-\int_{\Omega^h} \mathbf{u}^h \cdot \boldsymbol{\nabla} \psi_I^{w,2D} \mathrm{d}\Omega + \int_{\Gamma_s^h} \psi_I^{w,2D} \left(\mathbf{u}^h \cdot \mathbf{n} + w^h n_z \right) \mathrm{d}\tau = 0. \tag{4.37}$$

The similarities between the above expression and the discrete variational statement for the elevation, Eq. (4.28), are clear. By choosing the basis functions for the vertical velocity such that $\psi_I^{w,2D} = \psi_I^\eta$, where ψ_I^η is the two-dimensional elevation basis function, the second term in the discrete elevation equation (Eq. 4.28) is identical to the first term in Eq. (4.37). This leaves us with the following equality:

$$\int_{\Gamma_s^h} \psi_I^{w,2D} \left(\mathbf{u}^h \cdot \mathbf{n} + w^h n_z \right) \mathrm{d}\tau = \int_{\mathcal{T}^h} \psi_I^\eta \frac{\partial \eta^h}{\partial t} \, \mathrm{d}\tau = \int_{\Gamma_s^h} \psi_I^\eta \frac{\partial \eta^h}{\partial t} n_z \, \mathrm{d}\tau$$

where n_z is the Jacobian of the transformation of coordinates from $\mathcal{T}^h$ to Γ_s^h. The last expression thus becomes

$$\int_{\Gamma_s^h} \psi_i^w \left\{ \mathbf{u}^h \cdot \mathbf{n} + \left(w^h - \frac{\partial \eta^h}{\partial t} \right) n_z \right\} \mathrm{d}\tau = 0, \tag{4.38}$$

where we used the fact that ψ_i^w reduces to its two-dimensional structure on Γ_s^h. Eq. (4.38) is the discrete counterpart of the kinematic boundary condition on the vertical velocity, given by Eq. (4.7). Most importantly, this result demonstrates that global conservation can be achieved without breaking down consistency. When setting $C^h = 1$ in Eq. (4.30), the surface integral on Γ_s^h vanishes if the mesh velocity at the sea surface is $w_m^h = \frac{\partial \eta^h}{\partial t}$ and the same interpolation is used in the horizontal for the elevation and the vertical velocity. Under these two conditions, the surface integral can be discarded consistently in Eq. (4.32).

The discrete surface kinematic boundary condition is retrieved by adding up the discrete components of the continuity equation in the vertical. This is a consequence of the elevation and continuity equations being discretely compatible. And they should be since they express the same principle of volume conservation. It then turns out that the surface kinematic boundary condition is redundant, complying with the first-order nature of the continuity equation. In Appendix C.3, we show that integrating the continuity equation downward (with the imposition of the surface boundary condition) allows for automatically retrieving the seabed boundary condition, provided of course that the continuity and elevation equations are discretely compatible. Both directions of integration yield equivalent results (the correct boundary condition is retrieved) and the tracer conservation does not depend on it (the tracer is consistently conserved in both cases). It is easy to conjure up a way of breaking down consistency while preserving global conservation. By enforcing the surface tracer flux to vanish, global conservation is ensured. However, if there is no compatibility between the elevation and the continuity equations, this surface integral does not naturally vanish and consistency breaks down. Now, an opposite scenario can be imagined. Consistency is easily achieved by ensuring that the tracer and continuity equations are discretely compatible. Nevertheless, if the surface integral does not vanish and is computed (to ensure consistency), global conservation will break down for a tracer distribution different than a constant value throughout the domain.

The key results regarding conservation are summarized below. In the absence of source/sink terms and boundary fluxes, sufficient conditions to consistently achieve global tracer conservation in free-surface flows on moving meshes are the following.

1. The continuity and tracer equations are discretely compatible, which comes down to having the discrete advection terms in the tracer equation reduce to the discrete continuity equation when $C^h = 1$ (see Eq. 4.34).

2. The DGCL is satisfied elementwise (see Eq. 4.36).

3. The elevation and continuity equations are discretely compatible. This condition entails that the discrete surface kinematic boundary condition is retrieved when adding up all components of the discrete continuity equation in the vertical (see Eq. 4.38).

4. The mesh velocity at the surface Γ_s^h is upwards and has a magnitude $w_m^h = \frac{\partial \eta^h}{\partial t}$. Note that, in the interior, the mesh motion is not constrained unless element shape regularity requires it.

81

4.2.5 Which elements should we use ?

The above conditions restrict the choice of finite element subsets and, thereby, the choice of elements that should be used. These restrictions lead to the following guidelines:

1. The same element must be used for the vertical velocity and the tracer.

2. The nodes location in the horizontal must be the same for the elevation and the vertical velocity.

3. The two previous statements also imply that the nodes location in the horizontal must be the same for the elevation, the vertical velocity and the tracer.

4. In the vertical, the nodes location for the vertical velocity and the tracer is unconstrained, yet it must be identical for both variables.

In addition to these considerations, the mixed formulation used for the horizontal velocity and the elevation must be numerically stable. The mixed formulation should be devoid of spurious elevation and velocity modes. In the presence of spurious elevation modes, a stabilized formulation can usually filter out the modes. However, this requires to add a term to the discrete elevation equation, with the consequence of breaking down the discrete compatibility between the elevation and continuity equations. Velocity modes are less problematic insofar as a small amount of momentum diffusion is usually sufficient to filter them out. Based on the most recent studies, the two mixed formulations that turn out to be the most useful for hydrostatic marine modeling based on the primitive equations are the $P_1^{NC} - P1$ and the RT_0 pairs (*Hanert et al.*, 2003; *Le Roux*, 2005; *Le Roux et al.*, 2005, in press). The first pair was originally used by *Hua and Thomasset* (1984) for shallow-water flows and consists of a linear non-conforming interpolation for both components of the velocity and a linear interpolation for the elevation. It does not support any spurious oscillations. This pair has been used by *Hanert et al.* (2005) and *White et al.* (2006a) in two dimensions and by *White and Deleersnijder* (in press) in three dimensions. The second pair is called low-order Raviart-Thomas element. The normal velocity components are located at the middle of each side of the triangular element and the elevation is constant on each element. Shallow-water models using this formulation are described by *Miglio et al.* (1998) and *Walters* (2005).

Using the $P_1^{NC} - P_1$ pair requires to opt for a P_1 representation in the horizontal for the tracer and the vertical velocity (in order to consistently ensure global conservation). To fulfill the same property with the RT_0 element, the vertical velocity and the tracer must be constant in the horizontal on each element. In both cases, there is no constraint for the vertical interpolation: it could be of high order and discontinuous. Both schemes have advantages and disadvantages. A linear continuous representation for the tracers is not optimal for advection-dominated flows. Stabilization could be necessary (without impact on conservation). The finite volume scheme pertaining to the RT_0 element is certainly more stable but might be overdiffusive. Regarding the elevation, P_1 is more accurate than P_0 with the latter leading to twice as many degrees of freedom. Moreover, a P_1 interpolation for the elevation leads to a piecewise linear (and continuous) representation of the moving mesh. Finally, when using the

$P_1^{NC} - P_1$ pair, to be computationally competitive, the matrices of the systems to compute the vertical velocity and the tracer must be rendered at least banded diagonal through mass lumping

Note that these compromises arise because of the need to select a stable mixed formulation. If stability were not in jeopardy, the best choice would probably consist of a linear non-conforming representation for all variables. All conditions to consistently attain global conservation would be satisfied. Due to the orthogonality of the linear non-conforming shape functions in the horizontal, all system matrices would be at most banded diagonal (tridiagonal in case of a linear continuous interpolation in the vertical) without resorting to mass lumping. This interpolation would be ideally suited for advection-dominated flows. The momentum equation would inherit all conservation properties developed for the tracer equation. For this scheme to be usable, though, we would need to stabilize the elevation equation with a potential loss of mass conservation. This would be quite paradoxical since this interpolation choice would have been made to ensure conservation in the first place ! The same discontinuous (linear or higher-order) interpolation in the horizontal for all variables would also work out, as far as conservation is concerned. However, stability analyses in the lines of that presented by *Le Roux and Carey* (2005) (but in two dimensions) would be necessary to sanction this choice.

4.2.6 The issue of time stepping

In light of the developments carried out above, time discretization does not appear to be an issue. However, there is more into conservation than the proper choice of elements for spatial discretization. To ensure a discrete compatibility between the free-surface elevation and the continuity equations – and thus, to consistently ensure global tracer conservation –, the following property must be satisfied. The horizontal transport whose divergence is responsible for the change in the free-surface elevation must be equal to the horizontal transport associated with the horizontal velocity used to compute the vertical velocity. These transports are not necessarily equal and when that occurs, the three-dimensional horizontal velocity must be corrected so that its transport is equal to that used to compute the free-surface elevation. The main cause for this discrepancy originates from the choice of time stepping. If a semi-implicit scheme is considered for the inertia-gravity wave terms (with or without mode splitting), the horizontal transport causing the elevation change from time steps n to $n + 1$ is the mean transport computed from those at time steps n and $n + 1$. The three-dimensional horizontal velocity must then be corrected accordingly. Following this procedure, linearizing the elevation equation poses no problem as far as conservation is concerned. However, it has been suggested in the past that this approach prevents tracers to be conserved because the domain does not move (*Roullet and Madec*, 2000). In fact, when we opt for such a linearized elevation equation, we may still alter the domain geometry according to the free-surface motions. To preserve the property of consistent conservation (i.e., discrete compatibility between the elevation and continuity equations), the three-dimensional horizontal velocity must be corrected to yield a transport in the deformed domain that is equal to the transport (in the undeformed domain) used in the linearized elevation equation.
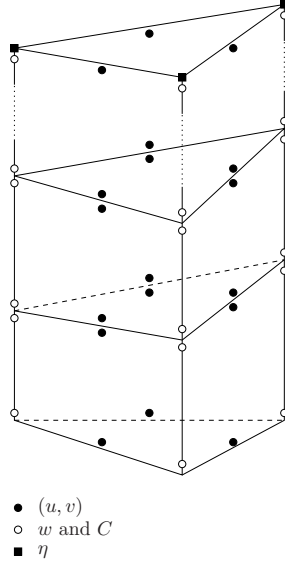
- ● (u, v)
- ○ w and C
- ■ η

Figure 4.3: Location of nodes within a column split into prisms. The top triangle is the surface triangle. The free-surface elevation η is linear and continuous. The horizontal velocity is linear non-conforming in the horizontal and linear discontinuous in the vertical (indicated by two nodes sharing a common physical edge). The discontinuous representation in the vertical is particularly well suited for shear regions, as it commonly occurs in baroclinic flows. The vertical velocity and tracers are linear everywhere, yet discontinuous in the vertical.

4.3   Illustrative experiments

A few numerical experiments are now presented. In its current configuration, the model conserves the volume and any tracer globally up to machine precision in a consistent way. We first discuss the Goldsbrough-Stommel circulation, induced by freshwater fluxes and invetigate the effect on salt concentration. We then illustrate the implications of a consistency breakdown.

4.3.1   Model description

The full description of the model is provided in Chapter 5. However, for the current chapter to be self-contained, we briefly describe here the most important features. The dynamics is split into a two-dimensional depth-averaged system for the evolution of the fast-propagating surface waves and a three-dimensional system for the vertical structure of the velocity. The same time step is used for both systems and all terms governing the propagation of inertia-gravity waves are semi-implicit in time. After the computation of the external mode and the three-dimensional horizontal velocity, the latter is corrected so that its horizontal transport is equal to the transport causing the change in the free-surface elevation. The elements used to interpolate the elevation and the velocity are depicted in Figure (4.3). The mixed formulation $P_1^{NC} - P_1$ is used for the horizontal velocity and the elevation, respectively. In order to be consistent

with this choice, a linear continuous interpolation is used for the vertical velocity and all tracers. The latter, as well as the horizontal velocity, are interpolated with linear discontinuous basis functions in the vertical.

4.3.2 The Goldsbrough-Stommel circulation

The Goldsbrough-Stommel circulation discussed by *Huang and Schmitt* (1993) and *Huang* (1993) arises from freshwater forcing and is absent in rigid-lid models. A decent rendition of the barotropic flow induced by freshwater forcing alone in the North Atlantic basin is obtained by assuming the following simple linear profile for the freshwater flux q_w (see Eq. 4.3):

$$q_w = -q_{w0} \left[1 - 2 \frac{(y - y_s)}{(y_n - y_s)} \right],$$

where y is the meridional coordinate and y_s and y_n are the southern and northern coordinates of the basin, respectively. The freshwater flux magnitude is given by q_{w0} (with units of a velocity). A negative value for q_w indicates evaporation and a positive value indicates precipitation and river runoffs. This linear profile is an idealization of observations (*Huang and Schmitt*, 1993) and integrates to zero over the domain so that the total volume remains constant. We aim at comparing our results with that previously presented by *Huang* (1993) and *Griffies et al.* (2001). In both studies, the models were set up in spherical coordinates on a basin confined between the equator and 60°N and extending 60° zonally. Our model was run on a square basin of size 5000 km and constant depth of 4000 m. Following *Huang* (1993), the coefficients of horizontal and vertical viscosity are 5×10^4 m^2 s^{-1} and 10^{-4} m^2 s^{-1}, respectively. The equations are solved in Cartesian coordinates on a β-plane centered at 30°N. Neglecting the earth curvature on these scales is questionable. However, the objective of this experiment is twofold. First, we want to assess the model's ability at naturally handling freshwater fluxes as a simple forcing term in the elevation equation. Second, we want to evaluate the model's response in terms of surface salinity due to a local volume variation.

As shown in Figure (4.4), our results compare well to that of *Huang* (1993) and *Griffies et al.* (2001). It should be noted, however, that the barotropic streamfunction does not render the full picture of the flow because the latter is not divergence-free. Three meshes were used, each one with increased resolution along the western boundary (see caption of Figure (4.4) for details on mesh resolution). Both the anticyclonic subpolar and cyclonic subtropical gyres are well represented. The separation between both gyres lies at three fifths of the domain extent, in good agreement with results by *Huang* (1993) and *Griffies et al.* (2001). The barotropic volume transport is less than one Sv (1 Sv = 10^6 m^3 s^{-1}), which is only a few percent of the wind-driven and thermally-driven transport. However, as hinted by Figure (4.5) representing the surface salinity after three years, this tiny freshwater flux can potentially drive a strong three-dimensional baroclinic circulation. The freshwater input and output locally causes an increase and decrease, respectively, in the ocean volume. This, in turn, locally dilutes and concentrates the salt and a horizontal salinity gradient builds up at the surface. This dilution/concentration effect is only due to a variation in the volume
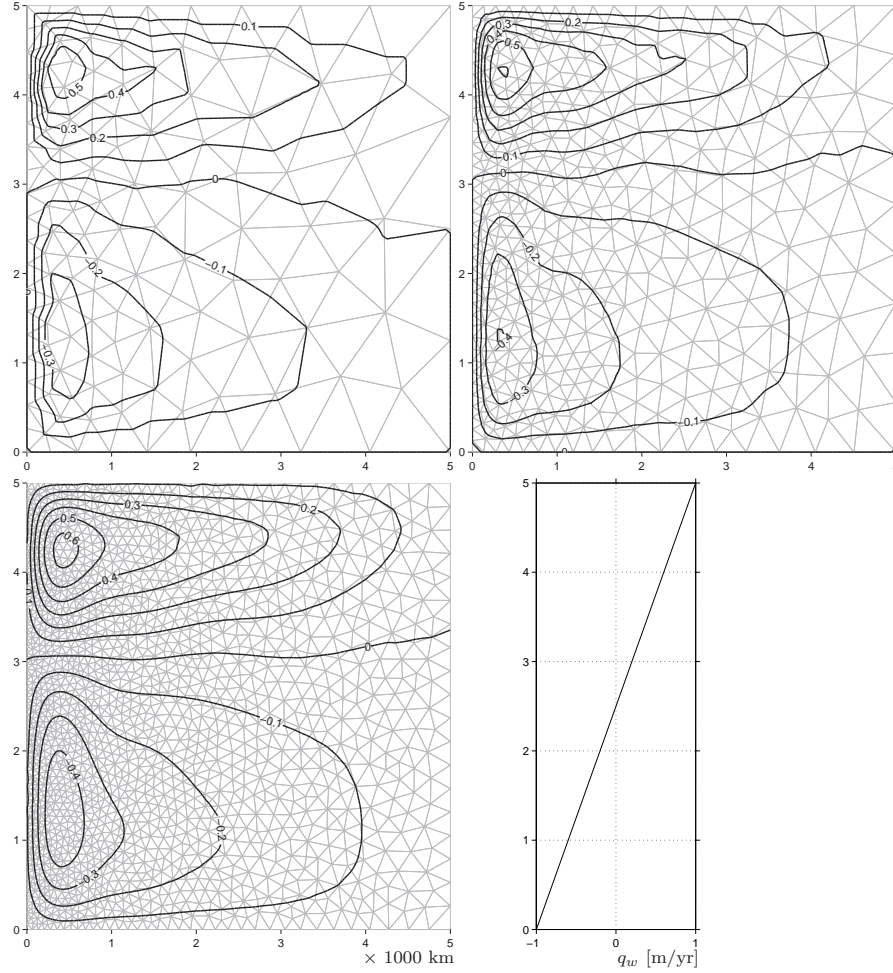
Figure 4.4: Barotropic streamfunction in Sv (1 Sv = 10^6 m^3 s^{-1}) for the freshwater-induced Goldsbrough-Stommel circulation on meshes with decreasing element sizes. The freshwater forcing q_w varies linearly in y between -1 and 1 m/year, respectively corresponding to evaporation in the south and precipitation in the north. Numerical experiments are carried out in a square basin of size 5000 km and depth 4000 m. Equations are solved on a β-plane centered at 30^oN. The coefficients of horizontal and vertical eddy viscosity are 5×10^4 m^2 s^{-1} and 10^{-4} m^2 s^{-1}, respectively. Meshes are refined along the western boundary of the basin. Resolution varies from 250 to 1000 km for the coarse mesh, from 125 to 500 km for the intermediate mesh and from 62.5 to 250 km for the fine mesh. The coarse mesh contains 215 elements. Upon refinement, the number of elements roughly quadruples.

86

Figure 4.5: Deviation in psu of surface salinity from the reference value after a three-year run. In this experiment, salinity acts as a passive tracer: it does not feed back the flow. The salinity gradient buildup has the potential of driving a strong baroclinic circulation.

of the ocean. The tracer flux at the sea surface is zero. In our experiment, salinity acts as a passive tracer: it does not feed back the flow. The coefficients of horizontal and vertical eddy diffusivity are 10^3 m^2 s^{-1} and 10^{-4} m^2 s$^{-1}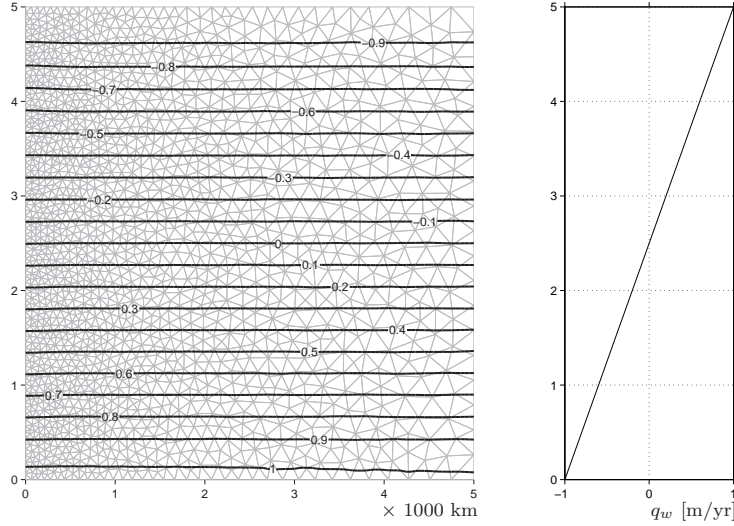$, respectively. For thorough studies of the freshwater-driven baroclinic circulation, see *Huang* (1993), *Huang and Chou* (1994) and *Rahmstorf* (1996).

4.3.3 When consistency breaks down

The results shown thus far have been obtained by solving the consistent discrete equations, with nodes location depicted in Figure (4.3). We now study cases in which the elements for the vertical velocity w and the tracer C are different and whereby consistency breaks down. In all experiments described in this section, the elements used for the vertical velocity and the elevation are those depicted in Figure (4.3). We use different elements for the tracer.

In Figure (4.6), three situations are compared. The model is run on a 10 km wide and 20 m deep square basin. The initial elevation field is a 2 m high Gaussian that we let freely evolve as a gravity wave over 1000 time steps of 72 s. The Gaussian magnitude decreases to one percent of its peak value over 3 km. The same initial condition is used in all experiments. The initial tracer concentration is 1 and should remain equal to 1 at all time (there is no boundary flux and no source/sink term). The surface integral in Eq. (4.32) is discarded to ensure global tracer conservation in all situations. In the first experiment, we use the same element for w and C. All consistency conditions are fulfilled and this is verified numerically. The deviations in the surface tracer concentration are zero (up to machine precision). In the second and third exper-
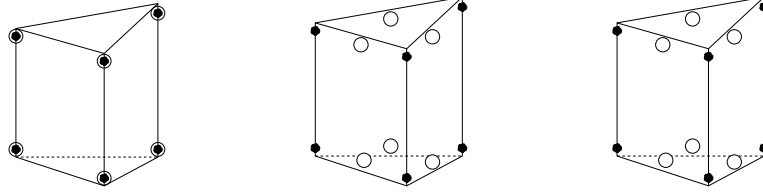
SURFACE TRACER CONCENTRATION (DEVIATION FROM 1)
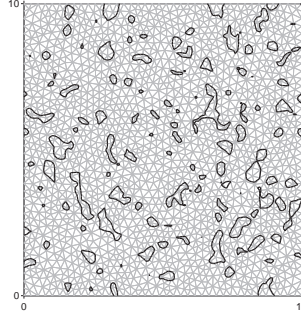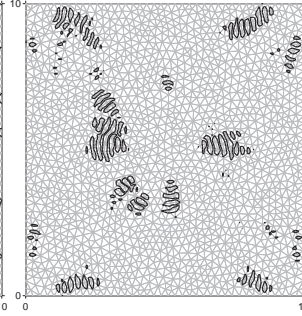
advection only   advection only   advection + diffusion ($\kappa = 10$ m^2/s)

Min: 2.1×10^{-14} Min: -1.8×10^2 Min: -3.7×10^{-2}

Max: 9.9×10^{-14} Max: 1.8×10^2 Max: 1.6×10^{-2}
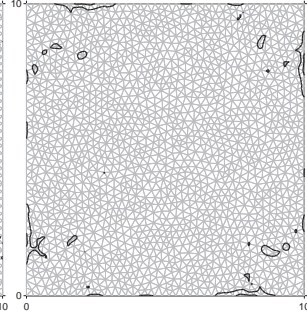
Contour at 5×10^{-14} Contour at $\pm 0.2 \times 10^2$ Contour at $\pm 1 \times 10^{-2}$

RELATIVE DEVIATION IN TOTAL TRACER CONTAINED IN Ω OVER 1000 TIME STEPS ($\times 10^{-13}$)
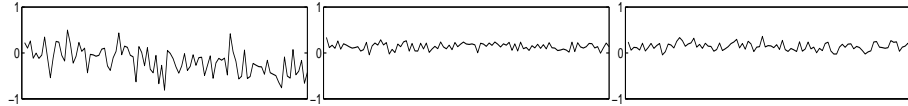
Figure 4.6: Illustration of consistency breakdown incurred when using different elements for the vertical velocity w and the tracer C. In all simulations, the tracer concentration is initially set to 1 and should remain equal to 1 at all time. The surface flux term (see Eq. 4.32) is discarded to ensure global conservation in all experiments (see lower panels). The domain is 10 km wide and 20 m deep. The initial elevation field is a 2-meter high Gaussian. The time step is 72 s. We use the P_1 element for the elevation in all runs. We clearly see that using the same elements for w and C consistently ensures global conservation (surface deviations are zero in machine precision).
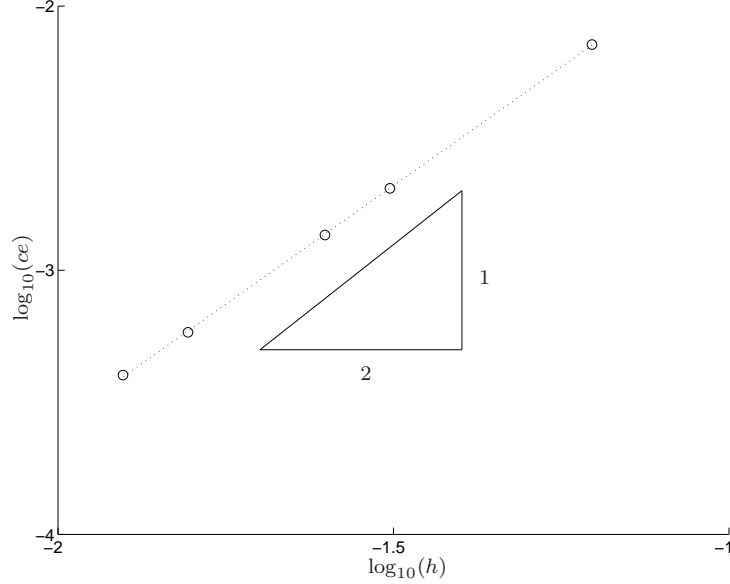
Figure 4.7: Convergence analysis of consistency errors on a tracer initially set to 1 within the domain. The errors are computed on structured meshes according to Eq. (4.39). The convergence rate is nearly quadratic (the slope is 1.8).

iments, the element for C is linear non-conforming and remain linear discontinuous in the vertical. The non-conforming representation in the horizontal is particularly well suited for advection-dominated flows (*Hanert et al.*, 2004), which is the reason behind this choice. When solving the advection equation for the tracer (i.e., without diffusion), the deviations at the surface reach very high values that are unbounded numerically and they grow unstably (see second experiment in Figure 4.6). In the third experiment, horizontal diffusion is added ($\kappa = 10\ \mathrm{m^2\ s^{-1}}$), which drastically reduces the deviations at the surface. Since the largest deviations are typically confined within the upper layers of the domain, they could be alleviated by choosing an appropriate diffusion coefficient.

To quantify to which extent consistency is lost, we may compute the following a posteriori estimate

$$ce = \sqrt{\frac{\int_{\Omega^h} \left(C^h - 1\right)^2 \mathrm{d}\Omega}{V}} \tag{4.39}$$

where V is the domain volume. In Figure (4.7), values of ce are plotted against the element size when the model is run in the same configuration as that considered previously (a 10 km by 10 km, 20 m deep, square basin starting with a 2 m high Gaussian). The mesh is refined in the horizontal only, which is the direction where consistency is lost. The rate of convergence is nearly quadratic.

89

a   b   c

10 km × 10 km   100 km × 100 km   1000 km × 1000 km

20 m deep   200 m deep   2000 m deep

$\mathcal{O}(\eta/d) = 10^{-1}$ $\mathcal{O}(\eta/d) = 10^{-2}$ $\mathcal{O}(\eta/d) = 10^{-3}$

1000 time steps ($\Delta t = 72$s)   1000 time steps ($\Delta t = 720$s)   1000 time steps ($\Delta t = 7200$s)

Figure 4.8: The above panels show the deviation of the tracer concentration at the surface of the domain. The tracer is initially set to 1 throughout te domain and should remain equal to 1 at all time. (a) Shelf scale: contour drawn for deviations of -20 and 20. (b) Intermediate scale: contour drawn for deviations of -0.005 and 0.005. (c) Basin scale: contour drawn for deviations of -0.001 and 0.001. The corresponding simulation features are given below each panel. The initial elevation field is a 2-meter high Gaussian.
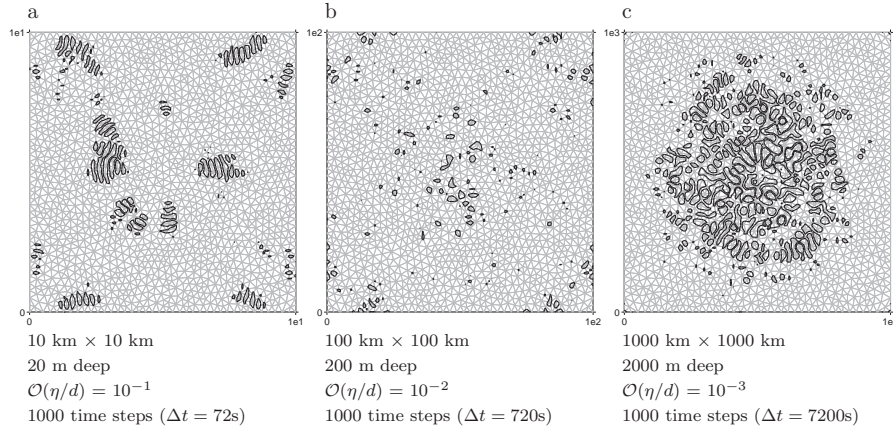
Finally, in Figure (4.8), similar experiments (without diffusion) are carried out on domains with spatial scales ranging from 10 km (shelf scale) to 1000 km (basin scale) with increasing depths, yet setting off all experiments with the same 2 m high Gaussian (the parameters of the simulation are recalled in the figure). These runs were carried out in an attempt at getting some insights on the effect of a consistency breakdown on flows spanning a wide range of spatial scales. As we have already seen, the consequences are quite dramatic for the smallest domain (which is the same experiment as that corresponding to the middle panel of Figure 4.6). For larger domains, the surface deviations remain below one percent. Since the deviations of the tracer are caused by the inconsistent treatment of the the advection terms, it might be expected that as soon as those terms grow larger in magnitude, those deviations will increase. For the small domain, the flow speed is on the order of 0.3 m s^{-1} while it decreases to roughly 0.08 m s^{-1} and 0.01 m s^{-1} for the intermediate and larger domains, respectively. If we set the order of magnitude of the advection terms to 1 for the small domain, advection has a relative magnitude of 7×10^{-3} and 10^{-5} for the intermediate and larger domains, respectively. This sheds light on the results obtained in Figure (4.8). It could be argued that for such weak barotropic flows in large domains, the inconsistency is not problematic and could be easily tackled by adding some horizontal diffusion. For the larger-scale basin circulations, advection is typically quite small in most of the domain (the Rossby number is typically on the order of 10^{-3}). However, in those regions where advection becomes important (typically where boundary currents prevail), severe inconsistencies might arise, leading to unphysical effects. Finally, modeling flows in coastal and shelf regions where advection is dominant definitely requires to use a consistent spatial scheme. Failing to do that may not only generate spurious currents but also numerical instabilities.

90

4.4 Conclusions

In this chapter, we have synthesized sufficient conditions in terms of the finite element spatial discretization of a three-dimensional, hydrostatic, free-surface, marine model to consistently conserve any tracer globally. A consistent (or discretely compatibility) spatial scheme is defined as one that maintains the uniform tracer concentration set initially (when there is no boundary flux and no source/sink term). The following conditions must be fulfilled to satisfy those properties. (i) The same interpolation must be used in the horizontal for the elevation, the vertical velocity and the tracer. (ii) The same interpolation in the vertical must be used for the vertical velocity and the tracer. (iii) The mesh update procedure must satisfy the Discrete Geometric Conservation Law. (iv) The mesh velocity at the surface must be equal to $\frac{\partial \eta}{\partial t}$. These considerations must be complemented by the necessity of choosing a stable finite-element pair for the primitive shallow-water equations.

Several numerical experiments were carried out to show the model's ability at responding to freshwater forcing. In particular, we showed how the variation in the domain volume naturally leads to dilution and concentration of salt. We finally performed a series of experiments in which consistency between the vertical velocity and the concentration was deliberately broken down. If consistency must be ensured for advection-dominated flows typical in coastal and shelf regions, it was shown that using an inconsistent scheme for larger-scale application could be a viable alternative. However, even for those problems, diffusion-based remedies could not work out in regions where advection becomes more important (e.g., boundary currents regions).

Chapter 5

A three-dimensional finite element marine model

Summary

The full three-dimensional model is presented. An in-depth description of the spatial discretization of the momentum equation is given. The time-stepping algorithm is detailed. The model is validated against an analytical solution and against a realistic flow around a shallow-water island for which field measurements are available.

The full three-dimensional model is presented in this chapter, which is written to be self-contained. In that respect, all equations are presented as well as their finite element discretization. Unlike Chapter 4, which addresses conservation issues within a general framework, the current chapter details the model for a given choice of elements, namely those depicted in Figure (4.3). The horizontal velocity is linear non-conforming in the horizontal and linear discontinuous in the vertical. The vertical velocity is linear continuous in the horizontal and linear discontinuous in the vertical. The elevation is linear continuous. Since the elevation and continuity equations have been given more focus in the previous chapter, an in-depth coverage of the momentum equation is considered in this chapter.

5.1   Governing equations

The equations will be formulated in a Cartesian framework, with the assumptions of constant fluid density (ρ_o) and under the hydrostatic approximation. The spatial coordinates are x, y and z and the three-dimensional velocity components are u, v and w, respectively. We also define $\mathbf{u} = (u, v)$ to be the horizontal velocity vector. The free-surface elevation (η) is defined with respect to the constant reference height $z = 0$ taken to be the mean sea level. The main notations are given in Figure (4.1). With these assumptions, the horizontal components of the three-dimensional momentum

equation read:

$$\frac{\partial \mathbf{u}}{\partial t} + \boldsymbol{\nabla} \cdot (\mathbf{uu}) + \frac{\partial}{\partial z}(w\mathbf{u}) + f\mathbf{e}_z \wedge \mathbf{u} = -g\boldsymbol{\nabla}\eta + \mathbf{D} + \frac{\partial}{\partial z}\left(\nu_z\frac{\partial \mathbf{u}}{\partial z}\right), \quad (5.1)$$

where f is the Coriolis parameter, $\mathbf{e}_z$ is the upward-pointing unit vector, g is the gravitational acceleration, ν_z is the vertical eddy viscosity coefficient and $\boldsymbol{\nabla}$ is the horizontal gradient operator. Horizontal momentum diffusion is parameterized by $\mathbf{D}$. Equation (5.1) is complemented with the continuity equation

$$\boldsymbol{\nabla}\cdot\mathbf{u} + \frac{\partial w}{\partial z} = 0, \quad (5.2)$$

and the free-surface evolution equation

$$\frac{\partial \eta}{\partial t} + \boldsymbol{\nabla}\cdot\left(\int_{-d}^{\eta}\mathbf{u}\,dz\right) = 0, \quad (5.3)$$

where d is the local unperturbed depth so that the total layer thickness is defined as $H(x,y,t) = d(x,y) + \eta(x,y,t)$.

The momentum horizontal diffusion term $\mathbf{D}$ and the vertical diffusion term both parameterize the effect of unresolved, small-scale processes on the resolved scales (*Blumberg and Mellor*, 1987; *Griffies and Hallberg*, 2000). However, momentum horizontal diffusion is generally employed both for physical parameterization and to ensure numerical stability (*Griffies and Hallberg*, 2000; *Griffies et al.*, 2000). With unstructured meshes, it is not uncommon to have the mesh size vary by up to two orders of magnitude between different parts of the domain (e.g., *Foreman et al.*, 1995; *Legrand et al.*, accepted, 2006). The range of unresolved scales thus varies widely within the domain of interest, which motivates the use of a nonconstant viscosity coefficient (ν_h). The Smagorinsky viscosity (*Smagorinsky*, 1963) is a function of the local horizontal rate of deformation times the local mesh size. In our model, the following expression is used:

$$\nu_h = c_s\Delta^2\left(\boldsymbol{\epsilon}:\boldsymbol{\epsilon}\right)^{1/2}, \quad (5.4)$$

where c_s is a nondimensional constant, Δ is the local mesh size and $\boldsymbol{\epsilon}$ is the two-dimensional strain-rate tensor expressed in terms of the depth-averaged horizontal velocity $\bar{\mathbf{u}} = (\bar{u}, \bar{v})$:

$$\boldsymbol{\epsilon} = \begin{bmatrix} \frac{\partial \bar{u}}{\partial x} & \frac{1}{2}\left(\frac{\partial \bar{u}}{\partial y} + \frac{\partial \bar{v}}{\partial x}\right) \\ \frac{1}{2}\left(\frac{\partial \bar{v}}{\partial x} + \frac{\partial \bar{u}}{\partial y}\right) & \frac{\partial \bar{v}}{\partial y} \end{bmatrix}. \quad (5.5)$$

For triangular meshes, Δ^2 is taken to be the surface area of the triangle (*Akin et al.*, 2003). A Laplacian form is considered for the momentum friction term $\mathbf{D}$:

$$\mathbf{D} = \frac{\partial}{\partial x}\left(\nu_h\frac{\partial \mathbf{u}}{\partial x}\right) + \frac{\partial}{\partial y}\left(\nu_h\frac{\partial \mathbf{u}}{\partial y}\right). \quad (5.6)$$

The Smagorinsky scheme enhances momentum diffusion in regions of large horizontal shear while reducing it in regions of smaller mesh spacing (Figure 5.1). Enhanced
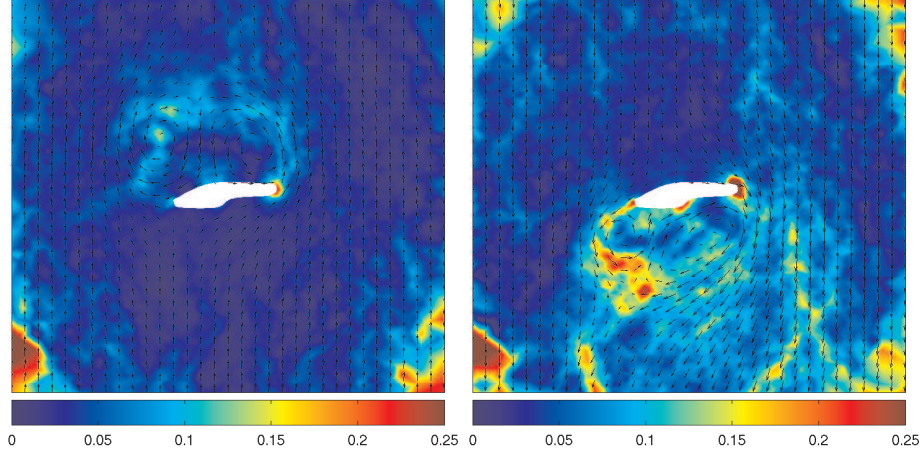
Figure 5.1: Horizontal viscosity coefficient ν_h [m² s⁻¹] at ebb (left panel) and flood (right panel) on the intermediate mesh of Figure (5.6). Notice the larger values in regions of high velocity shear in the island's wake where eddies form and in regions characterized by a lower mesh resolution.

versions of the model should consider the strain-rate tensor used in Eq. (5.4) defined in terms of the local velocity, which is more appropriate for baroclinic flows that may be characterized by large shears in the vertical. The advantage of defining (5.4) in terms of the depth-averaged velocity is that it allows part of the depth-averaged diffusion term to be time stepped in the equations for the external mode, rather than diffusion entering the external mode as a coupling term only. This enhances the numerical stability of the external mode.

Similar to *Fischer et al.* (1979) and *Deleersnijder et al.* (1992), for unstratified shallow seas, the vertical eddy viscosity is defined as

$$\nu_z = \kappa u_* \left(d + z\right) \left(1 - 0.6 \frac{d + z}{H}\right),$$ (5.7)

where κ is the von Karman constant and u_* is the bottom friction velocity, which obeys the following equality

$$u_*^2 = \frac{\|\boldsymbol{\tau}\|}{\rho_o}.$$ (5.8)

In the right-hand side of (5.8), $\|\cdot\|$ is the Euclidian norm and $\boldsymbol{\tau}$ denotes the constant bottom stress. The latter is parameterized by the following logarithmic law:

$$\boldsymbol{\tau}(x, y, \xi_b)/\rho_0 = \left[\frac{\kappa}{\ln(\xi_b/\xi_0)}\right]^2 \|\mathbf{u}_b(x, y, \xi_b)\|\mathbf{u}_b(x, y, \xi_b),$$ (5.9)

in which ξ_b is the distance to the seabed where the appropriate bottom velocity $\mathbf{u}_b$ is defined and ξ_0 is the roughness length. It should be pointed out that this turbulence

closure remains very simple. It was however designed for unstratified, shallow seas (*Fischer et al.*, 1979) and we believe it can be employed for modeling the flow around Rattray island, which lies in well-mixed water (*Wolanski et al.*, 1984) and consists of the main application presented in this chapter.

5.2 Boundary conditions

Although most boundary conditions depend on the physical context, some of them remain invariant. The horizontal velocity $\mathbf{u}$ is subject to a condition of no normal flow and full slip on the closed lateral boundary Γ_n:

$$\mathbf{u} \cdot \mathbf{n} = 0 \quad \text{and} \quad \nu_h \frac{\partial \mathbf{u}}{\partial n} = 0 \quad \text{on} \quad \Gamma_n, \tag{5.10}$$

where $\frac{\partial \mathbf{u}}{\partial n}$ is the normal derivative of $\mathbf{u}$, defined as

$$\frac{\partial \mathbf{u}}{\partial n} = \frac{\partial \mathbf{u}}{\partial x} n_x + \frac{\partial \mathbf{u}}{\partial y} n_y, \tag{5.11}$$

with n_x and n_y the x and y components, respectively, of the three-dimensional outward-pointing unit normal to $\partial \Omega$. Note that we could also assume partial slip along the lateral boundaries, amounting to a loss of momentum through lateral stress. At the bottom, a slip condition is enforced on the horizontal velocity by relating the bottom momentum flux to the bottom velocity:

$$\nu_h \frac{\partial \mathbf{u}}{\partial n} + \nu_z \frac{\partial \mathbf{u}}{\partial z} = \frac{\boldsymbol{\tau}}{\rho_0} \quad \text{on} \quad \Gamma_b, \tag{5.12}$$

where $\boldsymbol{\tau}/\rho_0$ is given by (5.9). At the free surface, the wind stress may be taken into account:

$$\nu_h \frac{\partial \mathbf{u}}{\partial n} + \nu_z \frac{\partial \mathbf{u}}{\partial z} = \frac{\boldsymbol{\tau}^s}{\rho_0} \quad \text{on} \quad \Gamma_s, \tag{5.13}$$

where $\boldsymbol{\tau}^s$ is the surface wind stress. For the vertical velocity, we have the usual kinematic boundary condition at the bottom

$$w = -\mathbf{u} \cdot \boldsymbol{\nabla} h \quad \text{on} \quad \Gamma_b \tag{5.14}$$

and top

$$w = \frac{\partial \eta}{\partial t} + \mathbf{u} \cdot \boldsymbol{\nabla} \eta \quad \text{on} \quad \Gamma_s, \tag{5.15}$$

or, equivalently (4.6) and (4.7). The open boundary conditions depend on the problem at hand and usually involve prescribing the normal velocity and/or a linear combination of the normal velocity and the elevation such as a radiation condition. For the sake of simplicity, we will not deal with open boundary conditions in the discussion that follows.

5.3 Numerical procedure

In this section, we describe the numerical technique used to solve the equations presented above. The mesh topology has already been described in Section 4.2.1 and Appendix C.1 and will not be reproduced here. There is no a priori constraint on the location of vertical nodes but we currently require that two adjacent columns comprise the same number of prisms. Hence, the three-dimensional mesh contains the same number of layers throughout. This constraint could be relaxed in the future by allowing adjacent columns to contain different number of prisms, the transition being assured by non-conforming prisms (e.g., with hanging nodes). All nodes are free to move in the vertical, which allows for tracking the free surface and preventing the occurrence of overly thin layers near the surface by vertical redistribution of the nodes. By permitting such freedom in the mesh motion, we implicitly allow for the use of generalized vertical coordinate systems (e.g., *Kasahara*, 1974; *Deleersnijder and Ruddick*, 1989; *Gerdes*, 1993; *Adcroft and Hallberg*, 2006; *Song and Hou*, 2006).

5.3.1 Variational statements

The variational statements will be written for the elements depicted in Figure (4.3), which are those suggested in Chapter 4. The horizontal velocity is linear and non-conforming in the horizontal and linear discontinuous in the vertical. The elevation is linear continuous. The vertical velocity is linear in all directions, but continuous in the horizontal (to be compatible with the elevation) and discontinuous in the vertical. The variational statements involve integration over mesh geometrical items in two and three dimensions. The notations (4.16) are used.

Momentum Equation

Since the mesh is allowed to move in the vertical, we write the ALE (Arbitrary Lagrangian-Eulerian) form for the variational statement of the momentum equation. The derivation is similar to that giving rise to the ALE form of the tracer equation, Eq. (4.23) in Chapter 4. For the momentum equation (5.1), the variational statement consists in finding $\mathbf{u}(x, y, z, t) \in \mathcal{U} \times \mathcal{U}$ such that

$$\sum_{e=1}^{N_p} \frac{\mathrm{d}}{\mathrm{d}t} \int_{\Omega_e(t)} \mathbf{u} \cdot \hat{\mathbf{u}} \, \mathrm{d}\Omega + \sum_{e=1}^{N_p} \int_{\Omega_e(t)} \left[\boldsymbol{\nabla} \cdot (\mathbf{u}\mathbf{u}) + \frac{\partial}{\partial z} (\tilde{w}\mathbf{u}) + f\mathbf{e}_z \wedge \mathbf{u} \right.$$
$$\left. + g\boldsymbol{\nabla}\eta - \mathbf{D} - \frac{\partial}{\partial z} \left(\nu_z \frac{\partial \mathbf{u}}{\partial z} \right) \right] \cdot \hat{\mathbf{u}} \, \mathrm{d}\Omega = 0 \quad \forall \hat{\mathbf{u}} \in \mathcal{U} \times \mathcal{U}, \tag{5.16}$$

where $\mathcal{U} \times \mathcal{U}$ is the suitable infinite-dimensional Sobolev space such that $\mathcal{U} = \mathcal{H}^1(\Omega^h)$. A definition of this functional space is given in Appendix C.2. The test function $\hat{\mathbf{u}}$ belongs to $\mathcal{U} \times \mathcal{U}$ and is sufficiently well behaved that the integrals in (5.16) make sense. The vertical velocity is modified to take into account the mesh motion so that vertical advection is relative to the moving mesh: $\tilde{w} = w - w_m$, where w_m is the mesh velocity, defined by Eq. (4.22).

Because the horizontal velocity is discontinuous, it is convenient to further manipulate the variational statement of the momentum equation (5.16) so that interelement boundary terms appear. This also permits to naturally enforce the boundary conditions (5.10)-(5.13). To do so, the horizontal advection term and all diffusion terms may be integrated by parts, which gives rise to

$$
\sum_{e=1}^{N_p} \frac{\mathrm{d}}{\mathrm{d}t} \int_{\Omega_e(t)} \mathbf{u} \cdot \hat{\mathbf{u}} \, \mathrm{d}\Omega + \sum_{e=1}^{N_p} \int_{\Omega_e(t)} \left[-\mathbf{u} \cdot (\mathbf{u} \cdot \boldsymbol{\nabla} \hat{\mathbf{u}}) - \tilde{w} \mathbf{u} \cdot \frac{\partial \hat{\mathbf{u}}}{\partial z} \right.
$$

$$
\left. + (f \hat{\mathbf{e}}_z \wedge \mathbf{u}) \cdot \hat{\mathbf{u}} + g \boldsymbol{\nabla} \eta \cdot \hat{\mathbf{u}} + \nu_h \frac{\partial \mathbf{u}}{\partial x} \cdot \frac{\partial \hat{\mathbf{u}}}{\partial x} + \nu_h \frac{\partial \mathbf{u}}{\partial y} \cdot \frac{\partial \hat{\mathbf{u}}}{\partial y} + \nu_z \frac{\partial \mathbf{u}}{\partial z} \cdot \frac{\partial \hat{\mathbf{u}}}{\partial z} \right] \mathrm{d}\Omega
$$

$$
\underbrace{ - \int_{\Gamma_s^h \cup \Gamma_b^h} \hat{\mathbf{u}} \cdot \left(\nu_h \frac{\partial \mathbf{u}}{\partial n} + \nu_z \frac{\partial \mathbf{u}}{\partial z} n_z \right) \mathrm{d}\tau }_{1} + \underbrace{ \int_{\Gamma_s^h \cup \Gamma_b^h} (\mathbf{u} \cdot \mathbf{n} + \tilde{w} n_z) \mathbf{u} \cdot \hat{\mathbf{u}} \, \mathrm{d}\tau }_{2}
$$

$$
+ \underbrace{ \int_{\Gamma_n^h} \left((\mathbf{u} \cdot \mathbf{n}) \mathbf{u} - \nu_h \frac{\partial \mathbf{u}}{\partial n} \right) \cdot \hat{\mathbf{u}} \, \mathrm{d}\Gamma }_{3} + \underbrace{ \sum_{e=1}^{N_f} \int_{F_e} < \mathbf{u} \cdot \mathbf{n}^e > < \mathbf{u} >_\lambda \cdot [\hat{\mathbf{u}}] \, \mathrm{d}\Gamma }_{4}
$$

$$
+ \underbrace{ \sum_{e=1}^{N_s} \int_{S_e} < \mathbf{u} \cdot \mathbf{n}^e + w n_z^e > < \mathbf{u} >_\lambda \cdot [\hat{\mathbf{u}}] \, \mathrm{d}\tau }_{5}
$$

$$
- \underbrace{ \sum_{e=1}^{N_s} \int_{S_e} \left\langle \nu_h \frac{\partial \mathbf{u}}{\partial n} + \nu_z \frac{\partial \mathbf{u}}{\partial z} n_z^e \right\rangle \cdot [\hat{\mathbf{u}}] \, \mathrm{d}\tau }_{6}
$$

$$
+ \underbrace{ \sum_{e=1}^{N_s} \int_{S_e} \sigma[\mathbf{u}] \cdot [\hat{\mathbf{u}}] \, \mathrm{d}\tau }_{7} = 0 \quad \forall \hat{\mathbf{u}} \in \mathcal{U} \times \mathcal{U},
$$

(5.17)

where the diffusion terms have been spelled out for clarity and all seven underbraced integrals (labeled 1 to 7) arise after integration by parts of either the advection or diffusion terms. These terms are explained hereafter.

1. The first integral is an expression of the diffusive momentum flux through the sea bottom and sea surface. Use can be made of boundary conditions (5.12)-(5.13) to compute the integral.

2. The second integral expresses the advective fluxes of momentum through the sea bottom and sea surface. Since those interfaces are impermeable, this integral is discarded. In light of Chapter 4, we may ask ourselves whether this integral automatically vanishes when we set $\mathbf{u} = 1$, in which case discarding this integral is consistent. However, this will be the case only if the spatial discretization used for the horizontal velocity is discretely compatible with that used for the elevation and vertical velocity. For reasons of numerical stability,

this is not the case[1]. In other words, the momentum equation does not inherit the properties of consistency derived for the tracer equation in Chapter 4.

3. The third integral comprises both the diffusive and advective momentum fluxes through the closed lateral boundary. This term vanishes with the enforcement of boundary condition (5.10). Note that any condition of partial slip could be naturally enforced by computing this integral, given an expression for $\nu_h \partial \mathbf{u}/\partial n$.

4. The terms labeled 4 and 5 arise by assembling all contributions of interelement boundary integrals from advection terms. Each one of the N_f integrals is an expression of the momentum flux by advection through the vertical face shared by two adjacent prisms. Similarly, each one of the N_s integrals is the advective flux through triangular faces shared by prisms stacked upon each other. Using the same notations as *Hanert et al.* (2004), we note $< f >$ the mean value of f on any face shared by two adjacent prisms and $< f >_\lambda$, its weighted average. That is,

$$ < f > = \frac{1}{2} f_{|\Omega_e} + \frac{1}{2} f_{|\Omega_f}, \quad < f >_\lambda = \left(\frac{1}{2} + \lambda \right) f_{|\Omega_e} + \left(\frac{1}{2} - \lambda \right) f_{|\Omega_f}, $$

for all three-dimensional elements Ω_e and Ω_f sharing a common face. The jump across the latter is noted $[f]$ and is defined by

$$ [f] = f_{|\Omega_e} - f_{|\Omega_f}, $$

with $f_{|\Omega_e}$ being the restriction of f on Ω_e. Note that the quantity being advected is $< \mathbf{u} >_\lambda$. In expression (5.18), the adjustable parameter $\lambda \in [-1/2, 1/2]$ allows for orienting the flux. In particular, taking $\lambda = \frac{1}{2} \text{sign}(\mathbf{u} \cdot \mathbf{n})$ is equivalent to an upwind-biased flux. This advection scheme was shown by *Hanert et al.* (2004) to be particularly effective in two dimensions. Here, we generalize it in three dimensions.

5. The terms labeled 6 and 7 (involving integrals over triangular faces shared by stacked prisms) originate from the integration by parts of the momentum diffusion term. *Hanert et al.* (2004) showed that the non-conforming nature of the interpolation in the horizontal ensures that no boundary term needs be computed across vertical faces as far as momentum diffusion is concerned. The sixth sum involves integrals of centered diffusive fluxes. There is no preferred orientation associated to it. The seventh term is a weak continuity constraint and involves the discontinuity-penalization parameter σ while solving problems that are not purely hyperbolic (*Houston et al.*, 2002). The expression for σ is proportional to the diffusivity coefficients.

To summarize, by discarding integrals 2, 3 and by using the boundary conditions (5.12) and (5.13) to compute integral 1, the variational statement for the momentum

---

[1]This is so because the element used for the horizontal velocity is P_1^{NC}.

equation reduces to

$$
\sum_{e=1}^{N_p} \frac{\mathrm{d}}{\mathrm{d}t} \int_{\Omega_e(t)} \mathbf{u} \cdot \hat{\mathbf{u}} \, \mathrm{d}\Omega + \sum_{e=1}^{N_p} \int_{\Omega_e(t)} \left[-\mathbf{u} \cdot (\mathbf{u} \cdot \boldsymbol{\nabla}\hat{\mathbf{u}}) - \tilde{w}\mathbf{u} \cdot \frac{\partial \hat{\mathbf{u}}}{\partial z} \right.
$$
$$
\left. + (f\hat{\mathbf{e}}_z \wedge \mathbf{u}) \cdot \hat{\mathbf{u}} + g\boldsymbol{\nabla}\eta \cdot \hat{\mathbf{u}} + \nu_h \frac{\partial \mathbf{u}}{\partial x} \cdot \frac{\partial \hat{\mathbf{u}}}{\partial x} + \nu_h \frac{\partial \mathbf{u}}{\partial y} \cdot \frac{\partial \hat{\mathbf{u}}}{\partial y} + \nu_z \frac{\partial \mathbf{u}}{\partial z} \cdot \frac{\partial \hat{\mathbf{u}}}{\partial z} \right] \mathrm{d}\Omega
$$
$$
- \int_{\Gamma_s^h} \hat{\mathbf{u}} \cdot \frac{\boldsymbol{\tau}^s}{\rho_0} n_z \, \mathrm{d}\tau - \int_{\Gamma_b^h} \hat{\mathbf{u}} \cdot \frac{\boldsymbol{\tau}}{\rho_0} n_z \, \mathrm{d}\tau
$$
$$
+ \sum_{e=1}^{N_f} \int_{F_e} <\mathbf{u} \cdot \mathbf{n}^e> <\mathbf{u}>_\lambda \cdot [\hat{\mathbf{u}}] \, \mathrm{d}\Gamma
$$
$$
+ \sum_{e=1}^{N_s} \int_{S_e} <\mathbf{u} \cdot \mathbf{n}^e + w n_z^e> <\mathbf{u}>_\lambda \cdot [\hat{\mathbf{u}}] \, \mathrm{d}\tau
$$
$$
- \sum_{e=1}^{N_s} \int_{S_e} \left\langle \nu_h \frac{\partial \mathbf{u}}{\partial n} + \nu_z \frac{\partial \mathbf{u}}{\partial z} n_z^e \right\rangle \cdot [\hat{\mathbf{u}}] \, \mathrm{d}\tau
$$
$$
+ \sum_{e=1}^{N_s} \int_{S_e} \sigma[\mathbf{u}] \cdot [\hat{\mathbf{u}}] \, \mathrm{d}\tau = 0 \quad \forall \hat{\mathbf{u}} \in \mathcal{U} \times \mathcal{U}.
$$

(5.18)

In the statement above, the surface integral on Γ_s^h (Γ_b^h) is positive (negative) because n_z is positive (negative) there. This respectively corresponds to a positive influx of momentum due to wind stress and a negative influx due to bottom stress. It is worth mentioning that in Eq. (5.17), boundary integrals 5 to 7 are the only means by which information is conveyed in the vertical between elements. These integrals need not be calculated in case a continuous representation is resorted to in the vertical. For flows that do not feature strong vertical shears, a continuous representation is likely the most cost-effective choice. Yet, for baroclinic flows, the shear in the vertical may be large and a discontinuous representation may be more optimal, especially if the mesh resolution is low in the vertical.

Free-surface equation

For the free-surface equation (5.3), the variational statement, which is the same as that derived in Chapter 4, consists in finding $\eta(x,y,t) \in \mathcal{H}$ such that

$$
\int_{\mathcal{T}^h} \frac{\partial \eta}{\partial t} \hat{\eta} \, d\tau - \int_{\Omega^h} \mathbf{u} \cdot \boldsymbol{\nabla}\hat{\eta} \, d\Omega = 0 \quad \forall \hat{\eta} \in \mathcal{H}, \tag{5.19}
$$

where $\mathcal{H}$ is the Sobolev space $\mathcal{L}_2(\mathcal{T}^h)$, defined in Appendix C.2.

Continuity Equation

The variational statement for the continuity equation (5.2) is readily obtained by considering the variational statement derived in Appendix C.1 for a discontinuous representation in all directions. With the element chosen for the vertical velocity, the

interpolation is continuous in the horizontal so that the third term of Eq. (C.4) simply vanishes, giving rise to

$$-\sum_{e=1}^{N_p} \int_{\Omega_e} \left(\mathbf{u} \cdot \boldsymbol{\nabla}\hat{w} + w\frac{\partial \hat{w}}{\partial z} \right) \mathrm{d}\Omega + \int_{\Gamma_s^h} \hat{w} \left(\mathbf{u} \cdot \mathbf{n} + wn_z \right) \mathrm{d}\tau$$
$$+\sum_{e=1}^{N_s} \int_{S_e} \langle \mathbf{u} \cdot \mathbf{n}^e \rangle \, [\hat{w}] \, \mathrm{d}\tau + \sum_{e=1}^{N_s} \int_{S_e} [\hat{w}] \, w_{|\Omega_e} \, n_z^e \mathrm{d}\tau = 0 \quad \forall \hat{w} \in \mathcal{W}.$$

(5.20)

5.3.2 Space discretization

Finite element approximations to Eqs (5.18)-(5.20) can be obtained by substituting $\mathbf{u}$, η and w for their respective approximations $\mathbf{u}^h$, η^h and w^h. Those approximate fields belong to finite-dimensional subspaces $\mathcal{U}^h \times \mathcal{U}^h \subset \mathcal{U} \times \mathcal{U}$, $\mathcal{H}^h \subset \mathcal{H}$ and $\mathcal{W}^h \subset \mathcal{W}$, respectively. We have

$$\mathbf{u} \quad \simeq \mathbf{u}^h = \sum_{j=1}^{N_u} \mathbf{U}_j(t)\psi_j^u(x,y,z),$$

$$\eta \quad \simeq \eta^h = \sum_{j=1}^{N_\eta} H_j(t)\psi_j^\eta(x,y),$$

(5.21)

$$w \quad \simeq w^h = \sum_{j=1}^{N_w} W_j(t)\psi_j^w(x,y,z),$$

where $\mathbf{U}_j$, H_j and W_j are the time-dependent nodal values and ψ_j^u, ψ_j^η and ψ_j^w are the associated polynomial basis functions. Finally, the nodal values are computed by resorting to the Galerkin method, which comes down to substituting the test functions $\hat{\mathbf{u}}$, $\hat{w}$ and $\hat{\eta}$ for $\psi_i^u \hat{e}_x + \psi_i^u \hat{e}_y$, ψ_i^w and ψ_i^η in (5.18) for $i = 1 \dots N_u$, in (5.19) for $i = 1 \dots N_\eta$ and in (5.20) for $i = 1 \dots N_w$, respectively.

5.3.3 Time-stepping algorithm

In order to lighten the notations, it is preferable to carry out the time discretization of Eqs (5.1) and (5.3) rather than their space-discretized counterparts. Since the vertical velocity is computed diagnostically, we shall not treat the continuity equation (5.2) here. Once time discretization is performed, it is straightforward to achieve discretization in space of the semi-discrete equations by following the procedure described in the previous section.

The most fundamental choice that we make in this model regarding the time discretization is to resolve all processes with the same time step. In order to circumvent the stability constraint incurred by the propagation of inertia-gravity waves, a semi-implicit or implicit (or any level of implicitness in between) free-surface method is required (*Dukowicz and Smith*, 1994). Hence, Eqs (5.1) and (5.3) must be solved

simultaneously for $(\mathbf{u}^{n+1}, \eta^{n+1})$, which leads to

$$
\begin{aligned}
\frac{\mathbf{u}^{n+1} - \mathbf{u}^n}{\Delta t} + \boldsymbol{\nabla} \cdot (\mathbf{u}^n \mathbf{u}^n) + \frac{\partial}{\partial z}(w^n \mathbf{u}^n) + f \hat{\mathbf{e}}_z \wedge \mathbf{u}^{n+\theta} \\
+ g \boldsymbol{\nabla} \eta^{n+\theta} - \mathbf{D}^n - \frac{\partial}{\partial z}\left(\nu_z^n \frac{\partial \mathbf{u}^{n+1}}{\partial z} \right) = 0,
\end{aligned}
\tag{5.22}
$$

for the momentum equation and

$$
\frac{\eta^{n+1} - \eta^n}{\Delta t} + (1-\theta)\boldsymbol{\nabla} \cdot \int_{-d}^{\eta^n} \mathbf{u}^n \, \mathrm{d}z + \theta \boldsymbol{\nabla} \cdot \int_{-d}^{\eta^{n+1}} \mathbf{u}^{n+1} \, \mathrm{d}z = 0, \tag{5.23}
$$

for the free-surface equation. In (5.22) and (5.23), Δt is the time step and

$$
g^{n+\theta} = \theta g^{n+1} + (1-\theta)g^n,
$$

where $0.5 \leq \theta \leq 1.0$. The choice $\theta = 0.5$ yields a semi-implicit scheme while $\theta = 1$ leads to an implicit scheme. Unless otherwise stated, we consider a Crank-Nicolson (CN) scheme ($\theta = 0.5$). This scheme is strictly energy-conserving for the propagation of linear inertia-gravity waves. In Eq. (5.22), the advection and horizontal diffusion terms are explicit in time while the vertical diffusion term is implicit (with the vertical eddy viscosity coefficient taken at the previous time step). The second integral in Eq. (5.23) can be split into an integral over the depth at time step n and an integral over the change in depth. Neglecting the latter, we simply obtain

$$
\frac{\eta^{n+1} - \eta^n}{\Delta t} + (1-\theta)\boldsymbol{\nabla} \cdot \int_{-d}^{\eta^n} \mathbf{u}^n \, \mathrm{d}z + \theta \boldsymbol{\nabla} \cdot \int_{-d}^{\eta^n} \mathbf{u}^{n+1} \, \mathrm{d}z = 0. \tag{5.24}
$$

In most applications, it is safe to neglect the nonlinear coupling term between the elevation at time step $n + 1$ and velocity at time step $n + 1$ because $\eta \ll h$. However, doing so was shown by *Hodges* (2004) to reduce the formal accuracy of the CN discretization to first-order in time. *Hodges* (2004) proposes to add a correction term to restore second-order accuracy but also shows that the accuracy order of the CN scheme degrades to first-order in time when the Courant-Friedrichs-Lewy (CFL) number is greater than unity and whether or not the correction term is added. For typical time and space scales in ocean modeling, the CFL number associated with surface gravity waves is far greater than unity and the CN accuracy reduces to first-order in time. We therefore chose to neglect the nonlinear coupling term in Eq. (5.24).

The solution $(\mathbf{u}^{n+1}, \eta^{n+1})$ can be found by solving the coupled system (5.22)-(5.24) involving the nodal values $(\mathbf{U}^{n+1}, H^{n+1})$. For large-scale applications, the computational overhead incurred by the resolution of this system becomes quickly unbearable. This is even more so considering the mesh is moving and the left-hand matrix of the system must be recomputed at each time step. A huge gain in performance may be obtained by splitting the dynamics into a two-dimensional depth-averaged system for the evolution of the inertia-gravity waves and a three-dimensional system for the vertical structure of the velocity (e.g., *Simons*, 1974; *Blumberg and Mellor*, 1987; *Killworth et al.*, 1991). Those systems are sometimes called external and internal modes, respectively.

The external mode equations are the traditional shallow-water equations, obtained by integrating the momentum equation (5.1) over depth and coupling the result with the free-surface equation (5.3) written in terms of the depth-averaged velocity $\overline{\mathbf{u}}$:

$$\frac{\partial \overline{\mathbf{u}}}{\partial t} + f\hat{\mathbf{e}}_z \wedge \overline{\mathbf{u}} + g\boldsymbol{\nabla}\eta = \mathbf{B}, \tag{5.25}$$

$$\frac{\partial \eta}{\partial t} + \boldsymbol{\nabla} \cdot (H\overline{\mathbf{u}}) = 0, \tag{5.26}$$

where $\mathbf{B}$ regroups the forcing and coupling terms originating from depth-integration of advection and diffusion terms (see Appendix D). It is important to note that some of these terms may be expressed in terms of the depth-averaged velocity – i.e., in terms of prognostic variables – and therefore can be time stepped with the left-hand side of (5.25). However, it remains unclear which terms should be time stepped and which terms should act as depth-averaged, forcing terms. It is context-dependent and, in this study, advection and horizontal diffusion are time stepped. The finite element resolution of the shallow-water equations is well documented (*Le Roux et al.*, 1998, 2000; *Hanert et al.*, 2003, 2005) and will not be reproduced here. We use the scheme proposed by *Hanert et al.* (2005). In particular, the nodal values of the depth-averaged velocity are located at the middle of the edges joigning elevation nodes. So, the depth-averaged velocity is interpolated with the so-called P_1^{NC} element (*Hua and Thomasset*, 1984). Note that this choice is coherent with the location of nodes for the three-dimensional horizontal velocity (see Figure 4.3). A theta-scheme applied to Eqs (5.25)-(5.26) gives the following time discretization

$$\frac{\overline{\mathbf{u}}^{n+1} - \overline{\mathbf{u}}^n}{\Delta t} + f\hat{\mathbf{e}}_z \wedge \overline{\mathbf{u}}^{n+\theta} + g\boldsymbol{\nabla}\eta^{n+\theta} = \mathbf{B}^n, \tag{5.27}$$

$$\frac{\eta^{n+1} - \eta^n}{\Delta t} + \boldsymbol{\nabla} \cdot \left(H^n \overline{\mathbf{u}}^{n+\theta}\right) = 0. \tag{5.28}$$

It is worth noticing that, unlike *Hanert et al.* (2005), Eq. (5.28) is not time stepped with a leap-frog scheme. The latter is to be avoided due to the existence of computational modes. Those could be time-filtered at the cost of breaking down consistency (*Griffies*, 2004), which, in our opinion, is highly undesirable.

A closer look at Eq. (5.28) indicates that the transport $\mathbf{M}$ (defined as the depth-integrated horizontal velocity) whose divergence causes the change in the free-surface elevation is given by

$$\mathbf{M} = H^n \left(\theta \overline{\mathbf{u}}^{n+1} + (1 - \theta)\overline{\mathbf{u}}^n\right). \tag{5.29}$$

Even by taking $\theta = 0.5$, the linearization in time of the term $H\overline{\mathbf{u}}$ in Eq. (5.28) precludes the transport from being formally centered in time. For being so, we ought to compute the divergence of $H^{n+\theta}\overline{\mathbf{u}}^{n+\theta}$, with $\theta = 0.5$. Although this computation would yield a time-centered transport, it has two drawbacks: (i) it requires the solution of a nonlinear system and (ii) it requires to hold in memory a mesh that is centered in time in addition to the meshes at times n and $n + 1$. Therefore, we are instead favorable to solving the linearized Eq. (5.28) for which the change in elevation is caused by a transport computed on the geometry at time step n, that is Eq. (5.29) with $\theta = 0.5$. This leads to a much faster algorithm at the cost of a very small loss

of accuracy. This design leads to the time staggered algorithm exposed in Section 5.3.4. The three-dimensional horizontal velocity structure (i.e., the internal mode) is determined by solving the following equation

$$\frac{\mathbf{u}^{k+1} - \mathbf{u}^k}{\Delta t} + \boldsymbol{\nabla} \cdot \left(\mathbf{u}^k \mathbf{u}^k\right) + \frac{\partial}{\partial z}\left(w^m \mathbf{u}^k\right) + f\hat{\mathbf{e}}_z \wedge \mathbf{u}^k - \mathbf{D}^k - \frac{\partial}{\partial z}\left(\nu_z^k \frac{\partial \mathbf{u}^{k+1}}{\partial z}\right) = 0.$$

where $k = n - 1/2$ and in which the depth-independent elevation gradient term is discarded because its effect on the velocity field is taken care of by the depth-integrated system (5.27)-(5.28).

The transport computed from the three-dimensional horizontal velocity field is not equal to the transport given by Eq. (5.29):

$$\int_{-h}^{\eta^n} \mathbf{u}^{n+1/2} \, \mathrm{d}z \neq \frac{H^n}{2}\left(\overline{\mathbf{u}}^{n+1} + \overline{\mathbf{u}}^n\right) \tag{5.30}$$

The origin of this discrepancy is twofold. First, we do not include the elevation gradient in the equation for the three-dimensional horizontal velocity field. Second, the separation between the external and internal modes is not exact and, even if the elevation gradient was added to Eq. (5.30), the discrepancy (5.30) would still exist. This is due to the nonlinear coupling terms included in $\mathbf{B}$ in Eq. (5.27). Hence, the three-dimensional horizontal velocity field must be corrected accordingly. Only in doing so will the vertical velocity be compatible with the free-surface elevation and tracer conservation consistenly ensured, as exposed in Chapter 4.

5.3.4 Overall time staggered algorithm

A schematic illustrating the time staggering of the overall algorithm is depicted in Figure (5.2). The elevation and tracers are known at integer time steps while the velocity is known at half-integer time steps. The mesh geometry needs to be known at integer time steps only. This follows from the linearization in time of the free-surface equation (5.28) and the fact that the three-dimensional horizontal velocity field is corrected on a mesh geometry known at an integer time step (see Eq. 5.30). To describe the sequence of computations, we will assume that we know the variables at the following steps: $\overline{\mathbf{u}}^n, \eta^n, \mathbf{u}^{n-1/2}, w^{n-1/2}$ and C^n, where C is any passive or active tracer. The mesh geometry is known at steps $n - 1$ and n. We will note these geometries $\mathcal{M}^{n-1}$ and $\mathcal{M}^n$, respectively. The overall algorithm is given hereafter.

1. Compute $(\overline{\mathbf{u}}^{n+1}, \eta^{n+1})$ knowing $(\overline{\mathbf{u}}^n, \eta^n)$ by solving Eqs (5.27)-(5.28).

2. Compute $(\mathbf{u}^{n+1/2})$ on $\mathcal{M}^n$ kowing $(\mathbf{u}^{n-1/2}, w^{n-1/2})$ on $\mathcal{M}^{n-1}$ by solving Eq. (5.30).

3. Correct $\mathbf{u}^{n+1/2}$ so that the horizontal transport is equal to (5.29).

4. Compute $w^{n+1/2}$ on geometry $\mathcal{M}^n$ knowing $u^{n+1/2}$ on the same geometry by solving Eq. (5.20).

5. Update both geometries. At this point, we have $\mathcal{M}^n$ and $\mathcal{M}^{n+1}$.
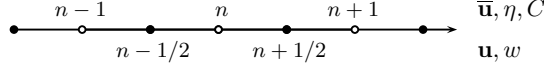
Figure 5.2: Schematic of the staggering used between elevation and tracers (on integer time steps) and velocity (on half-integer time steps). The mesh geometry needs to be known on integer time steps only, which is a consequence of the transport computed by Eq. (5.28) not being formally centered in time. The effect is that the velocity $(\mathbf{u}, w)^{n+1/2}$ is computed on mesh geometry n. The symbol C denotes any active or passive tracer.

6. Compute any tracer C^{n+1} on geometry $\mathcal{M}^{n+1}$ knowing the tracer C^n and the velocity $(\mathbf{u}^{n+1/2}, w^{n+1/2})$ on geometry $\mathcal{M}^n$.

7. Return to step 1.

The first action undertaken to improve efficiency – namely separating the dynamics into the slow and fast modes while using a single time step – has already been described. Upon inspection of the time-stepping algorithm outlined in the previous section, we may identify five main computational tasks: the fast mode, the horizontal velocity, the vertical velocity, the tracers and updating the mesh geometry. A few important comments can be made regarding those tasks. We note N_{2d} the number of two-dimensional triangle vertices and L the number of layers (a mesh containing L layers means that the total number of vertices is $(2L - 1) \times N_{2d}$ for $L > 1$). In a Delaunay two-dimensional mesh, the number of horizontal edges tends to $3N_{2d}$. The overall computational cost of the algorithm may be established in terms of these two variables:

1. The computation of $(\overline{\mathbf{u}}, \eta)$ requires to solve a system of $7N_{2d}$ unknowns. In a number of large-scale applications, it is legitimate to neglect the free-surface elevation in the divergence term of Eq. (5.26). Hence, the left-hand side matrix of the system is constant in time and needs only be factorized once at the onset of the time integration. The computational cost and memory storage requirement depend on the solver.

2. The computation of either component of $\mathbf{u}$ requires to solve a system of $2L \times 3N_{2d} = 6LN_{2d}$ unknowns. The factor $2L$ is a consequence of the discontinuous representation in the vertical. Due to the orthogonality of the non-conforming basis functions in the horizontal (*Hua and Thomasset*, 1984), the left-hand side matrix is banded diagonal, with a bandwidth of two. Note that without vertical momentum diffusion (which is implicit in time), the left-hand side of the linear system reduces to a tridiagonal matrix.

3. When solving Eq. (5.20) for w, we lump the left-hand side matrix of the system in the horizontal to obtain a tridiagonal matrix. The number of unknowns is $2L \times N_{2d} = 2LN_{2d}$ and the computational cost scales like $\mathcal{O}(LN_{2d})$. Note that, although the scaling is the same as that for $\mathbf{u}$, the cost of solving the system for w is roughly 10 times smaller than for either component of $\mathbf{u}$. The reason is that there are three times fewer unknowns for w than for u and v and that a tridiagonal matrix needs be factorized for w instead of a banded diagonal matrix for u and v.

4. In case we have a tracer, the number of unknowns is $2L \times N_{2d} = 2LN_{2d}$ and the computational cost scales like $\mathcal{O}(LN_{2d})$ if the left-hand side matrix of the system is lumped horizontally.

5. The cost of updating the mesh geometry (i.e., computing the normals, the element Jacobians and the new coordinates) is proportional to the number of elements, which scales like $\mathcal{O}(LN_{2d})$.

Therefore, the overall computational cost of the algorithm scales like $\mathcal{O}(LN_{2d})$. Doubling the number of triangles (i.e., doubling N_{2d}) and doubling the number of layers will quadruple the computational cost. The total number of unknowns (with two tracers) is $18LN_{2d} + 7N_{2d}$.

5.4 Convergence analysis

The numerical solution to the two-dimensional linearized shallow-water equations is now compared with an analytical solution to the propagation of gravity waves in a square basin of size L. The linearized shallow-water equations are obtained by substituting H^n for the unperturbed depth d in Eq. (5.28). We take $d = 1000$ m and $L = 1000$ km. The initial conditions are $u = 0$, $v = 0$, $w = 0$ and $\eta = \eta_0$, where the latter is a one-meter high Gaussian:

$$\eta_0 = \exp\left[-R\left(x^2 + y^2\right)\right]$$

with R controlling the stiffness of the initial Gaussian. The L_2-norm of the error on u, v, η and w is computed and reported in Figure (5.3) for a series of structured meshes with descreasing element size h. The L_2-norm of the function e in $\mathcal{T}^h$ is defined as

$$\|e\|_{L_2(\mathcal{T}^h)} = \sqrt{\int_{\mathcal{T}^h} e^2 \, \mathrm{d}\tau}.$$

Since we solve the two-dimensional shallow-water equations, the horizontal velocity is depth-independent and the vertical velocity is linear, reaching its maximum at the surface. We therefore choose to evaluate the error on the vertical velocity at the surface only. At the cost of a slight decrease in accuracy, a significant gain in performance is achieved by resorting to mass lumping for the vertical velocity. However, mass lumping is only performed in the horizontal, transforming the matrix of the system into a tridiagonal matrix. As the mesh resolution is increased, all errors decrease quadratically (Figure 5.3).
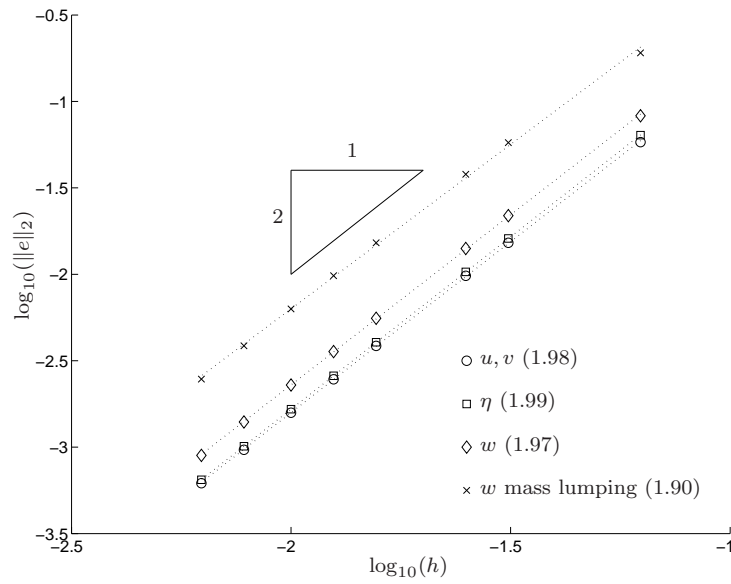
Figure 5.3: Convergence analysis of the L_2-norm of the error on u, v, η and w on structured meshes. The vertical velocity is computed without ($\diamond$) and with ($\times$) mass lumping. A quadratic rate of convergence is observed for all variables (the slope is indicated next to each variable).

5.5 Application to a shallow-water island

Seeking to validate the three-dimensional barotropic component of our model, we opted for a realistic test case. The latter had to be three-dimensional (without baroclinic effects) to be able to observe clear vertical motions. The momentum horizontal advection scheme had to be severly evaluated, so a problem featuring flow sepration and recirculation was deemed appropriate. We also wanted to compare the model results with that of previous finite difference models and show the effect of increased mesh resolution. Finally, we did not want the benchmark to fall short of physical interpretations. Hence, it had to be of interest for oceanographers and biologists.

In shallow coastal regions, flow disturbances caused by topographical features, such as islands, headlands, reefs and narrow passages, can have strong effects on marine ecosystems. Topographically generated circulation affects the distribution of sediments and can significantly influence the local dispersal of pelagic organisms (*Hamner and Hauri*, 1981; *Wolanski and Hamner*, 1988; *Wolanski et al.*, 1988; *Wolanski*, 1994; *Coutis and Middleton*, 1999, 2002). Of particular concern are the stable shallow-water eddies generated in the wakes of islands by oscillating tidal flows. By shallow water, it is meant here that the ratio of the water depth to the island width (facing the current) is much less than one. Among shallow-water islands for which stable tidal eddies are observed, Rattray Island (Great Barrier Reef, Northeast Australia – Figure 5.5) has been the focus of many studies in the past two decades (*Wolanski et al.*, 1984; *Falconer et al.*, 1986; *Black and Gay*, 1987; *Wolanski and Hamner*, 1988; *Deleersnijder et al.*, 1992; *Wolanski et al.*, 1996, 2003; *White and Deleersnijder*, in press). Aerial photographs (Figure 5.4) show turbid water in the wake of Rattray Island both at rising and falling tides, suggesting upwelling capable of carrying bed sediments upwards during the life span of the eddies.

5.5.1 Model setup

The domain of interest is shown in Figure (5.5). Because of its limited extent, the f-plane approximation is made with the latitude being 20ºS. The roughness length is taken to be $\xi_0 = 5 \times 10^{-3}$ m in Eq. (5.9) (*Black and Gay*, 1987). Because the last velocity node lies on the seabed, the bottom stress (5.9) is computed by using the mean value of the last two velocity nodes. The distance to the seabed ξ_b is calculated accordingly. We neglect surface stress as there was no significant wind during the field survey (*Wolanski et al.*, 1984). The constant c_s used in the parameterization of the horizontal momentum diffusion coefficient, Eq. (5.4), typically lies in the range $0.05 - 0.1$. It is on the same order of the value recommended by *Smagorinsky* (1963) and smaller than that used in usual finite element models such as that of *Lynch et al.* (1996).

The currents are dominated by the tides, whose ellipses are strongly polarized and essentially oriented from northwest to southeast (*Wolanski et al.*, 1984). The y-axis of the domain is rotated to be parallel to the major axis of the ellipses. We may thus assume the side boundaries to be impermeable. The southeast and northwest boundaries – hereafter referred to as lower and upper boundaries, respectively – remain open. Using available field measurements, the depth-averaged normal velocity and the eleva-

Figure 5.4: Eddy formation in the wake of Rattray Island during flood tide (photo courtesy of Eric Wolanski).
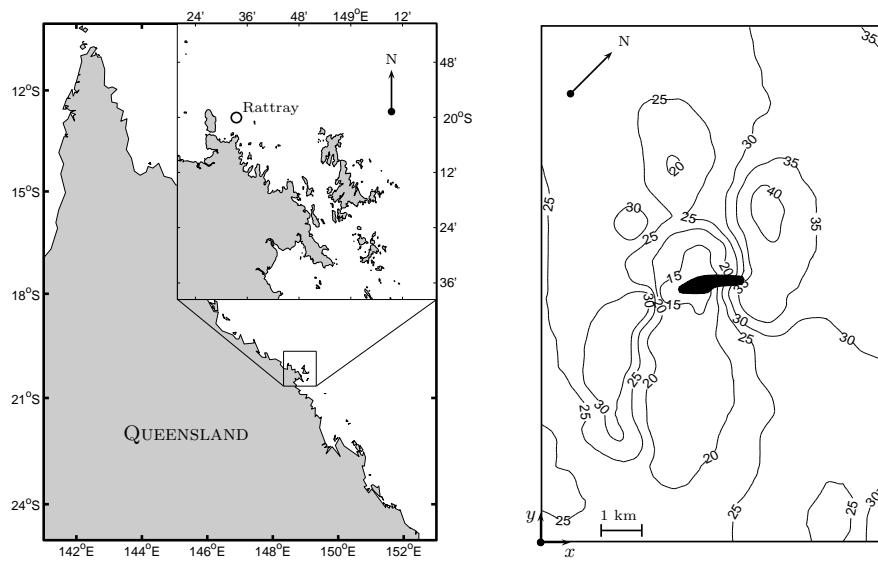

Figure 5.5: Rattray Island is located in the Great Barrier Reef (Northeast Australia). On the right panel, the domain of interest is represented in the (x, y) reference framework. Rattray Island is the black area at the center. Depths are in meters.

tion are imposed at both the lower and upper boundaries by prescribing the incoming characteristic variable $\bar{u}_n - \eta\sqrt{g/h}$, where $\bar{u}_n$ is the depth-averaged normal velocity. This is the so-called Flather boundary condition (*Flather*, 1976; *Ruddick et al.*, 1994). The phase lag between both boundaries is small and neglected in the model. Forcing used in the model corresponds to a 3.5 m spring tide recorded between 23 November 1982 and 4 December 1982. Rising tide flows southeastward. All results below are presented on 4 December 1982. This is the only day (with 2 December) for which all currentmeters were deployed.

5.5.2 Results and discussion

The model was run on meshes M_1, M_2 and M_3 of Figure (5.6) with 6, 8 and 10 layers, respectively. The time step is 10 s, 3 s and 1 s, respectively. It is constrained by advective processes off the island's tips where the speed approaches 1 m s^{-1} where the mesh resolution is typically the highest (e.g., less than 10 meters on mesh M_3). In all experiments, the Smagorinsky constant c_s is equal to 0.08.

Flow pattern

In Figures (5.7)-(5.8), the velocity field predicted by the model is compared with that measured at 25 locations where current meters were deployed and at three different times during rising tide. As can be seen in Figure (5.7), when using mesh M_1 (the coarsest), the model is unable to faithfully predict the recirculation pattern in the wake of the island. In particular, at 9h30, the model predicts a very sluggish flow close to the island whereas a swifter flow, parallel to the island, was measured in the field. At 11h30, the model reproduces the clockwise-rotating eddy in the island's wake. However, the recirculation strength closest to the island is too weak by roughly 50 percent and the eddy is too narrow. As depicted by field measurements (and suggested by aerial photographs), the right-hand side eddy should extend across the entire wake and should keep growing until the time of tide reversal. However, a vector plot of the modeled velocity field (not shown) accounts for two counter-rotating eddies within the island's wake. The left-hand side eddy is too large and, by the time of tide reversal (about 13h45), it has grown to a size and intensity similar to that of the right eddy. However, the velocity field taken at measuring sites does not suggest the existence of an eddy of that size on the southern side of the island at rising tide.

Results obtained on mesh M_2 and shown in Figure (5.8) present a higher degree of similarity. All features pertaining to the measured velocity field are found in the model. The recirculation intensity is larger than that obtained with the coarser mesh and quite similar to that of the measured field. The right-hand side eddy is larger and well reproduced by the model. It extends across the entire island's wake. This is particularly obvious at 13h45. The velocity field obtained with mesh M_3 (not shown) is basically the same as that obtained with mesh M_2, which corroborates the previous model output.

In Figure (5.9), we compare the predicted velocity field for the three meshes on 4 December 1982. The circulation patterns obtained with meshes M_1 and M_2 are quite different, as was already made obvious through comparison of Figures (5.7) and (5.8). Although two counter-rotating eddies are predicted with both meshes, the right-hand side eddy is larger for mesh M_2, complying with field measurements as we have
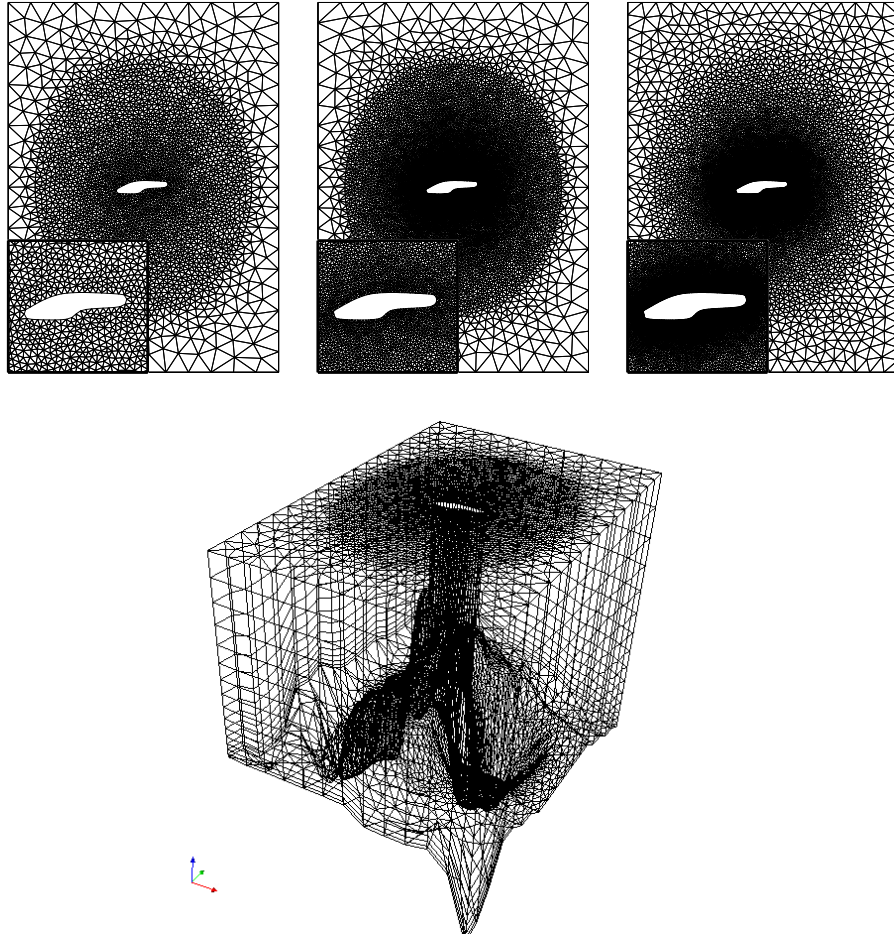
Figure 5.6: From left to right, the meshes contain approximately 6100, 14,000 and 18,600 triangles, respectively. The resolution for the left mesh (M_1) varies from 80 m to 600 m. The resolution for the center mesh (M_2) varies from 40 m to 600 m and for the right mesh (M_3), it varies from 20 m to 400 m. The main difference between the center and right meshes is a higher resolution around the island and a smoother transition (from the island toward the domain boundaries) for the right mesh. At the bottom: M_1-extruded, three-dimensional mesh with smaller vertical spacing near the seabed.

111

Figure 5.7: Comparison between the measured velocity field (left panels) and that predicted by the model (right panels) on mesh M_1 (the coarsest of the three meshes) at three different times on 4 December 1982. High water level occurs just before 13h45.

Figure 5.8: Comparison between the measured velocity field (left panels) and that predicted by the model (right panels) on mesh M_2 (the intermediate mesh in terms of resolution) at three different times on 4 December 1982. Hight water level occurs just before 13h45.
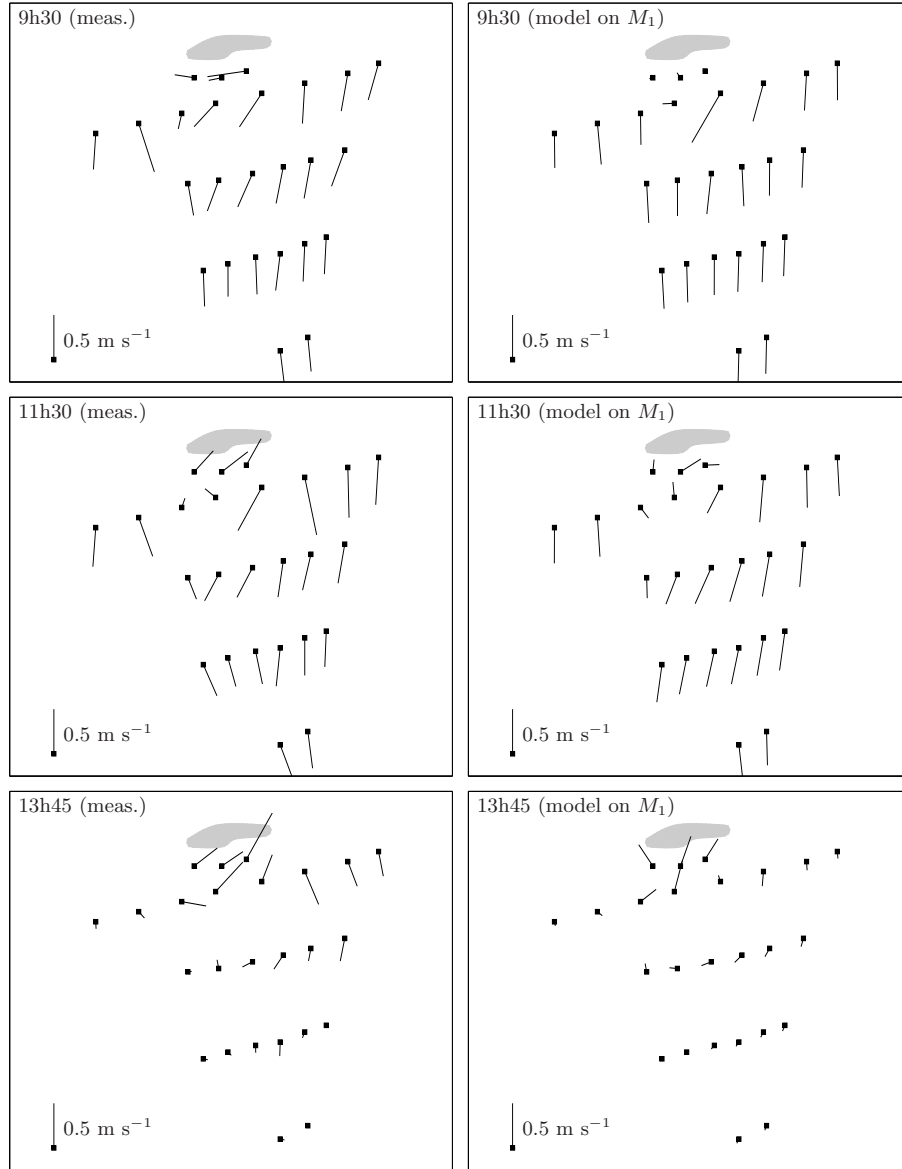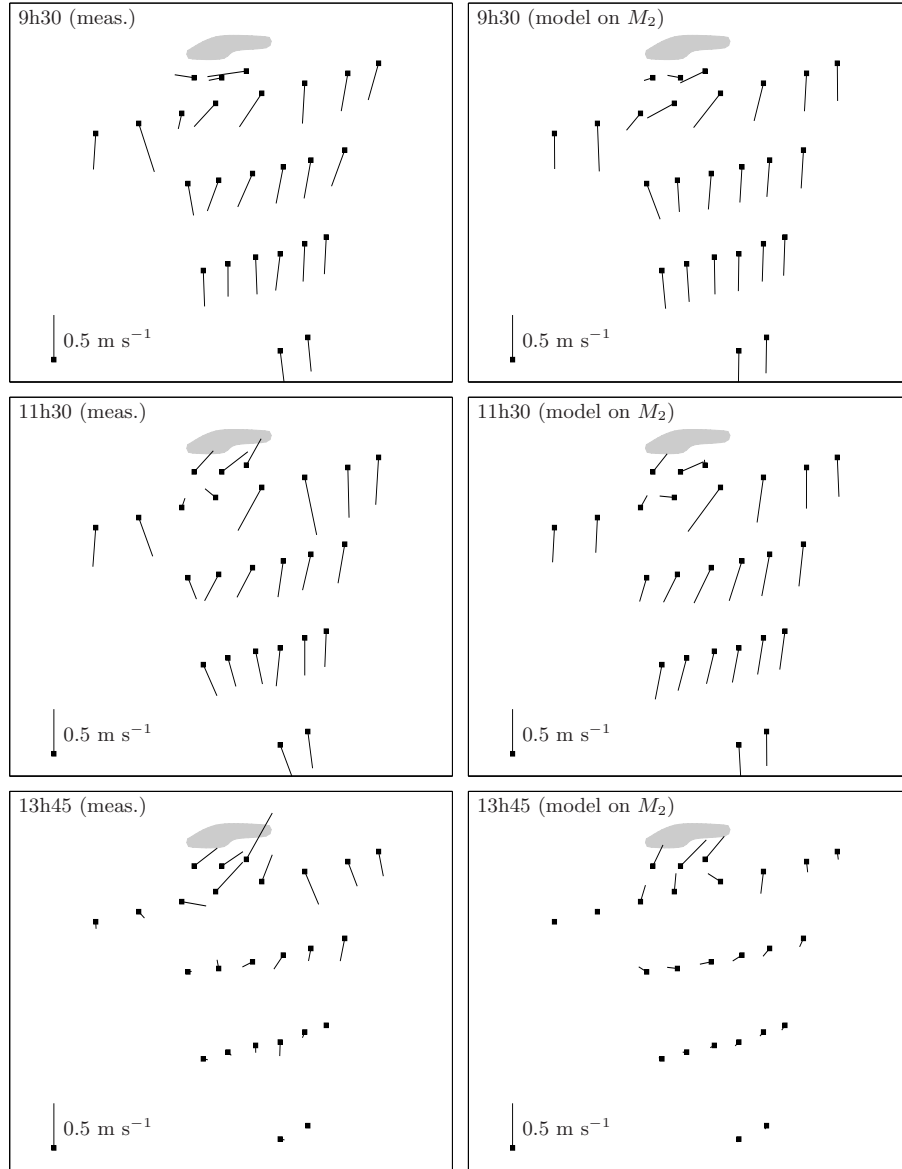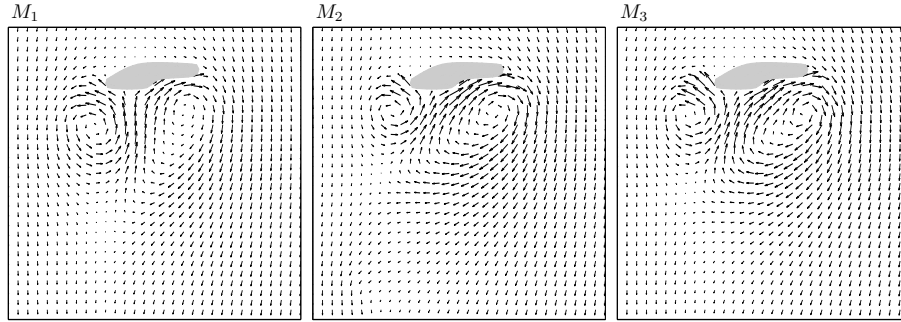
Figure 5.9: Comparison between the numerical predictions on the three meshes (M_1 to M_3 from left to right) on 4 December 1982 at 13h10. Notice how the circulation pattern differs between meshes M_1 and M_2 and is barely altered when using a finer mesh (M_3). The velocity field has been interpolated on a 160 m × 160 m structured mesh.
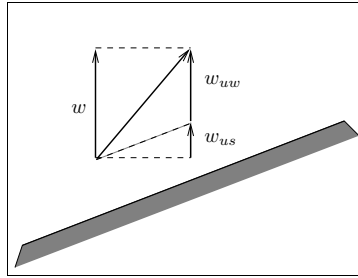
Figure 5.10: The total vertical velocity w can be split into a topography-induced component, the so-called upsloping velocity (w_{us}) and the upwelling velocity (w_{uw}), due to intrinsic upwelling mechanisms.

already stressed above. The circulation pattern obtained on mesh M_3 is very similar to that obtained on mesh M_2, even though the resolution is halved in the vicinity of the island. This is a clear indication of the convergence properties of the model for this application. It should be borne in mind that both the bathymetry and the island geometry play a role in shaping and sizing the eddies. Running the model without bathymetry (not shown) gives rise to two eddies of similar size.

Upwelling and downwelling

In a three-dimensional model, intrinsic upwelling and downwelling mechanisms can be detected by resorting to the concept of upwelling velocity described by *Deleersnijder* (1989) and used by *Deleersnijder* (1994) and *White and Deleersnijder* (in press). The upwelling velocity is the component of the vertical velocity from which we subtract the topography-induced component (see Figure 5.10). In what follows, the upwelling velocity is always computed at mid-depth.

In Figure (5.11), we show the upwelling velocity on the three meshes. For the top panels, we consider a range of $[-20, 10]$ mm s^{-1} while for the lower panels, we restrict the range to $[-6, 3]$ mm s^{-1}. The coarse mesh is unable to capture any of

Figure 5.11: Upwelling velocity in [mm s^{-1}] for the three meshes. Notice how the coarse mesh fails at capturing the intense vertical motions off the right island's tip.

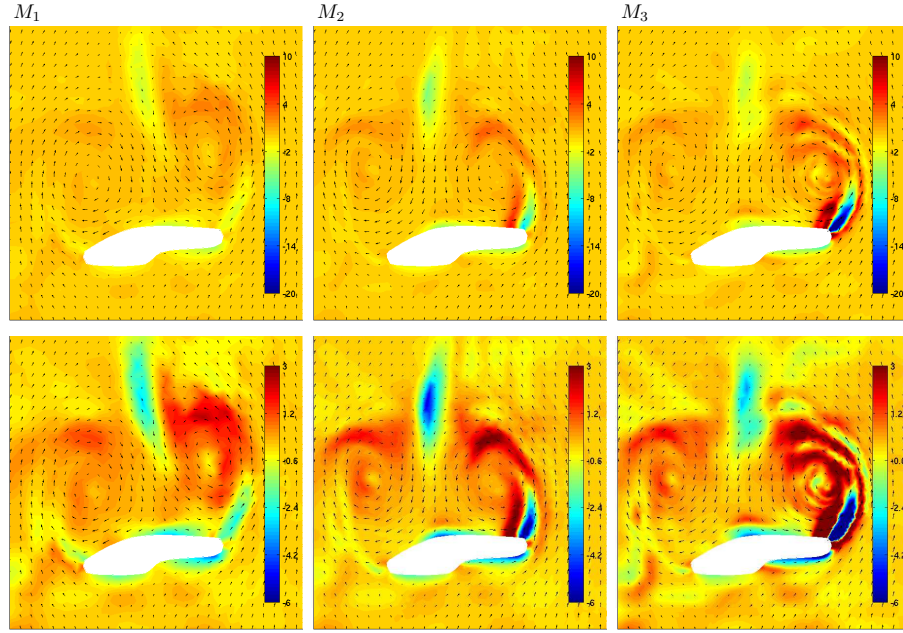the intense downwelling and upwelling processes that are resolved on the two other meshes (see the top panels). In particular, we can see that intense upwelling extends further downstream – and recirculates within the wake – when computations are carried out on the finest mesh. Note that much less intense zones of upwelling are already predicted on the coarse mesh (see bottom left panel). This upwelling is on the order of 1 to 2 mm s^{-1} , which is at least one order of magnitude smaller than the upwelling predicted off the northern island's tip.

Upwelling and downwelling at four different times during rising tide is depicted in Figure (5.12) for the finest mesh. A key feature in all snapshots is the presence of an intense upwelling zone (> 20 mm s^{-1}) off the northern island's tip. Strong downwelling also occurs downstream of the right tip and is confirmed by observations (*Wolanski, personal communication, 2006*). Weaker upwelling is also predicted downstream of the left tip (not visible with the range considered).

A comparison between five three-dimensional, finite-difference models for representing the tidal flow around Rattray Island is reported by *Wolanski et al.* (2003). All models used the same bathymetry, the same horizontal resolution (200 m) and the same forcing at open boundaries. They all predicted an upwelling near the center of the eddies on the order of 1 mm s^{-1}. According to *Wolanski et al.* (2003), the upwelling intensity near the eddy center must be at least 5 mm s^{-1} to account for the presence of bed sediments near the free surface (the eddy lives for about 2 hours). The results obtained with our finite element model shows that, regardless of the horizontal mesh resolution, we predict upwelling of less than 2 mm s^{-1} near the eddy center. However, during both tidal phases, intense upwelling > 20 mm s^{-1} is predicted off
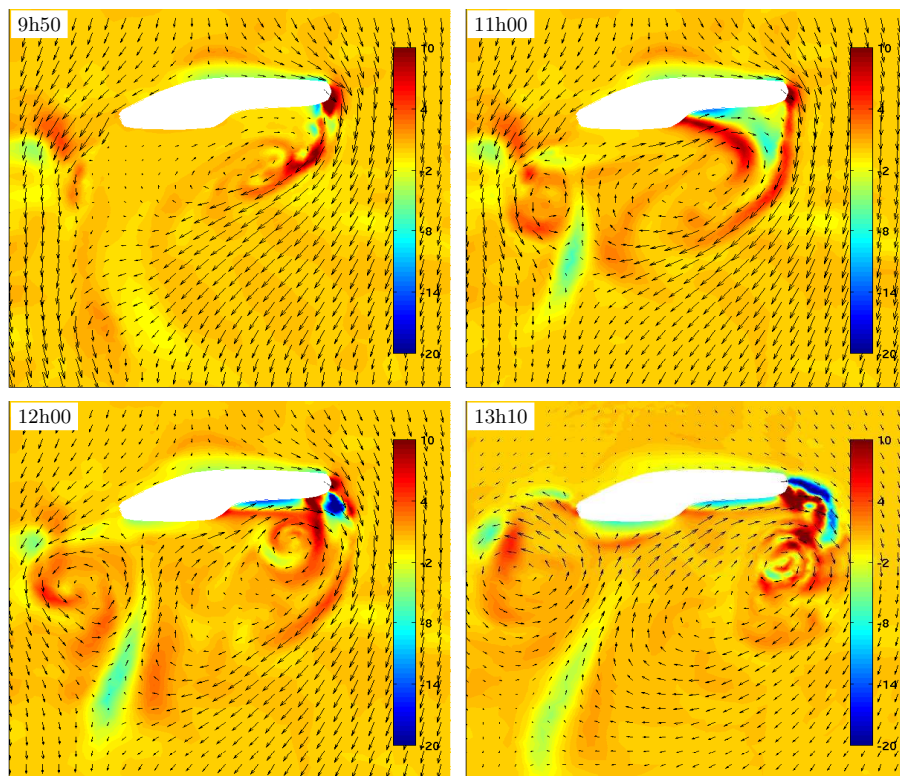
Figure 5.12: Upwelling velocity [mm s^{-1}] at four different times on 4 December 1982 during rising tide on mesh M_3. Notice the intense upwelling off the right tip in all spapshots.

the island's northern tip. This upwelling could be responsible for carrying bed sediments upwards, given that this vertical motion exists for at least two hours (see Figure 5.12). Once reaching the surface, those fine sediments are trapped in the flow and recirculates within the wake. This could explain the high turbidity of the water observed during rising tide. These findings confirm the results obtained recently by *White and Deleersnijder* (in press), who used a diagnosis based on the age to quantify the time needed for bottom water masses to reach the surface.

5.6 Conclusions

We have presented a new three-dimensional, unstructured mesh finite element marine model. The current configuration is suitable for studying flows without baroclinic effects. The model has a free surface and is hydrostatic. The mesh is unstructured in the horizontal and moves in the vertical to track the free-surface motions. We have described the numerical treatement of the hydrodynamical equations with the finite element method. The model was validated against a realistic flow around a shallow-water island for which field measurements were available. As the mesh resolution was increased, the model was able to predict the correct velocity field in the island's wake. Very intense upwelling was also predicted off the northern island's tip during ebb and flood. We suggested that this upwelling might be the main cause for the presence of mud at the surface, rather than the much weaker upwelling predicted near the center of the eddies.

Chapter 6

Diagnosing vertical transport in a 3D marine model

Summary

Diagnoses based on the concept of age are considered to quantify vertical transport in a three-dimensional finite element model for the tidal flow around an island. Two types of age for the bottom water are defined. The first age is a measure of the time elapsed since the bottom water left the seabed. The second age is the time required for the bottom water to travel from the seabed to the sea surface. Results are interpreted.

Marine flows are so complex that it is often very difficult to gain insight on their functioning by simple inspection of the model results. The latter are typically analyzed by resorting to two-dimensional cuts at some given times, the choice of which are left to the user's appreciation and feeling. All processes are not only three-dimensional but also time-dependent and a big picture of the flow is usually missing when opting for this simplistic approach. In addition, focusing on a single variable sometimes fails at taking into account the interactions between processes. Singling out one variable merely allows for pinning down one component of a given process that typically involves several variables. In the end, we are left with the impression that only a tiny portion of the model results has been exploited.

The use of other interpretation techniques to understand the results of such complex models is deemed necessary. Among these techniques are auxiliary timescales such as the age and the residence time. These timescales are inherent properties of the flow and may be evaluated diagnostically (*Delhez et al.*, 1999) to help understand the processes under consideration. In addition, the associated diagnoses are holistic in that they account for several processes and for the interactions between several variables. A historical review for the use of these timescales is beyond the scope of the present work and can be found elsewhere (*Delhez et al.*, 1999; *Deleersnijder et al.*, 2001; *Delhez et al.*, 2004). In this chapter, we present an application of the age to diagnose vertical transport in a tidal flow in the vicinity of a shallow-water island. We do not intend on laying out the theoretical framework for the age and residence time but

refer the reader to appropriate contributions (*Deleersnijder et al.*, 2001; *Delhez and Deleersnijder*, 2002)

In the previous chapter, the three-dimensional model SLIM was applied to study the tidal flow around Rattray Island. The model predicted some upwelling near the center of the eddies in the wake of the island, both during flood and ebb. However, we were also able to predict much stronger upwelling off the island's tips. There is now little doubt that the flow around the island is strongly three-dimensional. However, if strong vertical motions exist in the vicinity of the island, we might wonder which one in particular could be responsible for the suspension of sediments in the island's wake. The best answer would probably be provided by a sediment transport model that would take into account the buoyancy of the particles. However, before rushing into the application of such a model, we might want to resort to a simpler diagnosis, yet sophisticated enough to account for all physical processes, and their history, responsible for vertical transport.

6.1 Methods

The concept of age, which is a component of CART[1] (*Delhez et al.*, 1999; *Deleersnijder et al.*, 2001; *Delhez and Deleersnijder*, 2002) provides such a holistic approach. The age of a particle of seawater is defined as the time elapsed since the particle under consideration left the region in which the age is prescribed to be zero. The basic observation that the water is turbid in the island's wake leads to the simple, following two questions. How much time does it take bottom water to reach the surface during ebb and flood ? And where does this bottom water originate ? In this context, bottom water is composed by those water particles touching the seabed at a given time. In that respect, bottom water can be viewed as a passive tracer and its age is set to zero when it touches the seabed. Note that it is not uncommon to regard water masses as passive tracers (*Cox*, 1989; *Hirst*, 1999; *Goosse et al.*, 2001). Once the water particles leave the seabed and rise, carried upwards by some upwelling, the age increases. Depending on the fate of these water particles when they touch the sea surface, we end up with two different ages. The first age of a sample of water particles is defined as the arithmetic average of the times that have elapsed since the particles left the seabed for the last time. The age of a water particle keeps increasing as long as it does not touch the seabed again. Once a water particle touches the seabed, its age is reset to zero. Hence, the first age answers the more intuitive question as to how old bottom water is at the surface. The second age is defined to be the time needed to travel from the seabed to the sea surface. Similarly to the first type of age, the age of a water particle is reset to zero when it touches the seabed. However, once the water particle touches the sea surface, it is disregarded until it touches the seabed again. This key difference between both types of age is illustrated in Figure (6.1). From now on, all variables associated with the type of age i will have a subscript i. The ages will be referred to as age 1 and age 2.

---

[1]Constituent-oriented Age and Residence time Theory, `http://www.climate.be/CART`
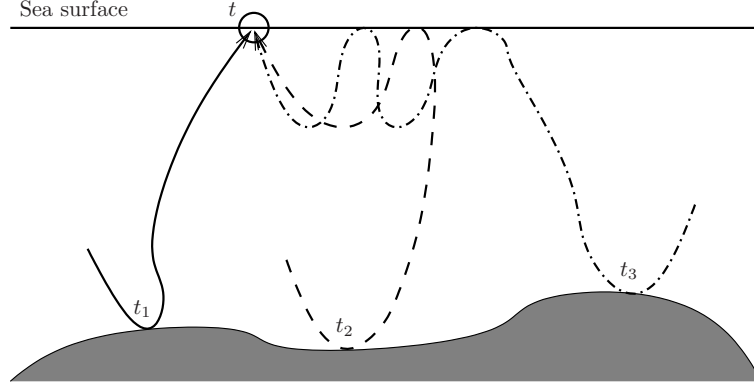
Figure 6.1: A water sample containing three water particles is taken at the sea surface at time t. Each particle has a different history, as illustrated by their trajectories. For the first type of age, the age keeps increasing as long as the particle does not touch the seabed again. Therefore, the first age is $a_1 = [(t - t_1) + (t - t_2) + (t - t_3)]/3$. For the second age, the particle is disregarded when it touches the sea surface. Therefore, only the first particle need be accounted for: $a_2 = (t - t_1)$.

To compute the age, we have to solve advection-diffusion equations for the bottom water concentration C_i and the age concentration α_i. Once those two variables are known, the age a_i is given as the ratio of the age concentration to the water concentration:

$$a_i = \frac{\alpha_i}{C_i} \qquad (i = 1, 2). \tag{6.1}$$

The water concentration C_i is solution to (*Delhez et al.*, 1999)

$$\frac{\partial C_i}{\partial t} + \boldsymbol{\nabla} \cdot (\mathbf{u} C_i) + \frac{\partial}{\partial z} (w C_i) = \frac{\partial}{\partial z} \left(K_z \frac{\partial C_i}{\partial z} \right) + D \qquad (i = 1, 2), \tag{6.2}$$

where K_z is the vertical eddy diffusivity coefficient and D parameterizes turbulent horizontal diffusivity with a Smagorinsky scheme similar to Eq. (5.4). The age concentration α_i obeys the following equation (*Delhez et al.*, 1999):

$$\frac{\partial \alpha_i}{\partial t} + \boldsymbol{\nabla} \cdot (\mathbf{u} \alpha_i) + \frac{\partial}{\partial z} (w C_i) = C_i + \frac{\partial}{\partial z} \left(K_z \frac{\partial \alpha_i}{\partial z} \right) + D \qquad (i = 1, 2), \tag{6.3}$$

where the water concentration C_i is the so-called aging term. Note that the water concentration varies between 0 and 1. Boundary conditions are yet to be prescribed to close the system. Because the vertical eddy diffusivity at the bottom is zero, it is convenient to introduce a bottom roughness length ξ_b. This is similar to the roughness length introduced for the computation of the bottom stress. We may similarly define a surface roughness length ξ_s. The bottom and surface boundary conditions will be enforced at $z_b = -h + \xi_b$ and $z_s = \eta - \xi_s$. At sea bottom, the water concentration is 1 and the age concentration is 0 for both ages:

$$[C_i]_{z=z_b} = 1 \quad \text{and} \quad [\alpha_i]_{z=z_b} = 0 \qquad (i = 1, 2), \tag{6.4}$$

which translates the fact that we want to track water particles that leave the seabed with the age reset to 0. At the sea surface, we have to distinguish between age 1 and age 2. Since the free surface is impermeable to the first age, we have

$$\left[K_z \frac{\partial C_1}{\partial z}\right]_{z=z_s} = 0 \quad \text{and} \quad \left[K_z \frac{\partial \alpha_1}{\partial z}\right]_{z=z_s} = 0, \tag{6.5}$$

which means that age 1 keeps increasing even when water particles touch the free surface. For the second age, we have to implement the fact that once a particle touches the surface, it is disregarded. In other terms, the water concentration is zero at the surface:

$$[C_2]_{z=z_s} = 0. \tag{6.6}$$

Now, the age concentration is defined by (*Delhez et al.*, 1999)

$$\alpha_2 = \int_0^\infty c_2(x, y, z, t, \tau) \, \mathrm{d}\tau,$$

where c_2 is the water concentration distribution function and τ is the age variable, that is an independent variable not to be confused with the mean age a. Since the water concentration is assumed to be zero at the surface, c_2 is zero and so is α_2:

$$[\alpha_2]_{z=z_s} = 0. \tag{6.7}$$

The conditions applied on lateral boundaries depend on whether they are closed or open. Along closed boundaries, a no-flux condition is enforced on the water and age concentrations. At outflow open boundaries, both the water and age concentrations are advected out of the domain. At inflow open boundaries, incoming water and age concentrations must be prescribed to compute the advective flux. The incoming water (age) concentration is taken to be the mean outgoing water (age) concentration. In other terms, the incoming age is prescribed to be the mean outgoing age, leading to periodic boundary conditions on the age in the mean sense. This is based on the hypothesis that horizontal age constrasts appear close to the island and that homogeneity prevails far away from it.

At this point, two remarks can be formulated.

(i) We will take the vertical eddy diffusivity coefficient K_z to be equal to the vertical eddy viscosity coefficient ν_z. In other words, the Prandtl number – which is the ratio of viscosity to diffusivity – is assumed to be equal to one. This hypothesis is generally accepted for unstratified fluids and it therefore applies to Rattray Island (*Munk and Anderson*, 1948).

(ii) The computation of age 2 at the surface implies to evaluate an indeterminate limit of type $0/0$. We have to make sure that the limit exists.

Some numerical issues associated with the computation of both types of age, such as the existence of the bottom logarithmic layer, are addressed in detail by *White and Deleersnijder* (in press) and are not reproduced here.

6.2   Results and discussion

For the computation of the age, the coarsest mesh of Figure (5.6) was employed with 16 layers in the vertical based on sigma-coordinates. Figures (6.2) and (6.3) show ages 1 and 2, respectively, at the surface, at four different times during a tidal cycle. Note that experiments on extended meshes (in the free stream direction) have been made to assess the sensitivity of the predicted age on the distance at which boundary conditions are imposed. In all cases, the predicted age remains within a few percent of that computed with the original mesh (not shown). Hence, the boundaries are located far enough from the island. At the onset of the simulation, the water concentration is prescribed to be the solution of the water-column model presented by *White and Deleersnijder* (in press). The initial age concentration is zero. For age 1, the water concentration is never computed and remains equal to one throughout the domain and at all time. For age 2, both the water and age concentrations are computed.

Let us first concentrate on age 1. A striking feature is visible in Figure (6.2a) and (6.2c), where bottom water (the blue elongated patches) emanates off the island's tips. This water is less than one hour old at both tips. The fact that the age of the bottom water is roughly the same off both island's tips can be explained by the depth difference. Off the right tip, the depth is about 30 m while off the left tip, it is about 15 m. However, upwelling on the right is found to be at least twice as intense as that on the left, which could explain the resulting symmetry. When the tide keeps rising, some of the bottom water recirculates within the island's wake while the rest is advected downstream. At the end of rising tide, age 1 is about two to three hours downstream of the island, as shown in Figure (6.2b). Finally, at the end of falling tide, the age varies between three to four hours with a few exceptions of younger water located near the centers of both eddies. The age of these patches is about two hours. This is shown in Figure (6.2d). Since the age of bottom water within the island's wake shortly before tide reversal is roughly three hours, it could be hypothesized that this water mainly originates from the island's tips when the free-stream speed is large enough to initiate upwelling.

The interpretation of age 2 at the surface is more delicate. Although not as definite as for age 1, we may also discern young patches originating from the island's tips in Figures (6.3a) and (6.3c). Along the downstream edge of the island, a patch of older water is visible (reddish patch). These patches coincide with regions of very low horizontal velocity, as can be seen on the right panels showing the depth-averaged velocity field. Because of less intense circulation, vertical diffusion decreases, which has a direct impact on the age. Finally, shortly before tide reversal, age 2 behaves rather counter-intuitevely. The surface age pattern seems to be opposite to that for age 1 (see Figures (6.2b) and (6.3b)). The largest values of the surface age is found around the centers of the eddies, where the upwelling velocity is large. This is strinkingly clear for the left-hand side eddy in Figure (6.3b) and the right-hand side eddy in Figure (6.3d). This counter-intuitive behavior motivated an investigation on the effect of vertical advection on the age within eddies. Using a one-dimensional water-column model, *White and Deleersnijder* (in press) showed that flows characterized by a certain range of positive vertical Peclet numbers undergo an increase in age 2 at the center of

Figure 6.2: Age 1 (age of bottom water) in hours at four different times: a. peak flood velocity, b. tide reversal, c. peak ebb velocity, d. tide reversal. The velocity field (vectors) is interpolated on a structured grid for clarity.

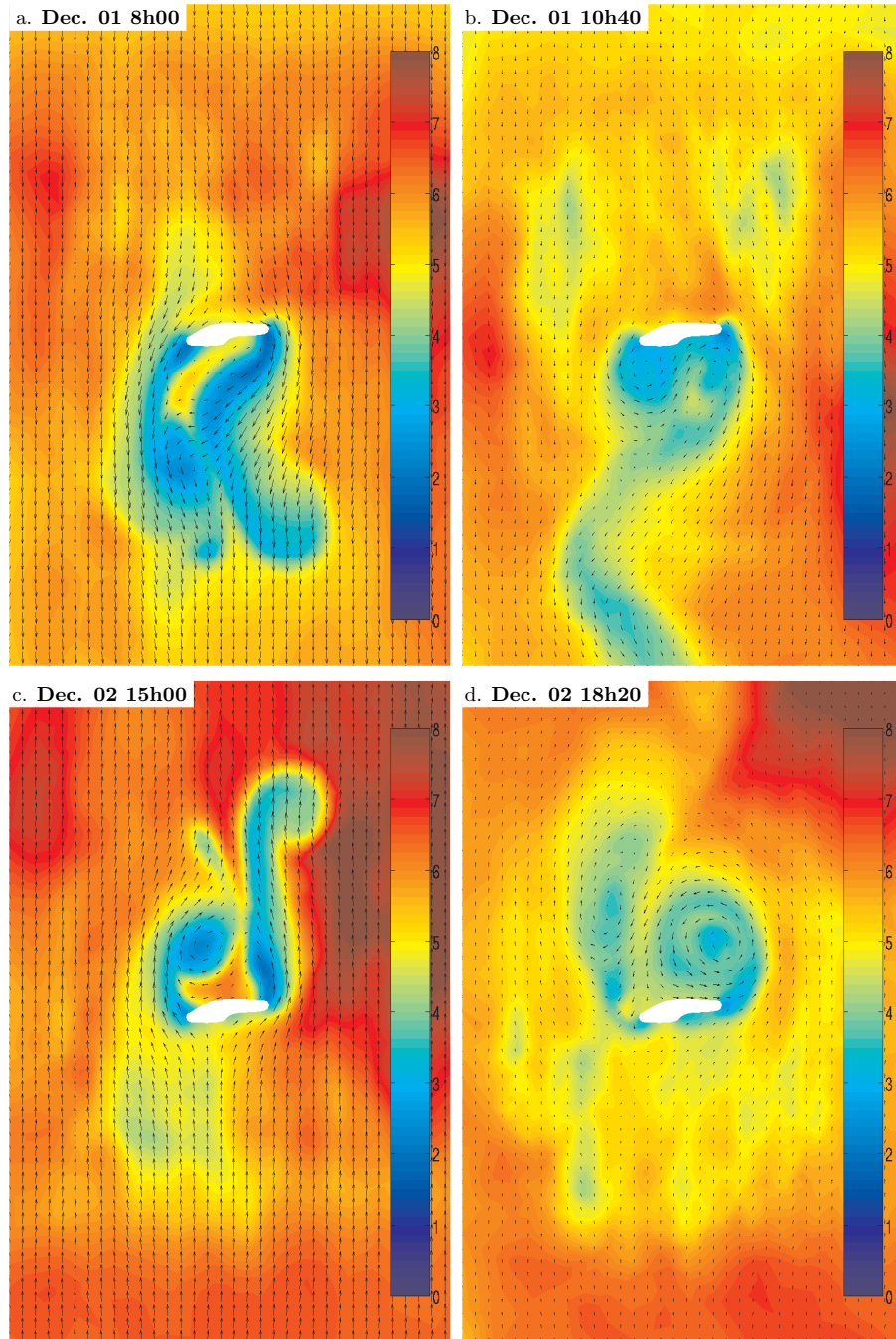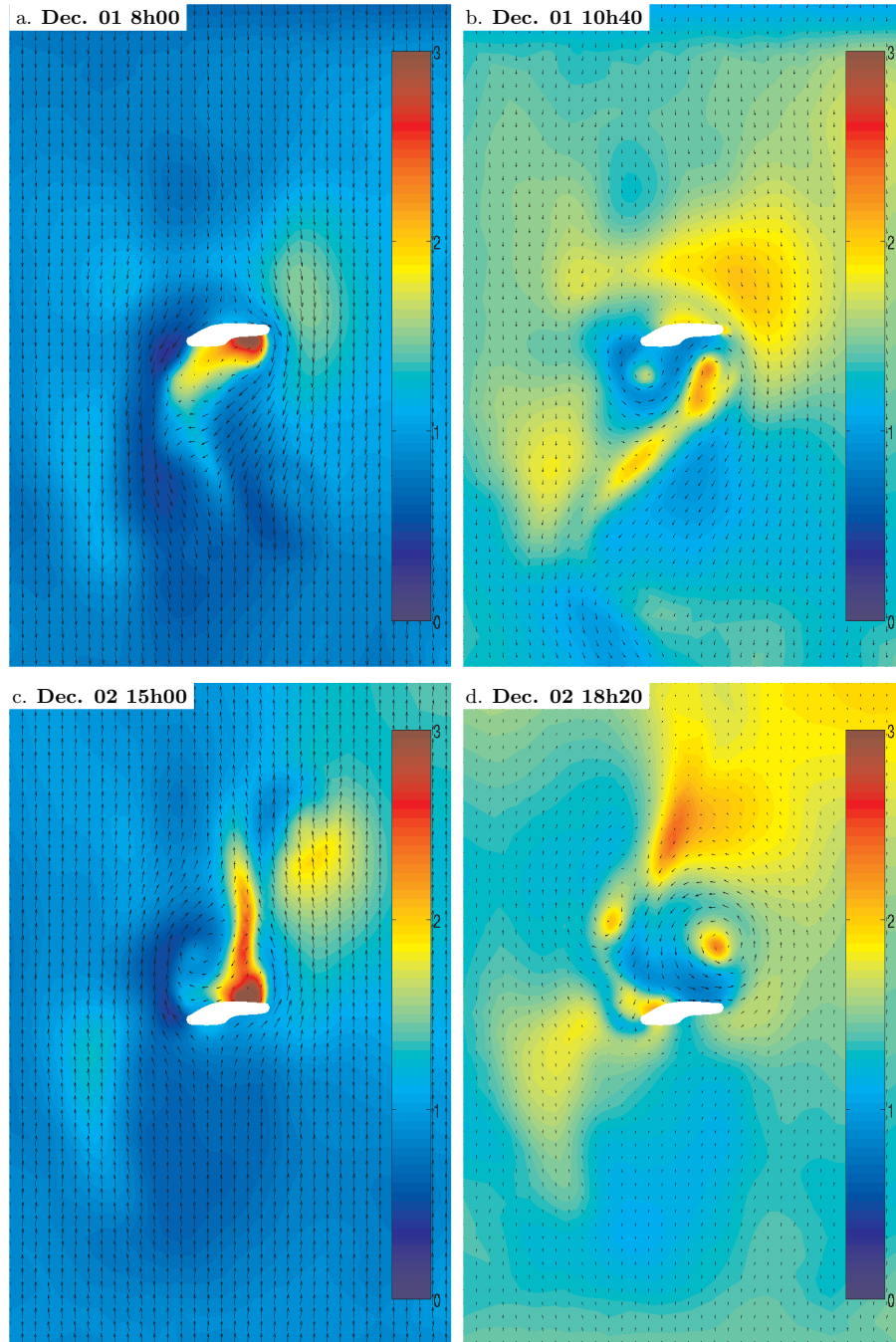**Figure 6.3:** Age 2 (time taken by bottom water ro reach the surface) in hours at four different times: a. peak flood velocity, b. tide reversal, c. peak ebb velocity, d. tide reversal. The velocity field (vectors) is interpolated on a structured grid for clarity.

the eddies. A typical value for the vertical Peclet number within an eddy in the wake of Rattray Island is one, which explains the predicted behavior.

6.3   Conclusion

The pattern of age 1 at the surface confirms the presence of intense upwelling off the island's tips. Most importantly, the value of age 1 at the surface, downstream of the island and shortly before tide reversal, suggests that the water at the surface originate from the tips of the island and recirculate within the wake. The role of the age in explaining this circulation pattern is crucial as the latter could not readily be proposed by a simple look at the upwelling velocity. Furthermore, this flow description is somewhat in contradiction with the sketch proposed by *Wolanski and Hamner* (1988), in which upwelling only takes place within the eddies. The results presented in this work motivate further research toward a better understanding of the three-dimensional flow circulation around shallow-water islands.

The pattern pertaining to age 2 also exhibits upwelling off the island's tips. However, within the eddies where upwelling velocity is the largest, the surface age increases. This counter-intuitive behavior was validated by a simplified water-column model including both advection and diffusion. Nevertheless, at this stage, the effect of advection upon age 2 remains physically not well understood. Drawing conclusions based on age 2 is not straightfoward and, undoubtedly, requires additional effort.

Chapter 7

Conclusion and perspectives

In this research work, conducted under the auspices of the SLIM[1] project, we have developed a three-dimensional, marine model using the finite element method. The model solves the hydrostatic primitive equations. The three-dimensional mesh is made up of prisms and is obtained by extruding an unstructured, triangular two-dimensional mesh. The free-surface dynamics is included in the model and the computational domain is dynamically deformed to accommodate the free-surface motions. The interior mesh motion is unconstrained and can be regulated by any criterion that is deemed appropriate (e.g., isopycnal coordinates). At large scales, the computational domain motion allows for resolving the dynamics incurred by freshwater fluxes (precipitation and evaporation). At smaller scales, it allows for taking into account the layers thinning and thickening undergone by tidal dynamics. Potentially, the mesh motion would also permit the inclusion of a wetting and drying algorithm.

In its current version, the model lacks a baroclinic component. However, it is conceived in such a way that any tracer can readily be added and will evolve in a conservative fashion. In addition, the finite element discretization of the elevation, continuity and tracer equations is consistent. Hence, a uniform tracer concentration remains equal to the initial value at all time, no matter which dynamics is considered but provided that there is no source term and no boundary flux. To achieve these properties of conservation *and* consistency while using a stable mixed formulation, the following interpolations are used in the horizontal. The horizontal components of the velocity are linear and non-conforming (P_1^{NC}). The elevation, the vertical velocity and all tracers are linear (P_1). We have almost unlimited freedom regarding the interpolation in the vertical, except that it must be the same for the vertical velocity and the tracers.

The development of the three-dimensional structure of the future OGCM SLIM has always been the main objective. Nevertheless, in fulfilling this objective, secondary problems were addressed. We evaluated some finite element methods for the resolution of the equations for the external mode using a challenging benchmark. The discontinuous Galerkin method outperformed the other methods provided that the right numerical fluxes were computed. This very test case was especially enlightening to

---

[1] Second-generation Louvain-la-Neuve Ice-ocean Model, `http://www.climate.be/SLIM`

understand how Riemann solvers work in dimensions higher than one by projecting the equations along the one-dimensional normal to the edge (in 2D) or face (in 3D). We further assessed the barotropic component of the model in resolving barotropic instabilities. The equations solved were inviscid, making it challenging for numerical methods designed to resolve advective processes with some kind of numerical stabilization. In that case, the mesh resolution must be sufficiently high to prevent numerical dissipation from inhibiting the growing of physical instabilities.

During this doctoral research, we have developed some structural components of SLIM. Nevertheless, the model still lacks many features of a full-fledged OGCM, coupled with a sea-ice model, set out as objective by 2009. The SLIM team, comprising 11 PhD students and 4 supervisers at the time of this writing, is more active than ever at fulfilling this objective. In the **short term** (within a year and a half), the model must be enhanced to operate in spherical geometry, with no constraint from any horizontal coordinate system whatsoever. The barotropic component must be fully validated on the basis of some or all of the seven Williamson test cases (*Williamson et al.*, 1992). Within the same time frame, the baroclinic component must be developed and validated. This entails devising an advection scheme for tracers that is as monotonic as possible to avoid the occurrence of unphysical extrema. We will also need to investigate the necessity of stabilizing (following e.g., *Ilinka et al.*, 2000) the advection term for the tracer equation (a P_1 discretization is not optimal for advection-dominated flows). An adequate element for the baroclinic pressure must also be selected. Appropriate test cases should include realistic benchmarks. In order to run the model on large domains without too much constraint on mesh resolution, the current code must be modified so that the model is able to run on parallel computers.

In the **medium term** (within two years), the full three-dimensional, baroclinic model will have to be tested in spherical geometry on the world ocean. Preliminary results should be validated by using diagnoses in terms of transports across typical straits (Drake, Indonesia, etc.) and poleward heat fluxes. This validation process will require a long period of fine parameterization tuning and should start as early as possible. The aforementioned diagnoses should be performed using adequate interpretation techniques, such as the age (*Deleersnijder et al.*, 2001; *Delhez and Deleersnijder*, 2002), which should be built-in within the model. The choice of vertical coordinates will have to be carefully thought out. Terrain-following coordinates are better suited for flows in shallow seas than for the large-scale circulation in the oceans. An approach based on z-coordinates is probably more appropriate to avoid numerical errors in the computation of the horizontal pressure gradient (*Haney*, 1991). However, to avoid a staircase representation of the seabed and to circumvent the constraint of using the same number of prisms in adjacent columns, non-conforming prisms (with hanging nodes, see *Rivière and Girault* (2006)) could be employed, preferably in the interior of the ocean where the dynamics is less active and less prone to inducing numerical errors. Developments regarding this mesh setup in three dimensions should begin at the start of the second year. Hence, the technique should probably be first mastered in two dimensions during the first year. Coupling the finite element sea-ice model with the ocean model should begin during that second year as well.

In the **longer term** (beyond two years from now), steps toward adaptive modeling will have to be taken. This includes mesh adaptivity without which the full potential of the finite element method will not be unleashed. However, if dynamic mesh adaptivity is tempting, it also brings about complications in terms of interpolations between meshes that must be mass- and tracer-conserving. Mesh adaptivity – in addition to a varying mesh resolution in space – raises the question of determining how to dynamically adapt the model subrid-scale parameterizations, not only in space but also over time. Great care will have to be taken to ensure that the physical processes we seek to resolve regulate the numerical method, and not the other way around ! In that respect, mesh adaptivity is extremely delicate and must be considered with great care. In principle, adaptive modeling consists in much more than simply adapting the mesh and the underlying parameterizations. The set of equations could legitimately be adapated in the course of the simulation to account for those physical processes that could be resolved as the mesh resolution allows for it. Although the large-scale ocean circulation is very well approximated by solving the hydrostatic equations, a few non-hydrostatic processes (e.g., deep convection (*Marshall et al.*, 1997)) could be resolved locally by adapting the mesh and the equations (we would then locally solve the non-hydrostatic primitive equations). Because SLIM aims at being a multi-purpose marine model, capable of being applied to estuaries, coastal oceans and ocean basins, non-hydrostatic modeling should be on the agenda in the longer term. This state of mind is reinforced by the belief that the computational power of future computers will allow to run simulations on higher resolution meshes for which the hydrostatic approximation might become questionable.

Appendix A

Complementary material to Chapter 2

A.1 Analytical solution

The solution to (2.6) on $[0, 1]$, subject to an arbitrary initial condition on the elevation, say $\eta_0(x)$, is developed herein. Using the method of seperation of variables, we define $u(x, t)$ to be

$$u(x, t) = F(x)T(t)$$

so that replacing u by that product into (2.6) yields

$$T''F + TF = \alpha^2 TF''$$

or

$$\frac{T''}{T} = \alpha^2 \frac{F''}{F} - 1 = C$$

where C is a constant expressing the fact that both sides of the first equality must not depend upon neither x nor t. The solution to the time-dependent part, $T(t)$, must be of the form

$$T(t) = A\sin(\omega t)$$

to account for the initial condition on u. Note that the constant C is deemed negative to avoid growing exponential-type solutions in time. By twice differentiating T, the constant C is found to be: $C = -\omega^2$. The space-dependent part, $F(x)$, obeys

$$F'' = -\frac{\omega^2 - 1}{\alpha^2}F,$$

where it is required that $\omega^2 > 1$ to avoid an exponential dependence on x, which could not satisfy the boundary conditions. For the same reason, solutions involving cosine cannot exist. Thus, we have

$$F(x) = B\sin(kx),$$

where $k^2 = \frac{\omega^2 - 1}{\alpha^2}$. Now, to satisfy both boundary conditions, we must have $k = k_n = (2n - 1)\pi$, which constrains ω to $\omega = \omega_n = \sqrt{1 + \alpha^2 k_n^2}$. Combining the time and space dependences, the velocity $u(x, t)$ is given by an infinite sum of those harmonics:

$$u(x, t) = \sum_{n=1}^{\infty} D_n \sin(\omega_n t) \sin(k_n x), \tag{A.1}$$

where the constant D_n is to be determined. To do so, we may write Eq. (2.3) at $t = 0$:

$$\begin{aligned} \alpha^2 \frac{\partial \eta}{\partial x} &= -\frac{\partial u}{\partial t} \\ &= -\sum_{n=1}^{\infty} D_n \omega_n \sin(k_n x). \end{aligned}$$

This equality is satisfied provided that the initial elevation field $\eta_0(x)$ take the following form

$$\eta_0(x) = \sum_{n=1}^{\infty} H_n \cos(k_n x),$$

where the coefficients H_n are given by

$$H_n = 2 \int_0^1 \eta_0(x) \cos(k_n x) \, dx. \tag{A.2}$$

Thus, for each n, we have

$$D_n = \frac{\alpha^2 k_n}{\omega_n} H_n$$

and the final expression for $u(x, t)$ is

$$u(x, t) = \sum_{n=1}^{\infty} H_n \frac{\alpha^2 k_n}{\omega_n} \sin(\omega_n t) \sin(k_n x). \tag{A.3}$$

Now that $u(x, t)$ is known, we may seek the expression for $v(x, t)$ by using Eq. (2.4) and the initial condition $v(x, 0) = 0$, which yields

$$v(x, t) = \sum_{n=1}^{\infty} H_n \frac{\alpha^2 k_n}{\omega_n^2} [\cos(\omega_n t) - 1] \sin(k_n x). \tag{A.4}$$

Finally, the elevation field $\eta(x, t)$ is easily infered from Eq. (2.3). A few algebraic manipulations lead to

$$\eta(x, t) = \sum_{n=1}^{\infty} H_n \cos(k_n x) \left\{ 1 - \frac{\alpha^2 k_n^2}{\omega_n^2} [1 - \cos(\omega_n t)] \right\}. \tag{A.5}$$

Depending on the initial condition, an analytical expression can be found for H_n. For the sign function, coefficients H_n amount to

$$H_n = \frac{4(-1)^n}{k_n}.$$

A.2 Details on the variational statement for DG

We focus on the continuity equation to show how formulations (2.14) and (2.15) are derived. Integration by parts of the term involving the spatial derivative generates an extra term, as shown hereafter:

$$\sum_{e=1}^{N_e} \int_{\Omega_e} \frac{\partial u^n}{\partial x} \hat{\eta} \, \mathrm{d}x = - \sum_{e=1}^{N_e} \int_{\Omega_e} u^n \frac{\partial \hat{\eta}}{\partial x} \, \mathrm{d}x + \sum_{e=1}^{N_e} |u^n \hat{\eta}|_{\partial \Omega_e} \, . \tag{A.6}$$

The last sum of (A.6) may be expanded so that the index now runs on physical nodes:

$$\begin{aligned}
\sum_{e=1}^{N_e} |u^n \hat{\eta}|_{\partial \Omega_e} &= \sum_{i=1}^{N_v} \left\{ u^n(X_i^-)\hat{\eta}(X_i^-) - u^n(X_i^+)\hat{\eta}(X_i^+) \right\} \\
&= \sum_{i=1}^{N_v} \left\{ \langle u^n(X_i) \rangle \, [\hat{\eta}(X_i)] + [u^n(X_i)] \, \langle \hat{\eta}(X_i) \rangle \right\},
\end{aligned} \tag{A.7}$$

where $\langle f(X_i) \rangle$ and $[f(X_i)]$ are the average and jump of f at physical node X_i, defined as

$$\begin{aligned}
\langle f(X_i) \rangle &= \frac{1}{2} \left(f(X_i^-) + f(X_i^+) \right) \\
[f(X_i)] &= f(X_i^-) - f(X_i^+).
\end{aligned}$$

The last sum of (A.7) is obtained from the following equality:

$$ac - bd = \frac{1}{2} (a + b)(c - d) + \frac{1}{2}(a - b)(c + d) \, .$$

Next, the sum $\mathcal{S}_2$ in (2.13) may be rewritten so as to run on physical node indices as well. We have

$$\begin{aligned}
\sum_{e=1}^{N_e} |a(\hat{\eta}) \, [u^n]|_{\partial \Omega_e} &= \sum_{e=1}^{N_e} a\left(\hat{\eta}(X_{e+1}^-)\right) [u^n(X_{e+1})] - a\left(\hat{\eta}(X_e^+)\right) [u^n(X_e)] \\
&= \sum_{i=1}^{N_v} [a(\hat{\eta}(X_i))] \, [u^n(X_i)] \, .
\end{aligned} \tag{A.8}$$

Combining (A.6), (A.7) and (A.8) yields formulation (2.14). Finally, we arrive at formulation (2.15) by putting together both sums. That is, we can write

$$
\sum_{i=1}^{N_v} \langle u^n(X_i) \rangle [\hat{\eta}(X_i)] + [u^n(X_i)] \langle \hat{\eta}(X_i) \rangle + \sum_{i=1}^{N_v} [a(\hat{\eta}(X_i))] [u^n(X_i)]
$$

$$
= \sum_{i=1}^{N_v} \langle u^n(X_i) \rangle [\hat{\eta}(X_i)]
$$

$$
+ \sum_{i=1}^{N_v} [u^n(X_i)] \left(\langle \hat{\eta}(X_i) \rangle + \left(\lambda - \frac{1}{2} \right) \hat{\eta}(X_i^-) - \left(\lambda + \frac{1}{2} \right) \hat{\eta}(X_i^+) \right) \qquad \text{(A.9)}
$$

$$
= \sum_{i=1}^{N_v} \langle u^n(X_i) \rangle [\hat{\eta}(X_i)] + \sum_{i=1}^{N_v} [u^n(X_i)] \lambda [\hat{\eta}(X_i)]
$$

$$
= \sum_{i=1}^{N_v} [\hat{\eta}(X_i)] \langle u^n(X_i) \rangle_\lambda ,
$$

where $\langle f(X_i) \rangle_\lambda$ is a weighted average:

$$
\langle f(X_i) \rangle_\lambda = \left(\frac{1}{2} + \lambda \right) f(X_i^-) + \left(\frac{1}{2} - \lambda \right) f(X_i^+).
$$

Appendix B

Complementary material to Chapter 3

Any given zonal shear flow $(\bar{u}(y), 0)$ – henceforth called basic state – is solution to the *steady-state* nonlinear system of equations (3.4)-(3.6), provided that the elevation $\bar{\eta}$ be in geostrophic equilibrium. In this case, the equations reduce to

$$(1 + \beta y)\bar{u}(y) = -\frac{d\bar{\eta}}{dy},$$

whereupon $\eta(y)$ can be solved for, up to an arbitrary additive constant. Now, given such a basic flow $(\bar{u}(y), 0, \bar{\eta}(y))$, and beyond knowing whether it is stable or not, we are interested in the evolution of perturbations (u', v', η') of this basic state. We may recast the problem unknowns in terms of sums of (known) basic state variables and perturbations unknowns, the latter being much smaller in amplitude than the basic state variables. We thus rest within the realm of linear stability analysis insofar as all products of perturbation variables may safely be neglected. In so doing, we have

$$
\begin{aligned}
u(x, y, t) &= \bar{u}(y) + u'(x, y, t), \\
v(x, y, t) &= v'(x, y, t), \\
\eta(x, y, t) &= \bar{\eta}(y) + \eta'(x, y, t),
\end{aligned}
$$

and substituting these variables into (3.4)-(3.6) yields the following linearized evolution equations for the perturbations

$$\frac{\partial u'}{\partial t} + \bar{u}\frac{\partial u'}{\partial x} + v'\frac{d\bar{u}}{dy} - (1 + \beta y)v' = -\frac{\partial \eta'}{\partial x}, \tag{B.1}$$

$$\frac{\partial v'}{\partial t} + \bar{u}\frac{\partial v'}{\partial x} + (1 + \beta y)u' = -\frac{\partial \eta'}{\partial y}, \tag{B.2}$$

$$\frac{\partial \eta'}{\partial t} + \alpha^2\frac{\partial u'}{\partial x} + \alpha^2\frac{\partial v'}{\partial y} = 0. \tag{B.3}$$

Wavy disturbances in the x-direction are solutions to (B.1)-(B.3):

$$
\begin{aligned}
u'(x,y,t) &= U(y)e^{ik(x-ct)}, \\
v'(x,y,t) &= V(y)e^{ik(x-ct)}, \\
\eta'(x,y,t) &= H(y)e^{ik(x-ct)}.
\end{aligned}
$$

where k is the zonal wavenumber, $c = c_r + ic_i$ is the complex phase speed and kc_i denotes the growth rate. Substituting these expressions into (B.1)-(B.3) yields the following coupled system of ordinary differential equations (ODEs) in $U(y)$, $V(y)$ and $H(y)$:

$$
\begin{aligned}
-kc\, U(y) + ik\, \bar{u}\, U(y) - (1+\beta y)V(y) &= -ik\, H(y), \\
-kc\, V(y) + ik\, \bar{u}\, V(y) + (1+\beta y)U(y) &= -\frac{dH}{dy}, \\
-kc\, H(y) + \alpha^2\, ik\, U(y) + \alpha^2\, \frac{dV}{dy} &= 0,
\end{aligned}
$$

to which the trivial solution $U = V = H = 0$ is to be ruled out. In order to have instability, it is required that the disturbances grow exponentially in time. Deriving necessary (and sufficient) conditions for instability – in terms of the basic state and the flow parameters – is far from being tractable if we deal with the above system of ODEs, where $\bar{u}(y)$ is itself a function of y. However, it is a very well-known problem for rigid-lid formulations (*Pedlosky*, 1979; *Cushman-Roisin*, 1994). In that case, the time derivative of the elevation disappears from the continuity equation (B.3) and the pressure gradient replaces the elevation gradient in the momentum equations (B.1) and (B.2). We are then free to define a perturbation stream function and the eigenvalue problem reduces to one that involves a single equation in the perturbation stream function,

$$
\left(\frac{\partial}{\partial t} + \bar{u}\frac{\partial}{\partial x}\right)\nabla^2\psi' + (\beta - \frac{d^2\bar{u}}{dy^2})\psi' = 0,
$$

whose general solution is

$$
\psi'(x,y,t) = \phi(y)e^{ik(x-ct)},
$$

with $u' = -\frac{\partial\psi'}{\partial y}$ and $v' = \frac{\partial\psi'}{\partial x}$. This leads to an ODE for $\phi(y)$

$$
\frac{d^2\phi}{dy^2} - k^2\phi + \frac{\beta - \frac{d^2\bar{u}}{dy^2}}{\bar{u} - c}\phi = 0. \tag{B.4}
$$

Requiring that $c_i > 0$ to have growing instabilities translates to necessary conditions on the basic state. Assuming the existence of parallel boundaries at $y = y_1$ and $y = y_2$, where the perturbation stream function ψ' vanishes, integral properties may be established (*Kuo*, 1978; *Cushman-Roisin*, 1994). Multiplying (B.4) by the conjugate function ϕ^* and integrating the result across the entire domain gives rise to

$$
-\int_{y_1}^{y_2}\left(\left|\frac{d\phi}{dy}\right|^2 + \kappa^2|\phi|^2\right)dy + \int_{y_1}^{y_2}\frac{\beta - d^2\bar{u}/dy^2}{\bar{u} - c}|\phi|^2\,dy = 0, \tag{B.5}
$$

whose imaginary part is

$$c_i \int_{y_1}^{y_2} \left(\beta - \frac{d^2 \bar{u}}{dy^2} \right) \frac{|\phi|^2}{|\bar{u} - c|^2} \, dy = 0. \tag{B.6}$$

Therefore, requiring that $c_i > 0$ implies that the integrand of (B.6) must change sign. This leads to the first necessary condition for instability, namely that the expression $\beta - d^2 \bar{u}/dy^2$ must vanish within the domain. Considering the real part of (B.5), we get

$$\int_{y_1}^{y_2} (\bar{u} - c_r) \left(\beta - \frac{d^2 \bar{u}}{dy^2} \right) \frac{|\phi|^2}{|\bar{u} - c|^2} \, dy = \int_{y_1}^{y_2} \left(\left| \frac{d\phi}{dy} \right|^2 + \kappa^2 |\phi|^2 \right) \, dy. \tag{B.7}$$

Now, if the flow is unstable, the integral in (B.6) vanishes so that we may multiply it by $(c_r - \bar{u}_0)$, for any real constant $\bar{u}_0$, and add the result to (B.7) to obtain

$$\int_{y_1}^{y_2} (\bar{u} - \bar{u}_0) \left(\beta - \frac{d^2 \bar{u}}{dy^2} \right) \frac{|\phi|^2}{|\bar{u} - c|^2} \, dy > 0, \tag{B.8}$$

which is equivalent to demanding that the expression

$$(\bar{u} - \bar{u}_0) \left(\beta - \frac{d^2 \bar{u}}{dy^2} \right)$$

be positive in some finite portion of the domain. Hence, for the flow to be unstable, the following criteria must be met:

1. $\beta - \frac{d^2 \bar{u}}{dy^2}$ must vanish at least once within the domain,

2. $(\bar{u} - \bar{u}_0) \left(\beta - \frac{d^2 \bar{u}}{dy^2} \right)$ must be positive in at least some finite portion of the domain.

In the second condition, $\bar{u}_0$ is the value of $\bar{u}(y)$ where the expression of the first condition vanishes because it must be true for any real constant.

137

Appendix C

Complementary material to Chapter 4

C.1 Derivation of variational statements for DG

We now derive the variational formulations of the elevation, continuity and tracer equations for the discontinuous Galerkin method. The latter requires to evaluate integrals on interior geometric items, which are hereafter defined. In two dimensions, we consider the set E^h of all interelement edges $E_e = \partial \overline{\mathcal{T}_e} \cap \partial \overline{\mathcal{T}_f}$ with $e > f$ (Figure 4.2). This set comprises all edges shared between adjacent triangles belonging to $\mathcal{T}^h$. We thus have

$$\overline{E^h} = \bigcup_{e=1}^{N_e} \overline{E_e} \qquad \text{and} \qquad E_e \cap E_f = \emptyset \quad (e \neq f),$$

where N_e is the number of such interelement edges. To each edge E_e corresponds a unique normal vector $(\mathbf{n}^e, n_z^e)$ pointing from $\mathcal{T}_e$ to $\mathcal{T}_f$. Similarly to the velocity, the horizontal components of the unit normal are written in vector form and denoted by $\mathbf{n}^e$. In three dimensions, we consider the set F^h of all interelement vertical rectangular faces $F_e = \partial \overline{\Omega_e} \cap \partial \overline{\Omega_f}$ with $e > f$ (Figure 4.2). This set comprises all faces shared between adjacent prisms in adjacent columns but does not comprise those faces shared by two prisms within the same column. It is important to keep in mind that those faces remain vertical at all time. We have

$$\overline{F^h} = \bigcup_{e=1}^{N_f} \overline{F_e} \qquad \text{and} \qquad F_e \cap F_f = \emptyset \quad (e \neq f),$$

where N_f is the number of such vertical interelement faces. To each face F_e corresponds a unique normal vector $(\mathbf{n}^e, n_z^e)$ pointing from Ω_e to Ω_f. Finally, the set S^h comprises those triangular faces shared by prisms within the same column, that is shared by prisms stacked upon one another. Each of those triangular faces will be

noted $S_e = \partial\overline{\Omega_e} \cap \partial\overline{\Omega_f}$ with $e > f$ (Figure 4.2). We have

$$\overline{S^h} = \bigcup_{e=1}^{N_s} \overline{S_e} \qquad \text{and} \qquad S_e \cap S_f = \emptyset \quad (e \neq f),$$

where N_s is the number of such triangular faces. A unique normal $(\mathbf{n}^e, n_z^e)$, pointing from Ω_e to Ω_f, is associated to each triangular face S_e.

In what follows, we use the same notation for all the functional spaces as that used for the continuous Galerkin method. We must be aware, though, that the spaces are different and must be defined elementwise since the sought approximtions remain undefined across element boundaries. We do not want to delve into this here and prefer to refer the interested reader to appropriate references (*Cockburn et al.*, 2000; *Flaherty et al.*, 2002).

Free-surface elevation equation

Starting from Eq. (4.17), integrating the divergence term by parts and defining the depth-averaged velocity as follows,

$$\overline{\mathbf{u}} = \frac{1}{H} \int_{-d}^{\eta} \mathbf{u} \, dz,$$

the variational statement becomes

$$\sum_{e=1}^{N_t} \int_{\mathcal{T}_e} \left\{ \frac{\partial\eta}{\partial t}\hat{\eta} - \left(\int_{-h}^{\eta} \mathbf{u} \, dz \right) \cdot \boldsymbol{\nabla}\hat{\eta} \right\} d\tau$$

$$+ \sum_{e=1}^{N_t} \int_{\partial\mathcal{T}_e} H\overline{\mathbf{u}} \cdot \mathbf{n}\hat{\eta} \, ds = 0 \quad \forall\hat{\eta} \in \mathcal{H},$$

where $\partial\mathcal{T}_e$ denotes the boundary of $\mathcal{T}_e$. By using the fact that $\boldsymbol{\nabla}\hat{\eta}$ is independent of z, the above expression can be rewritten as

$$\sum_{e=1}^{N_t} \int_{\mathcal{T}_e} \frac{\partial\eta}{\partial t}\hat{\eta} \, d\tau - \sum_{e=1}^{N_p} \int_{\Omega_e} \mathbf{u} \cdot \boldsymbol{\nabla}\hat{\eta} \, d\Omega$$

$$+ \sum_{e=1}^{N_t} \int_{\partial\mathcal{T}_e} H\overline{\mathbf{u}} \cdot \mathbf{n}\hat{\eta} \, ds = 0 \quad \forall\hat{\eta} \in \mathcal{H}. \tag{C.1}$$

The last term in Eq. (C.1) involves integrals on interelement edges (interior edges) and integrals on boundary edges. The latter, that is the integral on $\partial\mathcal{T}^h$, vanishes by weakly enforcing the impermeability condition on the transport $H\overline{\mathbf{u}}$. The last summation in Eq. (C.1) thus involves only integrals over interior edges and can be expressed as the following new summation:

$$\sum_{e=1}^{N_t} \int_{\partial\mathcal{T}_e} H\overline{\mathbf{u}} \cdot \mathbf{n}\hat{\eta} \, ds = \sum_{e=1}^{N_e} \int_{E_e} \left\{ (H\overline{\mathbf{u}})_{|\Omega_e} \cdot \mathbf{n}^e\hat{\eta}_{|\Omega_e} - (H\overline{\mathbf{u}})_{|\Omega_e} \cdot \mathbf{n}^e\hat{\eta}_{|\Omega_f} \right\} ds$$

$$= \sum_{e=1}^{N_e} \int_{E_e} \left\{ \langle H\overline{\mathbf{u}} \cdot \mathbf{n}^e \rangle [\hat{\eta}] + [H\overline{\mathbf{u}} \cdot \mathbf{n}^e] \langle\hat{\eta}\rangle \right\} ds, \tag{C.2}$$

where the following equality has been used

$$ac - bd = \frac{1}{2}(a + b)(c - d) + \frac{1}{2}(a - b)(c + d)$$

and the jump and mean operators are defined as

$$[g] = g_{|\mathcal{T}_e} - g_{|\mathcal{T}_f},$$
$$\langle g \rangle = \frac{1}{2}\left(g_{|\mathcal{T}_e} + g_{|\mathcal{T}_f} \right),$$

respectively. In Eq. (C.2), we discard the term $[H\overline{\mathbf{u}} \cdot \mathbf{n}^e]\,\langle \hat{\eta} \rangle$ to weakly enforce the continuity of the flux $H\overline{\mathbf{u}} \cdot \mathbf{n}^e$. Therefore, Eq. (C.2) becomes

$$\sum_{e=1}^{N_t} \int_{\partial \mathcal{T}_e} H\overline{\mathbf{u}} \cdot \mathbf{n}\hat{\eta}\,\mathrm{d}s = \sum_{e=1}^{N_e} \int_{E_e} \langle H\overline{\mathbf{u}} \cdot \mathbf{n}^e \rangle\,[\hat{\eta}]\,\mathrm{d}s.$$

We end up with the following variational statement:

$$
\begin{aligned}
&\sum_{e=1}^{N_t} \int_{\mathcal{T}_e} \frac{\partial \eta}{\partial t}\hat{\eta}\,\mathrm{d}\tau - \sum_{e=1}^{N_p} \int_{\Omega_e} \mathbf{u} \cdot \boldsymbol{\nabla}\hat{\eta}\,\mathrm{d}\Omega \\
&+ \sum_{e=1}^{N_e} \int_{E_e} \langle H\overline{\mathbf{u}} \cdot \mathbf{n}^e \rangle\,[\hat{\eta}]\,\mathrm{d}s = 0 \quad \forall \hat{\eta} \in \mathcal{H}.
\end{aligned}
\tag{C.3}
$$

Continuity equation

By integrating (4.19) by parts and after some algebraic manipulations (involving the weak enforcement of the flux continuity across element boundaries), we obtain

$$
-\sum_{e=1}^{N_p} \int_{\Omega_e} \left(\mathbf{u} \cdot \boldsymbol{\nabla}\hat{w} + w\frac{\partial \hat{w}}{\partial z} \right)\mathrm{d}\Omega + \underbrace{\int_{\Gamma_n^h} \hat{w}\,\mathbf{u} \cdot \mathbf{n}\,\mathrm{d}\Gamma}_{1} + \underbrace{\int_{\Gamma_b^h} \hat{w}\,(\mathbf{u} \cdot \mathbf{n} + wn_z)\,\mathrm{d}\tau}_{2}
$$

$$
+ \underbrace{\int_{\Gamma_s^h} \hat{w}\,(\mathbf{u} \cdot \mathbf{n} + wn_z)\,\mathrm{d}\tau}_{3} + \underbrace{\sum_{e=1}^{N_f} \int_{F_e} \langle \mathbf{u} \cdot \mathbf{n}^e \rangle\,[\hat{w}]\,\mathrm{d}\Gamma}_{4} + \underbrace{\sum_{e=1}^{N_s} \int_{S_e} \langle \mathbf{u} \cdot \mathbf{n}^e \rangle\,[\hat{w}]\,\mathrm{d}\tau}_{5}
$$

$$
+ \underbrace{\sum_{e=1}^{N_s} \int_{S_e} [\hat{w}]\,w_{|\Omega_e}\,n_z^e\mathrm{d}\tau}_{6} = 0 \quad \forall \hat{w} \in \mathcal{W}.
$$

A closer look at the terms labeled 1 to 6 will shed light on their meaning. By enforcing boundary conditions (4.1) and (4.6), integrals 1 and 2 vanish. Integral 3 does not vanish and must be computed in order to know the vertical velocity on Γ_s^h. The remaining three sums involve integrals over interior geometric items. Integrals 4 occur over interior vertical faces, which explains why the vertical velocity does not appear. Similarly, integrals 5 occur over all interior triangles (which are merely the lower and

upper faces of each prism). Despite the cumbersome notations, summations 4 and 5 are intuitive and simply state that the mean horizontal velocity must be used when computing the fluxes. Integrals 6 state that whenever the normal velocity is integrated over an interior triangle S_e, we use the vertical velocity lying within the lower element – that is Ω_e according to Figure (4.2) – rather than the mean vertical velocity. This amounts to integrating the continuity equation from the bottom upwards will full up-wind weighting on the vertical velocity belonging to the element below the triangular face. In an intuitive interpretation, the continuity equation can be viewed as a steady-state advection equation (with the advective velocity equal to one) with source term (the horizontal velocity divergence), which might help clarify the approach described herebefore. Note that the boundary condition (4.6) at the seabed is a natural boundary condition that is automatically incorporated into the variational statement. The latter becomes

$$
-\sum_{e=1}^{N_p} \int_{\Omega_e} \left(\mathbf{u} \cdot \boldsymbol{\nabla} \hat{w} + w \frac{\partial \hat{w}}{\partial z} \right) \mathrm{d}\Omega + \int_{\Gamma_s^h} \hat{w} \left(\mathbf{u} \cdot \mathbf{n} + w n_z \right) \mathrm{d}\tau
$$

$$
+ \sum_{e=1}^{N_f} \int_{F_e} \langle \mathbf{u} \cdot \mathbf{n}^e \rangle \, [\hat{w}] \, \mathrm{d}\Gamma + \sum_{e=1}^{N_s} \int_{S_e} \langle \mathbf{u} \cdot \mathbf{n}^e \rangle \, [\hat{w}] \, \mathrm{d}\tau \qquad \text{(C.4)}
$$

$$
+ \sum_{e=1}^{N_s} \int_{S_e} [\hat{w}] \, w_{|\Omega_e} \, n_z^e \mathrm{d}\tau = 0 \quad \forall \, \hat{w} \in \mathcal{W}.
$$

Tracer equation

Due to consistency requirements, the variational statement for the tracer equation is very closely related to that for the continuity equation. Because the DG variational statement includes a great number of terms, we only include advection. Considering Eq. (4.23) and integrating the second term by parts leads to

$$
\sum_{e=1}^{N_p} \int_{\Omega_e(t)} \left(\boldsymbol{\nabla} \cdot (\mathbf{u}C) + \frac{\partial (\tilde{w}C)}{\partial z} \right) \hat{C} \, \mathrm{d}\Omega =
$$

$$
- \sum_{e=1}^{N_p} \int_{\Omega_e(t)} C \left(\mathbf{u} \cdot \boldsymbol{\nabla} \hat{C} + \tilde{w} \frac{\partial \hat{C}}{\partial z} \right) \mathrm{d}\Omega + \int_{\Gamma_s^h} C \hat{C} \left(\mathbf{u} \cdot \mathbf{n} + \tilde{w} n_z \right) \mathrm{d}\tau
$$

$$
+ \sum_{e=1}^{N_f} \int_{F_e} \langle C \mathbf{u} \cdot \mathbf{n}^e \rangle \, [\hat{C}] \mathrm{d}\Gamma + \sum_{e=1}^{N_s} \int_{S_e} \langle C \mathbf{u} \cdot \mathbf{n}^e \rangle \, [\hat{C}] \mathrm{d}\tau \qquad \text{(C.5)}
$$

$$
+ \sum_{e=1}^{N_s} \int_{S_e} [\hat{C}] C \tilde{w}_{|\Omega_e} \, n_z^e \mathrm{d}\tau.
$$

Note that the left-hand side of Eq. (C.5) is nothing but the variational statement of the continuity equation (see Eq. C.4) in which the velocity is multiplied by the tracer concentration C, the test function $\hat{w}$ is replaced by $\hat{C}$ and the modified vertical velocity $\tilde{w}$ is used in place of the vertical velocity w. Now, substituting the second summation in Eq. (4.23) for Eq. (C.5), the variational statement consists in finding $C \in \mathcal{G}$ such

that

$$
\sum_{e=1}^{N_p} \frac{\mathrm{d}}{\mathrm{d}t} \int_{\Omega_e(t)} C\hat{C} \, \mathrm{d}\Omega - \sum_{e=1}^{N_p} \int_{\Omega_e(t)} C \left(\mathbf{u} \cdot \boldsymbol{\nabla} \hat{C} + \tilde{w} \frac{\partial \hat{C}}{\partial z} \right) \mathrm{d}\Omega
$$

$$
+ \int_{\Gamma_s^h} C\hat{C} \left(\mathbf{u} \cdot \mathbf{n} + \tilde{w} n_z \right) \mathrm{d}\tau \sum_{e=1}^{N_f} \int_{F_e} \langle C\mathbf{u} \cdot \mathbf{n}^e \rangle [\hat{C}] \mathrm{d}\Gamma \tag{C.6}
$$

$$
+ \sum_{e=1}^{N_s} \int_{S_e} \langle C\mathbf{u} \cdot \mathbf{n}^e \rangle [\hat{C}] \mathrm{d}\tau + \sum_{e=1}^{N_s} \int_{S_e} [\hat{C}] C \tilde{w}_{|\Omega_e} n_z^e \mathrm{d}\tau = 0 \quad \forall \hat{C} \in \mathcal{G}.
$$

C.2 Functional spaces

The space $\mathcal{L}_2(\Omega)$ contains those functions that are square integrable, i.e.,

$$
\mathcal{L}_2(\Omega) = \left\{ f : \int_\Omega |f|^2 \, \mathrm{d}\Omega < \infty \right\}.
$$

The space $\mathcal{H}_1(\Omega)$ contains those functions belonging to $\mathcal{L}_2(\Omega)$ and whose first weak derivatives belong to $\mathcal{L}_2(\Omega)$ as well. That is

$$
\mathcal{H}_1(\Omega) = \{ f \in \mathcal{L}_2(\Omega) : \forall i = 1 \ldots d, \ \partial_{x_i} f \in \mathcal{L}_2(\Omega) \},
$$

where d is the dimension of the space ($d = 3$ for the usual physical space). The space $\mathcal{H}_{div}(\Omega)$ contains those functions that belong to $\mathcal{L}_2(\Omega)$ and whose divergence belongs to $\mathcal{L}_2(\Omega)$:

$$
\mathcal{H}_{div}(\Omega) = \left\{ \mathbf{f} = (f_1, \ldots, f_d) \in \mathcal{L}_2(\Omega)^d : \frac{\partial f_i}{\partial x_i} \in \mathcal{L}_2(\Omega) \right\}.
$$

Finally, the space $\mathcal{W}$ involved in the variational statement for the continuity equation, Eq. (4.19), is defined as

$$
\mathcal{W} = \left\{ \hat{w} \in \mathcal{L}_2(\Omega) : \int_\Omega |u \frac{\partial \hat{w}}{\partial x} + v \frac{\partial \hat{w}}{\partial y} + w \frac{\partial \hat{w}}{\partial z} | \mathrm{d}\Omega < \infty, \ \forall (u, v, w) \in \mathcal{H}_{div}(\Omega) \right\}.
$$

C.3 Downward integration of the continuity equation

In Chapter 4, the continuity equation is integrated upwards after imposing the kinematic boundary condition at the seabed. By doing so, and provided that the continuity and elevation equations be discretely compatible, the discrete surface kinematic boundary condition is automatically retrieved. Herein, we show that an equivalent result is obtained by integrating the continuity equation downwards after imposing the kinematic boundary condition at the surface. Let us consider the discrete variational statement for the continuity equation, inferred from Eq. (4.29), in which boundary conditions are yet to be prescribed. We have

$$
- \int_{\Omega^h} \left[\mathbf{u}^h \cdot \boldsymbol{\nabla} \psi_i^w + w^h \frac{\partial \psi_i^w}{\partial z} \right] \mathrm{d}\Omega + \int_{\Gamma_b^h} \psi_i^w \left(\mathbf{u}^h \cdot \mathbf{n} + w^h n_z \right) \mathrm{d}\tau
$$

$$
+ \int_{\Gamma_s^h} \psi_i^w \left(\mathbf{u}^h \cdot \mathbf{n} + w^h n_z \right) \mathrm{d}\tau = 0 \quad \forall i = 1, 2, \ldots, N_w.
$$

Imposing the discrete counterpart of the surface kinematic boundary condition (4.7) gives rise to

$$- \int_{\Omega^h} \left[\mathbf{u}^h \cdot \boldsymbol{\nabla} \psi_i^w + w^h \frac{\partial \psi_i^w}{\partial z} \right] \mathrm{d}\Omega + \int_{\Gamma_b^h} \psi_i^w \left(\mathbf{u}^h \cdot \mathbf{n} + w^h n_z \right) \mathrm{d}\tau$$

$$+ \int_{\Gamma_s^h} \psi_i^w \frac{\partial \eta^h}{\partial t} n_z \mathrm{d}\tau = 0 \quad \forall \, i = 1, \, 2, \, \ldots, \, N_w.$$

We may now add up all components of the above expression pertaining to those test functions ψ_i^w sharing the same two-dimensional support (the indices belong to the set I). This yields the following expression, written for the two-dimensional projection of ψ_i^w ($i \in I$), noted $\psi_I^{w,2D}$:

$$- \int_{\Omega^h} \mathbf{u}^h \cdot \boldsymbol{\nabla} \psi_I^{w,2D} \mathrm{d}\Omega + \int_{\Gamma_b^h} \psi_I^{w,2D} \left(\mathbf{u}^h \cdot \mathbf{n} + w^h n_z \right) \mathrm{d}\tau$$

$$+ \int_{\Gamma_s^h} \psi_I^{w,2D} \frac{\partial \eta^h}{\partial t} n_z \mathrm{d}\tau = 0.$$

If we choose the basis functions for the vertical velocity such that $\psi_I^{w,2D} = \phi_i$, where ϕ_i is the two-dimensional elevation basis function associated with the same nodal position in the (x, y)-plane, the first and third terms of the above equation are identically equal to the discrete elevation equation, Eq. (4.28), which leaves us with

$$\int_{\Gamma_b^h} \psi_I^{w,2D} \left(\mathbf{u}^h \cdot \mathbf{n} + w^h n_z \right) \mathrm{d}\tau = 0,$$

namely the discrete counterpart of the kinematic boundary condition at the seabed, Eq. (4.6).

Appendix D

Complementary material to Chapter 5

To garner details on the coupling term $\mathbf{B}$ occurring in Eq. (5.25), we may spell out the equation in terms of its $x-$ and $y-$components. For the $x-$component, we have

$$
\begin{aligned}
\frac{\partial \overline{u}}{\partial t} + \overline{u}\frac{\partial \overline{u}}{\partial x} + \overline{v}\frac{\partial \overline{u}}{\partial y} - f\overline{v} + g\frac{\partial \eta}{\partial x} = \\
-\frac{1}{H}\frac{\partial}{\partial x}\int_{-d}^{\eta}\tilde{u}\tilde{u}\,\mathrm{d}z - \frac{1}{H}\frac{\partial}{\partial y}\int_{-d}^{\eta}\tilde{v}\tilde{u}\,\mathrm{d}z \\
+\frac{1}{H}\int_{-d}^{\eta}\boldsymbol{\nabla}\cdot(\nu_h\boldsymbol{\nabla}u)\,\mathrm{d}z + \frac{1}{\rho_0 H}\left(\tau_x^s - \tau_x\right)
\end{aligned}
\tag{D.1}
$$

while the $y-$component reads

$$
\begin{aligned}
\frac{\partial \overline{v}}{\partial t} + \overline{u}\frac{\partial \overline{v}}{\partial x} + \overline{v}\frac{\partial \overline{v}}{\partial y} + f\overline{u} + g\frac{\partial \eta}{\partial y} = \\
-\frac{1}{H}\frac{\partial}{\partial x}\int_{-d}^{\eta}\tilde{u}\tilde{v}\,\mathrm{d}z - \frac{1}{H}\frac{\partial}{\partial y}\int_{-d}^{\eta}\tilde{v}\tilde{v}\,\mathrm{d}z \\
+\frac{1}{H}\int_{-d}^{\eta}\boldsymbol{\nabla}\cdot(\nu_h\boldsymbol{\nabla}v)\,\mathrm{d}z + \frac{1}{\rho_0 H}\left(\tau_y^s - \tau_y\right)
\end{aligned}
\tag{D.2}
$$

In Eqs (D.1) and (D.2), we have defined

$$
\tilde{\mathbf{u}} = \mathbf{u} - \overline{\mathbf{u}},
$$

which is the deviation of the velocity relative to the depth-averaged velocity. The terms involving products of those deviations arise from depth-integration of advection terms. The bottom and surface stresses are denoted by $\boldsymbol{\tau}$ and $\boldsymbol{\tau}^s$, respectively. In Eqs (D.1)-(D.2), all terms involving the prognostic variables $(\overline{u}, \overline{v})$ can be time stepped. The momentum diffusion term is purposely written in terms of the full velocity field. Only when writing the variational statement of Eqs (D.1)-(D.2) are we able to elegantly derive expressions involving the depth-averaged and deviatory velocity components. It is carried out below. Upon inspection of Eqs (D.1)-(D.2), we

145

see that the right-hand side $\mathbf{B}$ of Eq. (5.25) is

$$\mathbf{B} = -\overline{u}\frac{\partial \overline{\mathbf{u}}}{\partial x} - \overline{v}\frac{\partial \overline{\mathbf{u}}}{\partial y} - \frac{1}{H}\frac{\partial}{\partial x}\int_{-d}^{\eta}\tilde{u}\tilde{\mathbf{u}}\,\mathrm{d}z - \frac{1}{H}\frac{\partial}{\partial y}\int_{-d}^{\eta}\tilde{v}\tilde{\mathbf{u}}\,\mathrm{d}z$$
$$+ \frac{1}{H}\int_{-d}^{\eta}\boldsymbol{\nabla}\cdot(\nu_h\boldsymbol{\nabla}\mathbf{u})\,\mathrm{d}z + \frac{1}{\rho_0 H}\left(\boldsymbol{\tau}^s - \boldsymbol{\tau}\right). \tag{D.3}$$

Let us now focus on the momentum diffusion term in the variational statement associated with Eq. (D.1). After multiplying the equation by a two-dimensional test function $\hat{u}$ and integrating over the unperturbed, two-dimensional domain $\mathcal{T}^h$, we obtain

$$\int_{\mathcal{T}^h}\frac{\hat{u}}{H}\int_{-d}^{\eta}\boldsymbol{\nabla}\cdot(\nu_h\boldsymbol{\nabla}u)\,\mathrm{d}z\,\mathrm{d}\tau = \quad -\int_{\mathcal{T}^h}\boldsymbol{\nabla}\left(\frac{\hat{u}}{H}\right)\cdot(H\nu_h\boldsymbol{\nabla}\overline{u})\,\mathrm{d}\tau$$
$$-\int_{\Omega^h}\boldsymbol{\nabla}\hat{u}\cdot(\nu_h\boldsymbol{\nabla}\tilde{u})\,\mathrm{d}\Omega \tag{D.4}$$
$$+\int_{\Omega^h}\frac{\hat{u}}{H^2}\boldsymbol{\nabla}H\cdot(\nu_h\boldsymbol{\nabla}\tilde{u})\,\mathrm{d}\Omega.$$

In Eq. (D.4), the first term in the left-hand side can be time stepped because it is expressed in terms of the prognostic variable $\overline{u}$. In that case, the term dissipates depth-averaged horizontal momentum.

Bibliography

Adcroft, A., and R. Hallberg (2006), On methods for solving the oceanic equations of motion in generalized vertical coordinates, *Ocean Model.*, *11*, 224–233.

Aizinger, V., and C. Dawson (2002), A discontinuous Galerkin method for two-dimensional flow and transport in shallow water, *Adv. Water Resour.*, *25*, 67–84.

Akin, J. E., T. Tezduyar, M. Ungor, and S. Mittal (2003), Stabilization parameters and Smagorinsky turbulence model, *Journal of Applied Mechanics*, *70*(1), 1–9.

Ballantyne, V. A., M. G. G. Foreman, W. R. Crawford, and R. Jacques (1996), Three-dimensional model simulations for the north coast of British Columbia, *Cont. Shelf Res.*, *16*, 1655–1682.

Beckers, J.-M., and E. Deleersnijder (1993), Stability of a FBTCS scheme applied to the propagation of shallow-water intertia-gravity waves on various space grids, *J. Comput. Phys.*, *108*(1), 95–104.

Berger, R. C., and S. E. Howington (2002), Discrete fluxes and mass balance in finite elements, *Journal of Hydraulic Engineering*, *128*(1), 87–92.

Bernard, P.-E., N. Chevaugeon, V. Legat, E. Deleersnijder, and J.-F. Remacle (accepted), High-order h-adaptive discontinuous Galerkin methods for ocean modeling, *Ocean Dynamics*.

Black, K. P., and S. L. Gay (1987), Eddy formation in unsteday flows, *J. Geophys. Res.*, *92*(C9), 9514–9522.

Blain, C. A., and T. C. Massey (2005), Application of a coupled discontinuous-continuous Galerkin finite element shallow water model to coastal ocean dynamics, *Ocean Model.*, *10*, 283–315.

Bleck, R. (1978), On the use of hybrid vertical coordinates in numerical weather prediction models, *Mon. Weather Rev.*, *106*, 1233–1244.

Blumberg, A. F., and G. L. Mellor (1987), A description of a three-dimensional coastal ocean circulation model, in *Three-Dimensional Coastal Ocean Models*, vol. 4, edited by N. S. Heaps, pp. 1–16, American Geophysical Union.

Bryan, K. (1969), A numerical method for the study of the circulation of the world ocean, *J. Comput. Phys.*, *4*, 347–376.

Campin, J.-M., A. Adcroft, C. Hill, and J. Marshall (2004), Conservation of properties in a free-surface model, *Ocean Model.*, *6*, 221–244.

Casulli, V., and R. A. Walters (2000), An unstructured grid, three-dimensional model based on the shallow-water equations, *Int. J. Numer. Methods Fluids*, *32*(3), 331–346.

Casulli, V., and P. Zanolli (2005), High resolution methods for multidimensional advection-diffusion problems in free-surface hydrodynamics, *Ocean Model.*, *10*, 137–151.

Cockburn, B., G. E. Karniadaki, and C.-W. Chu (Eds.) (2000), *Discontinuous Galerkin Methods: Theory, Computations and Applications*, 470 pp., Springer, Berlin.

Cockburn, B., G. E. Karniadakis, and C.-W. Chu (2001), Runge-Kutta discontinuous Galerkin methods for convection-dominated problems, *J. Sci. Comput.*, *16*(3), 173–261.

Coutis, P. F., and J. H. Middleton (1999), Flow-topography interaction in the vicinity of an isolated, deep ocean island, *Deep-Sea Res. Part I-Oceanogr. Res. Pap.*, *46*, 1633–1652.

Coutis, P. F., and J. H. Middleton (2002), The physical and biological impact of a small island wake in the deep ocean, *Deep-Sea Res. Part I-Oceanogr. Res. Pap.*, *49*, 1341–1361.

Cox, M. D. (1989), An idealized model of the world ocean. part I: the global-scale water masses, *J. Phys. Oceanogr.*, *19*, 1730–1752.

Cushman-Roisin, B. (Ed.) (1994), *Geophysical Fluid Dynamics*, Prentice Hall, Upper Saddle River, NJ.

Cushman-Roisin, B., and C. E. Naimie (2002), A 3D finite-element model of the Adriatic tides, *J. Mar. Syst.*, *37*(4), 279–297.

Danilov, S., G. Kivman, and J. Schröter (2004), A finite-element ocean model: principles and evaluation, *Ocean Model.*, *6*, 125–150.

Danilov, S., G. Kivman, and J. Schröter (2005), Evaluation of an eddy-permitting finite-element ocean model in the North Atlantic, *Ocean Model.*, *10*, 35–49.

Dawson, C., J. J. Westerink, J. C. Feyen, and D. Pothina (2006), Continuous, discontinuous and coupled discontinuous-continuous Galerkin finite element methods for the shallow water equations, *Int. J. Numer. Methods Fluids*, *52*, 63–88.

Deleersnijder, E. (1989), Upwelling and upsloping in three-dimensional marine models, *Appl. Math. Model.*, *13*, 462–467.

Deleersnijder, E. (1993), Numerical mass conservation in a free-surface sigma coordinate marine model with mode splitting, *J. Mar. Syst.*, *4*, 365–370.

Deleersnijder, E. (1994), An analysis of the vertical velocity field computed by a three-dimensional model in the region of the Bering Strait, *Tellus Ser. A*, *46*, 134–148.

Deleersnijder, E., and J.-M. Campin (1995), On the computation of the barotropic mode of a free-surface world ocean model, *Ann. Geophys.*, *13*, 675–688.

Deleersnijder, E., and K. G. Ruddick (1989), A generalized vertical coordinate for 3D marine models, *Bulletins de la Société Royale des Sciences de Liège*, *61*(6), 489–502.

Deleersnijder, E., A. Norro, and E. Wolanski (1992), A three-dimensional model of the water circulation around an island in shallow water, *Cont. Shelf Res.*, *12*(7/8), 891–906.

Deleersnijder, E., J.-M. Campin, and E. J. M. Delhez (2001), The concept of age in marine modelling: I. Theory and preliminary results, *J. Mar. Syst.*, *28*, 229–267.

Delhez, E. J. M., and E. Deleersnijder (2002), The concept of age in marine modelling: II. Concentration distribution function in the English Channel and the North Sea, *J. Mar. Syst.*, *31*, 279–297.

Delhez, E. J. M., J.-M. Campin, A. C. Hirst, and E. Deleersnijder (1999), Toward a general theory of the age in ocean modelling, *Ocean Model.*, *1*, 17–27.

Delhez, E. J. M., A. W. Heemink, and E. Deleersnijder (2004), Residence time in a semi-enclosed domain from the solution of an adjoint problem, *Estuar. Coast. Shelf Sci.*, *61*, 691–702.

Dickey, T. D. (2003), Emerging ocean observations for interdisciplinary data assimilation systems, *J. Mar. Syst.*, *40-41*, 5–48.

Dickinson, R. E., and F. J. Clare (1973), Numerical study of the unstable modes of a hyperbolic-tangent barotropic shear, *J. Atmos. Sci.*, *30*, 1035–1049.

Donea, J., A. Huerta, J.-P. Ponthot, and A. Rodríguez-Ferran (2004), Arbitrary Lagrangian-Eulerian methods, in *Encyclopedia of Computational Mechanics*, edited by E. Stein, R. de Borst, and T. J. R. Hughes, chap. 14, John Wiley and Sons.

Dukowicz, J. K., and R. D. Smith (1994), Implicit free-surface method for the Bryan-Cox-Semtner ocean model, *J. Geophys. Res.*, *99*(4), 7991–8014.

Falconer, R. A., E. Wolanski, and L. Mardapitta-Hadjipandeli (1986), Modeling tidal circulation in an island's wake, *J. Waterw. Port Coast. Ocean Eng.-ASCE*, *112*, 234–254.

Farhat, C., P. Geuzaine, and C. Grandmont (2001), The discrete geometric conservation law and the nonlinear stability of ALE schemes for the solution of flow problems on moving grids, *J. Comput. Phys.*, *174*, 669–694.

Fischer, H. B., E. Y. List, R. C. Y. Koh, J. Imberger, and N. H. Brooks (1979), *Mixing in inland and coastal waters*, Academic Press, New York.

Fix, G. J. (1975), Finite element models for ocean circulation problems, *SIAM J. Appl. Math.*, *29*, 371–387.

Flaherty, J. E., L. Krivodonova, J.-F. Remacle, and M. S. Shephard (2002), Aspects of discontinuous Galerkin methods for hyperbolic conservation laws, *Finite Elements in Analysis and Design*, *38*(10), 889–908.

Flather, R. A. (1976), A tidal model of the northwest European continental shelf, *Mémoires de la Société Royale des Sciences de Liège*, *6*(10), 141–164.

Ford, R., C. C. Pain, M. D. Piggott, A. J. H. Goddard, C. R. E. de Oliveira, and A. P. Umpleby (2004a), A non-hydrostatic finite element model for three-dimensional stratified oceanic flows. Part I: model formulation, *Mon. Weather Rev.*, *132*, 2816–2831.

Ford, R., C. C. Pain, M. D. Piggott, A. J. H. Goddard, C. R. E. de Oliveira, and A. P. Umpleby (2004b), A non-hydrostatic finite element model for three-dimensional stratified oceanic flows. Part II: model validation, *Mon. Weather Rev.*, *132*, 2832–2844.

Foreman, M. G. G., R. A. Walters, R. F. Henry, C. P. Keller, and A. G. Dolling (1995), A tidal model for the eastern Juan de Fuca Strait and the southern Strait of Georgia, *J. Geophys. Res.*, *100*(C1), 721–740.

Formaggia, L., and F. Nobile (2004), Stability analysis of second-order time accurate schemes for ALE-FEM, *Comput. Meth. Appl. Mech. Eng.*, *193*, 4097–4116.

Fortunato, A. B., A. M. Baptista, and R. A. Luettich (1997), A three-dimensional model of tidal currents in the mouth of the Tagus estuary, *Cont. Shelf Res.*, *17*(14), 1689–1714.

Fringer, O. B., M. Gerritsen, and R. L. Street (2006), An unstructured-grid, finite-volume, nonhydrostatic, parallel coastal ocean simulator, *Ocean Model.*, *14*, 139–173.

Gent, P., and J. C. McWilliams (1990), Isopycnal mixing in ocean circulation models, *J. Phys. Oceanogr.*, *20*, 150–155.

Gerdes, R. (1993), A primitive equation ocean circulation model using a general vertical coordinate transformation 1. Description and testing of the model, *J. Geophys. Res.*, *98*(C8), 14,683–14,701.

Gill, A. E. (1976), Adjustment under gravity in a rotating channel, *J. Fluid Mech.*, *77*, 603–621.

Gill, A. E. (1982), *Atmosphere-Ocean Dynamics*, Academic Press.

Goosse, H., J.-M. Campin, and B. Tartinville (2001), The sources of Antarctic bottom water in a global ice-ocean model, *Ocean Model.*, *3*, 51–65.

Gorman, G. J., M. D. Piggott, C. C. Pain, C. R. E. de Oliveira, A. P. Umpleby, and A. J. H. Goddard (2006), Optimisation based bathymetry approximation through constrained unstructured mesh adaptivity, *Ocean Model.*, *12*, 436–452.

Greenberg, D. A., F. E. Werner, and D. R. Lynch (1998), A diagnostic finite element ocean circulation model in spherical-polar coordinates, *J. Atmos. Ocean. Technol.*, *15*, 942–958.

Gresho, P. M., and R. L. Sani (1987), On pressure boundary conditions for the incompressible Navier-Stokes equations, *Int. J. Numer. Methods Fluids*, *7*, 1111–1145.

Gresho, P. M., and R. L. Sani (1998), *Incompressible flow and the finite element method*, John Wiley and Sons.

Gresho, P. M., S. T. Chan, R. L. Lee, and C. D. Upson (1984), A modified finite element method for solving the time-dependent, incompressible Navier-Stokes equations. Part 1: theory., *Int. J. Numer. Methods Fluids*, *4*, 557–598.

Griffies, S. M. (2004), *Fundamentals of Ocean Climate Models*, 496 pp., Princeton University Press, Princeton (New Jersey).

Griffies, S. M., and R. W. Hallberg (2000), Biharmonic friction with a Smagorinsky-like viscosity for use in large-scale eddy-permitting ocean models, *Mon. Weather Rev.*, *128*, 2935–2946.

Griffies, S. M., C. Böning, F. O. Bryan, E. P. Chassignet, R. Gerdes, H. Hasumi, A. Hirst, A.-M. Treguier, and D. Webb (2000), Developments in ocean climate modelling, *Ocean Model.*, *2*, 123–192.

Griffies, S. M., R. C. Pacanowski, M. Schmidt, and V. Balah (2001), Tracer conservation with an explicit free surface method for z-coordinate ocean models, *Mon. Weather Rev.*, *129*, 1081–1098.

Hallberg, R. (1997), Stable split time stepping scheme for large-scale ocean modeling, *J. Comput. Phys.*, *135*, 54–65.

Ham, D. A., J. Pietrzak, and G. S. Stelling (2005), A scalable unstructured grid 3-dimensional finite volume model for the shallow water equations, *Ocean Model.*, *10*, 153–169.

Hamner, W. M., and I. R. Hauri (1981), Effects of island mass: water flow and plankton pattern around a reef in the Great Barrier Reef lagoon, Australia, *Limnol. Oceanogr.*, *26*(6), 1084–1102.

Hanert, E., V. Legat, and E. Deleersnijder (2003), A comparison of three finite elements to solve the linear shallow water equations, *Ocean Model.*, *5*, 17–35.

Hanert, E., D. Y. Le Roux, V. Legat, and E. Deleersnijder (2004), Advection shemes for unstructured grid ocean modelling, *Ocean Model.*, *7*, 39–58.

Hanert, E., D. Y. Le Roux, V. Legat, and E. Deleersnijder (2005), An efficient Eulerian finite element method for the shallow water equations, *Ocean Model.*, *10*, 115–136.

Haney, R. L. (1991), On the pressure gradient force over steep topography in sigma coordinates, *J. Phys. Oceanogr.*, *21*, 610–619.

Hart, J. E. (1974), On the mixed stability problem for quasi-geostrophic ocean currents, *J. Phys. Oceanogr.*, *4*, 349–356.

Higdon, R. L. (2002), A two-level time-stepping method for layered ocean circulation models, *J. Comput. Phys.*, *177*, 59–94.

Higdon, R. L., and R. A. d. Szoeke (1997), Barotropic-baroclinic time splitting for ocean circulation modeling, *J. Comput. Phys.*, *135*, 30–53.

Hirst, A. C. (1999), Determination of water component age in ocean models: application to the fate of North Atlantic Deep Water, *Ocean Model.*, *1*, 81–94.

Hodges, B. R. (2004), Accuracy order of Crank-Nicolson discretization for hydrostatic free-surface flow, *Journal of Engineering Mechanics*, *130*(8), 904–910.

Houston, P., C. Schwab, and A. Süli (2002), Discontinuous hp-finite element methods for advection-diffusion-reaction problems, *SIAM J. Numer. Anal.*, *39*(6), 2133–2163.

Howard, L. N. (1964), The number of unstable modes in hydrodynamics stability problems, *Journal de Mécanique*, *3*, 433–443.

Hua, B.-L., and F. Thomasset (1984), A noise-free finite element scheme for the two-layer shallow water equations, *Tellus Ser. A*, *36*, 157–165.

Huang, R. X. (1993), Real freshwater flux as a natural boundary condition for the salinity balance and thermohaline circulation forced by evaporation and precipitation, *J. Phys. Oceanogr.*, *23*, 2428–2446.

Huang, R. X., and R. L. Chou (1994), Parameter sensitivity study of the saline circulation, *Clim. Dyn.*, *9*, 391–409.

Huang, R. X., and R. W. Schmitt (1993), The Goldsbrough-Stommel circulation of the World Ocean, *J. Phys. Oceanogr.*, *23*, 1277–1284.

Hughes, T. J. R., L. Engel, L. Mazzei, and M. G. Larson (2000), The continuous Galerkin method is locally conservative, *J. Comput. Phys.*, *163*, 467–488.

Ilinka, F., J.-F. Hétu, and D. Pelletier (2000), On stabilized finite element formulations for incompressible advective-diffusive transport and fluid flow problems, *Comput. Meth. Appl. Mech. Eng.*, *188*, 235–255.

Iskandarani, M., D. B. Haidvogel, and J. P. Boyd (1995), A staggered spectral element model with application to the oceanic shallow water equations, *Int. J. Numer. Methods Fluids*, *20*(5), 393–414.

Iskandarani, M., D. B. Haidvogel, and J. C. Levin (2003), A three-dimensional spectral element model for the solution of the hydrostatic primitive equations, *J. Comput. Phys.*, *186*, 397–425.

Kasahara, A. (1974), Various vertical coordinate systems used for numerical weather predictions, *Mon. Weather Rev.*, *102*, 509–522.

Killworth, P. D. (1980), Barotropic and baroclinic instability in rotating stratified fluids, *Dynam. Atmos. Oceans*, *4*, 143–184.

Killworth, P. D., D. Stainforth, D. J. Webb, and S. M. Paterson (1991), The development of a free-surface Bryan-Cox-Semtner ocean model, *J. Phys. Oceanogr.*, *21*, 1333–1348.

Kinnmark, I. (1986), *The Shallow Water Wave Equations: Formulation, Analysis and Applications*, *Lecture Notes in Engineering*, vol. 15, 187 pp., Springer-Verlag.

Kolar, R. L., J. J. Westerink, M. E. Cantekin, and C. A. Blain (1994), Aspects of nonlinear simulations using shallow-water models based on the wave continuity equation, *Comput. Fluids*, *23*(3), 523–538.

Kubatko, E. J., J. J. Westerink, and C. Dawson (2006a), hp Discontinuous Galerkin methods for advection dominated problems in shallow water flow, *Comput. Meth. Appl. Mech. Eng.*, *196*, 437–451.

Kubatko, E. J., J. J. Westerink, and C. Dawson (2006b), An unstructured grid morphodynamic model with a discontinuous Galerkin method for bed evolution, *Ocean Model.*, *15*, 71–89.

Kuo, A. C., and L. M. Polvani (1996), Time-dependent fully nonlinear geostrophic adjustment, *J. Phys. Oceanogr.*, *27*, 1614–1348.

Kuo, H. L. (1949), Dynamic instability of two-dimensional non-divergent flow in a barotropic atmosphere, *Journal of Meteorology*, *6*, 105–122.

Kuo, H. L. (1973), Dynamics of quasigeostrophic flows and instability theory, *Advances in Applied Mechanics*, *13*, 247–330.

Kuo, H. L. (1978), A two-layer model study of the combined barotropic and baroclinic instability in the tropics, *J. Atmos. Sci.*, *35*, 1840–1860.

Labeur, R. J., and J. D. Pietrzak (2005), A fully three dimensional unstructured grid non-hydrostatic finite element coastal model, *Ocean Model.*, *10*, 51–67.

Le Roux, D. Y. (2001), A new triangular finite-element with optimum constraint ratio for compressible fluids, *SIAM J. Sci. Comput.*, *23*(1), 66–80.

Le Roux, D. Y. (2005), Dispersion relation analysis of the $P_1^{NC} - P_1$ finite-element pair in shallow-water models, *SIAM J. Sci. Comput.*, *27*(2), 394–414.

Le Roux, D. Y., and G. F. Carey (2005), Stability/dispersion analysis of the discontinuous Galerkin linearized shallow-water system, *Int. J. Numer. Methods Fluids*, *48*, 325–347.

Le Roux, D. Y., A. Staniforth, and C. A. Lin (1998), Finite elements for shallow-water equation ocean models, *Mon. Weather Rev.*, *126*, 1931–1951.

Le Roux, D. Y., C. A. Lin, and A. Staniforth (2000), A semi-implicit semi-lagrangian finite element shallow-water ocean model, *Mon. Weather Rev.*, *128*, 1384–1401.

Le Roux, D. Y., A. Sène, V. Rostand, and E. Hanert (2005), On some spurious mode issues in shallow-water models using a linear algebra approach, *Ocean Model.*, *10*, 83–94.

Le Roux, D. Y., V. Rostand, and B. Pouliot (in press), Analysis of numerically-induced oscillations in 2D finite-element shallow-water models. Part I: inertia-gravity waves, *SIAM J. Sci. Comput.*, in press.

Legrand, S., V. Legat, and E. Deleersnijder (2000), Delaunay mesh generation for unstructured-grid ocean general circulation model, *Ocean Model.*, *2*, 17–28.

Legrand, S., E. Deleersnijder, E. Hanert, V. Legat, and E. Wolanski (2006), High-resolution unstructured meshes for hydrodynamic models of the Great Barrier Reef, Australia, *Estuar. Coast. Shelf Sci.*, *68*, 36–46.

Legrand, S., E. Deleersnijder, E. Delhez, and V. Legat (accepted), Unstructured, anisotropic mesh generation for the Northwestern European continental shelf, the continental slope and the neighboring ocean, *Cont. Shelf Res.*

Levin, J. C., M. Iskandarani, and D. B. Haidvogel (2006), To continue or discontinue: Comparison of continuous and discontinuous Galerkin formulations in a spectral element ocean model, *Ocean Model.*, *15*, 56–70.

Luettich, R. A., and J. J. Westerink (1995), Continental shelf scale convergence studies with barotropic tidal model, in *Quantitative skill assessment for coastal ocean models*, *Coastal and Estuarine Series*, vol. 47, edited by D. R. Lynch and A. M. Davies, pp. 349–371, American Geophysical Union.

Lynch, D. R., and W. R. Gray (1979), A wave equation model for finite element tidal computations, *Comput. Fluids*, *7*, 207–228.

Lynch, D. R., and C. E. Naimie (1993), The M2 tide and its residuals on the outer banks of the Gulf of Maine, *J. Phys. Oceanogr.*, *23*, 2222–2253.

Lynch, D. R., and F. E. Werner (1987), Three-dimensional hydrodynamics on finite elements. Part I: linearized harmonic model, *Int. J. Numer. Methods Fluids*, *7*, 871–909.

Lynch, D. R., and F. E. Werner (1991), Three-dimensional hydrodynamics on finite elements. Part II: non-linear time-stepping model, *Int. J. Numer. Methods Fluids*, *12*, 507–533.

Lynch, D. R., J. T. C. Ip, C. E. Naimie, and F. E. Werner (1996), Comprehensive coastal circulation model with application to the Gulf of Maine, *Cont. Shelf Res.*, *16*, 875–906.

Marshall, J., C. Hill, L. Perelman, and A. Adcroft (1997), Hydrostatic, quasi-hydrostatic, and nonhydrostatic ocean modeling, *J. Geophys. Res.*, *102*, 5733–5752.

Massey, T. C., and C. A. Blain (2006), In search of a consistent and conservative mass flux for the GWCE, *Comput. Meth. Appl. Mech. Eng.*, *195*, 571–587.

Mellor, G. L., and T. Yamada (1982), Development of a turbulence closure model for geophysical fluids problems, *Review of Geophysics and Space Physics*, *20*, 851–875.

Michalke, A. (1964), On the inviscid instability of the hyperbolic-tangent velocity profile, *J. Fluid Mech.*, *19*, 543–556.

Miglio, E., A. Quarteroni, and F. Saleri (1998), Finite element approximation of quasi-3D shallow water equations, *Comput. Meth. Appl. Mech. Eng.*, *174*, 355–369.

Muccino, J. C., W. G. Gray, and M. G. G. Foreman (1997), Calculation of vertical velocity in three-dimensional, shallow-water equation, finite element models, *Int. J. Numer. Methods Fluids*, *25*, 779–802.

Munk, W. H., and E. R. Anderson (1948), Notes on a theory of the thermocline, *J. Mar. Res.*, *3*, 276–295.

Myers, P. G., and A. J. Weaver (1995), A diagnostic barotropic finite-element ocean circulation model, *J. Atmos. Ocean. Technol.*, *12*, 511–526.

Nair, R. D., S. J. Thomas, and R. D. Loft (2005), A discontinuous Galerkin global shallow water model, *Mon. Weather Rev.*, *133*(4), 876–888, doi:10.1175/MWR2903.1.

Nechaev, D., J. Schröter, and M. Yaremchuk (2003), A diagnostic stabilized finite-element ocean circulation model, *Ocean Model.*, *5*, 37–63.

Pain, C. C., M. D. Piggott, A. J. H. Goddard, F. Fang, G. J. Gorman, D. P. Marshall, M. D. Eaton, P. W. Power, and C. R. E. de Oliveira (2004), Three-dimensional unstructured mesh ocean modelling, *Ocean Model.*, *10*, 5–33.

Pedlosky, J. (1964), The stability of currents in the atmosphere and the ocean: Part I, *J. Atmos. Sci.*, *2*, 201–219.

Pedlosky, J. (1979), *Geophysical Fluid Dynamics*, Springer-Verlag.

Pietrzak, J., E. Deleersnijder, and J. Schröter (Eds.) (2005), *The Second International Workshop on Unstructured Mesh Numerical Modelling of Coastal, Shelf and Ocean Flows*, *Ocean Model.*, vol. 10, 252 pp., Elsevier.

Pietrzak, J., M. Iskandarani, J. Schröter, and F. Lyard (Eds.) (2006), *The Third International Workshop on Unstructured Mesh Numerical Modelling of Coastal, Shelf and Ocean Flows*, *Ocean Model.*, vol. 15, 138 pp., Elsevier.

Piggott, M. D., C. C. Pain, G. J. Gorman, P. W. Power, and A. J. H. Goddard (2005), h, r, and hr adaptivity with applications in numerical ocean modelling, *Ocean Model.*, *10*, 95–113.

Power, P. W., M. D. Piggott, F. Fang, G. J. Gorman, C. C. Pain, D. P. Marshall, A. J. H. Goddard, and I. M. Navon (2006), Adjoint goal-based error norms for adaptive mesh ocean modelling, *Ocean Model.*, *15*, 3–38.

Rahmstorf, S. (1996), On the freshwater forcing and transport of the Atlantic thermohaline circulation, *Clim. Dyn.*, *12*, 799–811.

Redi, M. H. (1982), Oceanic isopycnal mixing by coordinate rotation, *J. Phys. Oceanogr.*, *12*, 1154–1158.

Remacle, J.-F., X. Li, M. S. Shephard, and J. E. Flaherty (2005), Anisotropic adaptive simulation of transient flows using discontinuous Galerkin methods, *Int. J. Numer. Methods Eng.*, *62*, 899–923.

Remacle, J.-F., S. Soarez Frazão, X. Li, and M. S. Shephard (2006), An adaptive discretization of shallow-water equations based on discontinuous Galerkin methods, *Int. J. Numer. Methods Fluids*, *52*, 903–923.

Rivière, B., and V. Girault (2006), Discontinuous finite element methods for incompressible flows on subdomains with non-matching interfaces, *Comput. Meth. Appl. Mech. Eng.*, *195*, 3274–3292.

Roe, P. L. (1981), Approximate Riemann solvers, parameter vectors and difference schemes, *J. Comput. Phys.*, *43*, 357–372.

Roullet, G., and G. Madec (2000), Salt conservation, free surface and varying levels: a new formulation for ocean general circulation models, *J. Geophys. Res.*, *105*(C10), 23,927–23,942.

Ruddick, K. G., E. Deleersnijder, T. De Mulder, and P. J. Luyten (1994), A model study of the Rhine discharge front and downwelling circulation, *Tellus Ser. A*, *46*, 149–159.

Schwanenberg, D., and M. Harms (2004), Discontinuous Galerkin finite-element method for transcritical two-dimensional shallow water flows, *Journal of Hydraulic Engineering*, *130*(5), 412–421.

Schwanenberg, D., R. Kiem, and J. Kongeter (2000), A discontinuous Galerkin method for the shallow-water equations with source terms, in *Discontinuous Galerkin Methods: Theory, Computations and Applications*, *Lecture Notes in Computational Science and Engineering*, vol. 11, edited by B. Cockburn, G. E. Karniadaki, and C.-W. Chu, pp. 419–424, Springer, Berlin.

Simons, T. J. (1974), Verification of numerical models of Lake Ontario: Part I. Circulation in spring and early summer, *J. Phys. Oceanogr.*, *4*(4), 507–523.

Smagorinsky, J. (1963), General circulation experiments with the primitive equations. 1 The basic experiment, *Mon. Weather Rev.*, *91*(5), 99–165.

Song, Y. T., and T. Y. Hou (2006), Parametric vertical coordinate formulation for multiscale, Boussinesq, and non-Boussinesq ocean modelling, *Ocean Model.*, *11*, 298–332.

Stuhne, G. R., and W. R. Peltier (2006), A robust unstructured grid discretization for 3-dimensional hydrostatic flows in spherical geometry: A new numerical structure for ocean general circulation modeling, *J. Comput. Phys.*, *213*, 704–729.

Walters, R. A. (1992), A three-dimensional, finite element model for coastal and estuarine circulation, *Cont. Shelf Res.*, *12*, 83–102.

Walters, R. A. (2005), Coastal ocean models: two useful finite element methods, *Cont. Shelf Res.*, *25*, 775–793.

Walters, R. A. (2006), Design considerations for a finite element coastal ocean model, *Ocean Model.*, *15*, 90–100, doi:10.1016/j.ocemod.2005.11.002.

Walters, R. A., and F. E. Werner (1989), A comparison of two finite element models of tidal hydrodynamics using the North Sea data set, *Adv. Water Resour.*, *12*, 184–193.

White, L., and E. Deleersnijder (in press), Diagnoses of vertical transport in a three-dimensional finite-element model of the tidal circulation around an island, *Estuar. Coast. Shelf Sci.*, doi:10.1016/j.ecss.2006.07.014.

White, L., J.-M. Beckers, E. Deleersnijder, and V. Legat (2006a), Comparison between free-surface and rigid-lid finite element models of barotropic instabilities, *Ocean Dynamics*, *56*, 86–103, doi:10.1007/s10236-006-0059-0.

White, L., V. Legat, E. Deleersnijder, and D. Le Roux (2006b), A one-dimensional benchmark for the propagation of Poincaré waves, *Ocean Model.*, *15*, 101–123, doi:10.1016/j.ocemod.2005.11.001.

White, L., E. Deleersnijder, and V. Legat (submitted), A three-dimensional unstructured mesh finite element marine model, with application to the flow around a shallow-water island, *J. Geophys. Res.*

Williamson, D. L., J. B. Drake, J. J. Hack, R. Jakob, and P. N. Swarztrauber (1992), A standard test set for numerical approximations to the shallow water equations in spherical geometry, *J. Comput. Phys.*, *102*, 211–224.

Wolanski, E. (1994), *Physical oceanographic processes of the Great Barrier Reef*, CRC Marine Science Series, CRC Press.

Wolanski, E., and W. M. Hamner (1988), Topographically controlled fronts in the ocean and their biological influence, *Science*, *241*(4862), 177–181.

Wolanski, E., J. Imberger, and M. L. Heron (1984), Island wakes in shallow coastal waters, *J. Geophys. Res.*, *89*(C6), 10,553–10,569.

Wolanski, E., E. Drew, K. M. Abel, and J. O'Brien (1988), Tidal jets, nutrient upwelling and their influence on the productivity of the alga Halimeda in the Ribbon Reefs, Great Barrier Reef, *Estuar. Coast. Shelf Sci.*, *26*(2), 169–201.

Wolanski, E., T. Asaeda, A. Tanaka, and E. Deleersnijder (1996), Three-dimensional island wakes in the field, laboratory experiments and numerical models, *Cont. Shelf Res.*, *16*(11), 1437–1452.

Wolanski, E., R. Brinkman, S. Spagnol, F. McAllister, C. Steinberg, W. Skirving, and E. Deleersnijder (2003), Merging scales in models of water circulation: perspectives from the Great Barrier Reef, in *Advances in Coastal Modeling*, *Elsevier Oceanography Series*, vol. 67, edited by V. C. Lakhan, chap. 15, pp. 411–429, Elsevier Science.

Vita

Laurent White was born on 10 November 1979 in Uccle, Belgium. He obtained his high school diploma from Collège Cardinal Mercier in Braine l'Alleud (Belgium). In 1997, he joined the Université catholique de Louvain in Louvain-la-Neuve (Belgium) to undertake studies in engineering. He obtained his diploma in Engineering in Applied Mathematics in June 2002 and then pursued studies at the University of Texas at Austin (Texas, USA). Under the supervision of Professor Ben R. Hodges, he earned a Master of Science in Civil Engineering in December 2003. Upon completion of his master's degree, he returned to Belgium to start a PhD at the Université catholique de Louvain with focus on finite element ocean modeling under the supervision of Professor Eric Deleersnijder and Professor Vincent Legat. He is currently a Research Fellow with the Belgian National Fund for Scientific Research (FNRS).